UNIVERSITÀ DEGLI STUDI DI MILANO

Scuola di Dottorato in Fisica, Astrofisica e Fisica Applicata

Dipartimento di Fisica

Corso di Dottorato in Fisica, Astrofisica e Fisica Applicata

Ciclo XXIX

Search for new physics in the diphoton channel at the ATLAS experiment at the LHC

Settore Scientifico Disciplinare FIS/04, FIS/01

Supervisori:
Prof. Leonardo CARMINATI
Dott. Marco DELMASTRO

Coordinatore: Professor Francesco RAGUSA

Tesi di Dottorato di:

Simone Michele MAZZA

Anno Accademico 2016/17

Commission of the final examination:

External Referee:
Guillaume UNAL (CERN)

Mauro DONEGA' (ETH Zurich)

External Members:
Karl JAKOBS (Physikalisches Institut Freiburg)

Marumi KADO (LAL, Orsay)

Tommaso TABARELLI (Universita' Milano Bicocca)

Final examination:

February 27th, 2017

Università degli Studi di Milano, Dipartimento di Fisica, Milano, Italy

To my mother, always in my heart

Cover illustration:

Photo of Mt. Blanc from the Reculet (1.718 m), Jura Mountains. November 2016.

MIUR subjects:

FIS/01
FIS/04

PACS:

14.70.Bh
14.80.Ec
14.70.Kv

Contents

Introduction

0.1 General introduction

During the three years of my PhD I worked in the ATLAS experiment which is one of the four main detectors installed at the proton-proton collider LHC at CERN. I first joined the collaboration back in 2010 for my bachelor thesis where I estimated the purity of photons with an in-situ method in the first fb^{-1} of data collected by ATLAS. I then did my master thesis in ATLAS on the search of an Higgs boson decaying in two photons + E_T^{miss} (Missing transverse momentum) on 20.7 fb^{-1} of data collected by ATLAS in 2012 at center of mass energy of 8 TeV. I presented my thesis work on the SIF annual conference of 2013 in Trieste and I was awarded a prize as second better communication. The prize consisted in a publication on Nuovo Cimento C [1].

During my thesis and afterwards I also contributed to the measurement of the Higgs boson mass in the diphoton decay channel by helping in deriving the signal parameterization and performing the optimization of the categories. I built a signal model with parameters depending on M_{Higgs} to fit simultaneously on several Monte Carlo sample that were obtained summing all the production modes of the SM Higgs. For my contribution I obtained the exceptional authorship for the Higgs mass measurement paper [2].

After my studies I started my PhD at the Milano University at the beginning of 2014. To become ATLAS author I performed my qualification in the computing area. I studied the feasibility to use PoD (Proof on Demand) for a large scale ATLAS analysis. With this tool it was possible for the user to create ad-hoc interactive clusters on the grid. I tested it on several Italian sites and proven it to be compatible with the (at the time) ATLAS software environment. This work eventually lead to a publication [3].

I was always interested in the big physics questions of the modern day and I wanted to work for a possible answer to one of them, in particular I was interested in the Hierarchy problem. I found fascinating how extra dimensions in the context of a theory of quantum gravity can give an answer to this question. For this reason during my PhD I committed myself to the search of gravitons in the diphoton channel.

I started contributing in the search for RS graviton's [4, 5] spin-2 resonances in the diphoton channel on 3.2 fb^{-1} collected in 2015 at $\sqrt{s} = 13$ TeV. Then I moved on to the general search of resonances in this final state, either spin-2 graviton or spin-0 Higgs (in run-I respectively [6],[7]) using the full statistic of 37.1 fb^{-1} collected in 2015 and 2016. During my work I acted as analysis contact for the spin-2 search from June until January and I was among the editors of the very first diphoton public note in December 2015 [8]. I found the physics behind this search very interesting both on the theoretical level and in the practical/experimental level. I found this analysis very exciting as I was deeply involved in the 750 GeV excess adventure from the very beginning.

The first sign of an excess was seen in November 2015, the news shocked the collaboration since it was a very promising excess and it was unexpected. The analysis team worked day and night to prepare the results for the December physics Jamboree. It was an overall very stressful period, especially because rumors were going around about a similar excess seen in the CMS collaboration. Outside of the ATLAS and CMS collaborations news about a potential new particle discovery where flying around. The results for the spin-0 analysis were made public in December 2015, then in the Moriond conference both analyses where made public.

Data from year 2016 were analyzed and the statistical results were produced in a few days after the first batch of data was released. The analysis team worked really hard to prepare the results in the very short time scale, I was among the first one to look at the results since I was taking care of the statistical environment. However the results were not exciting, the excess was gone with the new dataset. Despite the fact that the excess was not confirmed I found this period very important for my professional growth.

During my PhD I also worked in other fields other than pure analysis such as developing parts of the e-gamma group derivation framework, develop and maintain the tool taking care of photon/electron isolation corrections, derive these isolation corrections with an innovative method and some minor work for photon Identification. I contributed to the ATLAS data taking doing several shifts in control room for the Calo/forward desk and afterwards as hardware expert on call for the Liquid Argon (LAr) calorimeter. I also did some hardware work taking care and developing the framework of the LAr calorimeter high voltage system. My work on the high voltage of the ATLAS Liquid Argon calorimeter is introduced in more detail in Appendix B.

0.2 Thesis introduction

The topic of this thesis is the search for resonances in the diphoton invariant mass spectrum. These resonances are predicted by several models beyond the Standard Model. The analysis of data provided by the ATLAS detector [9] during the Run-2 (years 2015-2016) of LHC will be presented. The diphoton decay channel is used both for precision measurement, for example for the measurement of the Higgs boson mass, and for discovery of BSM physics, for example search for Gravitons in the extra dimension context and Higgs bosons in the Two Higgs doublet model (2HDM) context. Public results for this analysis were released in December 2015 [8], in Moriond 2016 [10] with 3.2 fb^{-1} of data collected in 2015 and in ICHEP 2016 [11] with the addition of

12.2 fb^{-1} of data collected in 2016. The same search was conducted by the CMS collaboration as reported in References [12, 13] for data from year 2015 and 2016 respectively.

In the ATLAS detector photons are reconstructed combining the information from the tracker and the electromagnetic calorimeter: the energy of the photons is measured in the calorimeter while the inner detector is used to reconstruct conversions. Their signature is quite simple and they are reconstructed and measured with a good energy resolution, purity and selection efficiency. The main background in photon-related analyses is coming from jets mis-identified as photons, therefore rectangular selection cuts are applied on the shower shapes of the photons. Furthermore an additional selection based on the isolation[1] of the candidates is applied.

The diphoton channel was proven to be a very interesting channel and it led to the discovery of the Higgs boson. It has a number of good features like the clean experimental signature, the excellent diphoton mass resolution, and modest jet background. Only particles with integer spin (but different than 1) can decay in a couple of photons. An excess in the diphoton spectrum at high-energy, together with a spin analysis, could be interpreted as the decay of a Graviton (spin-2) or an exotic Higgs boson (spin-0).

0.2.1 Graviton

A graviton would be the mediator of the gravitational force, it would be a tensor boson: a massless particle with spin 2. Graviton massive excited states are predicted by several models in the attempt to solve the hierarchy problem, which is: why the electroweak scale is 17 orders of magnitude smaller than the Planck scale? These models postulate the existence of extra spatial dimensions where only gravitons can propagate, while other SM particles are confined in the usual 3 space dimensions. In this way the gravitational force we observe would be only a projection of the true gravitational force, and so it would appear weak. Gravitons would be produced at LHC by gluons or quarks fusion as in Figure 1.

If the Randall-Sundrum (RS) model is considered, such gravitons would appear as a series of large separate resonances [14, 15] over the smoothly falling SM diphoton background. The RS model has two free parameters: the mass of the least energetic resonance and the coupling to the SM fields $k/\overline{M}_{\mathrm{Pl}}$which is proportional to the width of the resonance.

Another model which predicts Gravitons decays in the diphoton channel is the Arkani-Hamed, Dimopoulos, Dvali (ADD) [16] model: an ADD graviton exchange would result in a set of resonance too close in energy to be resolved by the ATLAS and CMS calorimeters, so a non-resonant deviation from the SM background expectation would be observed. In this thesis only the results regarding graviton from RS model will be discussed.

In run I ATLAS publication [17] based on 20.7 fb^{-1} at 8 TeV collision [18] no significant deviation from the expected background was observed (Figure 2). In the context of the RS model, a lower limit of 2.66 TeV at 95 % CL is set on the mass of the lightest graviton for coupling of $k/\overline{M}_{\mathrm{Pl}}$= 0.1. The search for extra dimension was also done at 7 TeV by the CMS experiment as seen in Reference [19].

[1] Energy in a cone around the candidate

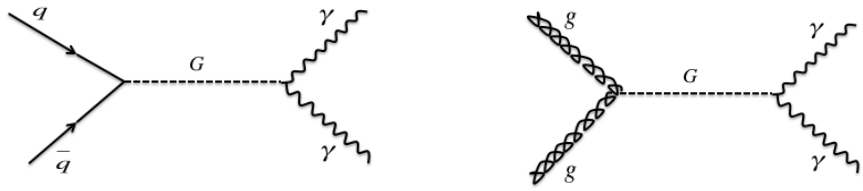

Figure 1: Production of Gravitons at LHC via gluon or quark fusion.

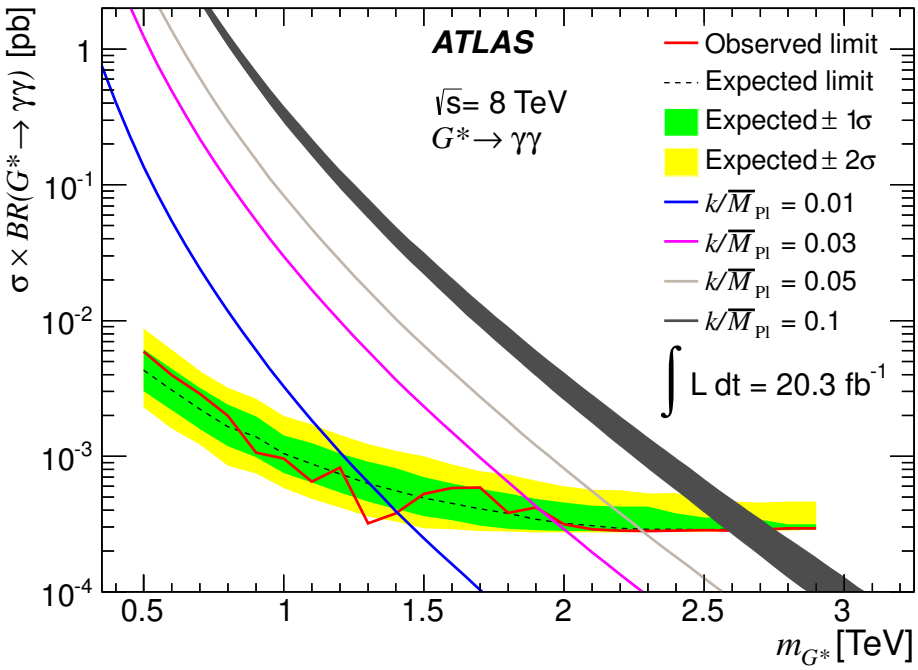

Figure 2: Expected and observed upper limits on σ x BR(G*$\longrightarrow \gamma\gamma$) expressed at 95% CL, as a function of the assumed value of the graviton mass. At large mG*, the -1σ and -2σ variations of the expected limit tend to be particularly close to the expected limit. This is expected, since signals with high m_G would appear in regions of $m_{\gamma\gamma}$where the background expectation is small and the Poissonian fluctuations around the mean expected background are highly asymmetric. The curves show the RS model prediction for given values of $k/\overline{M}_{\rm Pl}$ as a function of m_G. They are obtained using the PYTHIA generator plus a K-factor to account for NLO corrections. The thickness of the theory curve for $k/\overline{M}_{\rm Pl} = 0.1$ illustrates the PDF uncertainties expressed at 90% CL [17].

0.2.2 Higgs

If a particle with spin 0 is observed in the diphoton spectrum at high-energy it can be interpreted as the decay of a second Higgs boson. Several extensions of the Higgs sector foresee additional scalar states [20–26]; for example the 2HDM model predicts five physical states (h, H, A, H+, H-), h or H can be H(125), the other (H or h) can have sizable decay in two photons.

The search for an additional Higgs boson is in fact divided in two mass regions: High mass search (150 GeV on) and Low mass search (50-150 GeV). Low mass search is trickier, because the background from SM Higgs and electrons from Z^0 decay reconstructed as photons have to be considered. In the context of this thesis only the high mass search will be discussed. The resulting resonance is expected to have either zero intrinsic width (broadened by experimental effects) or a large instrinsic width.

Exotic higgs searches [7] in run 1 showed no significant deviation from SM model (Figure 3). CMS search for exotic Higgs in the 2HDM model can be found in Reference [27].

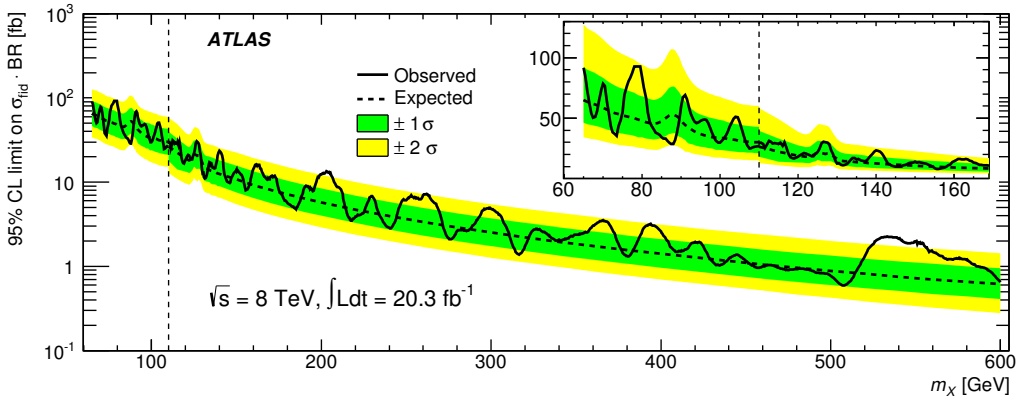

Figure 3: Observed and expected 95% CL limit on the fiducial cross-section times branching ratio BR(X$\longrightarrow$ $\gamma\gamma$) as a function of $M_X$in the range 65 < M_X< 600 GeV. The discontinuity in the limit at M_X= 110 GeV (vertical dashed line) is due to the transition between the low-mass and high-mass analyses. The green and yellow bands show the ± 1σ and ± 2σ uncertainties on the expected limit. The inset shows a zoom of the limit [7].

Part I

Theory introduction

CHAPTER 1

The Standard Model

1.1 Standard Model introduction

The Standard Model is a quantum field theory that describes three of the four known fundamental forces (strong and electro-weak interaction) among all the elementary matter particles. A summary of particles and force carriers can be found in Figure 1.1. In the SM there are six quarks with fractional charge $(2/3, 1/3)$, three charged leptons with unitary charge and three neutrinos. Interactions are described by gauge symmetry, $SU(3)$[1] for the strong interaction and $SU(2) \bigotimes U(1)$ for the electro-weak interaction.

The only force that is not included in the Standard Model is gravity. However several beyond Standard Model (BSM) models add quantum gravity to the SM, as will be discussed in Chapter 2.

An important feature of the Standard Model is that it is presently consistent with, or verified by, all available data, with no compelling evidence for physics beyond it.

1.2 Introduction to QED gauge model

Electromagnetism is a well-known example of a gauge theory [28]. In this case the gauge transformations are local complex phase transformations of the fields of charged particles. To preserve the gauge invariance a massless vector (spin-1) particle, called the photon, has to be introduced as the mediator of the electromagnetic interactions. The simple lagrangian of a free Dirac field ψ has the form:

$$\mathcal{L} = \bar{\psi} \left(i\gamma^{\mu} \partial_{\mu} - m \right) \psi \tag{1.1}$$

This type of lagrangian is invariant under a phase transformation of the field $\psi \rightarrow e^{iQ\omega}\psi$, where ω is coordinate independent. This means that the lagrangian is invariant under global U(1) transformations. A more interesting argument would be a lagrangian that is invariant under a local phase transformation, that is with parameters that depends on space-time coordinates. Such local transformations are called *gauge transformations*. We'll consider only the linear approximation of the transformation: $\psi \rightarrow e^{iQ\omega}\psi \rightarrow \psi + \delta\psi$ with $\delta\psi = iQ\omega(x)\psi(x)$. However the lagrangian in 1.1

[1] Special unity group

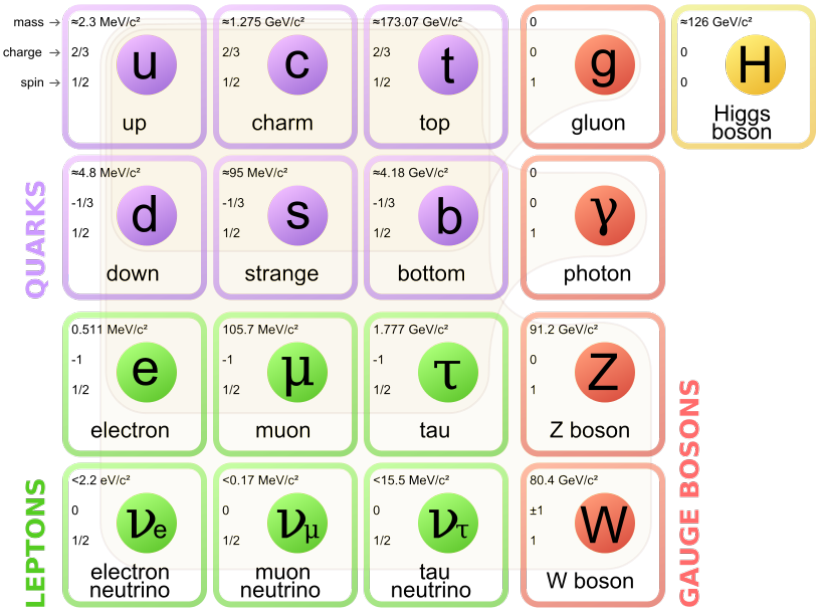

Figure 1.1: Standard model particles

is no longer invariant under this transformation, and to make it invariant we need an additional term $\delta\mathcal{L}$ in the lagrangian: the field ψ has to interact with a vector field and the partial derivative ∂ must change into a covariant derivative: $\partial_\mu + ieQA_\mu$. The vector field A_μ is called the *gauge field*.

In addition to make this working we must also assume that the gauge field also changes with phase transformation $A_\mu \rightarrow A_\mu + \delta A_\mu$ with a coordinate depending transformation. To achieve this we can add in the lagrangian the saturation of the Faraday tensor $F^{\mu\nu} = \partial_\mu A_\nu - \partial_\nu A_\mu$, which is invariant under phase transformation. We can now write the QED lagrangian that we derived under the general assumptions of phase invariance:

$$\mathcal{L} = -\frac{1}{4}F_{\mu\nu}F^{\mu\nu} + \bar{\psi}\left(i\gamma^\mu\left(\partial_\mu + ieQA_\mu\right) - m\right)\psi \tag{1.2}$$

Note that we are not allowed to add a mass term for the photon: a term such $M^2A_\mu A^\mu$ would break the phase invariance that we carefully built. Furthermore such an addition would result in a e^{-Mx} attenuation factor in the electromagnetic field strenght and it is known that the electromagnetic interaction is a long range interaction.

1.3 Introduction to electro-weak model

A long journey starting with the parity violation in beta decay has brought to the current modelization of the weak force. Today we know that weak and electromagnetic forces are tightly bound

together. In the 1950s Yang and Mills considered extending gauge invariance to include local non-abelian (i.e. non-commuting) transformations such as SU(2) [29]. In this case one needs a set of massless vector fields (three in the case of SU(2)), which were formally called Yang-Mills fields, but are now known as gauge fields. In order to apply such a gauge theory to weak interactions, one considers particles which transform into each other under the weak interaction, such as a u-quark and a d-quark, or an electron and a neutrino, to be arranged in doublets of weak isospin.

The three gauge bosons are interpreted as the W^+W^- and W^0 bosons, that mediate weak interactions in the same way that the photon mediates electro-magnetic interactions. This model only describes the weak interaction and the symmetry group has to incorporate electromagnetic interactions. The right symmetry group is $SU(2)_L \bigotimes U(1)_Y$: gauge invariance under SU(2) introduces three bosons W^+W^- and W^0 and U(1) only one boson B^0.

The subscript L (respectively, R) refers to the left or right handed chirality state of the fermion; $\psi_L = \Delta_L\psi, \psi_R = \Delta_R\psi$ where Δ_R, Δ_L are the right and left chirality projectors. The phenomenology of charged current weak interactions suggests that they arise from a local $SU(2)_L$ symmetry of the Lagrangian: the subscript L indicates that only left-handed chirality states of fermions participate to this kind of interactions. For this reason, left-handed particles are grouped into weak isospin doublets with $T = \frac{1}{2}$ and $T_3 = \pm\frac{1}{2}$.

The right-handed fermion states - which enter only in neutral current weak interactions and electromagnetic ones as well - are classified instead into weak isospin singlets ($T = 0, T_3 = 0$). Since it is an experimental evidence that neutrinos exist only in left-handed chirality states, right-handed neutrinos must have zero coupling both to SU(2) and U(1).

The actual physical boson are a rotation of angle $\sin^2(\theta_W) \cong 0.24$ where θ_W is the Weinberg angle. The corresponding real bosons are W^+W^-, Z^0 and γ (Formula 1.3). This accounts for the left and right symmetry breaking in the electro-weak sector, W^+W^- are only left current bosons, γ has the same coupling for left and right current and Z^0 has different left and right coupling. Furthermore $\cos(\theta_W)$ is the proportional constant between Z^0 and W^+W^- mass (Formula 1.4).

$$\begin{pmatrix} \gamma \\ Z^0 \end{pmatrix} = \begin{pmatrix} \cos(\theta_W) & \sin(\theta_W) \\ -\sin(\theta_W) & \cos(\theta_W) \end{pmatrix} \cdot \begin{pmatrix} B^0 \\ W^0 \end{pmatrix} \tag{1.3}$$

$$m_Z = \frac{m_W}{\cos(\theta_W)} \tag{1.4}$$

Within the unified framework, electromagnetic interaction arises from the exchange of a neutral gauge boson resulting from the mixing of the neutral gauge bosons from the $SU(2)_L$ group and the $U(1)_Y$ group. The resulting electric charge is not exactly the U(1) charge Y (hypercharge) but is given by the Gell-Mann-Nishijima formula:

$$Q = T_3 + \frac{Y}{2} \tag{1.5}$$

1.3.1 QCD and quarks

To introduce the quark sector of the electro-weak model a brief introduction on QCD must be done. The idea of an elementary component inside hadrons was first theorized in 1964 by physicists Murray Gell-Mann and George Zweig. This introduced the idea of elementary particles called partons which were free inside the hadrons. However the first evidence of physical existence of partons was in 1968 with the deep inelastic scattering experiments of electrons on nucleons done in the Stanford Linear Accelerator Center [30], [31].

This model lead to some discrepancies with the observed data. It was shown that only half of the hadron's momentum was carried by the partons and there was no theory explicating why the partons were confined in the hadrons and couldn't be seen in a free particle state. Furthermore the discovery of the hadron Δ^{++} composed of three quark up with spin=+3/2 shocked the particle world, because the quarks inside the hadron had the same quantum numbers and apparently didn't respect the Pauli principle. In 1965 two independent groups composed by Moo-Young Han with Yoichiro Nambu and Oscar W. Greenberg resolved the problem by proposing that quarks possess an additional SU(3) gauge degree of freedom, later called color charge. Afterwars the Quantum Chromo Dynamics (QCD) theory was established to describe the interactions between quarks and gluons. Evidence of this theory can be seen in many experiments like neutrino scattering with nuclei and the evidence of gluons was discovered in three-jet events at PETRA in 1979.

The new degree of freedom, the *color*, is similar to a charge in electrodynamics. Forces between quark of different colors are attractive and only colorless particle can be in free particle state. The force carriers of this theory are 8 (corresponding to the 8 generators of the SU(3) group) bi-colored gluons (carrying a color and an anti-color). Similarly to what we did for QED the QCD lagrangian can be studied under phase invariance (or gauge symmetry).

In the quark sector of the electro-weak model we can't classify the quark families as weak isospin doublets and singlets. This is a bit tricky because the flavour eigenstates do not correspond to the mass eigenstates. The result is a rotation matrix between the eigenstates of the two symmetry groups, this accounts for the flavor violation of some electroweak transitions. The rotation matrix is called the CKM[2] matrix:

$$\begin{pmatrix} d' \\ s' \\ b' \end{pmatrix} = \begin{pmatrix} V_{ud} & V_{us} & V_{ub} \\ V_{cd} & V_{cs} & V_{cb} \\ V_{td} & V_{ts} & V_{tb} \end{pmatrix} \cdot \begin{pmatrix} d \\ s \\ b \end{pmatrix} \tag{1.6}$$

This leads, considering the different masses of the quark families, to CP violation of some processes in the electroweak sector. CP violation was first observed in the context of mixing of the $K^0, \bar{K^0}$ oscillations.

[2] Cabibbo-Kobayashi-Maskawa

1.3.2 Electro-weak gauge model

Similar to the QED gauge theory[28] we can start from a free lagrangian for a Dirac massless field:

$$\mathcal{L}_{EW}^{free} = i\bar{\psi}_L\gamma^\mu\partial_\mu\psi_L + i\bar{\psi}_R\gamma^\mu\partial_\mu\psi_R \tag{1.7}$$

The local gauge transformations for the $SU(2)_L \bigotimes U(1)_Y$ symmetry group are:

$$\psi(x) \rightarrow \psi'(x) = e^{i\frac{g'}{2}\alpha_0 Y + ig\,\Sigma_{k=1}^{3}\alpha_k T^k}\psi(x) \tag{1.8}$$

Where Y is the hypercharge operator and T^k the three components of the weak isospin (k=1,2,3). α_0, α_k are parameters of transformation and g, g' are the coupling constants of the two symmetry groups. We will apply the same procedure as before (1.2) and build a covariant derivative:

$$D_\mu = \partial_\mu + i\frac{g'}{2}B_\mu Y + igT_k W_\mu^k \tag{1.9}$$

We must remember that the weak charged part only interact with the left part of the field, furthermore the left part of the spinor ψ_L is a weak doublet and the right part ψ_R is a weak singlet. The interaction term of the lagrangian becomes:

$$\mathcal{L}_{EW}^{int} = -\frac{g'}{2}\left(\bar{\psi}\gamma_\mu Y\psi\right)B^\mu - g\left(\bar{\psi}_L\gamma_\mu T^k\psi_L\right)W_k^\mu \tag{1.10}$$

Finally we can add the Yang-Mills term (or gauge fields term) as we did with the QED lagrangian:

$$\mathcal{L}_{EW}^{GF} = -\frac{1}{4}F_{\mu\nu}^k F_k^{\mu\nu} - \frac{1}{4}G_{\mu\nu}G^{\mu\nu} \tag{1.11}$$

with $F_k^{\mu\nu} = \partial_\mu W_\nu^k - \partial_\nu W_\mu^k - g\epsilon_{klm}W_\mu^l W_\nu^m$ and $G_k^{\mu\nu} = \partial_\mu B_\nu - \partial_\nu B_\mu$. The final lagrangian is the sum of the three terms:

$$\mathcal{L}_{EW} = \mathcal{L}_{EW}^{free} + \mathcal{L}_{EW}^{GF} + \mathcal{L}_{EW}^{int} \tag{1.12}$$

Note that in the previous calculations we didn't take into account neither the mass of the bosons or the mass of the fermions. Explicit mass terms would spoil the gauge invariance. Since we have experimental proof that both fermions and $W^\pm/Z_0$ have a non-zero mass a mechanism to reproduce mass terms in the electro-weak model has to be provided.

1.3.3 Symmetry breaking

In a physic system, that can be symmetric in the theory formulation, the fate can be decided by small fluctuations if a critical point is crossed, thus determining which branch of a bifurcation is taken. This choice would appear arbitrary to an outside observer unaware of these small fluctuations. This phenomenon is called symmetry breaking, such transitions usually bring the system from a symmetric but disorderly state into one or more definite states. Symmetry breaking

can be divided into two types: explicit symmetry breaking and spontaneous symmetry breaking. In the first one the equations of motion fail to be invariant, in the second one the ground state fails to be invariant.

Spontaneous symmetry breaking is a phenomenon that is by far not restricted to gauge symmetries. It is a subtle way to break a symmetry but still requiring that the Lagrangian remains invariant under the symmetry transformation. In order to illustrate the idea of spontaneous symmetry breaking, consider a pen that is completely symmetric with respect to rotations around its axis. If we balance this pen on its tip on a table, and start to press on it with a force precisely along the axis we have a perfectly symmetric situation. This corresponds to a Lagrangian which is symmetric (under rotations around the axis of the pen in this case). However, if we increase the force, at some point the pen will bend (and eventually break). The question then is in which direction will it bend. Of course we do not know, since all directions are equally probable. But the pen will pick one and by doing so it will break the rotational symmetry.

1.3.4 U(1) as a simple example of gauge theory with broken symmetry

As a simple more quantitative example we can use the abelian U(1) symmetry of the electromagnetic field. Let's consider a complex scalar field coupled both to itself and to an electromagnetic field:

$$\mathcal{L} = -\frac{1}{4}F_{\mu\nu}F^{\mu\nu} + |D_\mu\phi|^2 - V(\phi) \tag{1.13}$$

with $D_\mu = \partial_\mu + ieA_\mu$ the covariant derivative and a potential $V(\phi)$:

$$V(\phi) = \mu^2\phi^*\phi + \lambda|\phi^*\phi|^2 \tag{1.14}$$

with a mass term μ and a four-way interaction vertex λ for the gauge field ϕ. The lagrangian is invariant under the local U(1) phase transformation $\phi \rightarrow e^{-iw(x)}\phi$. The potential in 1.14 has a minimum in $\phi = 0$. However if the first term of the potential is changed to $-\mu^2$ the minimum is no longer in the origin but in some point $\phi = e^{i\theta}\sqrt{\frac{\mu^2}{2\lambda}}$ where θ can have any value from 0 to 2π. There is an infinite number of states each with the same lowest energy, i.e. we have a degenerate vacuum as seen in Figure 1.2.

The symmetry breaking occurs in the choice made for the value of θ which represents the true vacuum. For convenience we can choose $\theta = 0$ to be our vacuum. Such a choice constitutes a spontaneous breaking of the U(1) invariance, since a U(1) transformation takes us to a different lowest energy state. In other words the vacuum breaks U(1) invariance. In quantum field theory we say that the field ϕ has a non-zero vacuum expectation value. But this means that there are excitations with zero energy, that take us from the vacuum to one of the other states with the same energy. The only particles which can have zero energy are massless particles (with zero momentum). We therefore expect a massless particle in such a theory. To see that we do indeed

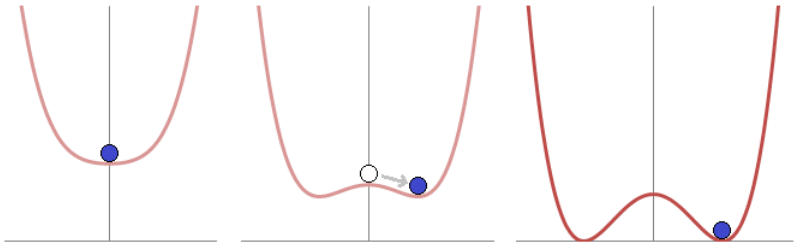

Figure 1.2: Spontaneous symmetry breaking simplified. At high energy levels (left) the ball settles in the center, and the result is symmetrical. At lower energy levels (right), the overall "rules" remain symmetrical, but the "Mexican hat" potential comes into effect: "local" symmetry is inevitably broken since eventually the ball must roll one way (at random) and not another.

get a massless particle, we can expand ϕ around its vacuum expectation value

$$\phi \cong \frac{1}{\sqrt{2}}\left(\frac{\mu}{\sqrt{\lambda}}\right) + H + i\phi \tag{1.15}$$

The fields H and ϕ have zero vacuum expectation values and these are the fields that are expanded in terms of creation and annihilation operators of the particles that populate the excited states. We now want to write the Lagrangian potential in terms of the H and ϕ fields.

$$V = \mu^2 H^2 + \mu\sqrt{\lambda}\left(H^3 + \phi^2 H\right) + \frac{\lambda}{4}\left(H^4 + \phi^4 + 2H^2\phi^2\right) + \frac{\mu^4}{4\lambda} \tag{1.16}$$

Note that there is a mass term for the H field but there is no mass term for the field ϕ. ϕ is a field for a massless particle called the *Goldstone boson*. Substituting the potential V into the kinetic term we can see that the gauge boson A_μ acquires a mass term $\frac{1}{2}g^2v^2A_\mu A^\mu = \frac{1}{2}M_A^2 A_\mu A^\mu$. Furthermore there is a coupling term between the gauge boson A^μ and the H field $gM_A A_\mu A^\mu H$. It is important to remember that this coupling is proportional to the mass of the gauge boson. Finally, there is also the bilinear term $-M_A\phi\partial_\mu A^\mu$. This mixes the Goldstone boson, ϕ, with the longitudinal component of the gauge boson, with strength M_A (when the gauge-boson field A_μ is separated into its transverse and longitudinal components). The H-field that corresponds to the 'Higgs' boson [32–34].

The number of goldstone bosons is connected to the symmetry group. Suppose we have a theory whose lagrangian is invariant under a symmetry group $\mathcal{G}$ with N generators T^α and the symmetry group of the vacuum form a subgroup $\mathcal{H}$ of $\mathcal{G}$, with m generators. This means that the vacuum state is still invariant under transformations generated by the m generators of $\mathcal{H}$, but not by the remaining N-m generators of the original symmetry group $\mathcal{G}$. Goldstone's theorem states that there will be N-m massless particle (one for each broken generator of the group). The case considered in this section is special since there is only one generator of the symmetry group (N=1) wich is broken by the vacuum. Thus there is no generator that leaves the vacuum invariant (m=0) and we get N-m=1 Goldstone bosons.

The longitudinal polarization components of the W and Z bosons correspond to the Goldstone bosons of the spontaneously broken part of the electroweak symmetry SU(2)$\bigotimes$U(1), which, however, are not observable. Because this symmetry is gauged, the three would-be Goldstone bosons are "eaten" by the three gauge bosons corresponding to the three broken generators; this gives these three gauge bosons a mass, and the associated necessary third polarization degree of freedom.

However the electroweak model doesn't contemplate mass for the fermions in the lagrangian. Similar to the boson mass problem we cannot add a mass term in the lagrangian, since a mass term mixes left-handed and right-handed fermions and we have assigned these to different multiplets of weak SU(2). However, if a SU(2) doublet Higgs is introduced, there is a gauge invariant interaction that will look like a mass when the Higgs gets a vacuum expectation value ('vev'). Such an interaction is called a 'Yukawa interaction'. As for the gauge bosons, the strength of the coupling of the Higgs to fermions is proportional to the mass of the fermions.

1.4 The Standard Model

As already stated the Standard Model comprehends three foundamental forces (strong and electro-weak interaction). The interactions are described by the already introduced gauge symmetry, SU(3) for the strong interaction and SU(2)$\bigotimes$U(1) for the electro-weak interaction. The full form of the standard model lagrangian containing all the three families can be separated in four components:

$$\mathcal{L} = \mathcal{L}_{gaugeBoson} + \mathcal{L}_{fermion} + \mathcal{L}_{Higgs} \tag{1.17}$$

where

$$\mathcal{L}_{gaugeBoson} = -\frac{1}{4}B_{\mu\nu}B^{\mu\nu} - \frac{1}{4}F^{a}_{\mu\nu}F^{a\mu\nu} - \frac{1}{4}F^{A}_{\mu\nu}F^{A\mu\nu} + \mathcal{L}_{gauge-fixing} + \mathcal{L}_{FPghost} \tag{1.18}$$

$$\mathcal{L}_{fermion} = \mathcal{L}_{Mass} + \mathcal{L}_{Kinetic} + \mathcal{L}_{Interaction} = \psi_i y_{ij} \psi_j \phi + h.c. + i\bar{\psi}\not{D}\psi + h.c. \tag{1.19}$$

$$\mathcal{L}_{Higgs} = |D_\mu \phi|^2 - V(\phi) \tag{1.20}$$

The interactions of the Standard Model can be summed up to Figure 1.3. Photon and Z boson are the carrier of neutral electroweak current, W^+W^- are carriers of the charged electro-weak current and the eight gluons [3] are the carriers of the strong force. Leptons have electro-weak interaction and quarks have both the electro-weak (but with fractional charge) and the strong interaction. As of today the Standard Model describes almost all the processes in particle physics field. However

[3] corresponding to the eight transition matrix of the SU(3) group

there are some limitations in the SM so that extensions have been proposed to look *beyond* the Standard Model as will be discussed in Chapter 2.

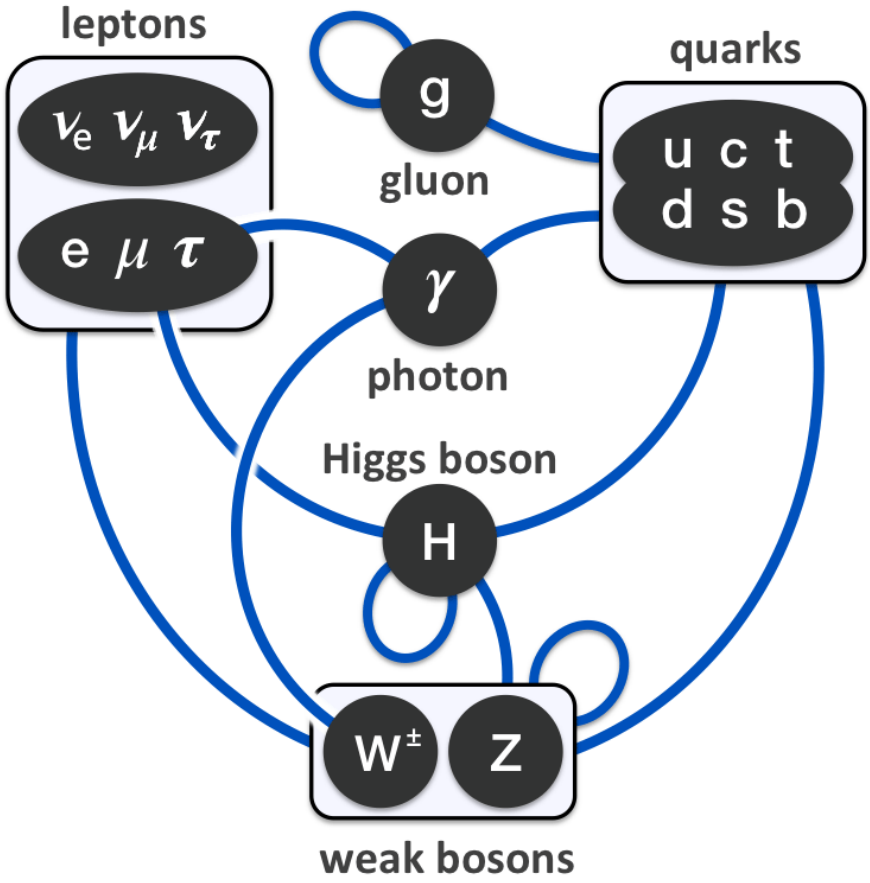

Figure 1.3: Summary of the Standard Model interactions between fermions and gauge mediators. Closed loop represent self-interaction: in case of the Higgs boson and gluons 3-way and 4-way vertices exists, in case of $W^{\pm}, Z_0$ the 3-way vertex $Z_0 \rightarrow W^+W^-$ and the 4-way vertex $Z_0Z_0 \rightarrow W^+W^-$ exist.

1.4.1 Standard model free parameters

The Standard Model predicts very well the constraints between observed physical quantities. The model has been used as a predictive theory and it has been capable to determine the proportional factor between the neutral and charged weak currents. However the available theoretical information is in form of relations between physical values, hence to have the absolute values it is necessary to measure some of the quantities in real life experiments.

The total number of free parameters in the model is 19 as seen in Table 1.1, and in 2012 with the discovery of the Higgs boson the picture is complete. These parameters include three independent gauge couplings and a possible CP-violating strong-interaction parameter, six quark and three charged-lepton masses, three generalized Cabibbo weak mixing angles and the CP-violating Kobayashi-Maskawa phase, as well as two independent masses for weak bosons. In addition at least nine more parameters must be introduced to accommodate neutrino oscillations: three neutrino masses, three real mixing angles, and three CP-violating phases, one of which is in principle observable in neutrino-oscillation experiments and the other two in neutrino-less double-beta decay experiments.

Symbol	Description	Renormalization scheme	Value
m_e	Electron mass		$(510.998928 \pm 1.1 \times 10^{-5})$ KeV
m_μ	Muon mass		$(105.6583715 \pm 3.5 \times 10^{-6})$ MeV
m_τ	Tau mass		(1776.82 ± 0.16) MeV
m_u	Up quark mass	$\mu_{\bar{M}S} = 2$ GeV	$(2.3^{+0.7}_{-0.5})$ MeV
m_d	Down quark mass	$\mu_{\bar{M}S} = 2$ GeV	$(4.8^{+0.5}_{-0.3})$ MeV
m_s	Strange quark mass	$\mu_{\bar{M}S} = 2$ GeV	(95 ± 5) MeV
m_c	Charm quark mass	$\mu_{\bar{M}S} = m_c$	(1.275 ± 0.025) GeV
m_b	Bottom quark mass	$\mu_{\bar{M}S} = m_b$	(4.18 ± 0.03) GeV
m_t	Top quark mass	On-shell	$(173.21 \pm 0.51 \pm 0.71)$ GeV
m_H	Higgs boson mass		(125.36 ± 0.41) GeV
β	CKM mixing angle		$(21.5 \pm 0.54)^\circ$
α	CKM mixing angle		$(85.4^{+3.9}_{-3.8})^\circ$
γ	CKM mixing angle		$(68.0^{+8}_{-8.5})^\circ$
δ	CKM CP-violating phase		0.995
g_1 or g'	U(1) gauge coupling	$\mu_{\bar{M}S} = m_Z$	0.357
g_2 or g	SU(2) gauge coupling	$\mu_{\bar{M}S} = m_Z$	0.652
g_3 or g_s	SU(3) gauge coupling	$\mu_{\bar{M}S} = m_Z$	1.221
θ_{QCD}	QCD vacuum angle		~ 0
v	vacuum expectation value		246 GeV

Table 1.1: Free parameters of the Standard Model. Since the coupling of QCD is running and depends on the energy, the mass of the quarks and the gauge coupling are reported for a given renormalization scale, that is written in the third column.

1.5 Higgs boson at the LHC

1.5.1 Higgs boson production

The Higgs boson is produced in the LHC from interaction of hadrons [35]. The production cross section of the processes at the LHC can be seen in Figure 1.5a. There are four main production modes at the LHC (Figure 1.4):

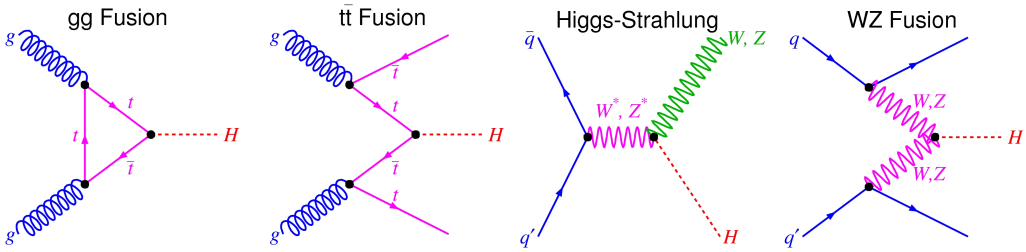

Figure 1.4: Feynman diagrams of the four Higgs production processes at the LHC.

- **Gluon gluon fusion production.** The Higgs boson cannot couple directly to massless particles, such as gluons. Nevertheless, this coupling is allowed via a virtual fermion loop with a heavy quark dominance. The gluon gluon fusion process is the leading production process since gluons are the dominant component of the proton's parton distribtion function at high energy (Figure 3.4). Gluon gluon fusion production takes up to the 87% of the production cross section.

- **Vector boson fusion production.** This production mode is generally associated to two jets with $p_T \sim M_W/2$ (where p_T is the transverse momentum and M_W the mass of the $W^{\pm}$ boson), because the production of high energy vector bosons usually comes from very energetic quarks. This kind of production mode takes up to 8% of the production cross section.

- **Associated production with Z and W (Higgs-strahlung).** This kind of production is a process similar to the Bremmsstrahlung of photon of high energy particles. A very high energy vector boson (W or Z) irradiates an Higgs boson, the final state is composed from the Higgs boson and a boson W or Z. Then the W or Z decays in jets or in leptons/neutrinos. This process takes a small fraction of the production cross section.

- **Top anti-top production.** The last production process is the fusion of a top and an anti-top quark. The final state usually presents a lot of missing E_T since two top/anti-top pairs are generated, one top and one anti-top generates the Higgs while both of the remaining top/anti-top decays in a b-quark plus a $W^{\pm}$. The $t\bar{t}$ production is important for the measurement of the Yukawa coupling between the Higgs field and fermions. This process takes a small fraction of the production cross section.

1.5.2 Higgs boson decay

The Standard Model is capable of predicting the theoretical production cross section and branching ratio of the Higgs boson as a function of the mass. Since the Higgs boson has a mass around 125 GeV several decay channels are possible as seen in Figure 1.5b, for a 125 GeV Higgs the possible decays are $\gamma\gamma$, ZZ, W^+W^-, $Z\gamma$, $\tau\tau$, $c\bar{c}$, $b\bar{b}$ and gg. In Higgs decays to Z, W, quarks or

τ the final observed state is composed by the decay products of the intermediate particles. This opens the possibility to study the Higgs boson in several experimental signatures. So the coupling with different particles and the mass of the Higgs boson itself can be measured with high precision.

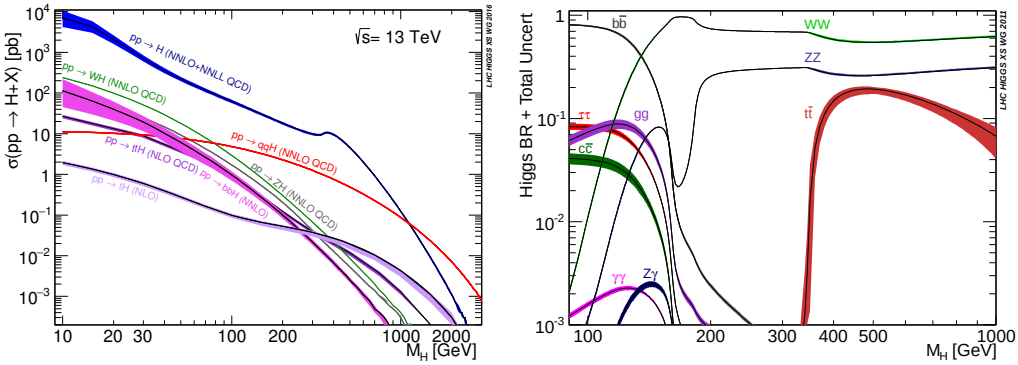

(a) **(b)**

Figure 1.5: Left: Higgs production cross section for 13TeV: σ on M_H for for the most relevant production mechanisms as a function of the Higgs-boson mass. Results for $gg \to H$, $q\bar{q} \to VH$, $b\bar{b} \to H$ are at NNLO in the QCD expansion. Weak boson fusion ($qq \to qqH$) and $t\bar{t}$ associated production are at NLO accuracy. Right: Theoretical branching ratio for the decay of the Higgs boson [36–38].

1.5.3 Discovery of the SM Higgs boson at LHC

The Higgs boson was searched in all possible decay channels in LHC's detector. The main research channels are: $H \to \gamma\gamma$, $H \to ZZ^* \to 4l$, $H \to WW^* \to lvlv$, $H \to b\bar{b}$ and $H \to \tau\tau$. In July 2012 ATLAS and CMS released the results of the combined Higgs search confirming the existence of a new particle, we can see the ATLAS and CMS results for the discovery p0 in Figure 1.7a, results are for 7 TeV and first part of 8 TeV data [39, 40]. The invariant mass spectrum in ATLAS for the Higgs signal is in Figure 1.6a for the Higgs in diphoton decay and in Figure 1.6b for the Higgs in four leptons. While the invariant mass spectrum in CMS is in Figure 1.6c and Figure 1.6d.

The p0 can be interpreted as "running the same experiment n times what is the number of times we would observe such a deviation from the expected distribution?", so if a 2 σ variation is observed, meaning 5 % chance, we would expect that running 100 times the experiment we would observe the same effect 5 times. For the Higgs boson discovery a 5 σ significance was observed, meaning that running the same experiment other 1000000 times we would get the same result only 1 time (which is a pretty slim chance). Conventionally in particle physics to claim the discovery of a new particle a 5 σ global significance has to be observed, a more detailed description of the statistic environment can be found in Chapter 10 and Appendix A.

Precise measurement for the Higgs boson mass and width was presented for the Run-I data by the ATLAS and CMS collaborations in 2015 [41] (Figure 1.7c, 1.7d), also the combined coupling

measurement was published in 2016 [42].

An updated result was published by the ATLAS collaboration in August 2016 for the Higgs boson observation in the diphoton [43] and in the four lepton channel [44], furthermore a combined measurement of the observed cross section in these two channels was made public [45]. The signal strength ($\mu = \sigma_{obs}/\sigma_{SM}$) measurement of Run-I and Run-II for the diphoton channel can be seen in Figure 1.8a. A combined measurement of diphoton and four lepton channel of the coupling of Higgs gluon gluon fusion and vector boson fusion production can be seen in Figure 1.8b, both measurements show good agreement with the Standard Model prediction.

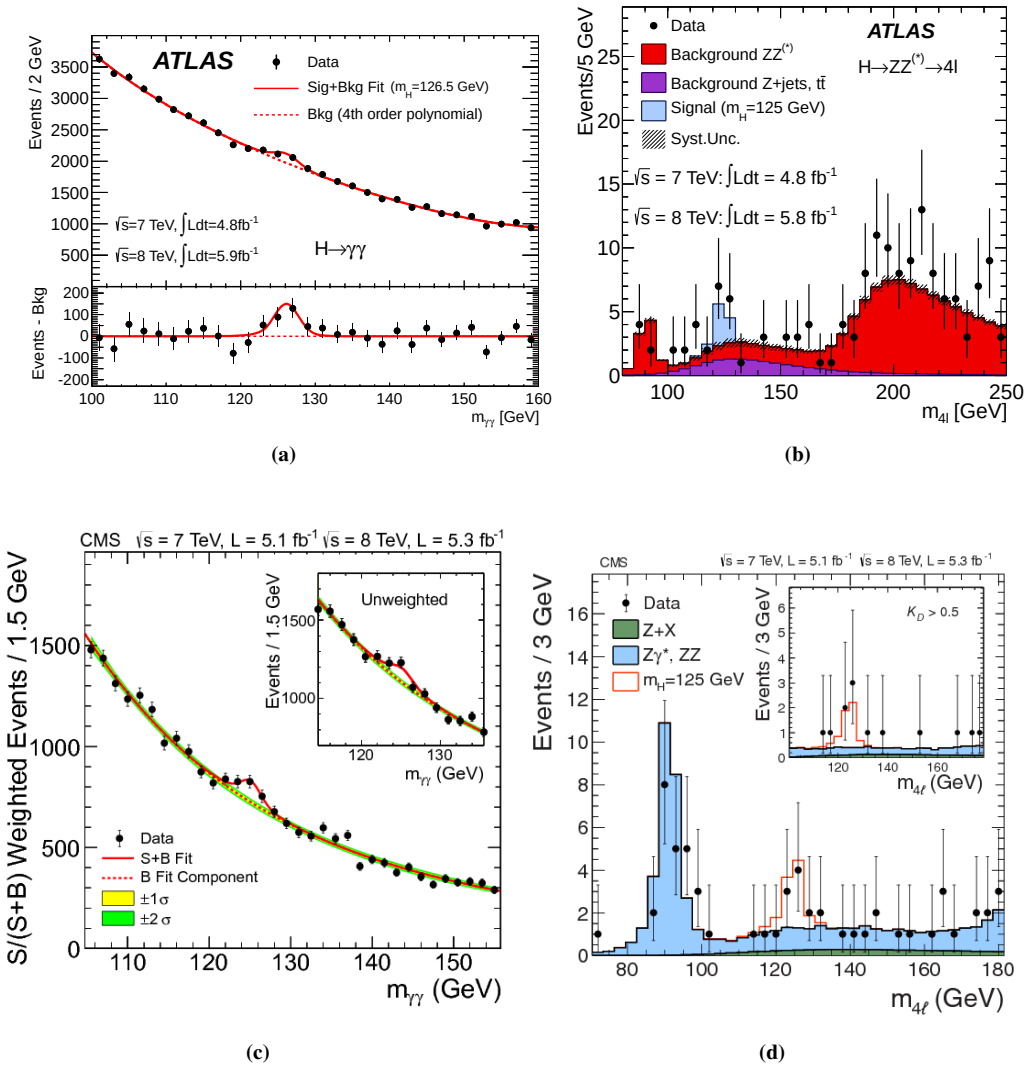

Figure 1.6: ATLAS, 1.6a: Invariant mass distribution of diphoton candidates for $\sqrt{s} = 7$ TeV and $\sqrt{s} = 8$ TeV data. The result of a fit of a signal component fixed to mH = 126.5GeV and a background component described by a fourth-order Bernstein polynomial is superimposed. The bottom inset displays the residuals of the data with respect to the fitted background component [39].

1.6b: The distribution of the four-lepton invariant mass, m4l, for the selected candidates, compared to the background expectation in the 80 to 250 GeV mass range, for $\sqrt{s} = 7$ TeV and $\sqrt{s} = 8$ TeV data. The signal expectation for a SM Higgs with mH = 125 GeV is also shown [39].

CMS, 1.6c: The diphoton invariant mass distribution with each event weighted by the S/(S+B) value of its category. The lines represent the fitted background and signal, and the colored bands represent the ±1 and ±1 standard deviation uncertainties in the background estimate [40].

1.6d: Distribution of the four-lepton invariant mass for the $H \to ZZ \to 4l$ analysis. The points represent the data, the filled histograms represent the background, a Higgs boson expected signal of mass m_H =125GeV (red) is added to the background expectation [40].

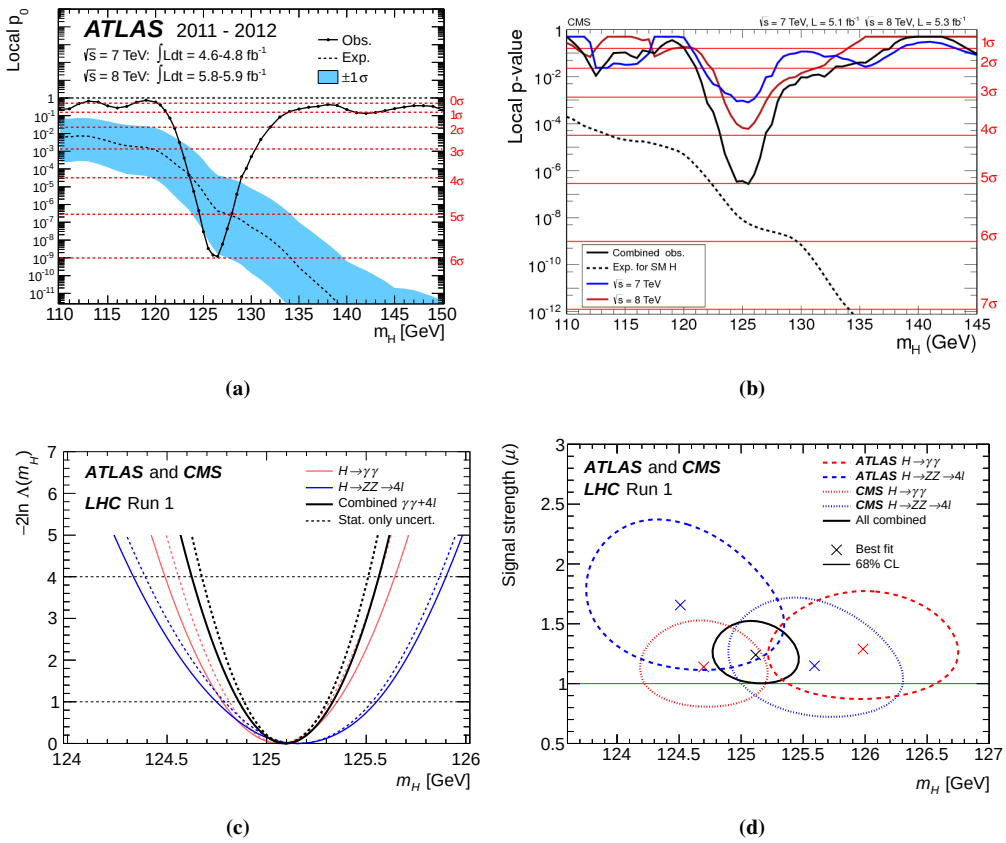

Figure 1.7: 1.7a: (ATLAS) The observed (solid) local p0 as a function of mH in the low mass range. The dashed curve shows the expected local p0 under the hypothesis of a SM Higgs boson signal at that mass with its plus/minus one sigma band. The horizontal dashed lines indicate the p-values corresponding to significances of 1 to 6 σ [39].
1.7b: (CMS) The observed local p-value for 7TeV and 8TeV data, and their combination as a function of the SM Higgs boson mass. The dashed line shows the expected local pp-values for a SM Higgs boson with a mass m_H [40].
1.7c: Scans of twice the negative log-likelihood ratio $-2\log(\Lambda)(m_H)$ as functions of the Higgs boson mass mH for the ATLAS and CMS combination of the $H \to \gamma\gamma$ (red), $H \to ZZ \to 4l$ (blue), and combined (black) channels. The dashed curves show the results accounting for statistical uncertainties only, with all nuisance parameters associated with systematic uncertainties fixed to their best-fit values. The 1 and 2 standard deviation limits are indicated by the intersections of the horizontal lines at 1 and 4, respectively, with the log-likelihood scan curves [41].
1.7d: Summary of likelihood scans in the 2D plane of signal strength μ versus Higgs boson mass mH for the ATLAS and CMS experiments. The 68% CL confidence regions of the individual measurements are shown by the dashed curves and of the overall combination by the solid curve. The markers indicate the respective best-fit values. The SM signal strength is indicated by the horizontal line at $\mu = 1$ [41].

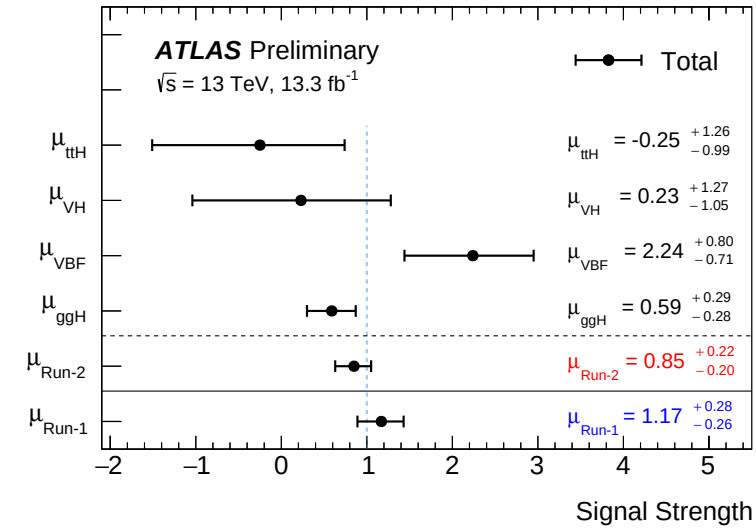

(a)

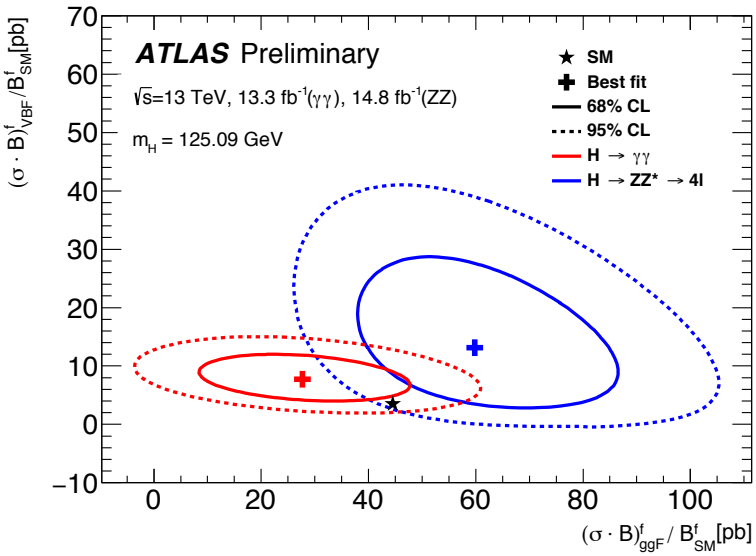

(b)

Figure 1.8: 1.8a: The signal strength measured for the different production processes (ggH, VBF, VH and tanti-tH) and globally (Run-2), compared to the global signal strength measured at 7 and 8 TeV (Run-1). The error bar shows the total uncertainty [45].
1.8b: The simultaneous measurement of the Higgs boson production cross section in the ggF and VBF production modes in the H→ $\gamma\gamma$ (red) and H→ $ZZ \rightarrow 4l$ (blue) channels. Both measurements show good agreement with the SM prediction (black star) [45].

CHAPTER 2

Beyond the Standard Model

2.1 Limits of the standard model

The Standard Model agrees with all available experimental data, but is theoretically very unsatisfactory. It does not explain the particle quantum numbers, such as the electric charge Q, weak isospin I, hypercharge Y and color. Furthermore it contains at least 19 arbitrary parameters as summarized in Section 1.4.1. The Standard Model does not include a gravitation theory, any present attempt of a quantum field theory of gravity generally breaks down before reaching the Planck scale ($\Delta_{Planck} = 1.22 \times 10^{19}$GeV) when gravitational effects comes into the game.

The Higgs mechanism gives rise to the hierarchy problem: the large discrepancy $\sim O(10^{24})$ between the strength of the weak nuclear force and gravity. Furthermore starting from the measured SM electro-weak parameters the running coupling constants for the three interactions (strong, electromagnetic and weak) do not converge to a single value when one extrapolates them at the Planck scale. Another problems arises in the fine tuning necessary between the Higgs mass corrections from top loop, gauge boson loop and Higgs self interaction: three large values are needed for the small observed Higgs mass.

Furthermore the Standard Model cannot explain the observed amount of dark matter in the universe. It is also difficult to accommodate within the model the observed predominance of matter over antimatter (matter/antimatter asymmetry). The isotropy and homogeneity of the visible universe over large distances seems to require a mechanism like cosmic inflation, which would also constitute an extension of the Standard Model.

The Standard Model is presently considered an *effective theory*, working only in electro-weak and strong energy scales. It is not a theory that works for every energy and size scale. Currently there is no proposed *theory of everything* that can explain all the physical processes of the universe.

In the following sections a brief introduction to some models beyond the SM will be given. First a quick overview of the Supersymmetry (SUSY) theory can be found. Then a more detailed description of extra dimension theories and two Higgs doublet model will be given.

2.2 Supersymmetry

One popular extension of the Standard Model is Supersymmetry (SUSY), there are numerous phenomenological motivations for supersymmetry close to the electroweak scale, as well as technical motivations for supersymmetry at any scale. In this theory, every fermion has a corresponding supersymmetric boson partner (bosinos). Likewise, for every boson in the standard model, there is a corresponding supersymmetric fermion superpartner (sfermions).

"Natural SUSY" is a supersymmetric scenario where the fine-tuning is as mild as possible and the superpatners should have a mass close to the EW scale (~TeV). However, since no hint of superpatners was found in LHC Run-II so far, this scenario is becoming unlikely.

To reconcile supersymmetry with actual experiments supersymmetry breaking was introduced. It is a spontaneous symmetry breaking process to obtain a seemingly non-supersymmetric physics from a supersymmetric theory. In this scenario the superpartners, whose mass would otherwise be close to the mass of the regular particles, become much heavier.

- A SUSY theory close to the electroweak scale can be a solution to the fine tuning needed to explain the big hierarchy problem, however it does not address why such a hierarchy exists in the first place.
- In the SM the weak, strong and electromagnetic couplings fail to unify at high energy, but with SUSY the running of the gauge couplings are modified and precise high-energy unification of the gauge couplings is achieved.
- In case of a TeV-scale SUSY (augmented with a discrete symmetry) a candidate dark matter particle, that would be the lightest supersymmetric particle, can be found at a mass scale consistent with thermal relic abundance calculations. Furthermore a SUSY theory could bring to more natural model of cosmological inflation.
- When supersymmetry is imposed as a local symmetry, Einstein's theory of general relativity is included automatically, and the result is said to be a theory of supergravity. It is also a necessary feature of the most popular candidate for a theory of everything which could be superstring theory.

There are many implementation of the supersymmetry theory. One of these models is the Minimal Supersymmetric extension of the Standard Model (MSSM), which also accounts for unification of the strong and electroweak interactions at very high energies. MSSM is the minimal supersymmetrical model as it considers only "the minimum number of new particle states and new interactions consistent with phenomenology". For MSSM, we have spin 1/2 fermions and their partners [chiral multiplet (1/2,0)], gauge bosons and their partners [gauge multiplets (1,1/2)], Higgs and its partner [a part of chiral multiplet (1/2,0)]. The interaction between the new superfields and field can be derived; for example the interaction between the gaugino $\bar{V}$, the sfermion $\bar{f}$ and the fermion f can be derived from the coupling strength g of the interaction between the fermion f and the gauge boson V.

In this model a single Higgsino (the fermionic superpartner of the Higgs boson) would lead to a gauge anomaly and would cause the theory to be inconsistent. However, if two Higgsinos are added, there is no gauge anomaly. For this reason the MSSM model includes a 2 Higgs doublet model (2HDM) since one extra doublet of scalar fields is added. This model introduces five Higgs bosons (three degrees of freedom are again re-absorbed to give mass to Z and $W^{\pm}$ bosons): two $H^{\pm}$ charged Higgs bosons and three neutral: h, H (both CP-even), and A (CP-odd). 2HDM will be introduced in more detail in Section 2.4.2.

2.3 Extra dimension theories

Other than SUSY there are beyond Standard Model exotic theories that try to solve the hierarchy problems. As already stated there are at least three hierarchy problems, in the context of extra dimension we will concentrate on the big and flavor ones: one is why gravity is so weak compared to other fundamental forces and the other is why the top quark is so heavy with respect to the other quarks. For the solution of the big hierarchy the supersymmetry was the most thoroughly investigated. However, SUSY does not address why such a hierarchy exists at all. It does not provide solutions to the mass hierarchy either. Extra dimension theories instead may possibly provide an answer to both questions, a useful source of information on the matter is Reference [46].

The idea of extra dimension is dated around 1926, immediately after the publication of Einstein's general relativity. Kaluza and Klein proposed a model to unify gravity and electromagnetism by extending the general relativity to a five-dimensional space-time [47]. This theory was recently rediscovered in two articles at the end of the 20^{th} century for models of quantum gravity: the Arkani-Hamed, Dimopoulos, Dvali (ADD) model [16] and the Randall-Sundrum (RS) model [4, 5]. These theories are brane theories: the main idea is that the visible, four-dimensional universe is restricted to a brane inside a higher-dimensional space, called the "bulk" (also known as 'hyperspace'). Only the gravity force carrier (graviton) propagates in the extra dimensions as well as in the 4-D space. The graviton would be a quantum excitation of the space-time metric tensor and hence would have spin 2.

As explained in detail in the next sections (Section 2.3.1.1), observing from our point of view (from the 4-D space) a particle propagating in the bulk (so in the (4+δ)-D space) we would see a series of resonances called Kaluza-Klein towers. These resonances corresponds to the momentum component of the particle in the additional dimensions: since these dimensions are limited the particle would be forced in discrete stationary modes. So several resonances would be observed and the masses of the resonances would be the energy of the corresponding normal mode of the particle in the extra dimensions.

There has been no experimental evidence that extra dimensions exist yet. If they do exist they are not of the same kind as the known 3-D spatial dimensions. They may be either flat and limited (compactified) or warped. In the next section two models using the concept of extra dimensions will be introduced (ADD and RS). A representation of a finite dimension can be seen in Figure 2.1.

Gravitons at colliders can be directly produced in processes such as $q\bar{q} \rightarrow gG$, $qg \rightarrow qG$,

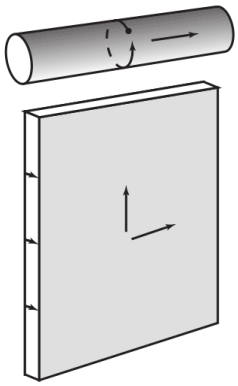

Figure 2.1: A small dimension of space may have two different forms. It may be curled up to form a cylinder, and the dimension transverse to its axis forms a closed cycle. But it may also form an interval line, the thickness of a box. It is impossible to go out of the box, as there is nothing there, not even vacuum. The direction in the extra dimension (circle or short arrows in the drawing) is said to be transverse to our space.

$gg \rightarrow gG$ in hadron colliders or $e^+e^- \rightarrow \gamma G$ in lepton colliders. Another process would be the excitation of the Kluza-Klein modes of the graviton (or virtual graviton exchange) for example $qq \rightarrow G$ or $gg \rightarrow G$.

If the graviton's coupling to the SM fields is low it is produced but does not interact and escapes the detector, for this reason the signature would be an energetic γ or jet back to back to E_T^{MISS}. If a virtual graviton exchange occurs it would not be observable in this case since nothing would be back to back with the graviton.

If the coupling with the planck brane is high enough a decay of the KK mode would be possible, for example $qq \rightarrow G \rightarrow \gamma\gamma$ (ex. Figure 2.2), $qq \rightarrow G \rightarrow e^+e^-$ or $gg \rightarrow gG \rightarrow g\gamma\gamma$. In this case the KK graviton mode decays into visible particles that can be directly observed; a deviation from SM expectation would appear in the final state invariant mass spectrum. Furthermore it would be possible to do measurement of the resonance proprieties such as the spin. The virtual graviton exchange with KK mode excitation is the topic of this thesis and will be taken into consideration in the following sections (except for the LEP results).

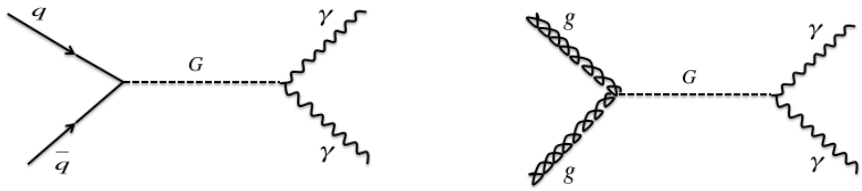

Figure 2.2: Virtual graviton exchange of Gravitons at LHC via gluon or quark fusion.

2.3.1 ADD model

The model proposed by Arkani-Hamed, Dimopoulos and Dvali assumes the existence of n additional flat (with euclidean metric) spatial dimensions, all compactified with radius R. Compactification means that the spatial dimension is curled in itself and the coordinate is confined in a circle ($0 \leq y < 2\pi R$ where R is the additional dimension radius). The Planck scale in the $4+\delta$ dimensions (M_D) is proportional to the reduced Planck scale ($\bar{M}_{pl}$): $M_D^{\delta+2} = \bar{M}_{pl}^2 R^{-\delta}$. This would solve the big hierarchy problem for small values of δ and appropriate values of the radius R. In the following sections this result will be explained starting from the Kaluza-Klein theory [47]. For an effective theory for the ADD model see Reference [15].

2.3.1.1 Kaluza Klein towers

In this section a brief discussion on the effect of only one additional compactified dimension will be made for simplicity. A (4+1)D space is taken where one dimension is compactified, meaning that its coordinate is confined in a circle of $0 \leq y < 2\pi R$ where R is the dimension of the compactified dimension. The metric for such a space would be $ds^2 = \eta_{\mu\nu}dx^\mu dx^\nu - dy^2$ (where the x are the coordinates in 4D). A massless free field $\Phi(x,y)$ in (4+1)D would follow $\Phi(x,y) = \Phi(x,y+2\pi)$ and can be easily expanded in its Fourier series in y.

$$\begin{aligned}\Phi(x,y) &= \frac{1}{\sqrt{2\pi R}} \sum_{n=-\infty}^{+\infty} \phi^{(n)}(x) e^{\frac{iny}{R}} \\ &= \frac{1}{\sqrt{2\pi R}}\psi^{(0)}(x) + \frac{1}{\sqrt{2\pi R}} \sum_{n=1}^{+\infty} \left(\psi^{(+n)}(x)\cos\frac{ny}{R} + \psi^{(-n)}(x)\sin\frac{ny}{R}\right)\end{aligned} \tag{2.1}$$

Where $\psi^{(0)} = \Phi^{(0)}$ and $\psi^{(\pm n, n>0)} = \frac{1}{\sqrt{2}}\Phi^{(+n)} \mp i\Phi^{(-n)}$. The action for such a field would be (integrating over y):

$$\begin{aligned}S^{((4+1)D)} &= \int d^4x \int_0^{2\pi R} dy \frac{1}{2}\left[\partial_\mu\Phi(x,y)\partial^\mu\Phi(x,y) - \partial_y\Phi(x,y)\partial^y\Phi(x,y)\right] \\ &= \int d^4x \frac{1}{2}\left[\partial_\mu\psi^{(0)}\partial^\mu\psi^{(0)} + \sum_{n=-\infty}^{+\infty}\left(\partial_\mu\psi^{(\pm n)}\partial^\mu\psi^{(\pm n)} - \frac{n^2}{R^2}\psi^{(\pm n)}\psi^{(\pm n)}\right)\right]\end{aligned} \tag{2.2}$$

The first term describes the conventional massless scalar field while the second term is an addition we obtained by going to (4+1)D. From the 4D point of view, we have acquired an infinite series of particles with masses $m_n = n/R$, these resonances are called Kaluza-Klein (KK) towers. So if a graviton described as a massless (4+1)D field exists we should be able to observe its KK tower and hence the sign of the extra dimensions.

In this framework the strength of the coupling constant can be also calculated. The field equation with a static point source would be (substituting for Eq. 2.1 and integrating over y):

$$\begin{aligned}\partial_M\partial^M\Phi(x^\mu,y) &= g_5\delta^3(x)\delta(y) \\ \sqrt{2\pi R}\partial_\mu\partial^\mu\phi^{(0)}(x^\mu) &= g_5\delta^3(x)\end{aligned}$$

Solving this equation brings to the relation between the coupling in 4D and in (4+1)D: $g_4^2 = \frac{g_5^2}{2\pi R}$. A full explanation can be found in Reference [46], Section 6.2. This means that the effective coupling strength in 4D is reduced by the volume factor $V = 2\pi R$ of the extra dimension. In general a coupling constant for δ additional dimension $g_{4+\delta}$ has mass dimension $-\delta/2$ and its strength is reduced effectively to:

$$g_{eff,4D}^2 = \frac{g_{4+\delta}^2}{(2\pi R)^\delta}$$

This reasoning applied to the gravitational force can be elaborated as the relation between the $D = 4 + \delta$ Planck's mass and the 4D Panck's mass: $M_D^{\delta+2} = \bar{M}_{pl}^2 R^{-\delta}$ which was the original goal. This is also consistent with the $4 + \delta$ dimensional gravitation force found in Section 2.3.1.3.

2.3.1.2 Phenomenology

As already stated in the previous sections an ADD graviton would produce several KK towers with mass splitting proportional to $\frac{1}{R}$.

$$\Delta m \sim \frac{1}{R} = \overline{M_D}\left(\frac{\overline{M_D}}{\overline{M_{pl}}}\right)^{\frac{2}{\delta}}$$

For example assuming that the $4 + \delta$ dimensional Planck's mass M_D is around 1 TeV a splitting of 20 keV, 7 MeV and 0.1 GeV would be present for $\delta = 4, 6, 8$. So the mass splitting would be comparable with the experimental resolution available only for a large number of extra dimensions.

However for large δ the total production cross section would be negligible. For this reason a number of extra dimension $\delta \leq 6$ is necessary for the observation in a modern-day experiment. Since the mass splitting of the KK towers in the allowed δ range is small in comparison to the experimental resolution the experimental signature of this phenomena would be a non-resonant deviation from the SM background expectation.

2.3.1.3 Classical constrain

A very quick remark regarding extra dimensions can be made taking into account that classically gravity has its roots in the geometry of space-time. Gravitational force in 4 and 4+D dimensions would be:

$$f(r) = \begin{cases} \frac{1}{M_{pl}^2}\frac{m_1 m_2}{r^2} & D = 4 \text{ dimensional} \\ \frac{1}{M_D^{2+\delta}}\frac{m_1 m_2}{r^{2+\delta}} & D = 4 + \delta \text{ dimensional} \end{cases}$$

We want to investigate a possibility that the energy scale of the fundamental constant M_D may not be too different from the electroweak scale that was conveniently set at 1 TeV. The $D = 4 + \delta$ formula should give back the usual Newton's law $1/r^2$ for $r >> R$, this happens if the gravitational force in the extra dimensions saturates at some value $r = R \sim 1/M_D$. This constrain would imply:

$$f(r >> R) = \frac{1}{M_D^2}\frac{m_1 m_2}{r^2}\frac{1}{(M_D R)^\delta} = \frac{1}{M_{pl}^2}\frac{m_1 m_2}{r^2}$$

$$R = \left(\frac{M_{pl}^2}{M_D^{2+\delta}} \right)^{\frac{1}{\delta}}$$

if $\delta = 1$ the new gravitational force would violate Newton's law for distances around the solar systema scale, so it is obviously excluded. If $\delta = 2$ the violation would be for distances around the mm. Since a deviation of the gravitational force from $1/r^2$ was not observed at the mm there is an initial constrain to the number of flat extra dimensions to be $\delta \geq 3$. In the next section regarding RS models this limit will be overcome by introducing the concept of warped extra dimensions.

2.3.1.4 Additional constrains

Constrains on δ were already introduced in the previous sections ($3 \leq \delta \leq 6$); imposing the continuity with the Newton's law (Section 2.3.1.3) and the observability in modern day colliders (Section 2.3.1.2). However more precise statements can be made following astrophysical observations. If the mass of the KK gravitons is small, astrophysical objects with temperature $T > m_{KK}$ can emit them and their presence can be inferred from astrophysical measurements. We can estimate the order of thermal graviton production rate (per unit time and volume) by multiplying the coupling strength of each graviton $\sim 1/M_{pl}$ by the number of accessible modes $(TR)^{\delta}$. Then if the available energy is comparable to the fundamental scale of the gravity, one gets observable effects in direct production or virtual exchange processes. The effect is larger as the temperature goes higher so the following high-temperature phenomena in astrophysics will be taken into consideration:

- **SN198A:** [48] The fact that the neutrinos were observed over an interval of several seconds was used to limit the total amount of cooling. So a limit can be imposed to the energy loss from KK towers production. Results are reported here:
  $M_D > 50$ TeV, $R < 3 \times 10^{-4}$ mm, $\delta = 2$
  $M_D > 4$ TeV, $R < 4 \times 10^{-7}$ mm, $\delta = 3$
  $M_D > 1$ TeV, $R < 2 \times 10^{-8}$ mm, $\delta = 4$.

- **Neutron star:** [49] After a supernova explosion, most of the KK gravitons stay gravitationally trapped in the remnant neutron star. The requirement that neutron stars are not excessively heated by KK particles decaying into photons leads to $M_D > 1700(76)$ TeV for $\delta = 2(3)$

- **Cosmic diffuse gamma rays (CDG):** [50] If the graviton's mass is as large as 100 MeV they would be decaying at present time contributing to the cosmic diffuse gamma ray background. This would result in a distortion of the CDG spectrum due to the graviton in di-photon decay. Constrains are $M_D > 100$ TeV for $\delta = 2$ and $M_D > 5$ TeV for $\delta = 3$.

- **Early universe:** [51] In the early universe KK gravitons are produced in great numbers since the temperature is extremely high. Part of them escapes to the extra dimensions and will cause and excessive cooling of the hot plasma. If the cooling rate due to the graviton exceeds that of Hubble cooling, the Hubble expansion will no longer be as we understand it.

Constrains from modern day particle colliders will be shown in Section 2.5.

2.3.2 RS model

Until this point extra dimensions were considered compactified because no evident clue about their existence is observed in nature. Because of the compactification assumption a small number of dimension ($\delta = 1, 2$) were excluded since no deviation from Newton's law is detected at the millimeter scale. However a different approach propose that the extra dimension doesn't need to be compactified and could even be infinite. To achieve this the concept of warped space needs to be introduced [4, 5] (Section 2.3.2.1).

In the Randall-Sundrum model the existence of an hyperspace with five dimensions is assumed. The five-dimensional bulk is extremely warped and contains two branes: the Planckbrane (where gravity is a relatively strong force; also called 'Gravity' brane) and the Tevbrane (our home with the Standard Model particles; also called 'Weak' brane). Standard Model particles are confined in the 'weak' brane, while gravity is generated in the 'Planck' brane and gravitons can propagate through the bulk.

The Planck's mass in the weak brane is corresponding to the Planck's mass in the Planck brane following the law: $M_D = M_{PI} e^{-k\pi R}$ (where k is the curvature of the additional dimension and R the radius of the dimension). For $kR \approx 12$ the model would reproduce the hierarchy scale between the weak force and the gravitational force [14].

The model would imply the presence of KK towers which mass and width can be fully described by the mass of the least energetic resonance and the coupling with the Standard Model $k/\bar{M}_{pl}$ ($\bar{M}_{pl} = M_{pl}/\sqrt{8\pi}$ reduced Planck mass). The coupling would be proportional to the width of the resonances.
The novelties of the RS model in respect of the ADD model are:

- The hierarchy between the fundamental five-dimensional Planck scale and the compactification scale, $1/R$ is only of order 50, as opposed to $(M_{pl}/\mathrm{TeV})^{2/\delta}$.
- There is only one additional dimension, as opposed to $n \geq 3$.
- There are no light Kaluza-Klein modes since the excitation scale is of order a TeV. Therefore, current constraints from particle physics, astrophysics and cosmology do not apply. So the scale at which gravity becomes strong can be quite low.
- The coupling of an individual KK excitation to matter or to other gravitational modes is set by the weak, not the Planck scale.
- The KK modes can be observed as distinct spin-2 resonances that can be reconstructed from their decay products.

In the next sections an introduction of warped dimension and gravity in this particular space-time will be given.

2.3.2.1 Warped geometry

Warped geometry means a (4+1)D space-time with the fifth dimension filled only with vacuum energy. This results in a metrical tensor of this kind:

$$ds_5^2 = G_{MN}dx^M dx^N = e^{-2\sigma(y)}g_{\mu\nu}dx^\mu dx^\nu - dy^2$$

where $e^{-2\sigma(y)}$ is referred to as the warp factor. This metric is indeed a solution to the Einstein equation in (4+1)D, starting from the (4+1)D action:

$$S^{((4+1)D)} = \int d^4x \int_{-\pi R}^{+\pi R} dy \left[\sqrt{-G}\left(\frac{\bar{M}_5^3}{2} R^{(5)} - \Lambda \right) \right] + S_{matter} \tag{2.3}$$

Where Λ is the cosmological constant term in (4+1)D, $R^{(5)}$ is the Ricci curvature and S_{matter} is the usual $L-V$ action. Passing through the equation of motion the solution for $\sigma(y)$ can be found and the actual warp factor $\sigma(y) = ky$ can be derived. The metrical tensor then becomes:

$$ds_5^2 = e^{-2ky}\eta_{\mu\nu}dx^\mu dx^\nu - dy^2, 0 < y < 2\pi$$

A full calculation can be found in Reference [46], Section 6.6.1. Starting from the (4+1)D bulk with the cosmological constant we have achieved the construction of a space-time flat in 4D but warped in the fifth dimension. The warp factor means an expanding space toward the brane at $y = \pi R$, an analogy with the expanding universe helps to understand it intuitively. An explanatory plot is in Figure 2.3.

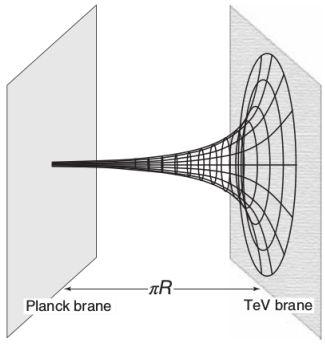

Figure 2.3: Warped space: rescaling across the fifth dimension. The gravitational field flux per unit area is diluted because of rapid expansion of the space. Gravity is strong at the Planck brane, but is weak at the TeV brane by a factor $e^{-k\pi R}$.

2.3.2.2 RS model gravity

In this section the effect of a warped extra dimension on Gravity will be studied. We consider a case k > 0 and assume that a 4D Higgs field (and other SM particles) is localized in the $y = \pi R$ brane. The brane at $y = 0$ is referred to as the Planck (or UV: ultraviolet) brane and that at $y = \pi R$ is referred to as the TeV (or IR: infrared). The action for the Higgs field in the 4D TeV brane is:

$$S^{(Higgs)} = \int d^4x \sqrt{-g^{(2)}} \left[-g^{(2)\mu\nu}\partial_\mu H \partial^\nu H - \lambda(|H|^2 - v_0^2)^2 \right] \tag{2.4}$$

where $g^{(2)\mu\nu} = e^{-2k\pi R} g^{(0)\mu\nu}$ is the interaction with gravity. Normalizing the Higgs wave function to $H = \hat{H} e^{-2k\pi R}$ and using everywhere $g^{(0)\mu\nu}$ we get:

$$S^{(Higgs)} = \int d^4x \sqrt{-g^{(0)}} \left[-g^{(0)\mu\nu} \partial_\mu \hat{H} \partial^\nu \hat{H} - \lambda \left(|\hat{H}|^2 - \left(\nu_0 e^{-k\pi R} \right)^2 \right)^2 \right] \tag{2.5}$$

the important piece of information is that the vacuum expectation value (VEV) in the TeV brane is re-normalized by a factor of $\nu = \nu_0 e^{-k\pi R}$. As the Higgs VEV determines the weak scale, the result is completely general. Any mass parameter on the TeV brane in the fundamental higher dimensional theory will be scaled down by the same factor. Thus a value of $kR \sim 12$ would reduce the Planck scale to the TeV scale, effectively solving the hierarchy problem.

2.3.2.3 Infinite extra dimension

Until now it was assumed that $0 < y < \pi R$, however it can be shown that the IR brane ($y = \pi R$) can be taken to infinity. This means that the 5th dimension doesn't need to be confined to a finite volume, this notion is in constrast with the compactified (limited) dimensions of the ADD model. It can be shown that if the zero mode of the graviton is localized at $y = 0$ and all the KK towers are pushed off to the IR brane their net effect on the Planck brane is negligible enabling to take the IR brane to infinity. Staring again from the (4+1)D action for the 0-mode KK tower:

$$S^{((4+1)D)} = \frac{\bar{M}_5^3}{2} \int d^4x \int_{-\pi R}^{+\pi R} dy \sqrt{-G} R^{(5)} \tag{2.6}$$

Where $R^{(5)} = G^{MN} R_{MN}$ is the (4+1)D Ricci curvature. After long calculations not reported here (See [46] section 6.6.3) we obtain:

$$\bar{M}_{pl}^2 = \frac{\bar{M}_5^3}{k} (1 - e^{-2k\pi R})$$

in constrast with the ADD relation $\bar{M}_{pl}^2 = \bar{M}_5^{2+\delta} V^\delta$, here there is a well-defined value for M_5 in the warped extra space even in the $R \to \infty$ limit. However only the zero mode KK tower of the graviton was taken into account. It is necessary to prove that the inclusion of all the higher KK towers does not affect the Newton's law of gravitation in 4D. This calculation will bring to the phenomenology of the KK towers for the RS model and it will be introduced in the next section.

2.3.2.4 Phenomenology

As it was already stated the field equation for the physical gravitational wave $h_{MN}(x, y)$ is the same for the massless (4+1)D scalar field except for the normalization factor. The (4+1)D action for the scalar field can be expressed as:

$$S_{scalar}^{((4+1)D)} = \int d^4x \int_{-\pi R}^{\pi R} dy e^{-4\sigma(y)} \sqrt{-g} \left[e^{-2\sigma(y)} \partial_\mu \Phi \partial^\mu \Phi - (\partial_y \Phi)^2 \right] \tag{2.7}$$

Φ can be expanded in terms of KK towers:

$$\Phi(x, y) = \sum_{n \neq 0} \psi_n(x) \phi_n(y)$$

after long calculations not reported here (See [46] section 6.6.4) we arrive at this formulation:

$$\begin{gathered}\phi_n(y) = e^{2\sigma}\chi_n(y), \quad \hat{\chi}_n(y) = e^{k|y|/2}\chi_n(y), \quad z = \operatorname{sgn}(y)\frac{e^{k|y|-1}}{k} \\ \left[\frac{1}{2}\partial_z^2 + V(z)\right]\hat{\chi}_n(z) = m_n^2\hat{\chi}_n(z), \quad V(z) = \frac{15k^2}{8(k|z|+1)^2} - \frac{3}{2}k\left[\delta(z) - \delta(z-z_1)\right]\end{gathered} \tag{2.8}$$

The potential $V(z)$ is referred to as the volcano potential. Solving this equation is complicated, however some qualitative remarks will be given. The delta function supports only one bound state localized at the origin, which is none other than our localized zero mode. As the potential is repulsive, all other states ($n \neq 0$ KK towers) are unbound and pushed toward $z = z_{max} = z_1$. That is, the KK modes are more or less localized in the $y = \pi R$ brane. The size $|z_{max}| \sim e^{k\pi R}/k$ defines the level intervals and mass of the KK towers would be $m_{KK}^2 \sim (nke^{-k\pi R})^2$.

In summary, by adopting the warped fifth dimension and placing gravity in the Planck brane, we have achieved a TeV scale gravity in the TeV brane. This can be done either assuming that the extra dimension is limited or infinite. It was shown that also for the RS model the hierarchy problem is solved and in this case with a parameter that is $kR \sim O(10)$ instead of a large parameter as in the case of ADD model. Since this time the mass splitting of the KK towers is large in comparison to the experimental resolution the experimental signature of this phenomena would be several separated resonances in the invariant mass spectrum.

2.4 Exotic Higgs

There are two principal avenues to searching for physics beyond the SM electroweak symmetry breaking (EWSB). The first one is to study the couplings of the SM-like Higgs itself, as the couplings of H are altered from their Standard Model values by mixing with additional scalars. However these deviations could be too small to observe with the available experiments. The second one is to search for new states in SM-like Higgs channels, since additional scalars share many of the same production and decay modes as the SM Higgs. Additional states can also be searched in different channels, such as those in which heavier scalars decay to final states involving the SM-like Higgs. There is a strong interplay between these two avenues, since the couplings of the SM-like Higgs are correlated with the variation in production and decay modes of additional scalars. Indeed, many types of extended EWSB sectors are already tightly constrained by measurements of the SM-like Higgs couplings alone.

Given the constraints imposed by the coupling fits of the SM-like Higgs, the most promising search channels are additional scalars at the LHC. Spin-0 resonances in the diphoton invariant mass spectrum are predicted in many theories with an extended Higgs sector [20–26]. The following paragraph will be focuses in the two-Higgs-doublet model (2HDM) that can be included in a MSSM.

2.4.1 SM-like Higgs boson limitations

Properties of the Higgs particle in the SM are determined by the Higgs potential. Its form was chosen for its simplicity with minimal requirements. So far, there are no observables that contradict this assumption. Besides, the minimal model has been an important guiding principle in exploring the origin and characteristics of spontaneous symmetry breaking theoretically as well as in planning experiments to discover the Higgs particles. However, as already stated, some problems arise like the small and big hierarchy problem. The big hierarchy problem was already discussed in extend in the previous sections.

Regarding the small hierarchy problem a more detailed introduction will be given here. There are three types of radiative corrections to the Higgs mass that arise from the Higgs boson Feynman propagator: Yukawa coupling to the top quark, gauge boson loop and Higgs 4-way interaction. These three large corrections have to conspire to give the small Higgs mass value of $\sim$ 100 GeV. It is a fine-tuning of about 1 part in 100 for a $\sim$10 TeV scale. If one avoids the fine-tuning, then one has to limit the energy scale of the new physics below 1-2 TeV.

Because of these issues it is important to consider more generic Higgs models that are allowed by phenomenology. When extending the SM there are two important observational constraints that has to be taken into account:

$$1) \quad \rho = \frac{m_W^2}{m_Z^2 \cos^2 \theta_W} \approx 1 \tag{2.9}$$

2) No flavour changing neutral currents (FCNC)

The first request is satisfied automatically if the additional Higgs is a member of doublets. Therefore, the simplest extension is to require an extra Higgs doublet. SUSY also requires a minimum of two Higgs doublets in the MSSM scenario. When two Higgs doublets are assumed, there are several ways to satisfy the second condition.

2.4.2 The two-Higgs-doublet model

As stated in the previous section two higgs doublets model is the simplest extension to respect the conditions in 2.9. To avoid FCNC the most conventional assumption (however also other formulations of 2HDM avoid FCNC) is to require that one Higgs doublet, which we denote as H_1, has the quantum number $Y = -1$ and couples only to up-type quarks (u,c,t) with $Q = +2/3$. While the other doublet, denoted as H_2, has the quantum number $Y = +1$ and couples only to down-type quarks (d,s,b) with $Q = -1/3$.

Starting from most general SU(2) gauge-invariant scalar potential we simplify it by imposing the SUSY. In order not to make the arguments too complicated, we adopt the MSSM (minimum supersymmetric extension of the Standard Model) assumption. In MSSM, as already stated, the H_1 doublet couples to down-type quarks while the other doublet H_2 couples to up-type quarks. For example the MSSM relates the coefficients of the quartic potential with the gauge coupling, the potential would be:

$$\begin{aligned} V_H = \mu_1^2 H_1^\dagger H_1 + \mu_2^2 H_2^\dagger H_2 - \mu_3^2(\epsilon_{ij} H_1^i H_2^j + h.c.) \\ + \frac{g_W^2 + g_B^2}{8}(H_1^\dagger H_1 - H_2^\dagger H_2) + \frac{g_W^2}{2}|H_1^\dagger H_2|^2 \end{aligned} \tag{2.10}$$

As $H_1^\dagger$ and H_2 have the same quantum number, we define two complex neutral and two charged scalar fields by $H_1 = \begin{bmatrix} \Phi_1^{0\dagger} \\ -\Phi_1^- \end{bmatrix}$ and $H_2 = \begin{bmatrix} \Phi_2^+ \\ -\Phi_2^0 \end{bmatrix}$. To break the symmetry spontaneously, we choose the VEVs to satisfy $< \Phi_1^+ >=< \Phi_2^- >= 0$. Then we assume that the minimum of the potential is at:

$$H_1 = \begin{bmatrix} 0 \\ \frac{v_1}{\sqrt{2}} \end{bmatrix}, \quad H_2 = \begin{bmatrix} 0 \\ \frac{v_2}{\sqrt{2}} \end{bmatrix} \tag{2.11}$$

The potential in equation 2.10 has to respect two conditions: $\mu_1^2 + \mu_2^2 > 2\mu_3^2$ (the potential has to be bound from below) and $\mu_3^4 > \mu_1^2\mu_2^2$ (the coefficient of the quadratic term must be negative). Expressing g_W and g_B with m_Z we find the relations:

$$\begin{aligned} \mu_1^2 &= \mu_3^2 \tan\beta - \frac{m_Z^2}{2}\cos 2\beta \\ \mu_2^2 &= \mu_3^2 \cot\beta + \frac{m_Z^2}{2}\cos 2\beta \end{aligned} \tag{2.12}$$

where $\tan\beta$ is a important parameter that will be used in the following, it is equal to the ratio of the vacuum expectation values for the two doublets, namely $\tan\beta = \frac{v_2}{v_1}$. Full calculations can be

found in [46] section 1.5.1. These two equations automatically satisfy the vacuum stability and the symmetry-breaking conditions. Expressing in terms of m_Z we find the constrain:

$$\mathrm{m}_Z = \frac{\mu_1^2 - \mu_1^2 \tan^2\beta}{\tan^2\beta - 1} \tag{2.13}$$

2.4.3 Higgs doublets mass spectrum

Two Higgs doublets introduce eight scalar fields, however three are taken up by the gauge bosons to give them mass, and five appear as physical particles. Three of them are neutral and the other two are charged. If the CP invariance is assumed, the real and imaginary parts of the scalar fields do not mix and the charged Higgses are also separated. The theory now contains four unknown masses ($m_h, m_H, m_A, m_H^{\pm}$) and two extra angles, α and β, that rotate the (CP-odd and charged) gauge fields and the (CP-even light and CP-even heavy) gauge fields into the $A\,/\,H^+$ and h/H mass eigenstates, respectively. From calculations (see reference [46] Section 1.5.3) we can find the following relations for the mass of the Higgses:

$$\begin{aligned} m_A^2 &= \frac{2\mu_3^2}{\sin 2\beta} \\ m_{H^\pm}^2 &= m_A^2 + m_W^2 \\ m_{H,h}^2 &= \frac{1}{2}\left[m_A^2 + m_Z^2 \pm \sqrt{(m_A^2 + m_Z^2)^2 - 4m_Z^2 m_A^2 \cos^2 2\beta}\right] \end{aligned} \tag{2.14}$$

the supersymmetric structure of the theory has imposed very strong conditions on the Higgs spectrum, of the original six parameters only two are free at the tree level: m_A and $\tan\beta$. However at higher order only a certain number of "benchmark sets" are chosen where the tree level parameters $\tan\beta$ and m_A are scanned while all other parameters are fixed. For the CP-conserving case three benchmark scenarios can be considered: the no-mixing scenario where the stop mixing parameter X_t is set to zero, the m_h-max scenario (maximal mixing), designed to maximise the theoretical upper bound on m_h, and the large-μ scenario, where the h0 decays to bb are suppressed [52–54]. From the above equations we can also derive the following relations:

$$\begin{aligned} m_{H^\pm}^2 &> m_W^2 \\ m_{H^0} &> \max(m_A, m_Z) \geq \min(m_A, m_Z)\cos 2\beta \geq m_h \\ m_h^2 + m_{H^0}^2 &= m_Z^2 + m_A^2 \end{aligned} \tag{2.15}$$

These relations mean that at least one of the three neutral Higgs particles is lighter than Z. Therefore, if one can prove the existence of a light Higgs h_0 with mass smaller than Z, the possibility of the SUSY, or at least its minimum version MSSM, is very large. Notice, however, that this story is valid only for the tree level approximation. Inclusion of radiative corrections modifies the mass value, especially those including the massive top and its spin 0 partner "stop" quark.

However, as seen in Figure 2.4 (Left) for maximal-mixing benchmark scenario, the mass value ($m_h = 125.7 \pm 0.4$ GeV) determined by LHC is near the upper limit of the SUSY predictions. It means that parameters of the MSSM to reproduce the observed value are near the boundaries of allowed regions.

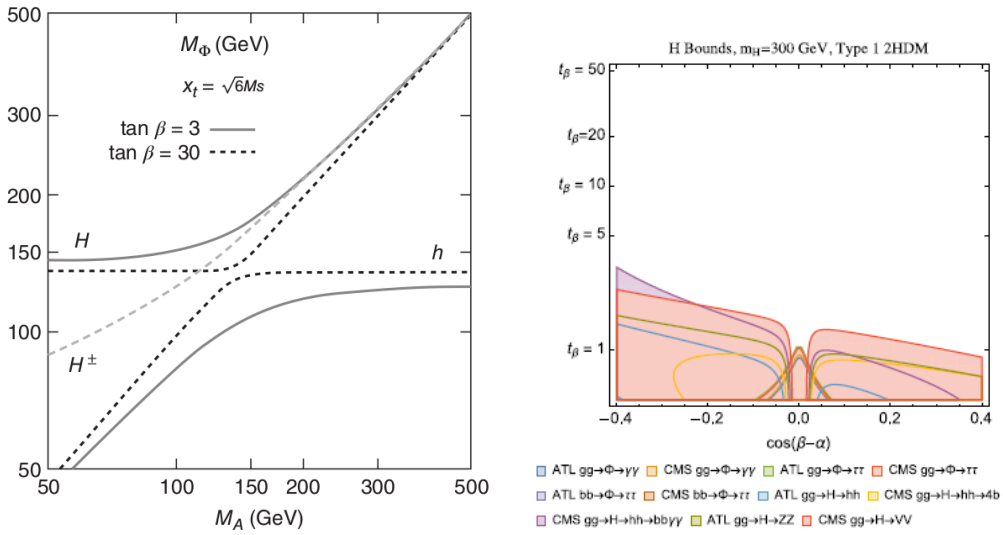

Figure 2.4: Left: Mass of the MSSM Higgs bosons as functions of m_A for two values of $\tan\beta = 3, 30$ with maximal mixing scenario with the stop ($\tilde{t}$) mass $\tilde{t} = 2$ TeV and all other SUSY parameters set to 1 TeV [55]. Right: Direct search limits for ATLAS and CMS of different final states on a 300 GeV CP even neutral scalar H as a function of $\cos(\beta-\alpha)$ and $\tan\beta$ in a Type 1 2HDM [56].

2.4.4 Phenomenology

As already stated a clear experimental signature of the 2HDM would be the observation of an additional scalar state in one of the decay channels of the SM Higgs. Another way would be the discrepancy of the couplings of the observed Higgs with SM prediction. The additional scalar state would be produced in the same way as the SM higgs and decay with the same final state.

Under the assumption that the recently observed Higgs boson is the light CP-even Higgs scalar of the 2HDM, the consistency of its couplings with those predicted by the SM pushes the model close to the so called alignment limit, where certain decay modes of heavy neutral Higgs bosons vanish, including H → VV (where V is a vector boson), H → hh, and A → Zh. At the same time, decays of H and A to $\gamma\gamma$ and $\tau\tau$ become increasingly important for $\cos(\beta-\alpha) \to 0$ (Figure 2.4, Right).

The electroweak production modes, such as vector boson fusion or production in association with a W or a Z boson, are predicted to be suppressed. Therefore the production of both H and A is dominated by gluon fusion.

The absence of tree-level flavor-changing neutral currents in multiple-Higgs-doublet theories is guaranteed by the Glashow–Weinberg condition. This condition is satisfied in the 2HDM by four discrete combinations of the Yukawa couplings of the fermions to the Higgs doublets. In the Type I scenario all fermions couple to one doublet, while in Type II up-type quarks couple to one doublet and down-type quarks and leptons couple to the other. A detailed description of other scenarios is given in Ref. [57].

2.5 Search for BSM particle in particle collider

Searches for beyond the Standard Model phenomena are done in several different ways depending on the searched particles, the requested final state and the underlying model. In the following chapters the attention will be focused on the search of BSM particle in the diphoton decay channel using data from the ATLAS detector. The signal region is well defined however a lot of effort is spent in modeling the shape of the background and the expected signal. The Landau–Yang theorem [58, 59] forbids the direct decay of a spin-1 particle into a pair of photons, however particles with zero or higher than 1 spin (0, 2, 3, 4...) can decay in two photons. In the following chapters only the cases of spin-0 and spin-2 will be discussed.

The diphoton final state provides an optimal channel for this kind of search due to the clean experimental signature, excellent diphoton mass resolution, and modest backgrounds. Searches for spin-0 and spin-2 resonances in the diphoton channel have been reported by Tevatron, LEP and during the run-I of LHC both for ATLAS and CMS collaborations [7, 18, 27, 60, 61].

2.5.1 Graviton search at Tevatron and LEP

At the Tevatron collider at Fermilab the production processes of the Graviton were the same as at LHC and the decay studied were $\gamma\gamma, e^+e^-, \mu^+\mu^-$. The results of RS graviton search for D0 [62] and CDF [63] experiments can be seen in Figure 2.5. Graviton were also studied at the LEP collider at Cern, however the main graviton final state was a graviton and a photon; $e^+e^- \to \gamma G$. Combined results for an ADD graviton for the experiments at LEP can be found in Reference [64] and in Figure 2.6. A summary tables of the limits of exclusion for Tevatron and LEP can be found in Tables 2.7.

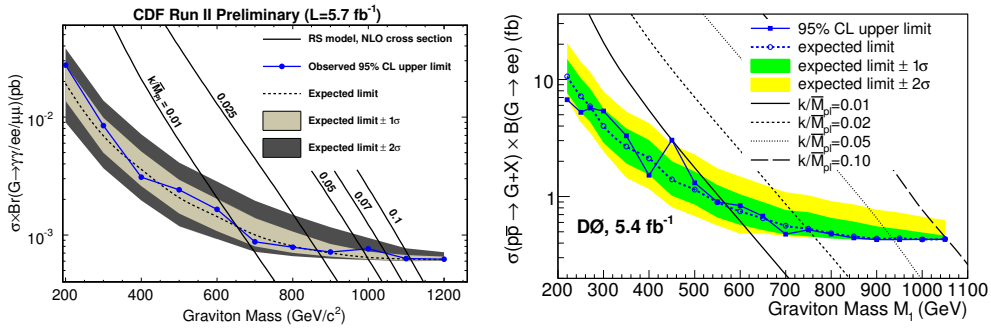

Figure 2.5: Exclusion limit for a RS graviton in $\gamma\gamma, e^+e^-, \mu^+\mu^-$ combination in the CDF (left) and D0 (right) experiments at Tevatron.

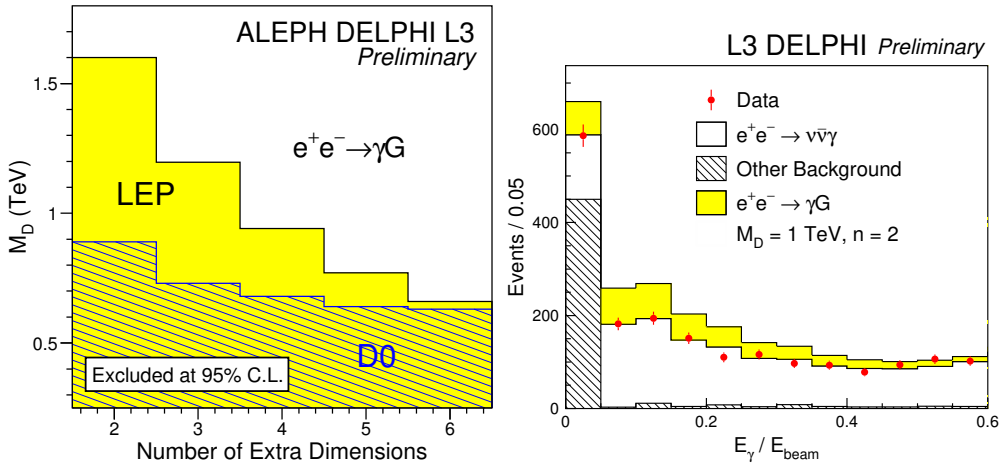

Figure 2.6: Left: the 95% exclusion contours in the M_D vn. n plane for the graviton-photon emission (ADD model) at LEP (ADL combined), current limit for D0 are also shown. Right: Distribution of the ratio of the photon energy to the beam energy for the single-photon events selected by DELPHI and L3, together with the SM prediction. Expected signal from the reaction $e^+e^- \to \gamma G$ (ADD model) is also shown for $M_D = 1$ TeV and $n = 2$.

RS-graviton mass limits (GeV/c^2)		
$k/\overline{M}_{Pl}$	$\mu\mu$ analysis	$\mu\mu + ee + \gamma\gamma$ analysis
0.01	327	642
0.025	510	865
0.05	677	984
0.07	774	1046
0.1	859	1111

n	M_D (TeV)			
	ALEPH [7]	DELPHI [8]	L3 [9]	OPAL [10]
2	1.26	1.31	1.50	1.09
3	0.95	1.02	1.14	0.86
4	0.77	0.82	0.91	0.71
5	0.65	0.67	0.76	0.61
6	0.57	0.58	0.65	0.53

Figure 2.7: Excluded masses for several couplings for a RS graviton in $\gamma\gamma, e^+e^-, \mu^+\mu^-$ combination in the Tevatron experiments for the RS model (left) and LEP experiments for the ADD model (right).

2.5.2 Exotic higgs search at Tevatron and LEP

The combined LEP data from the four collaborations (ALPEH, DELPHI, L3 and OPAL) were analyzed and compared to the prediction of a number of 2HDM 'benchmark' models. Within each of these model, the two tree-level parameters $\tan\beta$, m_A (CP-conserving scenario) or $m_\pm$ (CP-violating scenario) are scanned over broad ranges. Exclusion results for m_h can be seen in Figure 2.9, full results can be seen in Reference [65]. Combined results from the D0 and CDF collaboration at Tevatron regarding search for exotic Higgs boson can be found in Figure 2.8 and in reference [66].

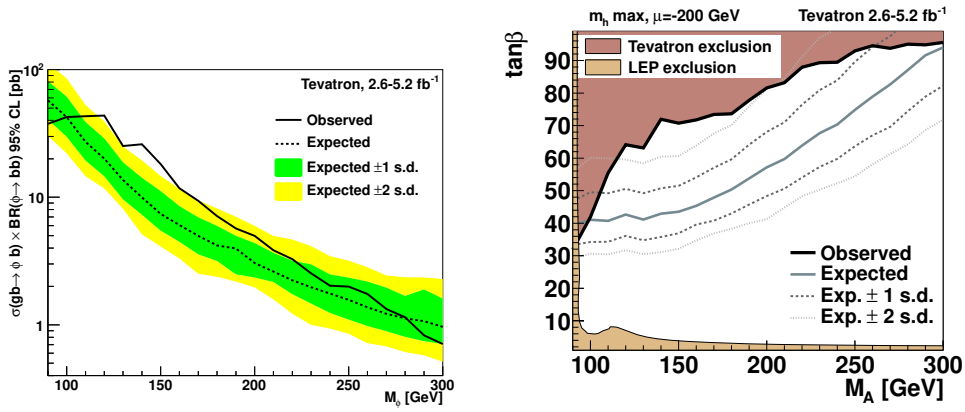

Figure 2.8: Left: Model independent 95% C.L. upper limits on the product of cross section and branching ratio for the combined analyses, assuming a mass degeneracy between two of the three neutral bosons and a Higgs boson width significantly smaller than the experimental resolution. The dark and light shaded regions (color online) correspond to the one and two standard deviation bands around the median expected limit. Right: 95% C.L. lower limit in the $(M_A, \tan\beta)$ plane for the m_h^{max}, μ =-200 GeV, including Higgs boson width effects. The exclusion limit obtained from the LEP experiments is also shown.

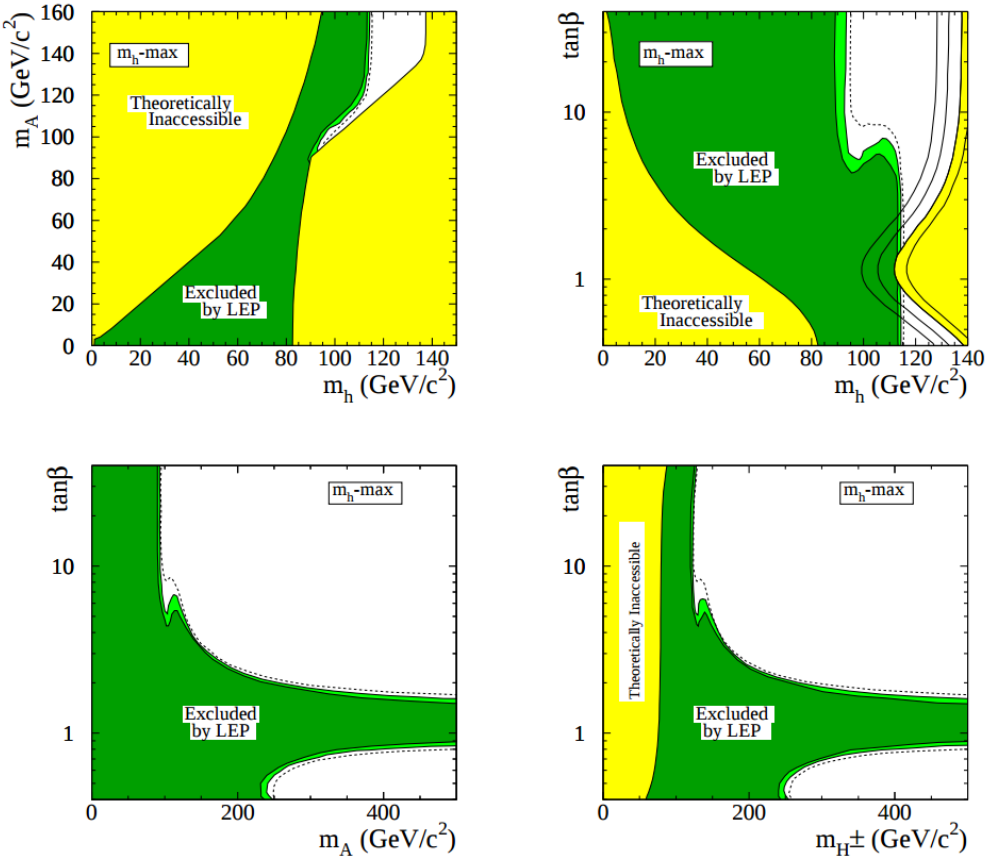

Figure 2.9: The MSSM exclusion, at 95% (light-green) and 99.7% (dark-green) for the $m_h - max$ benchmark scenario, with $m_t = 179.3$ GeV. The figure shows the excluded and theoretically inaccessible regions in four projections of the MSSM parameters, $m_h, m_A, \tan\beta, m_{H^+}$. The dashed lines indicate the boundaries of the regions expected to be excluded on the basis of Monte Carlo simulations with no signal. In the top right plots the upper edge of the parameter space is indicated for various top quark masses [65]. The maximal-mixing benchmark scenario (or m_h−max scenario) is the case where the mass of the lighest Higgs boson is maximal [52–54].

2.5.3 Exotic higgs and graviton search at LHC Run-I

At the LHC experiments in run I at 8 TeV both the searches for spin-2 and spin-0 resonances were conducted. RS Graviton search in ATLAS can be found in Reference [17] based on 20.7 fb^{-1} of collisions at 8 TeV [18] no deviation from the expected background was observed as seen in Figure 2.10 left, the combined search with ~ 5 fb^{-1} of data at 7 TeV in $G \rightarrow \gamma\gamma/ee/\mu\mu$ is shown in Figure 2.10 right. In the context of the RS model, a lower limit of 2.66 TeV at 95 % CL is set on the mass of the lightest graviton for coupling of $k/\overline{M}_{\rm Pl}$= 0.1. Search for ADD graviton was conducted with ~ 5 fb^{-1} of data at 7 TeV [67], lower limits of between 2.52 and 3.92 TeV at 95% CL are set on the M_S scale, depending on the number of extra dimensions and the theoretical formalism used (Table 2.11).

Regarding exotic higgs searches [7] in ATLAS data from run 1 no significant deviation from SM model was observed in the diphoton channel as seen in Figure 2.12. Charged Higgs was searched for in several channels [68–70]: $H^{\pm} \rightarrow W^{\pm}Z$, $H^{\pm} \rightarrow tb$, $H^{\pm} \rightarrow \tau\nu$. A summary of the exclusions for 8 TeV data can be found in Figure 2.13.

Search for large extra dimension in the diphoton channel in the CMS experiment at 7 TeV can be found in Reference [19]. While search for exotic Higgs in the 2HDM model and spin-2 Graviton at 8 TeV can be found in Reference [27]. Summary plots of the exclusion for spin-0 and spin-2 resonance can be seen in Figure 2.14.

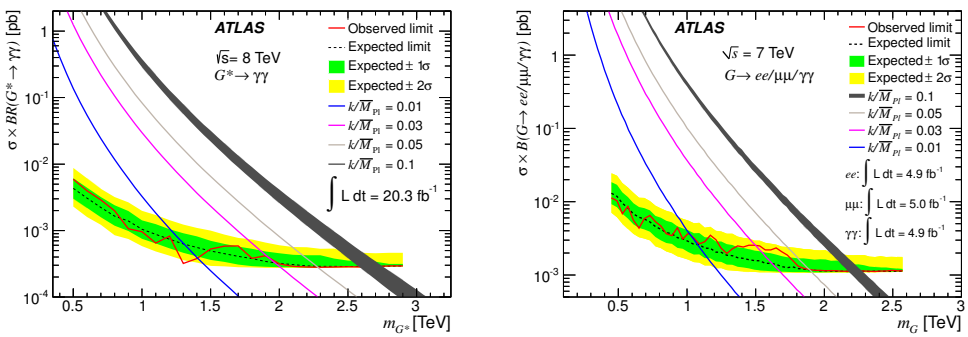

Figure 2.10: Left: Expected and observed upper limits on σ x BR(G*$\longrightarrow \gamma\gamma$) expressed at 95% CL, as a function of the assumed value of the graviton mass. The curves show the RS model prediction for given values of $k/\overline{M}_{\rm Pl}$ as a function of M_G. They are obtained using the PYTHIA generator plus a K-factor to account for NLO corrections (see text). The thickness of the theory curve for k/MPl = 0.1 illustrates the PDF uncertainties expressed at 90% CL. Right: Expected and observed 95% CL limits from the combination of $G \rightarrow \gamma\gamma/ee/\mu\mu$ channels on sigma x B, the product of the RS graviton production cross section and the branching ratio, as a function of the graviton mass. The -1σ and -2σ variations of the expected limit exhibit a tendency to be particularly close to the expected limit at large M_G. The theory curves are obtained using the Pythia generator, which implements the calculations from JHEP 0212 (2002) 03. A K-factor of 1.75 is applied on top of these predictions to account for NLO corrections.

K-factor value	ADD parameter	GRW	Hewett		HLZ					
			Neg.	Pos.	$n=2$	$n=3$	$n=4$	$n=5$	$n=6$	$n=7$
1	η_G	0.0115	–0.0191	0.0115			0.0115			
	M_S	3.05	2.40	2.73	3.11	3.63	3.05	2.76	2.57	2.43
1.70	η_G	0.0085	–0.0159	0.0085			0.0085			
	M_S	3.29	2.52	2.94	3.55	3.92	3.29	2.98	2.77	2.62

Figure 2.11: The observed 95% CL limits on the ADD model parameters η_G (TeV^{-4}) and M_S (TeV) for various ADD models.

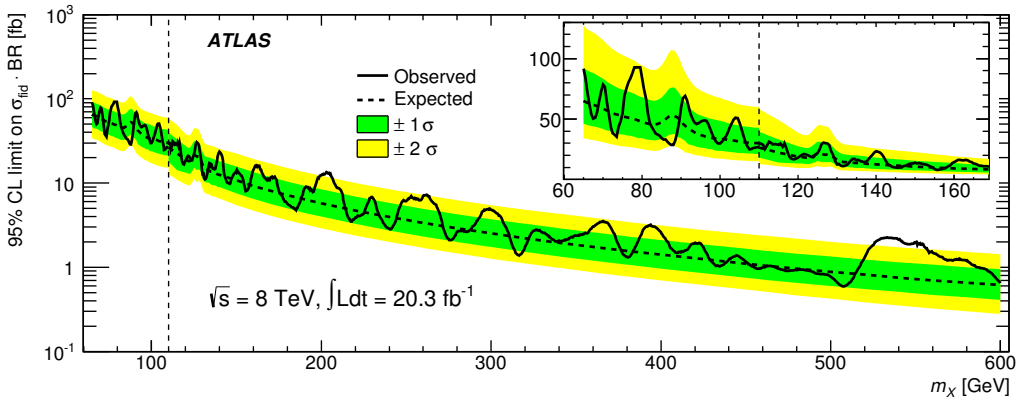

Figure 2.12: Observed and expected 95% CL limit on the fiducial cross-section times branching ratio BR(X$\longrightarrow \gamma\gamma$) as a function of mX in the range 65 < M_X< 600 GeV. The discontinuity in the limit at mX = 110 GeV (vertical dashed line) is due to the transition between the low-mass and high-mass analyses. The green and yellow bands show the ± 1σ and ± 2σ uncertainties on the expected limit. The inset shows a zoom of the limit.

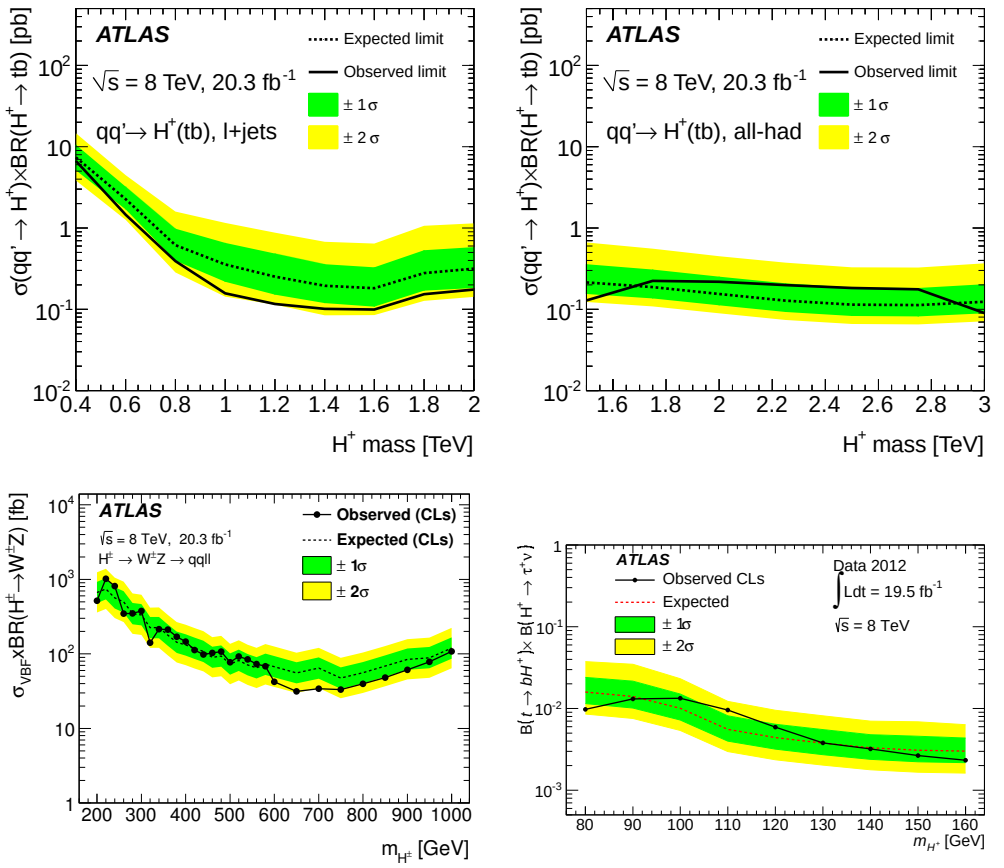

Figure 2.13: Top: Expected and observed 95% CL limits on the s-channel production cross section times branching fraction for $H+ \rightarrow tb$ as a function of the charged Higgs boson mass, in the (left) lepton+jets final state and (right) all-hadronic final state, including all systematic uncertainties, using a narrow-width approximation.

Bottom left: Exclusion limits in fb at the 95% CL for the vector-boson fusion production cross section of a H± boson times its branching fraction to W±Z assuming the signal has a narrow intrinsic width. Also included on the plot are the median, $\pm 1\sigma$ and $\pm 2\sigma$ values within which the limit is expected to lie in the absence of a signal.

Bottom right: Observed and expected 95% CL exclusion limits on the production and decay of charged Higgs bosons. The limit is computed for $\sigma(pp \rightarrow$anti-H+ + X)×cal B(Hp$\rightarrow \tau p\nu$), and is to be understood as applying to the total production cross section times branching ratio of H+ and H- combined.

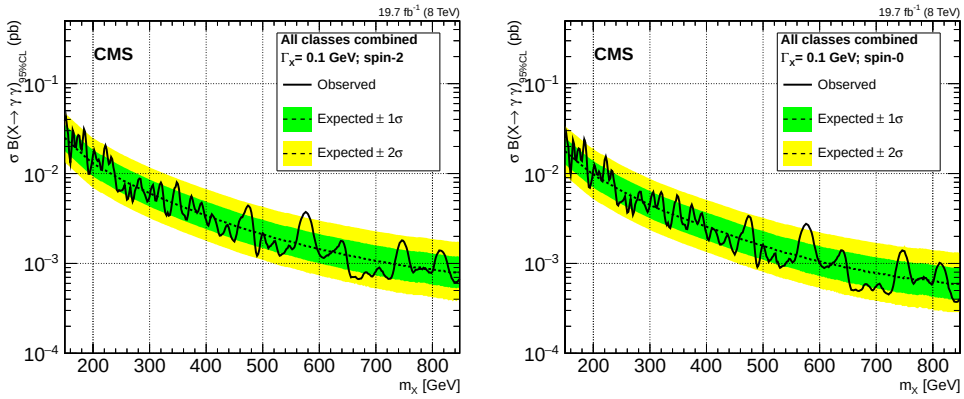

Figure 2.14: Right: Exclusion limit at 95% CL on the cross section times branching fraction of a new, narrow, spin-2 resonance decaying into two photons as a function of the resonance mass hypothesis, combining the four classes of events. Left: Exclusion limit at 95% CL on the cross section times branching fraction of a new, spin-0 resonance decaying into two photons as a function of the resonance mass hypothesis, combining the four classes of events. The results are for a narrow resonance hypothesis (α_X =0.1 GeV).

Part II

Experimental apparatus

CHAPTER 3

The Large Hadron Collider (LHC)

3.1 Particle colliders

Historically particles colliders were adopted to increase the available center of mass energy in collision with respect to the standard fixed target experiment. The available energy in a beam collider goes linearly with the beam energy ($E_{CM} \approx 2E_B$) while a target collider goes as $\sqrt{E}$.

Among particle colliders linear accelerators are easier to build, since no beam steering system is needed, but have energy limitations. To accelerate particles to high energy a long linear accelerator is needed and the beam is used only one time. Instead, in circular accelerators, only a short accelerator section is needed as the beam travels around the ring multiple time before it reaches the designed energy. Furthermore in circular colliders the beam, once brought to high energy, can be used for several collisions instead of a one-shot use. However the beams have to remain stable (beam stability) over a long period of time so they must be carefully bent and focused using dipoles and quadrupoles.

The main limitation to the beam energy in a electron-positron circular collider such as LEP is the energy loss from synchrotron radiation. Charged particles moving along a curved trajectory lose energy following the relation [71]:

$$\frac{dE}{dt} \propto \frac{E^4}{m^4 R} \tag{3.1}$$

where E and M are particle's energy and mass, while R is the trajectory's radius of curvature. This implies that at fixed energy and collider dimensions (radius), electrons lose $(m_p/m_e)^4 \sim 10^{12}$ times more energy than a proton beam with the same characteristics. To reach the current LHC beam energy with leptons it would have been necessary to build a synchrotron with a much larger radius or a linear accelerator.

3.1.1 Hadron colliders

At high energy hadron colliders the interaction is not between protons but between the elementary particles (quarks and gluons) inside the protons. The momentum of the proton is divided between its elementary components (following the parton distribution functions) so every hard collision has

a different center of mass energy. The energy of the collisions spans over a wide energy spectrum limited by the beam energy.

For every interesting hard collision several collisions take place between the remnants of the two hard-colliding hadrons (Figure 3.1, Left) which end up in forming color-less light hadrons, mesons or electromagnetic particles. Furthermore there are interactions between other hadrons in the same bunch in which protons interact as a whole (however still breaking into components), those are called soft collisions. These interactions have a small transferred momentum and the interaction's products have small $\langle p_T \rangle \simeq 500\,\text{MeV}$. The overlap of soft interactions between hadrons is called pile-up while the interaction between the other proton components in the same hard interaction is called underlying event.

The average number of interactions per bunch crossing in ATLAS is 14-24 (Figure 3.2) in run-II data taking conditions. This number corresponds to the mean of the poisson distribution of the number of interactions per crossing calculated for each bunch. It is calculated from the instantaneous per bunch luminosity as $\mu = L_{bunch} \times \sigma_{inel} / f_r$ where L_{bunch} is the per bunch instantaneous luminosity, σ_{inel} is the inelastic cross section and f_r is the LHC revolution frequency.

The istantaneous luminosity in the ATLAS experiment is calculated with a dedicated luminosity monitor called LUCID [72]. LUCID is made of two modules placed around the beam-pipe on both forward ends of ATLAS. Each module of the LUCID is composed of 16 photomultipliers (PMTs) that detect charged particles and 4 quartz fiber bundles read by PMTs themselves.

The cross section for hard collisions, which is the gateway for precision measurements and discovery new physics, is much smaller than the cross section for soft collisions (Figure 3.1, Right).

3.2 Luminosity

The total number of events (N) for a process with cross section σ that can be produced by a collider is $N = L\sigma$, where L is the integrated luminosity and is equal to $L = \int_0^T \mathcal{L} dt$. Where T is the length of the data taking in seconds and $\mathcal{L}$ is the instantaneous luminosity that depends only on parameters of the machine through the equation:

$$L = \frac{N_b^2 n_b f_r \gamma_r}{4\pi\epsilon_n \beta^*} F \tag{3.2}$$

where (the nominal parameters for the LHC are given in parenthesis):

- N_b is the number of particles per bunch ($\sim 10^{10} - 10^{11}$),
- n_b is the number of bunches per beam in 2016 (2736),
- f_r is the revolution frequency (10 kHz),
- γ_r the relativistic gamma factor (~ 7000),
- ϵ_n the normalized transverse beam emittance (3.75 μm),

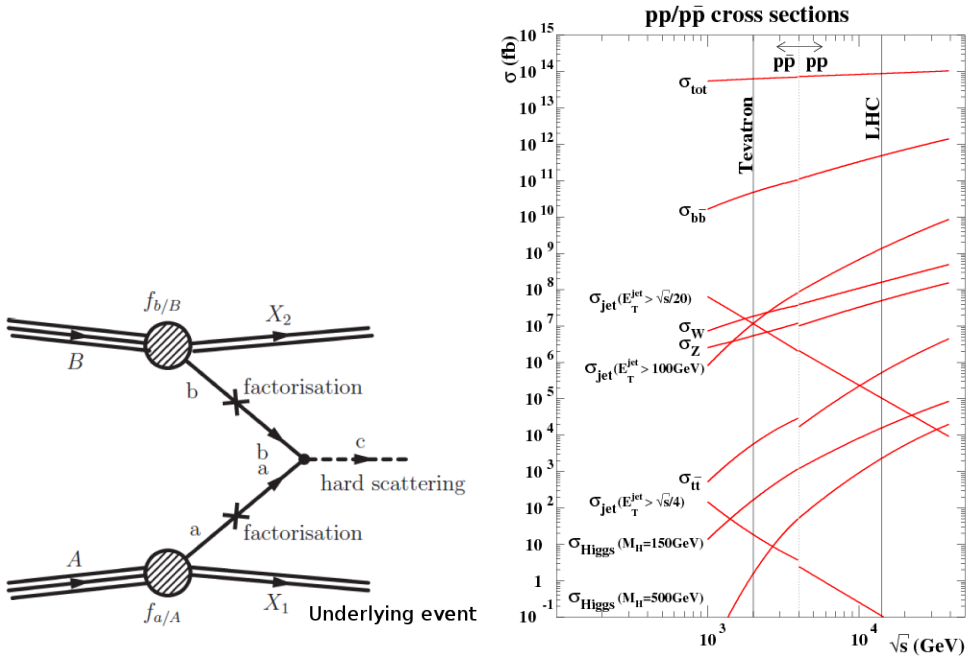

Figure 3.1: Left: Hard collision between two protons, the interaction is not between protons but between the quarks and gluons inside the protons. The interactions between the photon remnants are referred to as underlying event. Right: Production cross-sections for several representative processes at hadron colliders as a function of the machine center-of-mass energy.

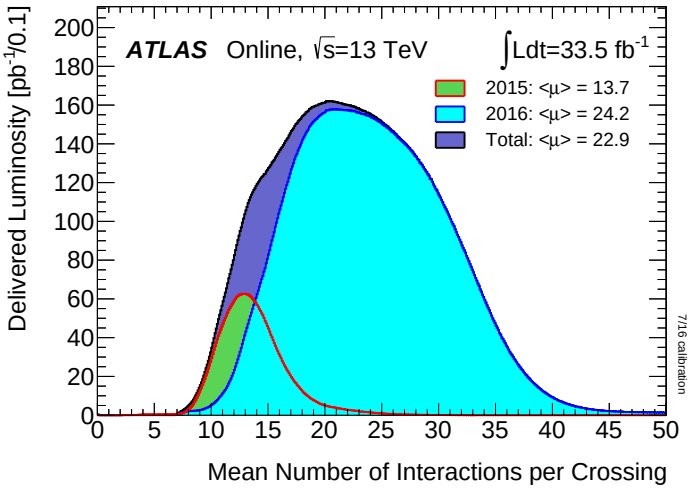

Figure 3.2: Luminosity-weighted distribution of the mean number of interactions per crossing for the 2015 and 2016 pp collision data at 13 TeV center-of-mass energy [73].

- β^* is the beta function at the collision point (0.55 m), related to the beam focusing,
- F is the geometric luminosity reduction factor if the beams do not collide head-on. A crossing angle of 285 μrad is used to prevent collisions outside the nominal interaction points, leading to $F = 0.84$.

The integrated and istantaneous luminosity for the LHC in the year 2015 and 2016 can be found in Figure 3.3.

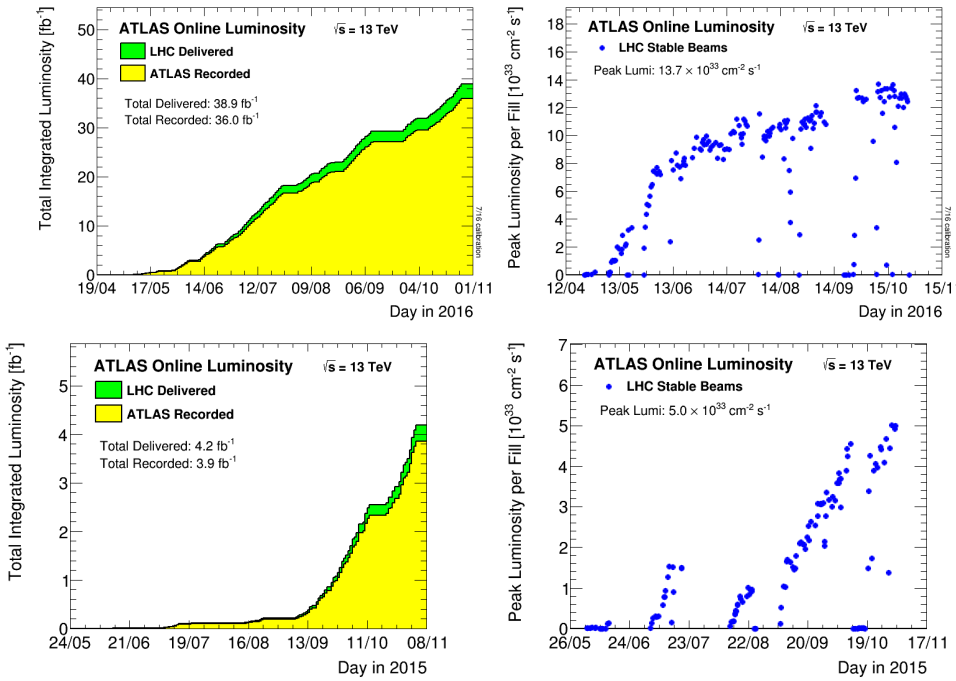

Figure 3.3: Right: ATLAS integrated luminosity over time for the year 2016 (top), 2015 (bottom). Left: ATLAS peak luminosity over time for year 2015 (top), 2016(bottom) [73].

3.3 Parton interactions

Proton is a complicated object made up of a sea of elementary components that behave as free particles thanks to asymptotic freedom. The sea is made up of gluon, virtual quark anti-quark pairs and valence quarks (the ones that carry the proton quantum numbers) called partons. The cross section of hard processes (processes with high transferred momentum Q^2) between protons can be calculated using perturbative QCD.

To evaluate $\sigma_{p+p\to X}$ (Figure 3.1) we have to take into account the probability to find a parton with momentum x_a within the hadron (and similarly for x_b). This probability density is called the parton distribution function (PDF in short), it is dependent on the energy scale of the process

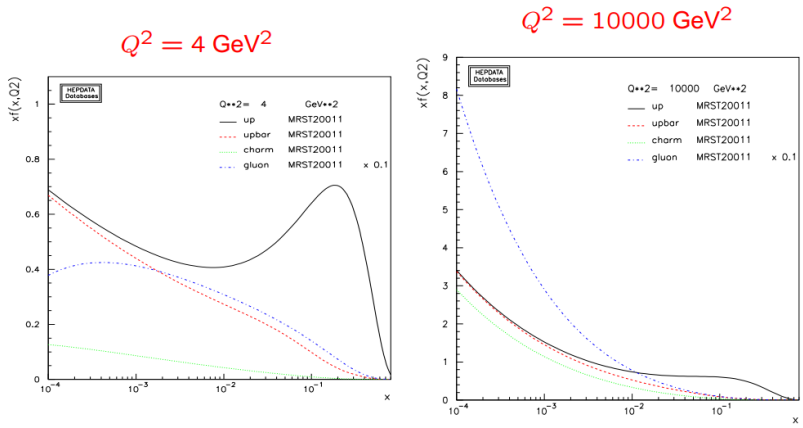

Figure 3.4: Parton distribution function dependance on x, for values of Q of 2 GeV and 100 GeV.

$f_{a,p}(x_a, E^2), f_{b,p}(x_b, E^2)$ (Figure 3.4). PDFs also carry information about the remaining parts of the hadron that interact softly (with low Q^2). They can be measured in other experiments and used to calculate theoretical cross sections. The cross section for a complex process can be calculated as the convolution of the cross section with the PDFs of the interacting hadrons:

$$\sigma_{pp\to X} = \sum_{a,b} \int_0^1 dx_a \int_0^1 dx_b f_{a,p}(x_a, \mu_F^2) f_{b,p}(x_b, \mu_F^2) \sigma_{a+b\to c}(p_a, p_b, \alpha_s(\mu_R^2), \mu_F^2) \tag{3.3}$$

Where the sum span over all the possible partons that can generate a final state resulting in the final state c. The PDFs depend from a scale μ_F called the factorization scale that represent the splitting between hard and soft collisions. The strong coupling constant α_s depends on μ_R^2 that is the renormalization scale. Theoretically the physical cross section is independent of this two parameters, because the dependence of the coefficients of the perturbative expansion of σ compensates with the scale dependence of the PDFs and coupling constant. To reduce the uncertainty of the theoretical cross section we need to evaluate the cross section at the highest possible perturbation order (to reduce the μ_F, μ_R dependance of the cross section).

3.4 LHC

The Large Hadron Collider (LHC) [74] is the world's most powerful tool for particle physics. It is a 26.7 km two-ring superconducting collider capable of accelerating counter-rotating proton beams to a center of mass energy $\sqrt{s} = 13$ TeV, and lead ions (Pb) to 2.8 TeV per nucleon. The two beams collide in four points across the accelerator ring corresponding where four main experiments are placed: ALICE, ATLAS, CMS, LHCb. The center of mass energy was at first 7TeV (2011), then it was raised to 8TeV (2012) and, after a technical shutdown of a couple of years, it was raised to 13

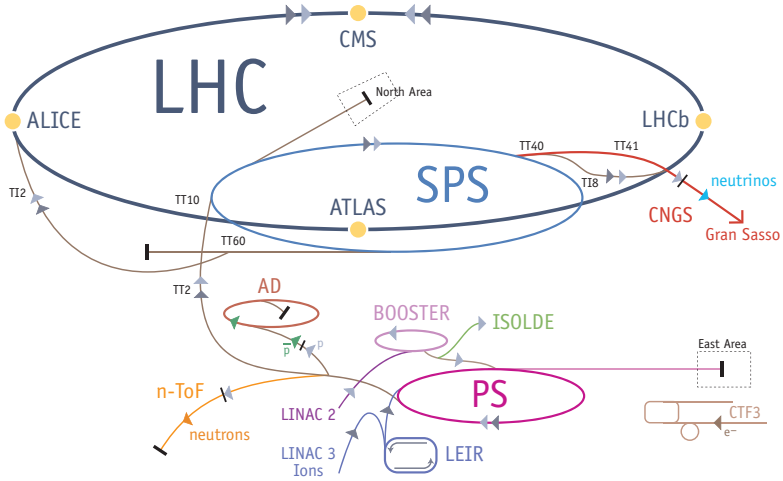

Figure 3.5: Cern accelerator complex

TeV (2015-2016).

The LHC project started in year 1984, when the scientific community began to design a high energy physics collider able to deliver a center of mass energy higher than the other already existing colliders (LEP and Tevatron). The main purpose of this new machine was the investigation of the nature of electroweak symmetry breaking and the search for physics beyond Standard Model at the TeV scale: this included the search for the Higgs boson and the clarification of the issues related to Higgs boson mass scale.

The tunnel that previously hosted the LEP accelerator is now used by the LHC. It comprises eight straight accelerator sectors and eight bending arcs and lies between 45 m and 170 m below the earth surface.

Center of mass energies achievable at the LHC are 7 times higher than the previous record, detained by the Tevatron. This is only possible through several steps that take place in the CERN accelerator complex before the beam injection at the LHC. The chain is illustrated in Figure 3.5. The protons are extracted from a hydrogen container at the beginning of the process. It takes a number of steps to get protons up to the LHC collision energy (Figure 3.5):

- A linear accelerator (LINAC 2) bring the beam energy to 50 MeV.
- Then a circular booster (PSB) is where the beams reach 1.4 GeV.
- In the Proton Synchrotron (PS) the particles attain 26 GeV.
- Then the Super Proton Synchrotron (SPS) is where the particles reach 450 GeV.

- Finally they enter the LHC and go in opposite directions where they will reach the final center of mass energy of 13 TeV in heads on collisions in the 4 interaction points corresponding to ALICE, ATLAS, CMS or LHCb

The beams are injected in bunches with a length corresponding to ~5.1 cm and nominally spaced by 25 ns. Consequently, the bunch crossing occurs at a frequency of 40 MHz.

Being a particle – particle collider (as opposed to particle – anti-particle), the LHC is composed of two separate beam-lines where the protons and ions are deflected by opposite magnetic fields to follow circular trajectories. A "two-in-one" magnet design was adopted to cope with restrictions in the tunnel diameter, with two coils sharing the same cooling infrastructure. Superconducting dipole magnets are the key elements of the machine, responsible for bending the beams with magnetic fields above 8 T. The 1232 dipoles, and the 392 quadrupoles responsible for focusing the beam operate at temperatures below 2 K maintained by superfluid helium. The acceleration is performed by radio-frequency (RF) cavities. A 400 MHz superconducting system increases the beam energy by 485 keV at each turn until it reaches 13 TeV. The energy limiting factor for the LHC is not the acceleration itself but the bending power of the dipole magnets.

3.5 Detectors at the LHC

The LHC beams can collide in four different points, all instrumented with large experiments: ATLAS (A Toroidal LHC ApparatuS), CMS (Compact Muon Solenoid), ALICE (A Large Ion Collider Experiment) and LHCb. The ATLAS detector will be discussed in more detail in the next chapter.

3.5.1 ATLAS and CMS

ATLAS [75] (A Toroidal LHC ApparatuS) and CMS [76] (Compact Muon Solenoid) are the main general purpose detectors of the LHC, they were built to take advantage of the full discovery potential of the accelerator. Several physics channel are under study: the search for supersymmetric and exotic particles, accurate measurement of the top and Higgs proprieties, CP violation in the decay of B mesons and SM precision measurements. In general the two experiments are different in the detector structure. CMS has only one magnetic field for all the detectors, the muon spectrometer uses the return flux of the magnet using iron inserts. Its electromagnetic calorimeter is made out of tungsten lead crystal (PWO_4). In ATLAS only the region of the inner detector is immersed in magnetic field, while the calorimeters are outside the magnetic field. The magnetic field for the air muon spectrometer is generated by a separate toroidal system. The ATLAS electromagnetic calorimeter and hadronic endcap instead is made of lead and liquid argon.

3.5.2 LHCb

The LHCb [77] detector is specialized in B meson study. It has the purpose of analyzing the proprieties of the b quark and the CKM parameters that describe the CP violation. This kind of

studies could lead to the understanding of the so-called *electroweak arrow of time* that would explain the large difference in quantity of matter and anti-matter in the universe. The geometry of the detector is asymmetric since b and $\bar{b}$ travel in the same direction following roughly the beam, so it is enough to cover one of the two forward regions, however loosing a factor of 2 in statistic.

3.5.3 ALICE

ALICE [78] (A Large Ion Collider Experiment) is dedicated to the study of heavy ions collisions to understand the behavior of high energy nuclei interaction. The purpose of this detector is to study the quark-gluon plasma. ALICE will mostly collect lead ions collisions, but will also register pp collisions to calibrate and to give an additional support to the other detectors measurements.

3.5.4 TOTEM and LHCf

TOTEM [79] is placed close to CMS and LHCf [80] is close to ATLAS. These two experiments have been built to study the soft collision between the beams, which are almost parallel to the beam axis and have a diffractive behavior. TOTEM has the purpose of measure the total cross section of elastic interaction and diffraction process, it also has the purpose of calibrating the LHC luminosity. LHCf has the purpose of measuring with high precision the pp cross section at 13 TeV.

CHAPTER 4

The ATLAS detector

The ATLAS (A Toroidal LHC ApparatuS) collaboration is composed by more than 3000 physicists from 38 countries and 174 universities and laboratories. Together with CMS, ATLAS is a general purpose detector, designed to explore a wide range of physical processes and take advantage of the full LHC discovery potential.

The detector (Figure 4.2) is cylinder with 12 meter of radius and 44 meter of length and it weights approximately 7000 tons. From the inside out there are layers of detectors: the inner detector, the calorimeters and the muon chambers. ATLAS has been built to cover the maximal solid angle around the interaction point. Conventionally the z axis is along the beam pipe and the x,y plane is the transverse plane.

All the transverse quantities ($P_T, E_T, E_{\mathrm{T}}^{\mathrm{miss}}$) are defined in the x,y plane (Figure 4.1). The azimutal angle is ϕ and describes the angle around the beam axis. The polar angle θ describes the angle from the beam axis. To have a Lorentz invariant angular coordinate system under boost along the z-axis around the interaction point the (η, ϕ) set of coordinates is used. η is the pseudo-rapidity and is defined as:

$$\eta = -\log \tan \frac{\theta}{2} \tag{4.1}$$

The angular distance ΔR between two objects in the (η, ϕ) space is:

$$\Delta R = \sqrt{(\delta\eta)^2 + (\delta\phi)^2} \tag{4.2}$$

The inner detector is able to measure tracks in the $|\eta| < 2.5$ range. The electromagnetic calorimeter provides precision measurement inside $|\eta| < 2.5$ but energy measurement for jets and particle showers are covered until $|\eta| < 4.9$.

4.1 Inner detector

The inner detector (Figure 4.3, left) is a 7 meter long and 1.15 meter of radius cylinder. It is placed inside a 2T solenoidal magnetic field. In the central part the tracking detectors are organized in cylinders of increasing radius, furthermore there are two end-cap parts, also made of tracking

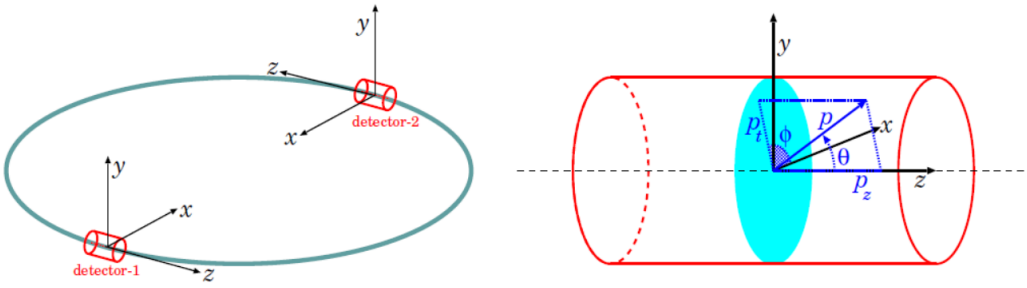

Figure 4.1: ATLAS coordinates system.

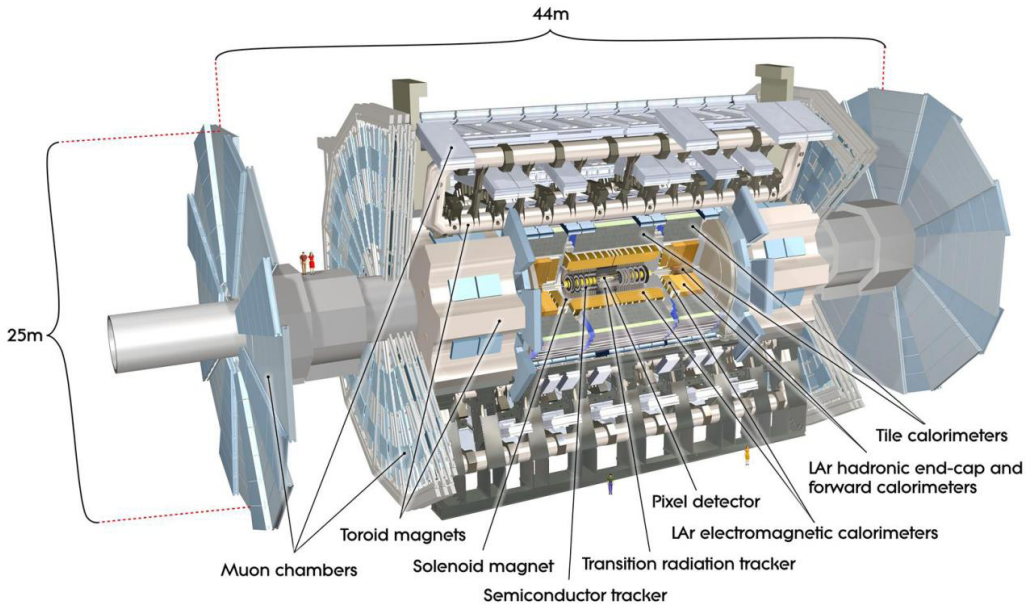

Figure 4.2: ATLAS detector cut-away to show the inner detector, the inner solenoid magnet, the calorimeters, the muon chambers and the thoroid magnet.

detectors, to complete the η coverage. The levels of the inner detector are: the first level is the IBL, the second level is the semiconductor pixel detectors, the third level is made of silicon micro-strip detectors (SCT: silicon tracker detector), then in the last level there is the transition radiation detector (TRT).

Precise tracking is achieved by the combination of high bending power and fine granularity position measurements for charged particles. The tracking software offers pattern recognition, momentum and vertex measurements, and electron identification capabilities. Giving the high number of tracks per events, the discrimination between different tracks and the recognition of the vertexes can be fulfilled only with high detector granularity.

Vertexes and tracks of the charged particles are reconstructed by using the information from all the layers with different techniques such as Hough transform and forward tracking. A further explanation of tracking techniques used in ATLAS can be found in Ref. [81, 82]. The inner detector is also crucial for detecting b-jets with b-tagging techniques. Before run-II (from 2016) an additional layer of pixel caller Insertable B Layer (IBL) was inserted between the beam line and the inner detector. This addition increased the performance of b-tagging algorithms.

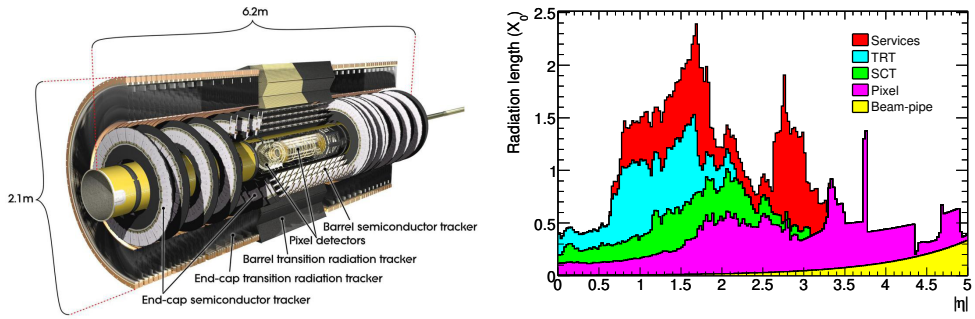

Figure 4.3: Left: ATLAS inner detector cut-away. Right: Material distribution at the exit of the Inner Detector envelope as a function of $|\eta|$ (averaged over ϕ). These figures do not take into account the IBL layer.

The high-radiation environment was a major concern for the design of the Inner Detector sensors, on-detector electronics, mechanical structure and services. The silicon detectors are kept at low temperatures (approximately -5 to -10 C) to minimize the noise after radiation damage. The straw-tubes, on the contrary, can operate safely at room-temperature.

The material budget was also carefully minimized, to avoid deterioration of the resolution of both tracking and calorimetry. Still, mainly due to the services and supports, it varies from 0.5 to 2.5 radiation lengths (X_0) depending on η (Figure 4.3, right). As a consequence, 40% of the photons convert into electron-pairs and electrons lose a sizeable fraction of their energy through bremsstrahlung before reaching the electromagnetic calorimeter.

The system is surrounded by a central solenoid that generates a uniform axial magnetic field with a strength of 2 T in the center. The solenoid extends over a length of 5.3 m with a diameter of 2.5 m. The operating temperature of 4.5 K is maintained by a cryostat shared with the barrel electromagnetic calorimeter. In the following a detailed description of the inner detector levels can

be found.

4.1.1 Insertable B-Layer (IBL)

During the LHC shut down in 2013 (Phase 0) an additional pixel layer was installed: the Insertable B-Layer (IBL). It was inserted between the current B-Layer and a new smaller diameter beryllium beam pipe, very close to the interaction point. The inner radius of the detector is 31 *mm* while the outer radius is 40 *mm*. The pixel detector in use until 2013 was designed for a peak luminosity of $10^{34}\text{cm}^{-2}\text{s}^{-1}$ and 50 Mrad dose, limit that was exceeded in the past years after LS1. The main motivation for IBL is to maintain excellent vertex detector performance as the LHC luminosity increase.

With a pixel area of $250 \times 50\,\mu\text{m}^2$, the IBL has a relatively low occupancy and preserves the tracking performances also with the increased luminosity of run-II. The space-point resolution per module is <10 μm in $R-\phi$ and 72 μm in z. Moreover, being very close to the interaction point, the IBL provides better quality of the impact parameters reconstruction for the tracks. Each one of the 14 supporting staves are equipped with with 12 Planar sensors, placed in the central region of the stave and 8 3D sensors in the forward region (4 for each side).

4.1.2 The pixel detectors and the silicon micro-strip trackers (SCT)

The precision tracking detectors (pixel and SCT) extend up to $|\eta| < 2.5$. They are arranged in concentric cylinders around the beam axis in the barrel, and disks perpendicular to this axis in the end-cap regions. Typically three pixel layers and four SCT strips are crossed by each track.

The pixel layers are positioned at radial distances of 50.5 mm, 88.5 mm and 122.5 mm in the barrel, and 49.5 mm, 58.0 mm and 65.0 mm in the end-caps. All pixel sensors are identical, segmented in $R-\phi$ and z, with a space-point resolution of $14\,\mu\text{m}^2$ in $R-\phi$ and 115 μm in z (R) in the barrel (end-cap). Approximately 80.4 million readout channels are used. The high-precision space point measurements allow the reconstruction of short lived particles and the associated production vertexes. This is of fundamental importance in the identification of b-quark jets.

After the pixel detectors in the radial coordinate, four double layers of silicon strips are placed with a small angle between the layer couples to measure the z coordinate, this provides four space point measurements for each track. The space-point resolution per module is 17 μm in $R-\phi$ and 580 μm in z (R) in the barrel (end-cap), with a total of 6.3 million readout channels.

4.1.3 The transition radiation tracker

The outer part of the Inner Detector is composed of layers of gaseous straw tubes inserted in transition radiation material. The tubes are filled with a non-flammable xenon-based gas mixture of 70% Xe, 20% CO_2 and 10% CF_4. This ensures high efficiency in the detection of ionization signals and transition radiation photons, produced in the polypropylene fibers in the barrel and foils in the endcap that surround the straws. Typically, seven to ten high-threshold hits from transition radiation are expected for electrons with energies above 2 GeV. With an average of 30 hits per charged

particle track, the transition radiation tracker (TRT) provides continuous tracking and electron identification complementary to that of the calorimeters over a wide range of energies. Enhanced pattern recognition and significant improvement of the momentum resolution are achieved with this detector, which extends radially from 56 to 107 cm over $|\eta| < 2.0$.

The TRT only provides $R - \phi$ information in the barrel and $z - \phi$ in the end-cap, with a resolution of 130 μm per straw. In the barrel region, straws with a diameter of 4 mm and 144 cm long are disposed parallel to the beam axis, with their wires divided around $\eta = 0$. In the end-cap region 37 cm long straws are arranged radially in wheels. The total number of TRT readout channels is approximately 351 000.

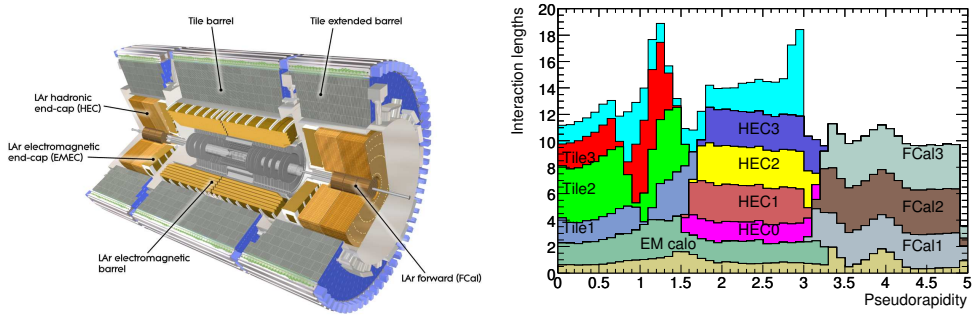

Figure 4.4: Left: ATLAS calorimeters structure. The barrel and end-cap regions of the EM calorimeter together with the end-cap region of the hadronic calorimeter use LAr as active medium. The barrel region of the hadronic calorimeter is made of scintillating tiles. Right: Cumulative amount of material, in units of interaction length, in front of and after the calorimeters as a function of $|\eta|$. Also shown for completeness is the total amount of material in front of the first active layer of the Muon Spectrometer (light blue). The peaks at $|\eta| \sim 1.3$ and $|\eta| \sim 3$ correspond to the TileCal extended barrel and a shielding disk, respectively. Details can be found in ref. [9].

4.2 Calorimeters

The calorimetric system is located between the Inner Detector and the Muon Spectrometer, covering the pseudo-rapidity range $|\eta| < 4.9$. Different techniques are used depending on η and R, according to the requirements of the wide range of physics processes and radiation tolerance. Measurements of electrons, photons and jets and inputs for missing transverse momentum are provided, given the full azimuthal coverage and good hermeticity of the detectors.

In the region covered by the inner tracker, showers produced by electrons and photons are contained in the finely segmented Liquid Argon (LAr) electromagnetic calorimeters (EM), which exhibit excellent performance in terms of energy and position resolution. Liquid Argon technology is also used for in the detection of hadronic activity in the end-cap and forward regions, instrumented by a Hadronic End-cap Calorimeter (HEC) and a Forward Calorimeter (FCal). Chosen for its intrinsic linear behavior, its response stability over time and its intrinsic radiation-hardness, the LAr detectors require an operating temperature around 88 K. The barrel EM calorimeter shares the cryostat with the central solenoid, eliminating two vacuum walls. The end-caps are hosted in their own cryostats, used for the EM, the HEC and the FCal calorimeters.

Hadronic calorimetry is complemented by a scintillator-tile detector, extending up to $|\eta| < 1.7$. A layout of the ATLAS calorimeters is presented in Figure 4.4 and the segmentation of each part is summarized in table 4.1. A section of the barrel/endcap transition is shown in the left panel of Figure 4.6. Each sub-calorimeter is described in the following subsections and their performance is discussed.

Calorimeter	Coverage		Granularity ($\Delta\eta \times \Delta\phi$)
EM calorimeter	**barrel**	**end-cap**	
Presampler	$\|\eta\| < 1.54$	$1.5 < \|\eta\| < 1.8$	0.025×0.1
Sampling 1	$\|\eta\| < 1.475$	$1.375 < \|\eta\| < 3.2$	0.003×0.1[a] 0.025×0.025[b] 0.003 - 0.025×0.1[c] 0.1×0.1[d]
Sampling 2	$\|\eta\| < 1.475$	$1.375 < \|\eta\| < 3.2$	0.025×0.025 0.075×0.025[b] 0.1×0.1[d]
Sampling 3	$\|\eta\| < 1.35$	$1.5 < \|\eta\| < 2.5$	0.05×0.025
Tile calorimeter	**barrel**	**extended barrel**	
Sampling 1 Sampling 2	$\|\eta\| < 1.0$	$0.8 < \|\eta\| < 1.7$	0.1×0.1
Sampling 3			0.2×0.1
Hadronic end-cap calorimeter			
Samplings 1-4	$1.5 < \|\eta\| < 3.2$		0.1×0.1[e] 0.2×0.2[d]

[a] $|\eta| < 1.4$, [b] $1.4 < |\eta| < 1.475$, [c] $1.375 < |\eta| < 2.5$, [d] $2.5 < |\eta| < 3.2$, [e] $1.5 < |\eta| < 2.5$

Table 4.1: Pseudo-rapidity coverage, longitudinal segmentation and granularity of the ATLAS calorimeters. The full numbers can be found in ref. [83].

4.2.1 Performance of the calorimeters on testbeam data

The energy resolution of each sub-calorimeter was evaluated with beams of electrons and pions before their insertion in the ATLAS detector. The experimental measurements, after noise subtraction, have been fitted with the expression:

$$\frac{\sigma(E)}{E} = \frac{b}{\sqrt{E/\mathrm{GeV}}} \oplus c, \tag{4.3}$$

where b is the stochastic term and c the constant term reflecting local non-uniformities in the response of the calorimeter. The design parameters, specified in Reference [84] were fulfilled, and the obtained performance is summarized in Table 4.2. An additional effective constant term c', that depends on the pseudo-rapidity η, to account for the difference between data and Monte Carlo energy resolution is measured on data (Section 5.5.4).

For what concerns the electronic noise, updated information was extracted during the cosmic-ray data taking periods, from 2007 to 2010 and during the first part of the year 2015. The noise was measured in intervals when no track was recorded in ATLAS. During LHC runs this is done in time windows when no collisions happen. The results correspond to the expectations for both the

LAr and Tile calorimeters and are shown in Figure 4.5. No major impacts on jet reconstruction above ~ 5 GeV or electron identification above ~ 0.5 GeV are expected from these noise levels.

Calorimeter	Particle	Energy Resolution	
		b (% $\sqrt{\text{GeV}}$)	c (%)
Electromagnetic	electrons	10.0 ± 0.4	0.4 ± 0.1
Hadronic End-Cap	pions	70.6 ± 1.5	5.8 ± 0.2
Forward	electrons	28.5 ± 1.0	3.5 ± 0.1
	pions	94.2 ± 1.6	7.5 ± 0.4
Tile	pions	56.4 ± 0.4	5.5 ± 0.1

Table 4.2: Resolution of the different calorimeters for pions and electrons evaluated with test beam data, given by the stochastic term b and the constant term c as in equation 4.3. The constant term for the full electromagnetic calorimeter is expected to be around 1%.

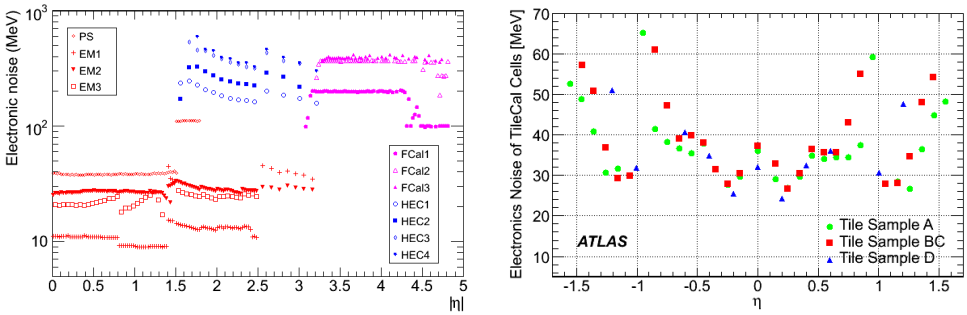

Figure 4.5: Left: electronic noise in the cells of the liquid argon calorimeters as a function of $|\eta|$. Right: electronic noise in the cells of the tile calorimeter as a function of η.

4.2.2 Electromagnetic calorimeter

The electromagnetic calorimeter is a cylinder of 2.25 meters of external radius and 6.65 meters of length. It covers the pseudo-rapidity region of $|\eta| < 3.2$. There is a central barrel that covers the beam pipe until $|\eta| < 1.475$ and two end-cap covering $1.375 < |\eta| < 3.2$ (Figure 4.7 and Figure 4.6, left). The calorimeter is a sampling calorimeter made of alternates layers of liquid argon as active medium and lead as passive medium.

Copper electrodes and lead absorbers bent in an accordion shape are immersed in a Liquid Argon vessel (Figure 4.6, Right). Using this kind of structure the full azimuthal angle ϕ is covered without non sensitive regions from the outgoing readout cables. In the barrel the accordion waves are parallel to the beam axis and their folding angle varies along the radius in order to keep the

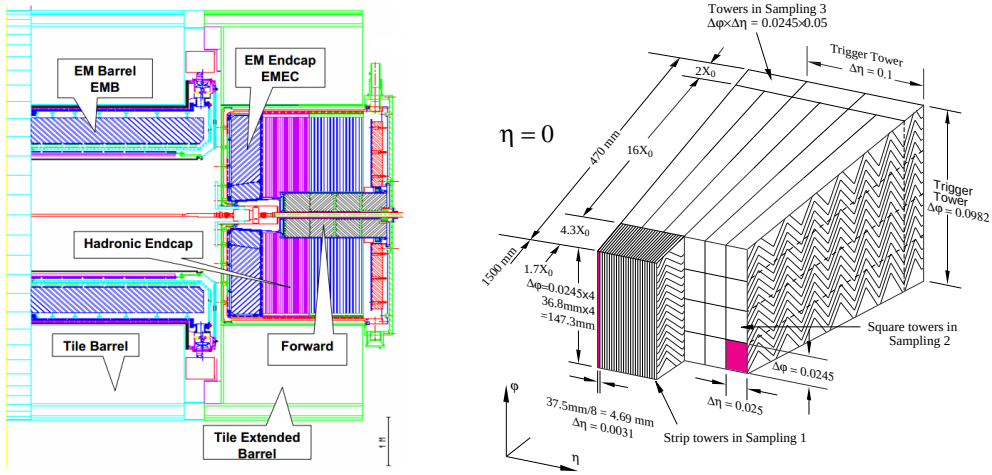

Figure 4.6: Left: ATLAS calorimeter transition between central region and end-cap region for the electromagnetic and hadron calorimeters. The output of the electronic of the detector travels in cables passes trough these 'crack' regions. Right: ATLAS electromagnetic calorimeter segmentation in (ϕ, η) for the tree layers.

liquid argon gap as constant as possible. In the electromagnetic endcaps, the accordion waves run axially and the folding angle varies with radius.

The energy design resolution for the EM calorimeter is:

$$\frac{\sigma}{E} = \frac{10 - 17\%}{\sqrt{E}} \oplus 0.7\% \tag{4.4}$$

The total EM calorimeter depth is approximately constant over η and is about 25 radiation lenghts. The calorimeter is segmented in 3 longitudinal layers in the region covered by the Inner Detector ($0 < |\eta| < 2.5$), and two in the higher-η region ($2.5 < |\eta| < 3.2$). An additional layer in front of the calorimeter in the regions up to $|\eta| < 1.8$ is called pre-sampler, it is a thin layer made only of liquid argon before the actual calorimeter to measure the energy deposits from electromagnetic showers starting before reaching the calorimeter.

The calorimeter is also segmented in both η and ϕ in cells to measure the position of the electromagnetic particle shower. The segmentation of the calorimeter in the pseudo-rapidity regions of $|\eta| < 1.475$ for the barrel and $1.375 < |\eta| < 3.2$ for the end-cap can be seen in table 4.1 and in the right panel Figure 4.6. A detailed description of the LAr control system and readout can be found in Appendix B. The energy calibration procedure of electron and photons from the energy deposited in the EM calorimeter is described in Section 5.5.

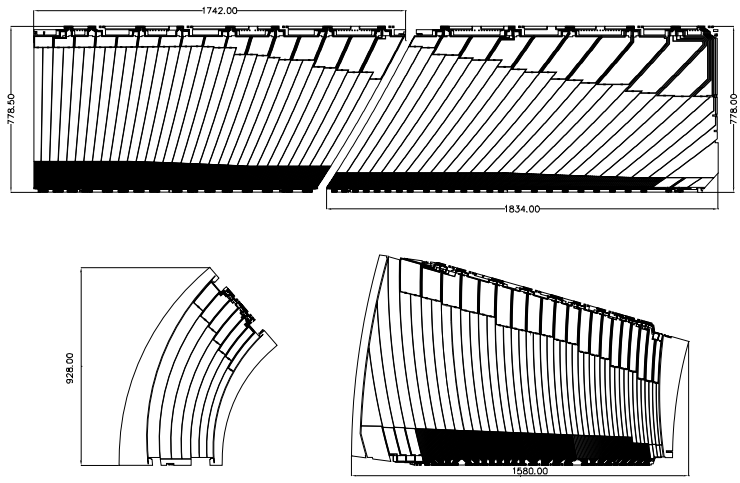

Figure 4.7: The fours types of electrodes of the electromagnetic calorimeter. The two top ones correspond to barrel electrodes: $|\eta| < 0.8$ (left) and $|\eta| > 0.8$ (right). The bottom left is an endcap inner wheel electrode and the bottom right is the outer wheel. Dimensions are in mm.

4.2.3 Hadronic calorimeter

The hadronic calorimeter is inside a cylinder of 4.25 meters radius and 6.10 meters long. It covers a pseudo-rapidity region of $|\eta| < 3.9$. Its purpose is to absorbs energy from particles that pass through the EM calorimeter, but do interact via the strong force.

In the central part $|\eta| < 1.7$ it is a sampling calorimeter (TileCal) with steel as passive material and scintillating tiles that measure the energy deposited. While the end-cap sections of the hadronic calorimeter (HEC) are still sampling calorimeters but using LArg as active material and copper as absorber. They are placed in separate cryostats together with the forward calorimeters. Radiation hardness and cost effectiveness drove the choice of the technology and the calorimeter geometry.

The overall thickness of the calorimeter is 11 interaction lengths in the $\eta = 0$ region. The total design energy resolution for hadronic jets (combined with electromagnetic calorimeter) is:

$$\begin{aligned} \frac{\sigma}{E} &= \frac{50\%}{\sqrt{E}} \oplus 3\% \quad for \quad |\eta| < 3 \\ \frac{\sigma}{E} &= \frac{100\%}{\sqrt{E}} \oplus 5\% \quad for \quad 3 < |\eta| < 5 \end{aligned} \tag{4.5}$$

TileCal The TileCal is divided into a 5.8 m long barrel, covering the region up to $|\eta| < 1.0$ and two extended barrels in the range $0.8 < |\eta| < 1.7$ with 2.6 m in length an inner radius of 2.28 m and an outer radius of 4.25 m. It is segmented in depth in three layers, with approximately 1.5, 4.1 and 1.8 interaction lengths (λ) for the barrel and 1.5, 2.6, and 3.3 λ for the extended barrel.

Cables and services from the detectors placed before the tile calorimeter occupy the 60 cm gap between the barrel and the extended barrel. In this region, scintillating tiles assembled in the so

called Intermediate Tile Calorimeter complement the energy measurement.

The geometry of TileCal is sketched in Figure 4.8, with the layers in depth noted as A, BC and D. The orientation of the scintillator tiles radially and normal to the beam line allows for full projective azimuthal coverage. On the other hand, the grouping of the readout fibres imply a "pseudo-projective" geometry in η. The granularity of the TileCal is $\Delta\eta\times\Delta\phi = 0.1\times0.1$.

HEC The HEC is formed by two wheels divided into two segments in depth, with a total of four compartments per end-cap. Each wheel is built out of 32 identical wedge-shaped modules, providing projective geometry in the ϕ direction but only "pseudo-projectivity" in η, as illustrated in Figure 4.8a. The size of the HEC cells is $\Delta\eta \times \Delta\phi = 0.1 \times 0.1$ up to $|\eta| < 2.5$ with twice those values in the rest of the coverage.

4.2.4 The forward calorimeter

The forward calorimeter (FCal) provides both electromagnetic and hadronic energy measurements, and extend the pseudo-rapidity coverage of the calorimetric system from $|\eta| = 3.1$ to $|\eta| = 4.9$. Although the system is not used for precision measurements, it provides valuable information for missing transverse momentum determination and reconstruction of very forward jets. The energy design resolution for the FCAL is:

$$\frac{\sigma}{E} = \frac{100\%}{\sqrt{E}} \oplus 10\% \tag{4.6}$$

Radiation tolerance is extremely important in this region, where high particle fluxes are expected. This has resulted in a design with very small liquid-argon gaps, separated by copper absorbers in the first compartment, and tungsten absorbers in the last two. Overall, the thickness of the FCal is of the order of 10 interaction lengths.

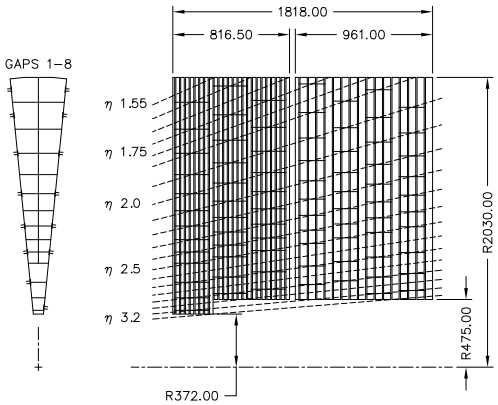

(a) Schematic views of the hadronic end-cap calorimeter in $R-\phi$ (left) and $R-z$ (right). The semi-pointing layout of the readout electrodes is indicated by the dashed lines. Dimensions are in mm.

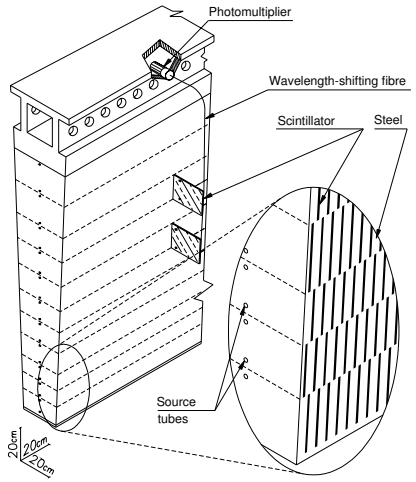

(b) Illustration of the components in a module of the tile calorimeter.

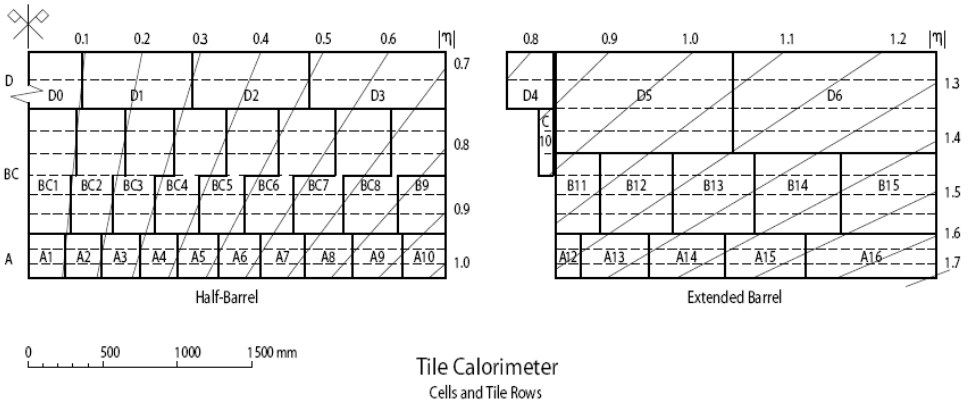

(c) $R-z$ view of the tile calorimeter. The diagonal lines indicate the semi-projective layout of the cells.

Figure 4.8: Schematic views of (a) hadronic end-cap calorimeter. Schematic views of (b) a module and (c) the full tile calorimeter geometry in the $R-z$ plane.

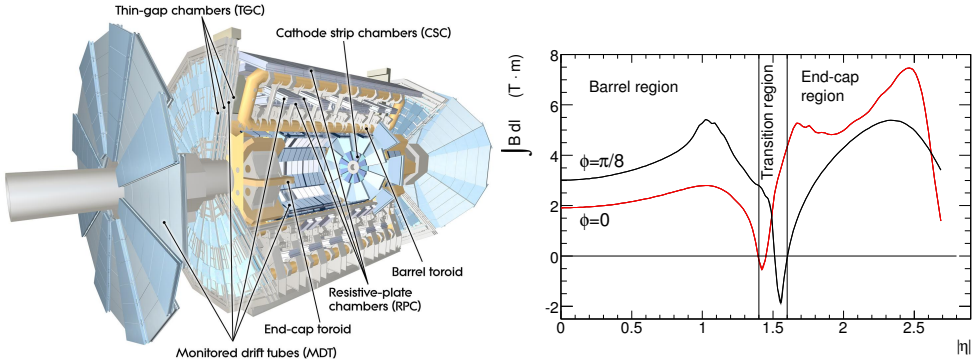

Figure 4.9: Left: ATLAS muon spectrometer, drift chambers are in the central region and in 'wheels' around the beam axis to cover the last η regions. Right: Predicted field integral as a function of $|\eta|$ inside the Muon Spectrometer.

4.3 Muon spectrometer

Muons are the only particles that pass the calorimeters with minimal interaction since they lose an average of 2 MeV/gr/cm^2 in matter. To measure them a tracking system after the calorimeters is needed. The Muon Spectrometer is the outermost part of the ATLAS detector, defining its overall dimensions. It is a combination of high-precision tracking chambers, represented in Figure 4.9, left panel. High-resolution momentum measurements independently of the Inner Detector are provided for $|\eta| < 2.7$, and triggering capabilities up to $|\eta| < 2.4$. Its large size is required to accurately measure the momentum of muons in air. The chambers can operate at room temperature, and four different technologies are used according to the requirements of precision, timing and radiation hardness. The reader is referred to [9, 83, 85, 86] for more information.

The muon spectrometer purpose is to measure with high precision the muon momentum, using the magnetic field generated by the external toroid magnets. Precise momentum measurement is performed by determining the track coordinate in the bending plane. Monitored Drift Tubes (MDTs) were chosen for this task because of their high measurement accuracy, predictability of mechanical deformations and simplicity of construction. In the forward region ($2.0 < |\eta| < 2.7$), the innermost layer is instead equipped with a radiation hard Cathode Strip Chambers (CSCs), better suited for handling the expected particle fluxes. CSCs provide measurements of both coordinates and additionally good timing resolution. Fast triggering and second coordinate (ϕ) determination is provided by Resistive Plate Chambers (RPCs) in the barrel and Thin Gap Chambers (TGCs) in the end-caps. Both systems are able to separate beam crossings with intrinsic timing accuracies of a few nanoseconds and provide rough estimates of the track momentum. A summary of the expected resolution and number of elements of each technology is given in table 4.3.

The driving performance goal is a stand-alone transverse momentum resolution of approximately 11% for 1 TeV tracks, with minimum charge misidentification. The associated sagitta of

500 μm for such tracks requires a resolution of 50 μm, obtained with precise knowledge of the magnetic field and chamber positioning.

Type	Chamber resolution			Measurements/track		Number of	
	z/R	ϕ	time	barrel	end-cap	chambers	channels
MDT	35 μm	–	–	20	20	1150	354k
CSC	40 μm (R)	5 mm	7 ns	–	4	32	30.7k
RPC	10 mm (z)	10 mm	1.5 ns	6	–	606	373k
TGC	2-6 mm (R)	3-7 mm	4 ns	–	9	3588	318k

Table 4.3: Parameters of the four chamber technologies used in the muon system: expected resolutions (not including alignment effects), maximum number of measurements per track, number of chambers and channels.

4.3.1 The toroid magnets

Over the range of $|\eta| < 1.4$, magnetic bending is provided by the large barrel toroid. Eight coils are arranged symmetrically around the beam axis, extending radially from 9.4 m to 22 m, with a length of 25.3 m. The toroidal configuration provides a field which is mostly orthogonal to the muon trajectories over a large volume and little material in the measurement regions, minimizing the degradation of resolution due to multiple scattering. For $1.6 < |\eta| < 2.7$, muon tracks are deflected by two smaller end-cap magnets inserted into both ends of the barrel system. The end-cap toroids are rotated in azimuth by an angle of 22.5 with respect to the barrel coils to provide for radial overlap, and to optimize the bending power in the transition region ($1.4 < |\eta| < 1.6$). Nevertheless, due to the finite number of coils, the field configuration is not perfectly toroidal. Small regions with degraded momentum resolution exist due to the low field integral, represented in Figure 4.9, right panel. The magnets are cooled down to 4.5 K by liquid helium and operate at a nominal current of 20.5 kA.

4.4 The ATLAS software framework

A common and robust analysis framework is a major requirement to deal with the huge amount of data produced by complex experiments like ATLAS. Moreover, combining the effort of different communities in a world-wide experiment with a few thousand collaborators all over the world requires the enforcement of a rather rigid structure for software development and the use of standard data formats. All that must be achieved combining flexibility and functionalities for common tasks.

A standard framework called ATHENA [87] is used by ATLAS for simulation, reconstruction and physics analyses. It is an implementation of the component-based architecture Gaudi, initially developed by the LHCb collaboration. Major design principles are the clear separation of data and algorithms, and between transient (in-memory) and persistent (in-file) data. All levels of processing of ATLAS data, from high-level trigger to event simulation, reconstruction and analysis, take place within the Athena framework. ATHENA is responsible for handling the configuration and execution of several C++ packages through python scripts called *jobOptions*. It takes care of the execution order, data flow and storage (persistification). In practice, the framework is composed by a series of components that take care of different tasks in the simulation, reconstruction and analysis chain.

4.4.1 Data management and data formats

The yearly data volume of order 40 Pb^{-1} (in Run-II) is used by data processing and analysis activities spread around the world. High degree of decentralisation and sharing of computing resources was promoted and met with the Grid paradigm. A three level Tier structure was implemented, in order to use all the available resources efficiently:

- One Tier-0 (CERN) is responsible for the primary event processing, storage of the RAW data and distribution of the data to Tier-1s.
- Approximately 10 Tier-1 facilities archive a copy of the RAW data, provide the reprocessing capacity, access to the various processed versions and allow scheduled analysis of the processed data by physics analysis groups.
- Several Tier-2 centers store analysis data and provide resources for calibration, simulation and analysis.

Some details about the several data formats handled in the framework, and foreseen in the ATLAS Event Data Model are given below. They correspond to different steps in the event processing and filtering, meeting the capabilities of the data storage centers and the needs of the end-users to perform physics analyses. The following types of data are available:

- **RAW data**: contains the output of the ATLAS detector, produced by real or simulated events after the High-Level Trigger. It comes in the “bytestream” format as they are delivered from

the detector, rather than object-oriented format. The size of each event is approximately 1.6 MB.

- **Event Summary Data (ESD)**: holds the detailed output of the reconstruction process. Both detector information and combined reconstruction objects like muons, electrons and jets are stored at this stage. An object-oriented format is adopted, and the typical event size is several MBs.

- **xAOD**: it is a subset of the ESD, with the physical objects used in analysis and reduced detector level information. This format of data was introduced in Run-II, it can be equally read from ROOT or from the ATHENA framework. The nominal event size is of the order of 300-500 KB.

- **DxAOD:** contains a small subset derived from the xAOD, specific for an analysis or performance group so that several derivations streams are produced. The data is reduced by removing unnecessary information, selecting objects and dropping information from those objects. During this process derived information can also be added. The derivations are run in a central way following the users directions. The final event size depends on the derivation process.

- **Event-index**: event-level meta-data containing a minimum set of information for fast event selection.

The availability of Event Summary Data is reduced, being restricted to basic studies on detector performance, specially in the initial phase of the experiment. Physics analyses are performed using xAOD or DxAOD. Lightweight data formats like TAGs are used for efficient event selection.

4.5 ATLAS research programme

The ATLAS detector was built to have a wide range of possible physics analyses. The main analysis was the discovery of the Higgs boson, however the detector also made possible precision measurement of the proprieties of several particles: mass measurement of top quark, Higgs couplings and Standard Model measurements in general. Furthermore physics beyond the Standard Model is searched for over a large range of possible signatures. In the following a brief overview of the research programme of the ATLAS detector is presented.

4.5.1 Higgs boson physics

The Higgs boson is studied in several decay channels: $H \to \gamma\gamma$, $H \to ZZ^* \to 4l$, $H \to WW^* \to e\nu\mu\nu$, $H \to b\bar{b}$ and $H \to \tau\tau$. The signal strenght, mass and couplings are measured for every channels and combinations are made. Updated results on Higgs boson physics can be found in Section 1.5.3.

4.5.2 Standard Model and Gauge bosons physics

During the first phase of the experiment, with 7-8 TeV of center of mass energy, precision measurement on QCD and W, Z bosons were made to test the predictive potential of the standard model theory. Thanks to the high production rate of electroweak vector gauge boson more throughout studies about the three gauge boson vertex interaction can be made. An accurate measure of the vector bosons and electroweak vertexes couplings can result in a more throughout understanding of all the free parameters in the Standard Model.

4.5.3 QCD

Thanks to the high available energy at LHC high precision studies can be made regarding the parton distribution function (PDF) of the proton. Furthermore the research program contains more accurate studies about the QCD prediction capability, like jets and prompt photon physics. Another important point is to understand the behavior of the strong coupling constant α_s at high energy scale.

4.5.4 b and t quark physics

The high production rate of bottom quark pairs allows a precision measurement of the CKM matrix coefficients. Another important research subject is to increase our knowledge of the CP violation interaction in this channel, to understand the so-called electroweak *arrow of time* that would answer many questions on the universe in the present day. This kind of studies are focused on the B meson decay. Furthermore thanks to the high production rate of top quark pairs the top mass and proprieties (like charge asymmetry and mass difference between top and anti-top) can be measured with precision.

4.5.5 Beyond the Standard Model

New physics is searched for in a large variety of possible models; SUSY, extra dimensions, quantum gravity, symmetry breaking phenomena outside the standard model, discovery of new gauge bosons signal, evidence of internal structure of leptons and quarks. In Chapter 2 a more detailed view about beyond the Standard Model theories can be found.

CHAPTER 5

ATLAS physic objects reconstruction and data analysis

5.1 ATLAS trigger system

At the instantaneous luminosity of LHC in 2016 data taking the ATLAS detector was exposed to an average of 23 proton proton interactions per bunch crossing and the time inverval between two collisions was 25 ns. The Trigger System had to reduce the input event frequency of 1 GHz to an average of 1 KHz. The trigger chain is composed of three different levels (as seen in Figure 5.1), the first level is a hardware trigger and implemented in the detector while the other two layers are software based:

- **Level one trigger**

  The level one trigger is a hardware trigger implemented in custom-built electronics. It uses coarse-granularity information from the muon chambers, calorimeters and forward detectors. The L1 calorimeter trigger is a mixed system, receiving data from the electromagnetic and hadronic calorimeters. It consists of three main sub-systems: the PreProcessor, the Cluster Processor and the Jet/Energy-sum Processor. The L1muon trigger receives low granularity input from dedicated trigger detectors. Two detector types are used: Resistive Plate Chambers (RPC) in the barrel region ($|\eta| < 1.05$) and Thin Gap Chambers (TGC) in the end-caps ($1.05 < |\eta| < 2.4$). The L1 decision is made by the Central Trigger Processor (CTP) with an overall latency of less than 2.5 ms reducing the event rate to about 75 kHz. If an event is accepted, the detector data are passed from front-end electronics to the Read-Out System (ROS) to be later accessed by the higher trigger levels.

- **The High level trigger**

  The High Level Trigger (HLT) is a software based trigger, running on large computer cluster. In Run-I it was subdivided into the Level-2 (L2) trigger and Event Filter (EF). For Run-2, the L2 and EF farms were merged into a single farm running a unified HLT process, that retains the on-demand data readout of the old Level-2 and to a larger extent uses offline based algorithmic code from the Event Filter. The HLT reconstruction is based on energy from the calorimeters and tracking information from the inner detector and muon spectrometer. It is used to refine the L1 decision to select interesting events in order to reduce the event

rate further to reach a maximum of 1 KHz within an average processing time of roughly 4 seconds.

Several trigger menus exist and are associated to different physics analysis. Some of them, especially the ones with a low energy cut, are also prescaled (meaning that only a fraction of events passing a rescaled trigger are stored). The trigger rates for several trigger at L1 and HLT can be found in Figure 5.2.

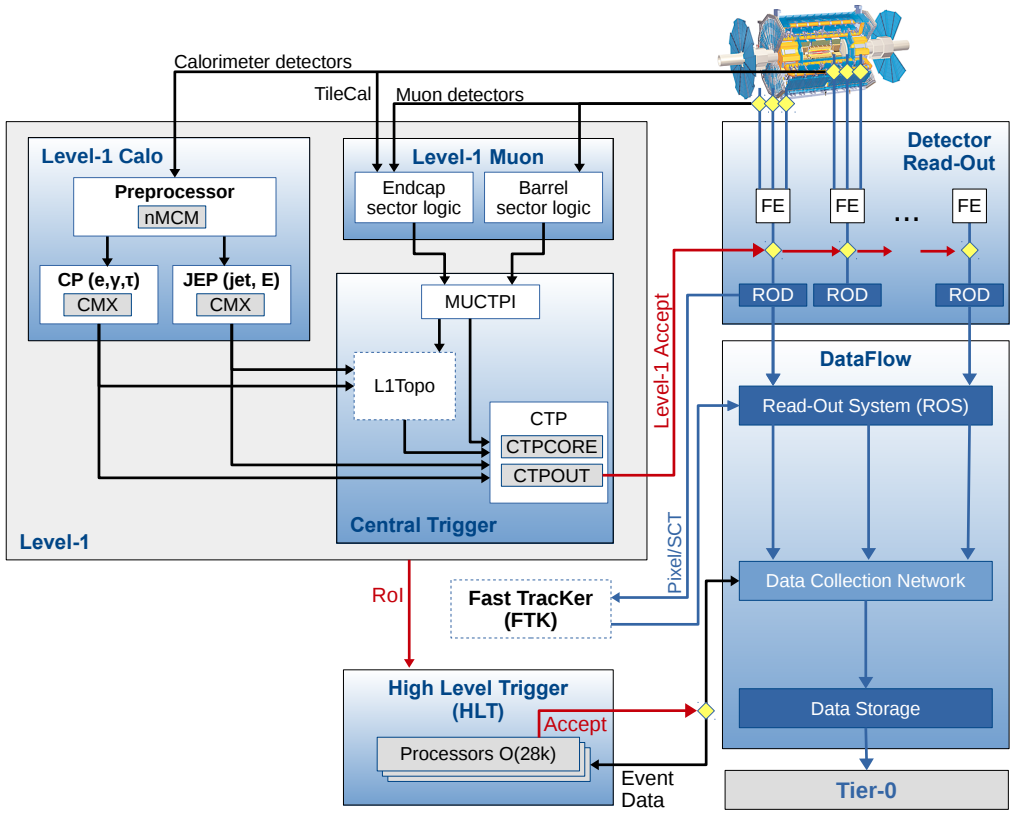

Figure 5.1: The ATLAS trigger and data acquisition system in 2015. New features with respect to the Run-I system are indicated with orange boxes [88].

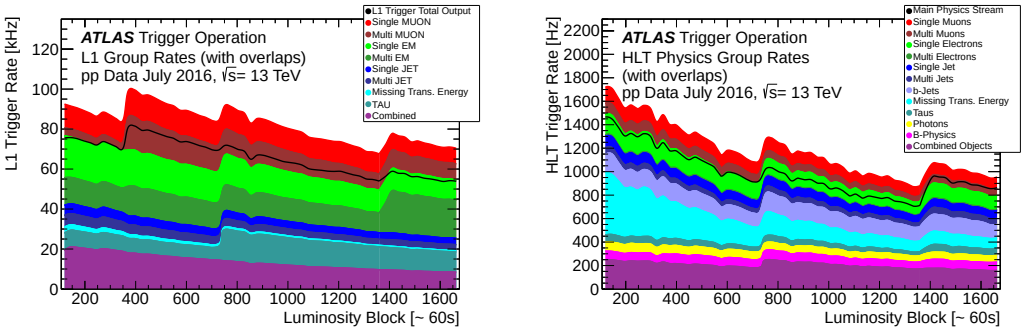

Figure 5.2: Physics trigger group rates at the Level 1 Trigger (Left) and High Level Trigger (Right) as a function of the number of luminosity blocks which correspond to on average 60s per luminosity block in a fill taken in July 2016 with a peak luminosity of L = 1.02 * 1034 $cm^{-2}s^{-1}$ and an average pile up of $\mu = 24.2$. Presented are the rate of the individual trigger groups specific for trigger physics objects. Overlaps are only accounted for in the total Main Physics Stream rate. Common features to all rates are their exponential decay with decreasing luminosity during an LHC fill. The rates periodically increase due to change of prescales to optimise the bandwidth usage, dips are due to deadtime [88, 89].

5.2 Monte Carlo generators

A typical event at LHC is expected to consist of about 100 charged particles and as many neutral ones. Many signals for new physics make use of collective properties of these particles, such as jets or missing transverse energy. Others are based on well identified particles, such as electrons, muons or photons, which then have to be selected with some degree of confidence.

A number of detailed questions need to be answered: how well is an electron coming from the signal process really isolated? How often do possible backgrounds give isolated electrons? and so on. The task of Monte Carlo simulation is to describe, as accurately as possible, the experimental characteristics of physics processes of interest.

The typical Monte Carlo flow is divided into separate subtasks, as seen in Figure 5.3, which can be summarized in the following components:

- **Hard scattering:** Calculation of hard scattering matrix elements between the two hard interacting partons inside the colliding hadrons. The differential cross-sections of the process is simulated and is given as the products of structure functions and the hard scattering matrix elements. All efforts are made to include the most accurate calculations available for the different processes.

- **Parton shower:** Partons inside the hadrons may radiate gluons in the final state or before the hard interaction. Radiated gluons then generate parton showers that might result in additional hadronic jets in the final state. Furthermore QED emission of photons can occur in the initial or final state. This perturbative radiation is the dominant mechanism for building up the

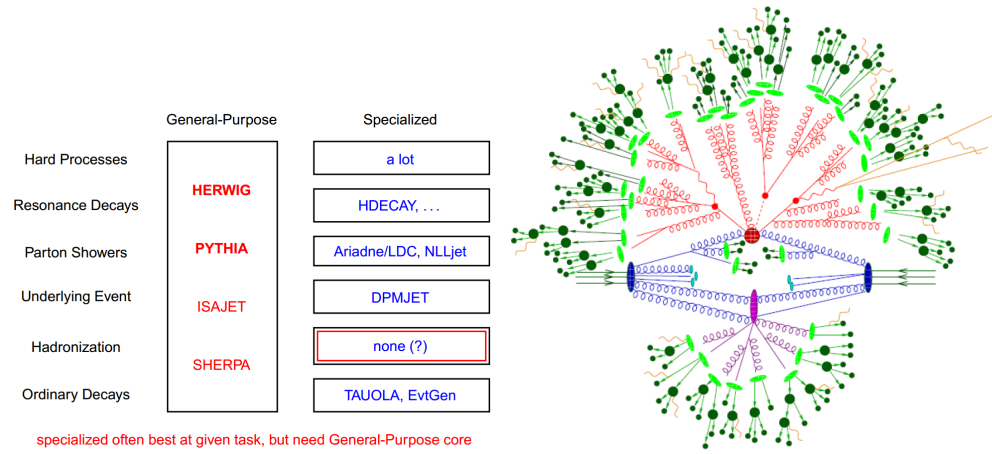

Figure 5.3: Left: different Monte Carlo generators with different purposes. Right: hard collision with color-coded separated stages of Monte Carlo simulation.

structure of (high-Pt) jets, with broad jet profiles and sub-jets. Approximated showering algorithms are exploited to take into account higher order corrections in these processes.

- **Underlying event, pileup:** Contributes from partons not involved in the hard interaction, both from the same proton and from other protons are evaluated.

- **Hadronization:** After the calculation of the initial state comes the simulation of the hadronization of the hard and soft QCD objects. This step simulates the final particles coming from the products of the initial hard interaction and soft contributes. Partons, once sufficiently removed from each other, are fragmented into a collection of hadrons. Many of these hadrons are unstable, and subsequently decay.

- **Simulation:** After the complete event is generated the simulation of the detector behavior is performed. This step is made simulating the response of the detector to the particles generated in the previous steps. The behavior of the detectors (how particles produced by the event generator traverse the detector, spiral in magnetic fields, shower in calorimeters, or sneak out through cracks, etc.) is simulated using the GEANT 4 simulator [90, 91].

- **Reconstruction:** The output of the simulation has the same format as the real data registered by the detector, therefore it can be put through the same event reconstruction and physics analysis chain. However with generators the truth information is available and can be used for several tasks (calibration, optimization, efficiency estimation ...). Therefore the final step of the process is the reconstruction of the physic objects in the finale state, as will be described in the following.

5.3 ATLAS objects reconstruction and identification

In the data format used at the analysis level, information from different sub-detectors are combined to build physics objects like electrons, photons, muons, $E_{\mathrm{T}}^{\mathrm{miss}}$ or jets. The object-building phase is called reconstruction. For some objects (like e, γ, μ, τ, etc...) after the reconstruction there is another phase called identification where a selection is applied on measured observables to decide whether the selected candidates can be considered a given particle. In this process a level of goodness of recognition is usually calculated for each object.

5.4 Electron and photon reconstruction and identification

Photons and electrons are both reconstructed starting from energy deposits in the EM calorimeter and tracks in the inner detector. After the reconstruction of an energy cluster in the EM calorimeter a selection is applied based on tracks, information from different layers of the electromagnetic calorimeter and leakage in the hadronic calorimeter.

This procedure allows to recognize if the energy deposit was originated by an electron or a photon. An electron candidate is created if a track matched to the cluster is found and no conversion is flagged. Otherwise, the candidate is classified as a photon. A photon candidate can be converted, therefore associated with a secondary vertex with one or two tracks, or unconverted, with no tracks in the detector pointing to the energy deposit.

5.4.1 Electron reconstruction

An detailed explanation of the electron reconstruction and identification process can be found in Reference [92]. The electron reconstruction in the central region of the ATLAS detector (i.e. with $|\eta| < 2.47$) proceeds in several steps:

- **Seed-cluster reconstruction:** A sliding window with a size of 3×5 in units of 0.025×0.025, corresponding to the granularity of the EM calorimeter middle layer, in $\eta \times \phi$ space is used to scan the calorimeter looking for cluster "seeds" that have transverse energy above 2.5 GeV. The clusters are then formed around the seeds using a clustering algorithm [93] that allows for duplicate clusters (If the distance between two clusters is $\Delta R < 0.3$, the clusters are considered to be duplicates) to be removed. The efficiency of the cluster reconstruction for a true e/γ ranges from 95% at $E_{\mathrm{T}} = 7$ GeV to more than 99% above $E_{\mathrm{T}} = 15$ GeV.

- **Track reconstruction:** Track reconstruction has two sub-steps: pattern recognition and track fit. The pattern recognition uses the pion hypothesis for energy loss due to interactions with the detector material, complemented with a modified pattern recognition algorithm that takes into account energy loss for possible bremsstrahlung. If a track seed (consisting of three hits in different layers of the silicon detectors) with a transverse momentum larger than 1 GeV can not be successfully extended to a full track and it falls within one of the

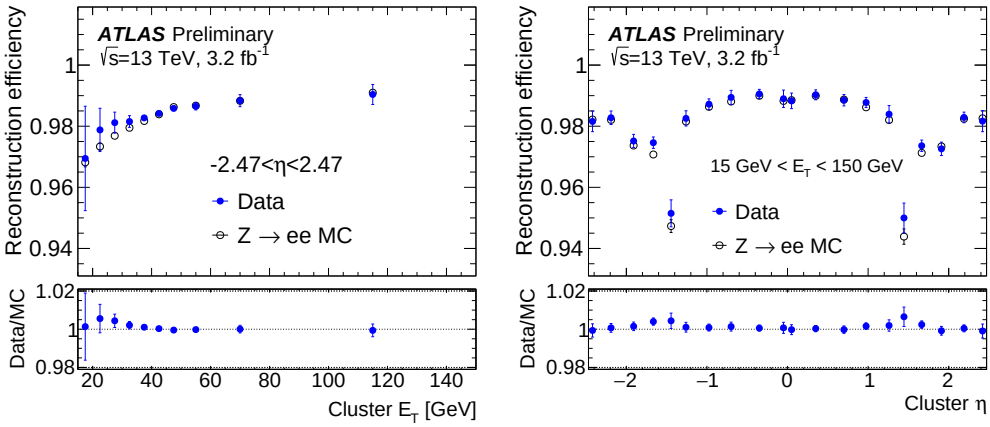

Figure 5.4: Measured reconstruction efficiencies for electrons as a function of E_T integrated over the full pseudorapidity range (left) and as a function of pseudo-rapidity for 15 GeV $< E_T <$ 150 GeV (right) for the 2015 dataset. The shown uncertainties are statistical plus systematic [92].

EM cluster region of interest (RoI)[1], a second attempt is performed using another pattern recognition with the electron hypothesis that allows for larger energy loss. Track candidates are then fitted using the ATLAS Global χ^2 Track Fitter [94] either with the pion hypothesis or the electron hypothesis.

- **Electron specific track fit:** The obtained tracks are matched to EM clusters using the distance in η and ϕ between the extrapolation of the track and the cluster barycenter. The matching conditions account for energy-loss due to bremsstrahlung and the number of precision hits in the silicon detector. Tracks associated to electron clusters that have significant number of precision hits are refitted using an optimized Gaussian Sum Filter (GSF) [95], which takes into account the non-linear bremsstrahlung effects.

- **Electron candidate reconstruction:** The matching of the track candidate to the cluster seed completes the electron reconstruction procedure. A similar matching as the one described above is repeated for the refit track with stricter conditions. If several tracks fullfil the matching condition, one track is chosen as "primary" track, the decision is based on cluster-track distance R calculated using different momentum hypotheses, the number of pixel hits and the presence of a hit in the first silicon layer [96]. Electron candidates without any associated precision hit tracks are removed and considered to be photons. The electron cluster is then re-formed using 3×7 (5×5) longitudinal towers of cells in the barrel (endcaps) of the EM calorimeter. The energy of the clusters is corrected to the original electron energy using multivariate techniques [97] based on simulated MC samples

[1] For each seed EM cluster passing loose shower shape requirements of $R_\eta > 0.65$ and $R_{\text{had}} < 0.1$ a region of interest with a cone-size of $\Delta R = 0.3$ around the seed cluster barycenter is defined.

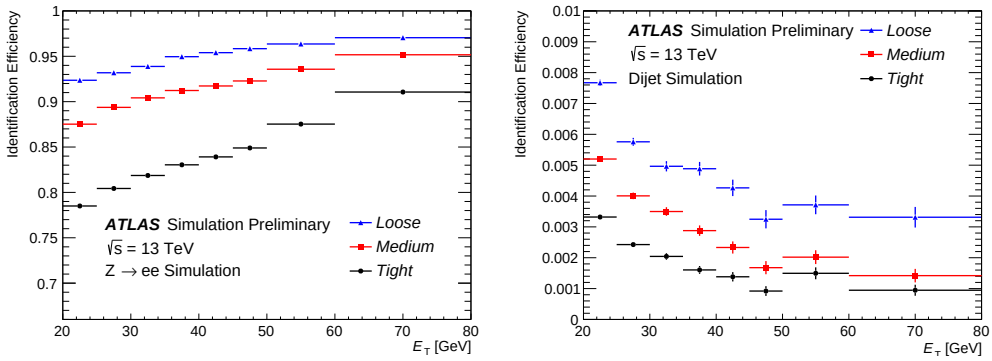

Figure 5.5: The efficiency to identify electrons from $Z \rightarrow ee$ decays (left) and the efficiency to identify hadrons as electrons (background rejection, right) estimated using simulated dijet samples. The background includes hadrons but also b-quarks decays with electrons in the final state and electrons from photons conversions. The efficiencies are obtained using Monte Carlo simulations, and are measured with respect to reconstructed electrons. The candidates are matched to true electron candidates for $Z \rightarrow ee$ events. For background rejection studies the electrons matched to true electron candidates are not included in the analysis. Note that the last bin used for the optimization of the ID is 45-50 GeV, which is why the signal efficiency increases slightly more in the 50 GeV bin than in others, and the background efficiency increases in this bin as well [92].

as explained in Section 5.5.

The four-momentum of the electrons is computed using information from both the final calibrated energy cluster and the best track matched to the original seed cluster. The energy is given by the final calibrated cluster, while the ϕ and η directions are taken from the track.

In Run-II analyses, the electron measurements are performed by requiring the track associated with the electron to be compatible with the primary interaction vertex of the hard collision, in order to reduce the background from conversions and secondary particles. To assess the compatibility with the primary vertex (the one with the highest sum of transverse momenta) Δz_0 between the track and the primary vertex is employed. The efficiency of the electron reconstruction process goes from 97% to 99% for electron with p_{T} >100 GeV (Figure 5.4).

5.4.2 Electron identification

To determine whether the reconstructed electron candidates are signal-like objects or background-like objects such as hadronic jets or converted photons, algorithms for electron identification (ID) are applied [92]. The ID algorithms use discriminant quantities related to the electron cluster and track measurements including calorimeter shower shapes, information from the transition radiation tracker, track-cluster matching related quantities, track properties, and variables measuring bremsstrahlung effects for distinguishing signal from background. These quantities are summarized in Table 5.1.

The optimization of the ID algorithms is based on MC simulation samples. Electron candidates from MC simulations of $Z \to ee$ and dijet events are used, in addition to $J/\psi \to ee$ and minimum bias events at low E_{T}. The distributions of several input variables in data tend to have differences with the MC simulation, due to inaccuracies in the detector description and the modeling of the shower shapes in GEANT [90]. To account for this, corrections derived from data in the form of simple linear shifts or width adjustments were applied to the MC distributions.

The baseline ID algorithm used for Run-II data analyses is the likelihood-based (LH) method. It is a multivariate analysis (MVA) technique that simultaneously evaluates several properties of the electron candidates when making a selection decision. The LH method uses the signal and background probability density functions (PDFs) of the discriminating variables. Based on these PDFs, an overall probability is calculated for the object to be signal or background. In addition to the variables used as input to the LH discriminant, simple selection criteria are used for the variables counting the number of hits on the track.

The distributions of electron shower shapes depend on the amount of material the electrons pass through, and therefore vary with the pseudorapidity of the electron candidates. In addition, sub-dominant changes to the shower shapes and track properties are expected with increasing energy. The ID operating points were consequently optimized in several bins in $|\eta|$ and E_{T}. Since the electron identification performance may be influenced by in time and out of time pileup the cut on the LH discriminant value is also loosened as a function of the number of primary vertexes. Furthermore for electron candidates with E_{T} above 125 GeV rectangular cuts (optimized on MC) on w_{stot} and E/p are applied for the tighter selection, these cuts were found to be particularly effective at discriminating signal from background at high E_{T}.

Three levels of identification operating points are typically provided for electron ID. These are referred to, in order of increasing background rejection, as *Loose*, *Medium*, and *Tight*. The *Loose*, *Medium* and *Tight* operating points are defined such that the samples selected by them are subsets of one another. The performance of the LH identification algorithm is illustrated in Figure 5.5.

5.4.3 Photon reconstruction

As photons and electrons have basically identical signals in the EM calorimeter, their reconstruction proceeds in parallel. A full description of photon reconstruction and identification process can be found in Reference [98] and can be summarized in the following:

- **Seed-cluster reconstruction:** The reconstruction of photon candidates in the region $|\eta| < 2.5$ begins with the creation with a sliding window algorithm of a preliminary set of seed clusters of EM calorimeter cells. The efficiency of the initial cluster reconstruction is estimated to be greater than 99% for photons with $E_{\mathrm{T}} > 20$ GeV. The procedure is the same as in section 5.4.1.

- **Track reconstruction:** Once seed clusters are reconstructed, a search is performed for inner detector tracks [81, 82] that are loosely matched to the clusters, in order to identify and reconstruct electrons and photon conversions. The procedure is the same as in section 5.4.1.

Type	Description	Name
Hadronic leakage	Ratio of E_{T} in the first layer of the hadronic calorimeter to E_{T} of the EM cluster (used over the range $\lvert\eta\rvert < 0.8$ or $\lvert\eta\rvert > 1.37$)	R_{had1}
	Ratio of E_{T} in the hadronic calorimeter to E_{T} of the EM cluster (used over the range $0.8 < \lvert\eta\rvert < 1.37$)	R_{had}
Back layer of EM calorimeter	Ratio of the energy in the back layer to the total energy in the EM accordion calorimeter. This variable is only used below 100 GeV because it is known to be inefficient at high energies.	f_3
Middle layer of EM calorimeter	Lateral shower width, $\sqrt{(\Sigma E_i \eta_i^2)/(\Sigma E_i) - ((\Sigma E_i \eta_i)/(\Sigma E_i))^2}$, where E_i is the energy and η_i is the pseudorapidity of cell i and the sum is calculated within a window of 3×5 cells	$w_{\eta 2}$
	Ratio of the energy in 3×3 cells over the energy in 3×7 cells centered at the electron cluster position	R_ϕ
	Ratio of the energy in 3×7 cells over the energy in 7×7 cells centered at the electron cluster position	R_η
Strip layer of EM calorimeter	Shower width, $\sqrt{(\Sigma E_i (i - i_{\mathrm{max}})^2)/(\Sigma E_i)}$, where i runs over all strips in a window of $\Delta\eta \times \Delta\phi \approx 0.0625 \times 0.2$, corresponding typically to 20 strips in η, and i_{max} is the index of the highest-energy strip	w_{stot}
	Ratio of the energy difference between the largest and second largest energy deposits in the cluster over the sum of these energies	E_{ratio}
	Ratio of the energy in the strip layer to the total energy in the EM accordion calorimeter	f_1
Track conditions	Number of hits in the innermost pixel layer; discriminates against photon conversions	n_{Blayer}
	Number of hits in the pixel detector	n_{Pixel}
	Number of total hits in the pixel and SCT detectors	n_{Si}
	Transverse impact parameter with respect to the beam-line	d_0
	Significance of transverse impact parameter defined as the ratio of d_0 and its uncertainty	d_0/σ_{d_0}
	Momentum lost by the track between the perigee and the last measurement point divided by the original momentum	$\Delta p/p$
TRT	Likelihood probability based on transition radiation in the TRT	eProbabilityHT
Track-cluster matching	$\Delta\eta$ between the cluster position in the strip layer and the extrapolated track	$\Delta\eta_1$
	$\Delta\phi$ between the cluster position in the middle layer and the track extrapolated from the perigee	$\Delta\phi_2$
	Defined as $\Delta\phi_2$, but the track momentum is rescaled to the cluster energy before extrapolating the track from the perigee to the middle layer of the calorimeter	$\Delta\phi_{\mathrm{res}}$
	Ratio of the cluster energy to the track momentum, a single cut is applied	E/p

Table 5.1: Definitions of electron discriminating variables.

- **Track conversion:** Tracks consistent with originating from a photon conversion are used to create conversion vertex candidates.
- **Track-cluster matching:** Conversion vertex candidates are then matched to seed clusters.
- **Cluster identification:** A final algorithm decides whether a seed cluster corresponds to an unconverted photon, a converted photon or a single electron based on the matching to conversion vertexes or tracks and on the cluster and track(s) four-momenta.

In the following the various steps of the reconstruction algorithms are described in more detail.

Double track conversion "Double-track" conversion vertex candidates are reconstructed from pairs of oppositely charged tracks in the ID that are likely to be electrons. For each track the likelihood to be an electron is required to be at least 10% (80%) for tracks with (without) hits in the silicon detectors. Since the tracks of a photon conversion are parallel at the conversion vertex, geometric requirements are used to select the track pairs. Track pairs are classified into three categories, whether both tracks (Si–Si), none (TRT–TRT) or only one of them (Si–TRT) have hits in the silicon detectors. A constrained fit with three degrees of freedom is performed to find the conversion vertex. This is made using the five measured helix parameters of each of the two participating tracks with the constraint that the tracks are parallel at the vertex.

Single track conversion Tracks without hits in the *b*-layer that either have an electron likelihood greater than 95%, or have no hits in the TRT, are considered as "single-track" conversion vertex candidates. In this case, since a conversion vertex fit cannot be performed, the conversion vertex is defined to be the location of the first measurement of the track. Tracks which pass through an inactive region of the *b*-layer are not considered as single-track conversions unless they are missing a hit in the second pixel layer.

Matching The matching of the conversion vertexes to the clusters relies on an extrapolation of the conversion candidates to the second sampling layer of the calorimeter, and the comparison of the extrapolated η and ϕ coordinates to the η and ϕ coordinates of the cluster center (ΔR). The details of the extrapolation depend on the type of the conversion vertex candidate.

For double-track conversion vertex candidates for which the track p_{T} differ by less than a factor of four from each other, each track is extrapolated to the second sampling layer of the calorimeter and is required to be matched to the cluster. If the difference in p_{T} is more than a factor of four the photon direction is reconstructed from the electron and positron directions determined by the conversion vertex fit. For single-track conversion vertex candidates, the track is extrapolated from its last measurement.

Conversion vertex candidates built from tracks with hits in the silicon detectors are considered matched to a cluster if the angular distance between the extrapolated tracks and the cluster center is smaller than 0.05 in both η and ϕ. If the extrapolation is performed for single-track conversions, the window in ϕ is increased to 0.1 in the direction of the bending. In case of tracks without hits in

the silicon detectors, the matching requirements are tighter regarding distance in ϕ (0.02/0.03) but looser in η (0.2/0.35) since the TRT does not provide a measurement of the pseudorapidity.

In the case of multiple conversion vertex candidates matched to the same cluster preference is given to double-track candidates over single-track candidates. Furthermore preference is given to the candidate with more tracks with hits in the silicon detectors and with the smaller ΔR between cluster and track. Fraction of converted/unconverted photons can be see in Figure 5.6.

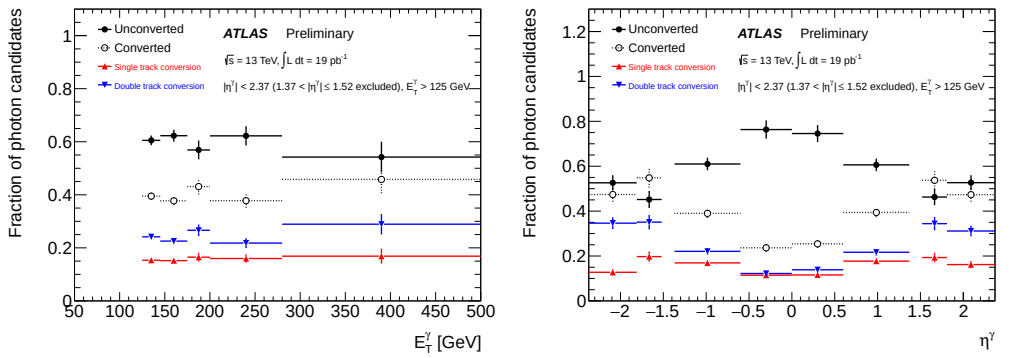

Figure 5.6: Fraction of photon candidates reconstructed as unconverted or converted photons as a function of the candidate transverse momentum (Left) and pseudorapidity (Right), in pp collisions at $\sqrt{s} = 13$ TeV. The photon candidates are required to pass the photon identification based on the shapes of the associated electromagnetic cluster and to be isolated. Converted photon candidates are also split into single-track and double-track conversions. The data sample was collected by ATLAS in June and July 2015, and corresponds to about 19 pb^{-1} of integrated luminosity. The contamination of background photons from the decays of neutral hadrons in jets is estimated to be smaller than 5% [99].

Electron photon separation The final arbitration between the unconverted photon, converted photon and electron hypotheses for the reconstructed EM clusters is performed as in Reference [100], however the procedure was changed with the latest reconstruction of Run-II:

- The candidate is flagged as a photon if no track with at least 4 silicon detector hits is matched to the cluster **or** a conversion vertex is found in the silicon detector and the electron track is part of the vertex and has no pixel detector hits.

- The candidate is flagged as an electron if no conversion vertex is matched **or** if a track with an innermost pixel detector hit is matched (or at least 2 pixel detector hits if the innermost layer is not expected) and no conversion vertex in the silicon detector is matched.

- The candidate is considered ambiguous otherwise **and** also if E(cluster)/P(track) > 10 GeV or track-P_t < 2.0 GeV or if the matched track has no pixel hits.

Studies on MC simulations on Run-I showed that 96% of true photons with $E_{\mathrm{T}} > 25$ GeV are expected to be reconstructed as photon candidates, while the remaining 4% are incorrectly reconstructed as electrons but not as photons. The reconstruction efficiencies are checked in data with a technique described in Ref. [97]. After the changes introduced in Run-II the performance has slightly improved; contamination between electrons and photons is reduced and converted/unconverted photons separation is slightly better.

5.4.4 Photon identification

To distinguish real photons from background photons an identification with different levels of signal efficiency and background rejection is performed. Photon identification in ATLAS is based on a set of cuts on several discriminating variables. Such variables, listed in Table 5.2, characterize the lateral and longitudinal shower development in the electromagnetic calorimeter and the shower leakage fraction in the hadronic calorimeter. Photons typically produce narrower energy deposits in the electromagnetic calorimeter and have smaller leakage to the hadronic one compared to background photons from jets, due to the presence of additional hadrons near the photon candidate in the latter case. In addition, background candidates from isolated $\pi^0 \to \gamma\gamma$ decays are often characterized by two separate local energy maxima in the finely segmented strips of the first layer, due to the small separation between the two photons.

Two sets of cuts or working points, a *Loose* one and a *Tight* one, are defined using a MVA classificator. The *Loose* selection is based only on shower shapes in the second layer of the electromagnetic calorimeter (Table 5.2) and on the energy deposited in the hadronic calorimeter. Instead The *Tight* selection, which is separately optimized for unconverted and converted photons, adds information from the finely segmented strip layer of the calorimeter. These additional variables provide good rejection of hadronic jets where a neutral meson carries most of the jet energy. The selection criteria are different in seven intervals of the reconstructed photon pseudorapidity (0.0–0.6, 0.6–0.8, 0.8–1.15, 1.15–1.37, 1.52–1.81, 1.81–2.01, 2.01–2.37) to account for the calorimeter geometry and for different effects on the shower shapes from the material upstream of the calorimeter, which is highly non-uniform as a function of $|\eta|$.

The efficiency of the *Loose* identification rises from 97% at $E_T^{\gamma} = 20$ GeV to above 99% for $E_T^{\gamma} > 40$ GeV for both the converted and unconverted photons, with the corresponding background rejection factor is about 1000 [100]. The efficiency of the *Tight* identification is 85% at $E_{\mathrm{T}}^{\gamma} = 40$ GeV and above 90% for $E_{\mathrm{T}}^{\gamma} \sim 1$ TeV for unconverted and converted photons, with a corresponding background rejection factor of about 5000 [100]. The performance of the *Tight* working point is measured on data using different techniques [101], as reported in Figure 5.7 for unconverted photons and in Figure 5.8 for converted photons. The techniques used to evaluate the *Tight* identification efficiency on data are three:

- Radiative Z decays, based on $Z \to \gamma ee$ events.
- $e \to \gamma$ extrapolation, based on a mapping technique (based on Smirnof transform) to extrapolate the photon efficiency from the electron efficiency.

- Matrix method, based on the variation of the track isolation selection requirement.

The scale factors applied to Monte Carlo to correct the efficiency difference between data and MC are calculated with the combination of the three methods.

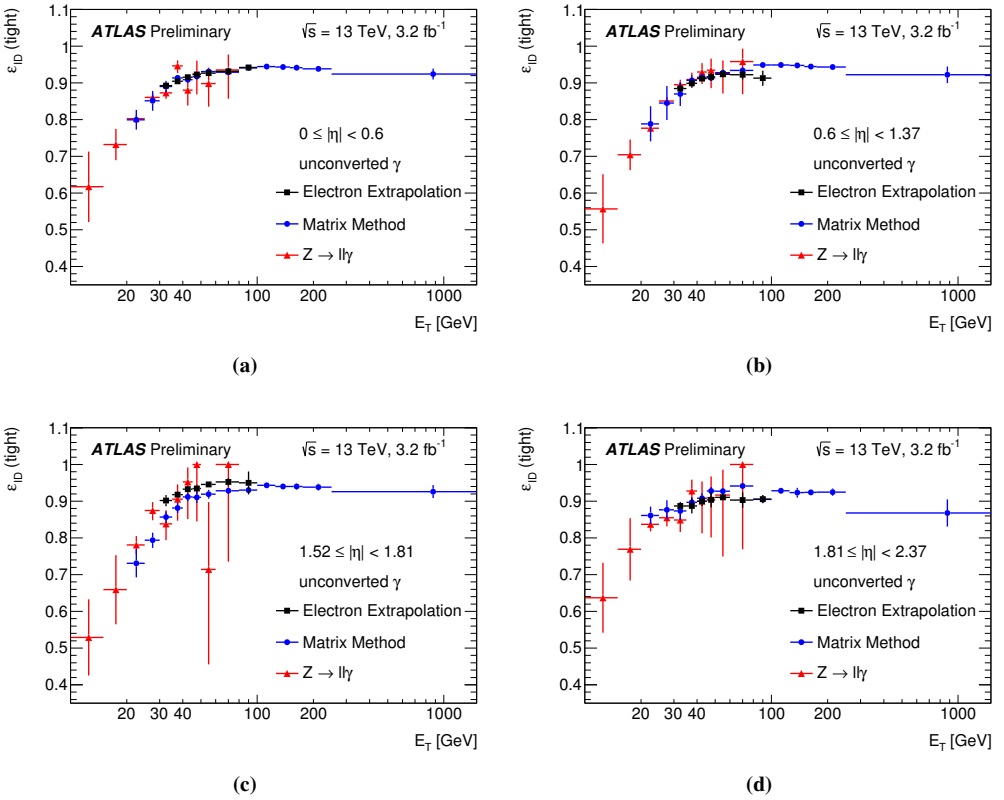

Figure 5.7: Comparison of the data-driven measurements of the identification efficiency for unconverted photons as function of E_T in the region $20 \leq E_T \leq 1500$ GeV, for the four pseudorapidity intervals. The uncertainty bars represent the sum in quadrature of the statistical and systematic uncertainties estimated in each method [101].

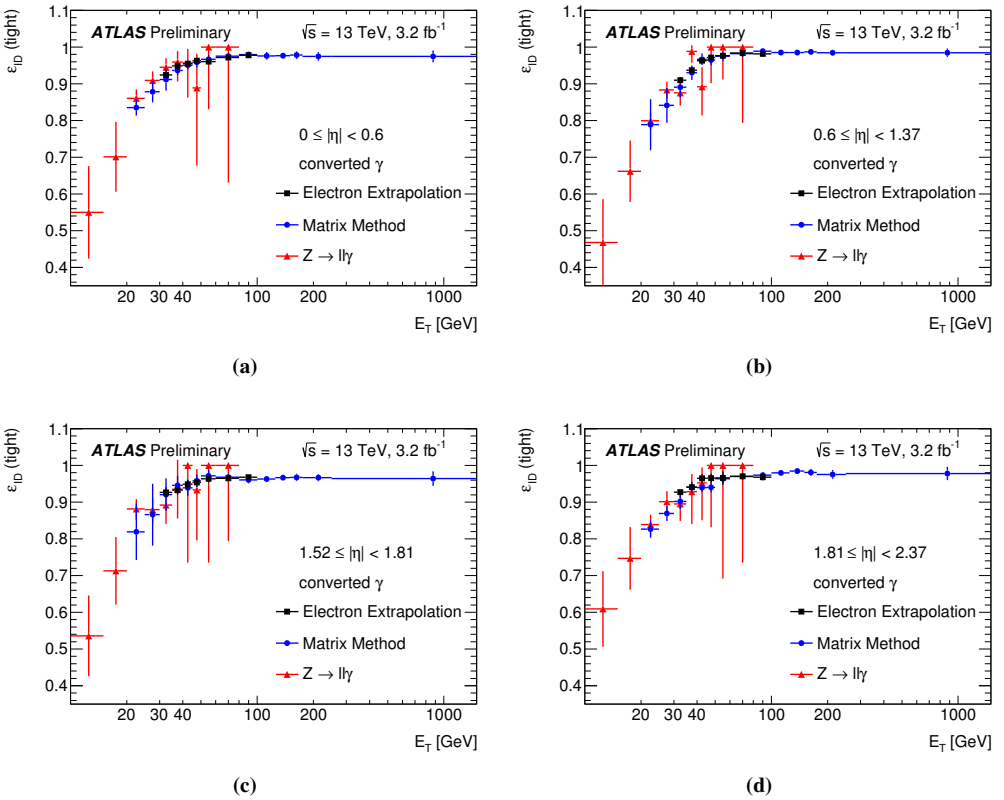

Figure 5.8: Comparison of the data-driven measurements of the identification efficiency for converted photons as function of E_T in the region $20 \leq E_T \leq 1500$ GeV, for the four pseudorapidity intervals. The uncertainty bars represent the sum in quadrature of the statistical and systematic uncertainties estimated in each method [101].

Category	Description	Name	*Loose*	*Tight*
Acceptance	$\|\eta\| < 2.37$, with $1.37 < \|\eta\| < 1.52$ excluded	–	✓	✓
Hadronic leakage	Ratio of E_{T} in the first sampling layer of the hadronic calorimeter to E_{T} of the EM cluster (used over the range $\|\eta\| < 0.8$ or $\|\eta\| > 1.37$)	R_{had_1}	✓	✓
	Ratio of E_{T} in the hadronic calorimeter to E_{T} of the EM cluster (used over the range $0.8 < \|\eta\| < 1.37$)	R_{had}	✓	✓
EM Middle layer	Ratio of 3×7 $\eta \times \phi$ to 7×7 cell energies	R_η	✓	✓
	Lateral width of the shower	w_{η_2}	✓	✓
	Ratio of 3×3 $\eta \times \phi$ to 3×7 cell energies	R_ϕ		✓
EM Strip layer	Shower width calculated from three strips around the strip with maximum energy deposit	$w_{s\,3}$		✓
	Total lateral shower width	$w_{s\,\mathrm{tot}}$		✓
	Energy outside the core of the three central strips but within seven strips divided by energy within the three central strips	F_{side}		✓
	Difference between the energy associated with the second maximum in the strip layer and the energy reconstructed in the strip with the minimum value found between the first and second maxima	ΔE		✓
	Ratio of the energy difference associated with the largest and second largest energy deposits to the sum of these energies	E_{ratio}		✓

Table 5.2: Discriminating variables used for *loose* and *tight* photon identification.

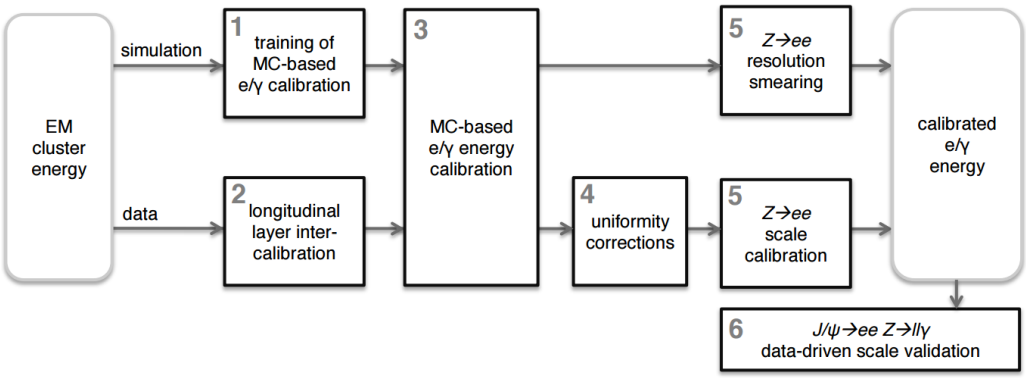

Figure 5.9: Schematic overview of the procedure used to calibrate the energy response of electrons and photons in ATLAS.

5.5 Electron and photon energy calibration

The calibration of the measured energy of electrons and photons is fundamental for many physics measurements, more information about the calibration can be found in References [102, 103]. A multivariate (MVA) regression algorithm based on simulation calibrates the energy of electromagnetic particles correcting for the energy deposited in front of the calorimeter, for the longitudinal and lateral leakage and for other local effects. Furthermore in order to account for any residual disagreement between data and simulation the energy scale of electrons is extracted using $Z \rightarrow ee$ events through an in-situ procedure. A fundamental pre-requisite of the whole calibration chain is that the detector geometry and the model of the particle interaction with matter are accurately handled in the simulation. The calibration procedure can be summarized as in Figure 5.9 and it is described in the following sections.

5.5.1 Detector non uniformity corrections

Data are corrected for measured time-dependent defects in specific regions. These corrections typically take into account non-nominal high-voltage regions or geometric effects not perfectly simulated. These corrections are needed because in a few sectors (of typical size $\Delta\eta \times \Delta\phi = 0.2 \times 0.2$) of the EM calorimeter, the HV is set to a non-nominal value due to short circuits occurring in specific LAr electrodes (For more information about the HV system of the LAr calorimeter see Appendix B). Another correction is associated with the different gains of the calorimeter cells readout (there are three readout gains: high, medium and low), since in the $Z \rightarrow ee$ events used to calculate the in-situ correction electrons have mostly cells in high gain. For more energetic objects with calorimeter cells in medium or low gain an additional correction is applied.

5.5.2 Layer intercalibration

Further corrections are needed in data to adjust residual effects not perfectly accounted for by simulation [97]. The intercalibration of the first and second calorimeter layers (E_1/E_2) uses muons from $Z \to \mu\mu$ decays as probes since muon energy deposits in the calorimeter are insensitive to the amount of passive material upstream of the EM calorimeter and constitute a direct probe of the energy response. Denoting $\langle E_{1/2}\rangle$ the ratio of the deposited energies in L1 and L2, the intercalibration result is defined as $\alpha_{1/2} = \langle E_{1/2}\rangle^{\text{data}}/\langle E_{1/2}\rangle^{\text{MC}}$. The L1/L2 calibration bias $\alpha_{1/2}$ is removed by applying an $|\eta|$-dependent correction to data to the energy measured in L2 ($E_2^{\text{corr}} = E_2 \times \alpha_{1/2}$). These coefficients are verified by a study of the electron energy response with $Z \to ee$ events.

The determination of the pre-sampler (PS) energy scale exploits the PS energy distributions of electrons in data and simulation. This is done after taking into account the possible mis-modeling of the upstream passive material calculated with a set of detector material variations in the simulation. It is estimated using electrons from W and Z decays. This is addressed by exploiting the expected correlation between $E_{1/2}$ and E_0 for electrons, at a given η value, under variations of the passive material upstream of the PS.

No dedicated intercalibration of the third EM longitudinal layer is carried out, as its contribution should be negligible in the energy range covered by the present calibration. However this effect was not tested yet with Run-II data.

5.5.3 MVA calibration

The core of the procedure is based on the optimization of the energy calibration using multivariate (MVA) techniques on large samples of single particles Monte Carlo simulation. The exploited regression multivariate technique is based on a boosted decision tree with gradient boosting. With this procedure the EM clusters are calibrated to the original electron and photon energy in the simulated MC samples. The calibration coefficients are calculated separately for electrons, converted and unconverted photons.

The quantities used in this process are the total energy measured in the calorimeter, E_{acc}; the ratio of the pre-sampler layer energy to the calorimeter energy, E_0/E_{acc}; the energy measured in the first two layers of the calorimeter E_1/E_2; the cluster barycenter pseudorapidity in the ATLAS coordinate system, $\eta_{cluster}$; and the cluster barycenter in η and ϕ within the $\eta \times \phi$ cells (EM calorimeter coordinates)[2]. The variable $\eta_{cluster}$ is included since it is correlated with the passive-material variations in front of the calorimeter. The inclusion of the barycenter location in the the $\eta \times \phi$ cells is important to accurately correct particles that hit the cell close to the edge.

For converted photons, the radius of conversion R_{conv} is used as an additional input to the MVA only if the p_{T} is above 3 GeV. For conversions with both tracks containing at least one hit in either the pixel or SCT detector, further quantities are considered: the ratio $p_{\text{T}}^{\text{conv}}/E_{\text{calo}}$ ($p_{\text{T}}^{\text{conv}}$ is the sum

[2]The ATLAS coordinate system takes into account deformations caused by several factors (e.g. gravity) and the mis-alignment of barrel/endcap. The EM calorimeter coordinate system however is only following the design calorimeter cell position.

p_{T} of the conversion tracks in the inner detector); and the fraction of the conversion momentum carried by the highest-p_{T} track, $p_{\mathrm{T}}^{\mathrm{max}} / p_{\mathrm{T}}^{\mathrm{conv}}$.

The MVA algorithm is optimized in different regions of the phase space, the sample is divided into bins of $\eta_{cluster}$, E_T^{acc} and according to the particle type. The binning is chosen to follow the known detector geometry variations.

In Run-II some improvements have been introduced to extend the pseudorapidity region covered by the calibration up to $|\eta| \in [0, 2.5]$ and to cover the transition region between the barrel and the endcap (crack) of the electromagnetic calorimeter. In the crack region the amount of material traversed by the particles before reaching the first active layer of the calorimeter is quite high (from 5 to almost 10 radiation lengths) and the energy resolution is very degraded. To improve the resolution the energy measured by the E4 scintillators installed in the transition region has been introduced as an additional variable to the training of the calibration.

5.5.4 In-situ corrections

After the application of the corrections for the non-uniformity of the detector response and of the simulation-based calibration, a residual disagreement in the energy scale and resolution may be present between data and simulation. In order to correct this residual mismatch a correction evaluated with an in-situ procedure developed in Run-1 [102] is applied. The energy mis-calibration is defined as the difference in response between data and simulation, and is parametrized as

$$E_i^{\mathrm{data}} = E_i^{\mathrm{MC}}(1 + \alpha_i) \tag{5.1}$$

where E_i^{data} and E_i^{MC} are the electron energies in data and simulation, and α_i represents the deviation from optimal calibration, in a given pseudorapidity region labeled i. The difference in energy resolution between data and simulation, which does not at first order depend on the energy, can be modeled by an additional effective constant term (c_i') for a given pseudorapidity region:

$$\left(\frac{\sigma(E)}{E}\right)_i^{\mathrm{data}} = \left(\frac{\sigma(E)}{E}\right)_i^{\mathrm{MC}} \oplus c_i' \tag{5.2}$$

Using $Z \to ee$ events selected in 3.2 fb^{-1} of 2015 data sample, the energy scale corrections (α_i) and additional constant terms for the energy resolution (c_i') have been estimated. The measured values are reported in Figure 5.10, along with the total systematic uncertainty of the in-situ calibration procedure. These corrections are applied both to electrons and photons. The measured values of the α_i are between -2% and +2% depending on η (with uncertainty from 0.1% to 0.5%), with the exception of the last bin in η. The c_i' values are between 0.005 and 0.03 depending on η (with uncertainty from 0.002 to 0.005). In the barrel region $-1.37 \leq \eta \leq 1.37$ the values of the c_i' are around 0.7% which is close to the designed constant term of the EM calorimeter.

5.5.5 $Z \to ee$ calibration applied to high energy electrons and photons

The corrections explained in the previous section are expected to be valid valid for electrons from Z decay, then it is assumed that the scale is the same for photons. The universality of the corrections

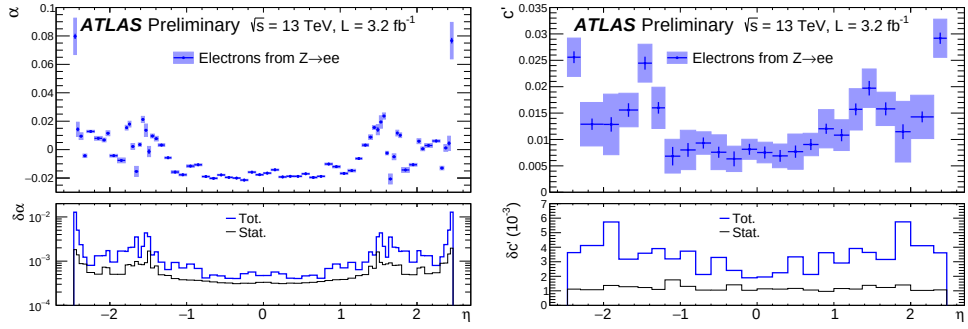

(a) (b)

Figure 5.10: (a) Energy scale factor α and (b) additional constant term c' for energy resolution from $Z \to ee$ events as a function of η. The uncertainty bands on the top plots represent the total uncertainties on these quantities, while the thin black (resp. thick blue) lines at the bottom represent the statistical (resp. total) uncertainties [103].

is tested using photons from radiative Z decays in the electron and muon channels. Residual miscalibrations between data and simulation are parameterized as $E_i^{\text{data}} = (1 + \delta\alpha_i)E_i^{\text{MC}}$ following a procedure similar to the procedure applied to electrons from Z decays in the previous section.

5.5.6 Systematic uncertainties on the e-gamma calibration

In this section the sources of systematic uncertainty for e/γ calibration will be review: both for the in situ corrections explained in Section 5.5.4 and for the energy scale and resolution for electrons and photons. The main sources of uncertainty on the energy scale and the ones that have been updated in Run-II are shown in Figure 5.11 for $|\eta| < 0.6$ and $5\,\text{GeV} < E_{\text{T}} < 1\,\text{TeV}$ for electrons, unconverted and converted photons. It can be seen that the systematics are low in the region near $m_Z \sim 91$ GeV (where the scale is measured from $Z \to ee$) and increase at lower and higher energies. The values of most of the systematic uncertainties have been taken from Run-1 results. In the following the systematic uncertainties are summarized:

- **Presampler**: uncertainty on the energy scale of the thin presampler layer.
- **Layer intercalibration**: uncertainty on the scale factors $\alpha_{1/2}$. An additional systematic uncertainty to take into account the possible differences between run-I and run-II ($\sim 1.5\%$) has been included in the uncertainty model. Furthermore an uncertainty relative to the muon to electron extrapolation is taken into account.
- **Layer 2 gain**: the dependence of the energy response from the gain used in the readout chain and its relative uncertainty is taken into account.
- **Material**: the uncertainties relative to the description of the material before the calorimeter for $|\eta| < 2.5$. This is done using simulation with distorted material geometry.

- **In-situ calibration** ($Z \rightarrow ee$): the uncertainty on the scale and additional constant term due to the selection criteria for the candidate electrons (identification, isolation and energy loss, differences data/simulation, selection criteria for the candidate Z and evaluation of the impact of the electroweak background) and on the methodology (different strategies for the extraction of α_i and c_i' parameters) have been evaluated.

- **Pedestal**: small baseline shifts were observed in data and an effect coming from the pedestal determination in electronics calibration. Data is corrected as a function of the bunch train position, given the high luminosity in Run-II this systematic uncertainty is estimated to be $\pm 20\,\text{MeV}$.

- **Pileup and temperature**: the in-situ calibration procedure accounts for possible differences in pileup and temperature conditions between data and simulation for 2015 data. In order to account for differences between 2015 and 2016 datasets in pileup conditions, an uncertainty of 0.02% has been added to the uncertainty model. Similarly an uncertainty of 0.05% has been added to account for temperature difference of the liquid argon between 2015 and 2016.

- **Tile scintillators**: four independent sources of uncertainty on the response of the scintillators in the crack region have been considered: data-simulation difference evaluated as the difference in the mean of the energy in the scintillators in $Z \rightarrow ee$ events (between 1% and 4.3%, depending on η). Uncertainty on the electromagnetic scale calibration factor that converts the Tile Calorimeter signals to the energy deposited by electrons (spread of 2.4%). Initial intercalibration using the Minimum Bias (MB) system[3]: 1%. Uncertainty of the calibration using laser over the whole year: 4%.

[3]Trigger system with the possible lowest requirement to ensure that an inelastic collision occurred, ATLAS has several complementary minimum bias triggers making use of the three levels of the trigger system.

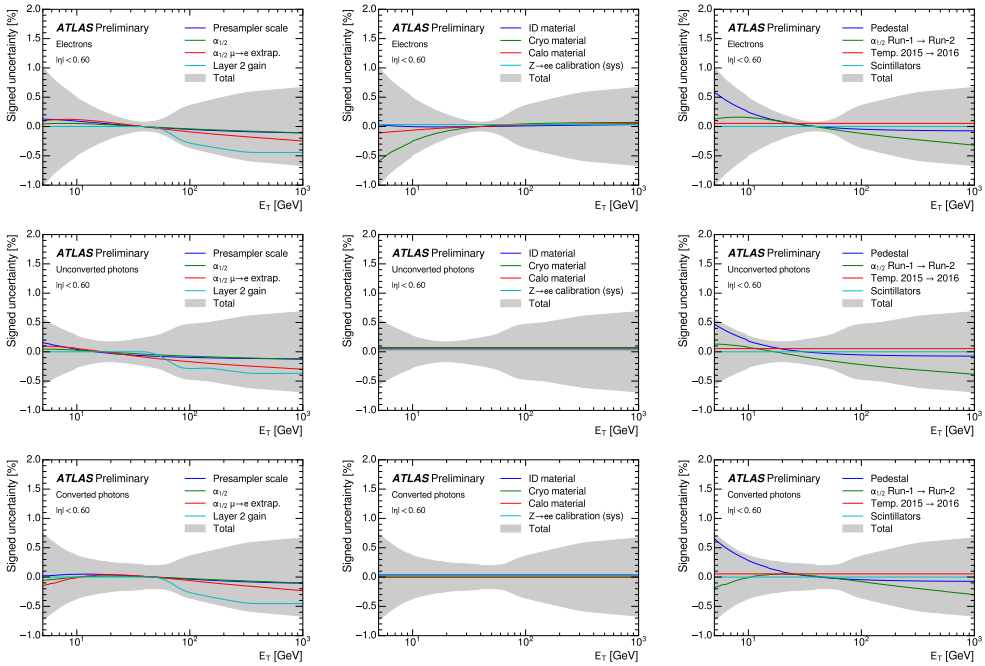

Figure 5.11: Main contributions to the systematic uncertainty on the energy scale after calibration corrections, shown as a function of E_{T} and for $|\eta| < 0.6$, in the case of electrons (top row), unconverted photons (middle row), and converted photons (bottom row). The total uncertainty bands represent the quadratic sum of all systematic uncertainty sources described in the text and represented in the various columns. The last column in particular shows the additional systematic uncertainties introduced from Run-1 to Run-2 and the temperature uncertainty added when comparing 2015 data to 2016 data [103].

5.6 Isolation

The isolation of a reconstructed objects describes the amount of activity in the area around the object which does not come from the object itself. This quantity normally is calculated for electrons, photons and muons. In the specific case of photons it can be used as a discriminant variable to further reject the jet background. The isolation is computed both in the calorimeter using the deposited energy and in the inner detector using tracks. Corrections are applied after the computation of the variable to correct for energy leakage of the object in the isolation cone and for pileup. The calculation of the different types of isolation and the relative corrections will be discussed in the following sections.

5.6.1 Track isolation

The Track Isolation (ptcone) is computed by summing the p_{T} of all Inner Detector tracks within a cone of dR = 0.X (0.2, 0.3, 0.4) centered around the lepton track or photon direction. A track selection is applied before summing the p_{T} of the tracks, as detailed in Table 5.3. The first five lines correspond to the Loose definition of track selection defined by the tracking working group. The last two lines are dedicated cuts optimized in the context of track isolation to maximise the fake lepton background rejection in $t\bar{t}$ events (p_{T} cut), and minimize the pile-up dependence of the track isolation ($|z_0 \sin\theta|$ cut). This variable is quite pileup robust for electrons because of the impact parameter cuts which constrain the tracks to come from the same vertex associated to the electron.

Criterium	Cut value
$\|\eta\|$	< 2.5
N_{Si}	≥ 7
$N_{\mathrm{mod}}^{\mathrm{sh}}$	≤ 1
$N_{\mathrm{Si}}^{\mathrm{hole}}$	≤ 2
$N_{\mathrm{Pix}}^{\mathrm{hole}}$	≤ 1
p_{T}	> 1 GeV
$\|z_0 \sin\theta\|$	< 3 mm

Table 5.3: Track selection for the track isolation. N_{Si} is the number of silicon (pixel + SCT) hits (including dead sensors); $N_{\mathrm{mod}}^{\mathrm{sh}}$ is the number of shared models *i.e.*$(N_{\mathrm{Pix}}^{\mathrm{sh}} + N_{\mathrm{SCT}}^{\mathrm{sh}}/2)$ where $N_{\mathrm{Pix}}^{\mathrm{sh}}$ and $N_{\mathrm{SCT}}^{\mathrm{sh}}$ are the number of shared hits, *i.e.* assigned to several tracks, in the pixel and SCT detectors; $N_{\mathrm{Si}}^{\mathrm{hole}}$ is the number of silicon holes, *i.e.* missing hits in the pixel and SCT detectors; $N_{\mathrm{Pix}}^{\mathrm{hole}}$ is the number of pixel holes; z_0 is the difference of longitudinal impact parameter of the track, and the position of a given vertex (by default the hardest vertex of the event)

Oppositely to the calorimeter isolation where a cone with a radius smaller than 0.2 cannot be used [4], the tiny tracker "cell size" allows to use smaller cone size when needed. A small cone

[4]The lepton/photon cluster has a size of 3×7 or 5×5 in middle cell calorimeter unit of 0.025, which corresponds

helps in situations where there are boosted signatures or very busy environnements, in which other objects can end up very close to the lepton/photon direction. For such cases, a variable-cone size track isolation [104], called ptvarcone, can be used. For this variable, the cone size gets smaller for larger transverse momentum of the lepton/photon:

$$\Delta R = \min\left(\frac{k_T}{p_{\mathrm{T}}}, R\right), \tag{5.3}$$

Where k_T is a constant fixed to 10 GeV and R is the maximum cone size (0.2 to 0.4). $k_T = 10$ GeV was optimized in Run-I on $t\bar{t}$ Monte Carlo events to maximise the background rejection coming from fake leptons.

The cut on $|z_0 \sin\theta|$ aims at selecting tracks that originate from the vertex that is chosen to be the relevant vertex of the process. In most of the cases, the relevant vertex corresponds to the "hardest" vertex of the event, *i.e.* which sum of transverse momenta of the associated tracks is the highest. In some special cases no hard tracks are associated to the process vertex, like the gluon fusion production of a Higgs Boson that decays to two photons without additional jets in the event. For such cases other information can be used to select the relevant vertex, such as the "pointing" direction coming from the shower shapes of the photon in the calorimeter (exploiting the longitudinal segmentation of the calorimeter).

The subtraction of the lepton/photon energy from the track isolation is done differently for muons, electrons and converted photons. For muons, the track corresponding to the muon is removed. For electrons and converted photons, the tracks associated to the e/γ object are removed [96]. However since electrons can emit Bremsstrahlung radiation and photons can convert into secondary electrons, that should be counted as part of the initial electron energy. Therefore, the tracks are extrapolated to the middle layer of the calorimeter, and all those that fall into a $\Delta\eta = 0.05 \times \Delta\phi = 0.1$ window around the electron cluster position are considered to be part of the electron/photon.

5.6.2 Calorimetric isolation

The TopoCluster based isolation, called **TopoEtCone** (represented in Figure 5.12), is computed as the sum of the topological clusters transverse energies within a cone of a radius dR = 0.X around the cluster barycenter. Usually this quantity is calculated for cones of radius 0.2, 0.3, 0.4 and the most used one is **TopoEtCone40** which is calculated for a cone of $dR = 0.4$. The electron and photon directions are given by the position of the associated rectangular calorimeter cluster used to reconstruct the electron/photon energy. The muon direction is given by the weighted mean of the extrapolated positions of the muon track into the electromagnetic calorimeter.

Topological clusters TopoClusters [105] are clusters seeded by cells with an energy more than four times above the noise threshold of that cell. The clusters are then expanded by adding neighboring cells that have an energy more than two times above the noise level. Neighboring cells

roughly to a cone of radius 0.1

are considered in the three spatial directions and across all calorimeter layers, however excluding the cells from the Tile gap scintillators. After the expansion around the cluster stops, a last layer of cells is added around the cluster.

Cluster summation All clusters within the cone are summed, however only positive energy topoclusters are used. The topological clusters used in the isolation computation are not further re-calibrated, they are simply calibrated at the electromagnetic scale. All positive energy topological clusters which barycenter falls within a cone centered around the lepton/photon direction are summed into what is called the raw TopoEtCone isolation $E_{\mathrm{T,raw}}^{\mathrm{isol}}$. After the summing procedure the energy from the core of the cone in the electromagnetic calorimeter (which is a grid of 5x7 cells) is subtracted from the sum. The actual core-removing procedure will be explained in Section 5.6.3.

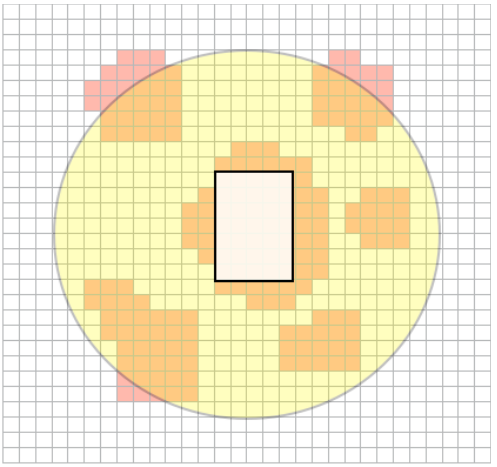

Figure 5.12: Scheme of the **topoEtCone** variable: the grid represents the middle calorimeter cells in the η and ϕ directions. The lepton/photon is located in the center of the yellow cone representing the isolation cone. All topological clusters, represented in red, which barycenter falls into the isolation cone are included in the isolation computation. The 5×7 cells white rectangle corresponds to the subtracted cells in the default "5x7 core subtraction" method.

Corrected TopoIsolation The fully corrected isolation is computed as the sum of the topoclusters minus the central core of the object, then corrections for leakage and pileup are applied:

$$E_{\mathrm{T,corr}}^{\mathrm{isol}} = E_{\mathrm{T,raw}}^{\mathrm{isol}} - E_{\mathrm{T,core}} - E_{\mathrm{T,leakage}}(p_{\mathrm{T}}) - E_{\mathrm{T,pile-up}}(\eta). \tag{5.4}$$

5.6.3 Core subtraction calorimeter isolation

The isolation energy as the sum of all topoclusters still includes the lepton/photon energy, called the core energy $E_{\mathrm{T,core}}$. This quantity needs to be subtracted from the sum to get the actual isolation variable. Several methods can be used to do so, for photons and electrons the technique in use is the 5x7 core subtraction (core57cells).

This technique, used since run 1, is used to remove the electron or photon core energy from the isolation calculation. The cells included in a 5×7 rectangle around the electron/photon direction are simply removed from the isolation variable. The advantage of this simple method is to have a stable subtraction for real or fake objects for any transverse momentum and pile-up. The disadvantage is that this does not subtract completely the electron/photon energy and an additional

leakage correction is needed. The additional pt-leakage correction are explained in section 5.6.5. At the moment this is the default core subtraction technique for electrons and photons in run-II.

5.6.4 Pile-up and underlying event correction

The pile-up and underlying event contribution to the isolation cone is estimated using the ambient energy density technique. The ambient energy is an estimate of the mean energy deposited by non-hard events in the calorimeter, it is evaluated for each event and it is computed in the following way [106]:

- Positive energy topological clusters are reconstructed in the whole calorimeter acceptance (up to $\eta = 5$) using anti-kT jet finding algorithm (see Section 5.8) of size 0.5, with no p_{T} threshold.
- The area A_{i} of each jet in the event is estimated from a Voronoi tessellation algorithm.
- The energy density of each jet is computed as $\rho_i = p_{\mathrm{T,i}}/A_{\mathrm{i}}$.
- The median of the distribution of all the energy densities in the event, ρ_{median}, is used as an estimator of the energy density of the event.

Figure 5.13 (left) shows the distribution of ρ_{median} as a function of η in 13 TeV $Z \to e^+e^-$ Monte Carlo events. For this figure, ρ_{median} is estimated from jets contained in a sliding window located between η and $\eta \pm 3$. The quantity ρ_{median} is flat in the central η region, and decreases in the forward η region. For simplicity, ρ_{median} is finally estimated on average in each of these regions: a central region with $|\eta| < 1.5$ and a forward region $1.5 < |\eta| < 3$. The right plot of 5.13 shows the distribution of ρ_{median} in these two regions.

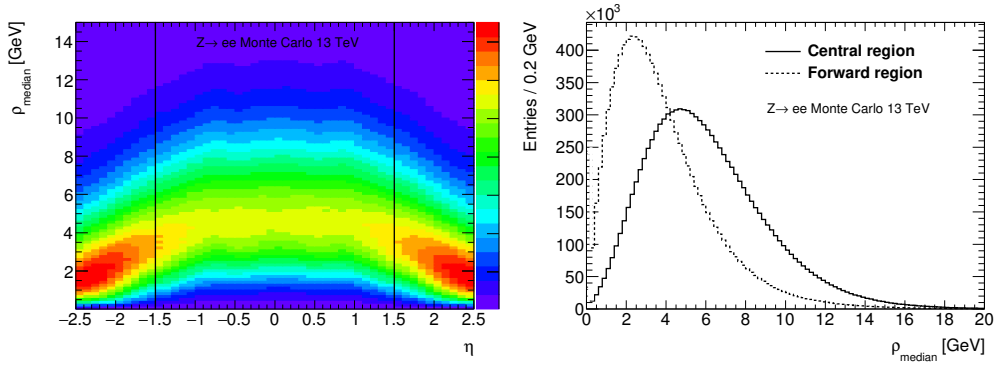

Figure 5.13: Left: distribution of ρ_{median} as a function of η. Right: distribution of ρ_{median} in the central and forward regions. Both figures are done for 13 TeV $Z \to e^+e^-$ Monte Carlo events.

The pile-up correction is then evaluated as:

$$E_{\mathrm{T,pile-up}}(\eta) = \rho_{median}(\eta) \times \left(\pi R^2 - A_{\mathrm{core}}\right), \tag{5.5}$$

where R is the radius of the isolation cone and A_{core} is the area of the 5x7 core that was subtracted, and corresponds to $5 \times 7 \times 0.025\pi/128$ (0.025 is $\eta \times \phi$ volume of one cell).

5.6.5 Electron and photon leakage correction

When the electron/photon core energy is subtracted from the isolation energy some remaining electron/photon energy leaking into the isolation cone remains and should be further subtracted. This leakage is evaluated using Monte Carlo samples of single electrons and photons without pile-up, which p_{T} spectrum going from 20 GeV up to 3 TeV. The technique used to derive this correction is explained in the following sections.

The correction is derived in 10 pseudo-rapidity bins (η corresponding to the barycenter of the energy deposited in the middle sampling of the electromagnetic calorimeter), and separate corrections are derived for electrons, converted photons and unconverted photons. The η binning was established to follow the distribution of the material of the EM calorimeter. The distribution of the isolation variable versus the p_{T} of the photon/electron in single slices in η can be seen in the two dimensional histograms in Figure 5.14.

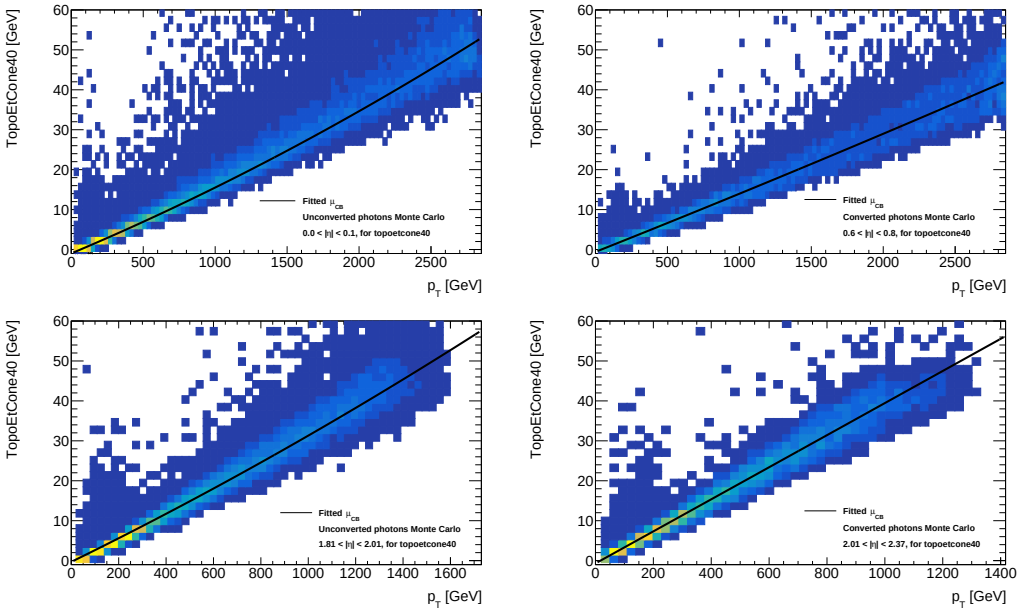

Figure 5.14: Two dimensional distribution of topoetcone40 vs the p_T of the photon for different η bins. Superimposed is the μ_{CB} which also corresponds to the applied pt-leakage correction.

Derivation of the correction. The isolation energy is fitted for each slice in η with a Crystal-Ball (CB) function, which consists of a Gaussian core portion and a power-low tail above a given

threshold, that has p_{T}-dependent parameters. The CB function is defined as Formula 5.6.

$$f(x;\alpha_{\mathrm{CB}},n,\mu_{\mathrm{CB}},\sigma_{\mathrm{CB}}) = N\cdot\begin{cases} e^{\frac{-(x-\mu_{\mathrm{CB}})^2}{2\sigma_{\mathrm{CB}}^2}} & , \; for \; \frac{x-\mu_{\mathrm{CB}}}{\sigma_{\mathrm{CB}}} > -\alpha_{\mathrm{CB}} \\ A\cdot\left(B-\frac{x-\mu_{\mathrm{CB}}}{\sigma_{\mathrm{CB}}}\right)^{-n} & , \; for \; \frac{x-\mu_{\mathrm{CB}}}{\sigma_{\mathrm{CB}}} \leq -\alpha_{\mathrm{CB}} \end{cases} \tag{5.6}$$

The parameters of the Crystal Ball are described in Formula 5.7. Err.f is the error function (Formula 5.8).

$$\begin{aligned} A &= \left(\tfrac{n}{|\alpha_{\mathrm{CB}}|}\right)^n \cdot e^{-\frac{|\alpha_{\mathrm{CB}}|^2}{2}} \\ B &= \tfrac{n}{|\alpha_{\mathrm{CB}}|} - |\alpha_{\mathrm{CB}}| \\ N &= \tfrac{1}{\sigma_{\mathrm{CB}}(C+D)} \\ C &= \tfrac{n}{|\alpha_{\mathrm{CB}}|}\cdot\tfrac{1}{n-1}\cdot e^{-\frac{|\alpha_{\mathrm{CB}}|^2}{2}} \\ D &= \sqrt{\tfrac{\pi}{2}}\left(1+Err.f\left(\tfrac{|\alpha_{\mathrm{CB}}|}{\sqrt{2}}\right)\right) \end{aligned} \tag{5.7}$$

$$Err.f(x) = \frac{2}{\sqrt{\pi}}\int_0^x e^{-t^2},dt \tag{5.8}$$

A two dimensional CB model with parameters depending on p_{T} of the photon, $CB(\text{topoEtConeX}, p_T)$ (where X is 20, 30, 40) is fitted on the single particle MC isolation distributions. The parameters depend on the p_{T} of the particle: the mean of the CB μ_{CB} and the width σ_{CB} of the Crystal-Ball depend quadratically on the p_{T}, the threshold parameter α_{CB} is fitted while the power of the power-law tail is fixed ($n = 10$).

$$\begin{aligned} \mu_{CB} &= a_1 + b_1 * p_T + c_1 * p_T^2, \\ \sigma_{CB} &= a_2 + b_2 * p_T + c_2 * p_T^2, \\ \alpha_{CB} &= a_3, \\ n &= 10 \end{aligned} \tag{5.9}$$

An unbinned maximum likelihood fit is performed on each η slice. The mean of the Crystal-Ball function, μ_{CB}, correspons to the effect of energy leakage in the isolation cone and is used as the correction. Examples can be seen in Figure 5.14, the two dimensional histogram is the distribution of topoEtCone20 vs the p_{T} of the photon and the black line represent the fitted μ_{CB} which is also the applied correction. In Figure 5.15 CB fits projection for single bins in $\eta \times p_T$ (intervals written in the plot) can be found. The actual correction applied can be seen in Figure 5.16.

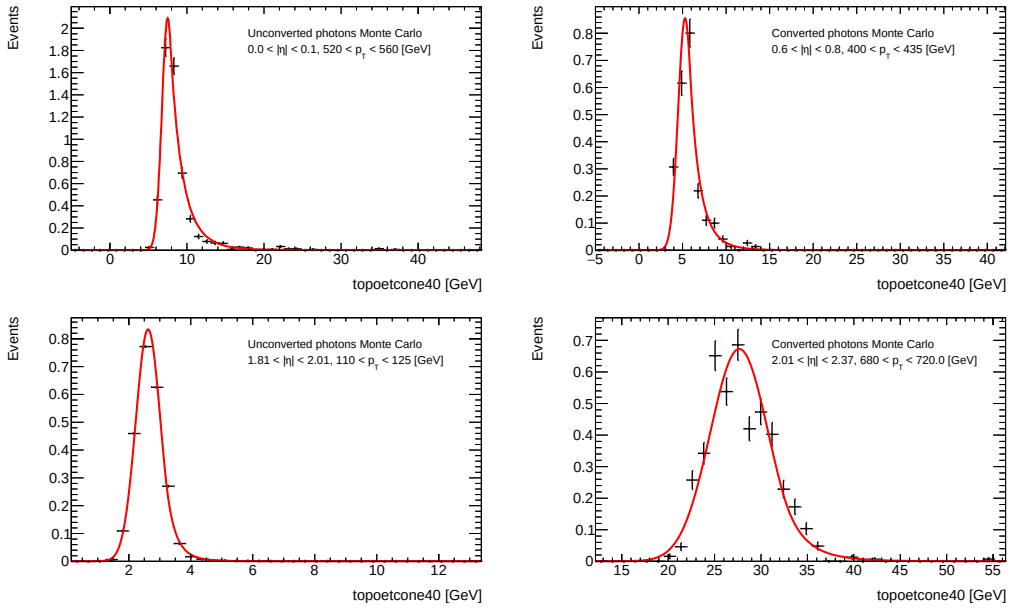

Figure 5.15: One dimensional CB fit for converted/unconverted photons and electrons for different bins of $\eta \times p_T$

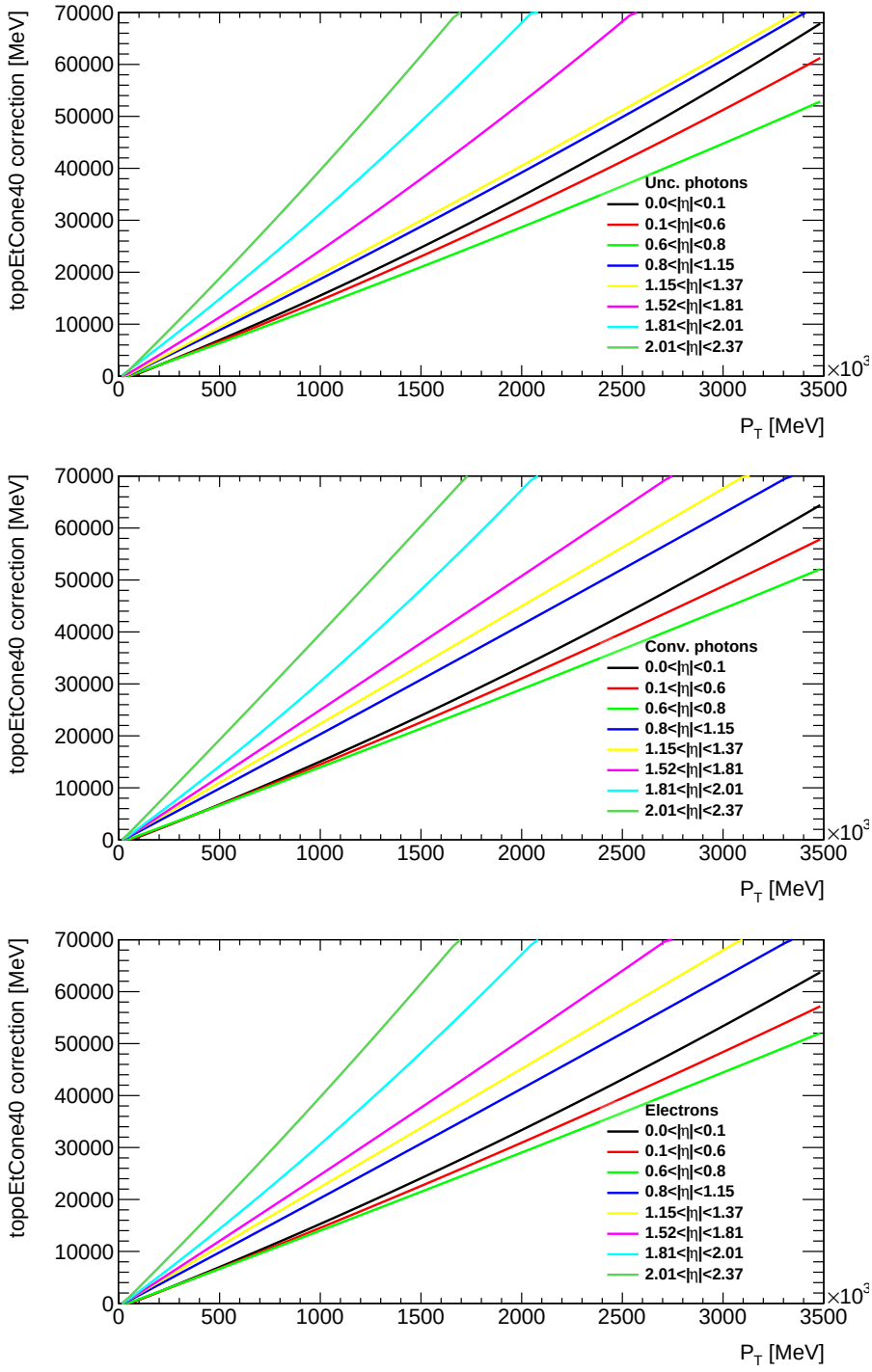

Figure 5.16: Applied correction to topoEtCone40 as a function of p_{T} and pseudorapidity for (from top to bottom) unconverted photons, converted photons and electrons.

Problematic cases Problems were observed at low p_{T} both for photons and electrons; a double peak is present at low energy ($E_T < 200$ GeV) for some categories of candidates (Figure 5.17). In photons the second peak was observed only for early asymmetric conversion, for this reason three categories were defined: unconverted, early asymmetric conversions and the remaining converted photons. For electrons the second peak was observed for electron which the reconstruction process tagged as ambiguous (as introduced in Section 5.4.3), therefore two categories were defined: ambiguous and non ambiguous. To take ambiguous electron into account the double peak a different kind of correction for troublesome categories for Pt < 250 GeV was used: the mean of the 90% of the events instead of the peak of the CB. For Pt > 250 the normal correction are used. The transition between the two types of corrections is smooth as seen in Figure 5.18.

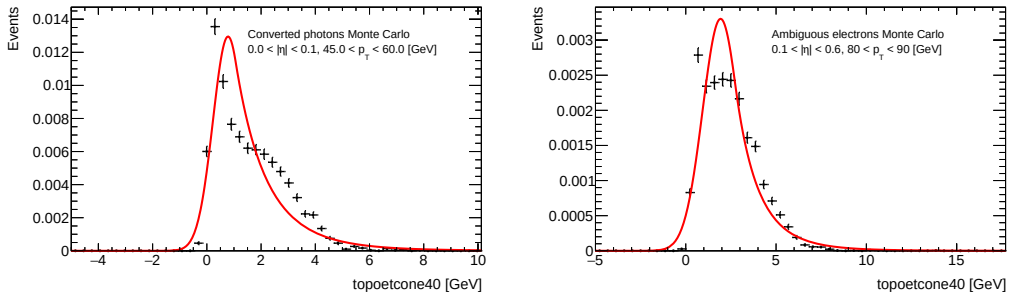

Figure 5.17: Two examples of isolation distribution for troublesome categories: early asymmetric conversions for photons (left) and electrons tagged as ambiguous (right).

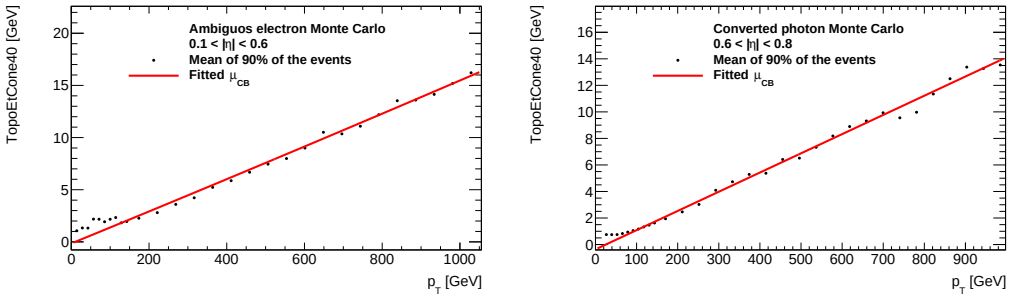

Figure 5.18: Two examples of isolation correction for troublesome categories for photons and electrons. The points represent the mean of 90 % of events while the read line is the output of the fit. For $p_T < 250$ GeV the points are used as correction, while for $p_T > 250$ GeV the red line is used as correction.

Correction validation To estimate the goodness of the corrections the single particle MC sample used is re-processed applying the corrections. A CB is fitted to the corrected sample in bins of $\eta \times p_T$ and the trend of μ_{CB} as a function of p_T is studied. The same procedure is done both for photons and electrons (Figure 5.19). As expected the mean of the isolation is flat in p_T after

applying the corrections. Some examples of the distribution of isolation variable versus η after the corrections are show in Figure 5.20.

This method to estimate le lateral leakage has some limitations, however it is very robust. It does not consider the shower shape fluctuations at a given p_{T}, which can get very large for high p_{T}. Furthermore it is evaluated from the Monte Carlo, whereas the ATLAS Monte Carlo is known to not well reproduce the lateral shower shapes for electrons and photons. Other methods for core subtraction are being studied within the ATLAS collaboration and will be refined in the next years.

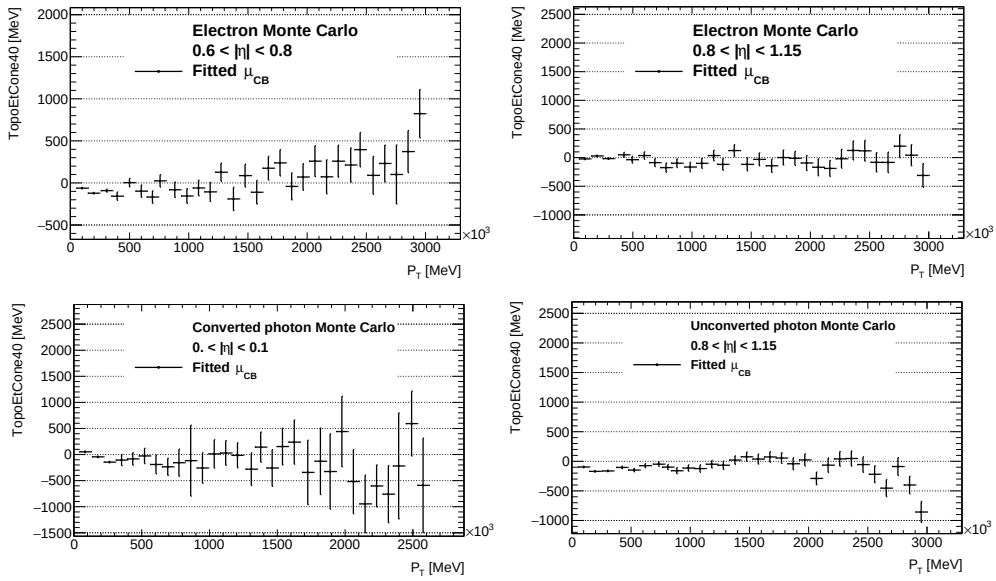

Figure 5.19: Mean of a crystal ball fit in p_T bins after the correction were applied for electrons (upper plots) and photons (lower plots) for different pseudorapidity bins.

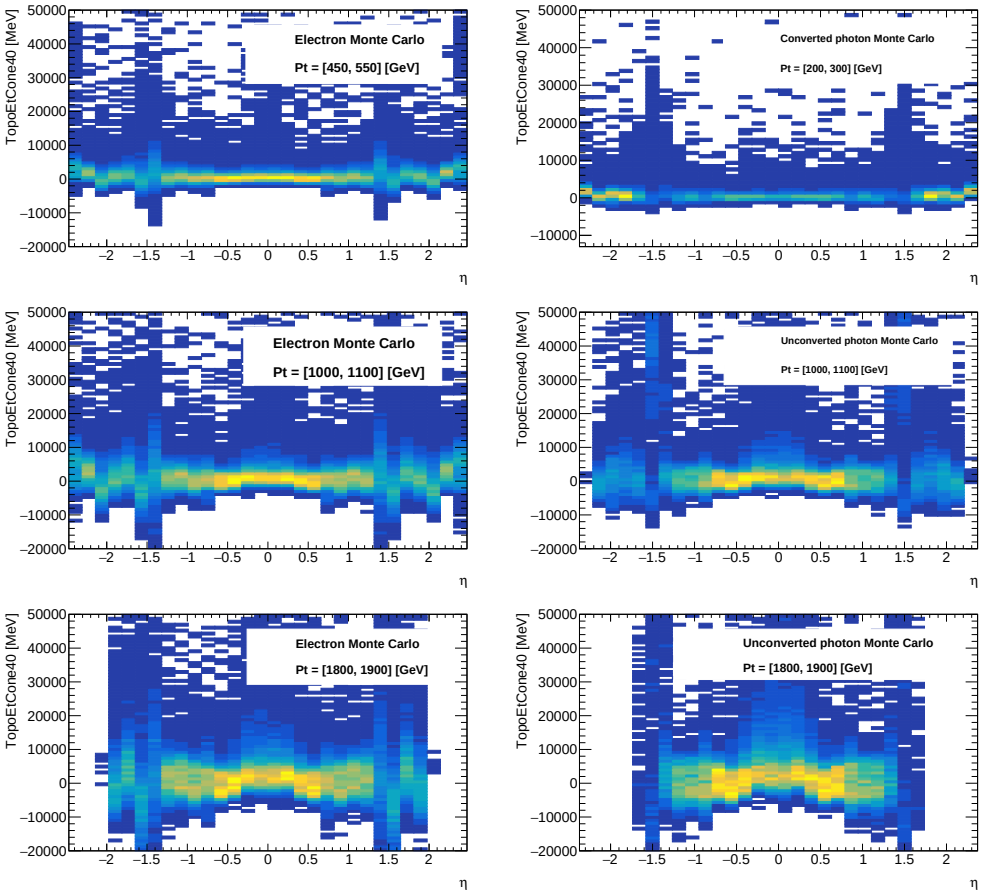

Figure 5.20: Isolation distribution versus η for electrons (left) and photons (right) for several p_T intervals after applying the corrections.

5.7 Muons

Muon reconstruction is first performed independently in the inner detector and muon system. The information from individual sub-detectors is then combined to form the muon tracks that are used in physics analyses. For a full explanation of the reconstruction and identification procedure for muon see Reference [107].

Muon reconstruction in the muon system Muon reconstruction in the muon system starts with a search for hit patterns inside each muon chamber to form segments. In each MDT chamber and nearby trigger chamber, a Hough transform [108] is used to search for hits aligned on a trajectory in the bending plane of the detector. The search algorithm includes a loose requirement on the compatibility of the track with the luminous region. Muon track candidates are then built by fitting together hits from segments in different layers. An overlap removal algorithm selects the best assignment to a single track, or allows for the segment to be shared between two tracks.

Combined reconstruction The combined inner detector – muon system muon reconstruction is performed according to various algorithms based on the information provided by the inner detector, muon system, and calorimeters. Four muon types are defined depending on which sub-detectors are used in reconstruction:

- Combined (CB) muon: track reconstruction is performed independently in the inner detector and MS, and a combined track is formed with a global refit that uses the hits from both the inner detector and muon system sub-detectors. Most muons are reconstructed following an outside-in pattern recognition, in which the muons are first reconstructed in the muon system and then extrapolated inward and matched to an inner detector track. An inside-out combined reconstruction is used as a complementary approach to recover the inefficiencies of the CB approach.

- Segment-tagged (ST) muons: a track in the inner detector is classified as a muon if, once extrapolated to the MS, it is associated with at least one local track segment in the MDT or CSC chambers.

- Calorimeter-tagged (CT) muons: a track in the inner detector is identified as a muon if it can be matched to an energy deposit in the calorimeter compatible with a minimum-ionizing particle.

- Extrapolated (ME) muons: the muon trajectory is reconstructed based only on the muon system track and a loose requirement on compatibility with originating from the interaction point. Overlaps between different muon types are resolved before producing the collection of muons used in physics analyses.

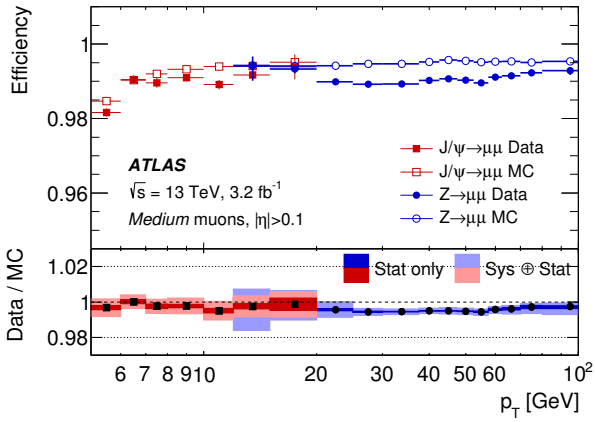

Figure 5.21: Reconstruction efficiency for the Medium muon selection as a function of the pT of the muon, in the region $0.1 < |\eta| < 2.5$ as obtained with $Z \rightarrow \mu\mu$ and $J/\psi \rightarrow \mu\mu$ events. The error bars on the efficiencies indicate the statistical uncertainty. The panel at the bottom shows the ratio of the measured to predicted efficiencies, with statistical and systematic uncertainties [107].

Muon identification Muon identification is performed by applying quality requirements that suppress background, mainly from pion and kaon decays and hadron calorimeter punch-through, while selecting prompt muons with high efficiency and/or guaranteeing a robust momentum measurement. Muon candidates originating from in-flight decays of charged hadrons in the ID are expected to have a poor fit quality of the resulting combined track and that the momentum measured in the ID and MS may not be compatible. Several variables offering good discrimination between prompt muons and background muon candidates are studied in simulated $t\bar{t}$ events. Four muon identification selections (*Medium*, *Loose*, *Tight*, and *High-*p_{T}) are provided to address the specific needs of different physics analyses. *Loose*, *Medium*, and *Tight* are nested categories so that muons identified with tighter requirements are also included in the looser categories. Recontruction efficiency for *Medium* muon selection can be seen in Figure 5.21.

5.8 Hadronic jets

Hadronic jets used for ATLAS physics analysis [109, 110] are reconstructed by an Anti-Kt jet algorithm [111]. The inputs to this algorithm are topologically connected clusters of calorimeter cells (topoclusters) [112], seeded by cells with energy significantly above the measured noise. These topoclusters are at the electromagnetic (EM) energy scale, which correctly measures the energy deposited by electromagnetic showers in the calorimeter.

Anti-Kt jet finding Topoclusters are used in the jet finding algorithm Anti-Kt04 or Anti-Kt06 [111], this algorithms runs on all the topological energy deposits in the hadronic calorimeter and associate every inputs with a distance d_{ij} and a beam distance d_{iB}.

$$\begin{aligned} d_{ij} &= min(1/p_{ti}^2, 1/p_{tj}^2)\Delta R_{ij}^2/R^2 \\ d_{Bi} &= 1/p_{ti}^2 \end{aligned} \tag{5.10}$$

The distances depend of the quantities $1/p_{ti}^2$ and a median jet radius R that can be 0.4 or 0.6 (hence AntiKt04 or AntiKt06). Then it finds the minimum d_{min} of all the d_{ij}, d_{iB}. If d_{min} is a d_{ij} merge clusters i and j into a single cluster, summing their four-momenta. If it is a d_{iB} then declare particle i to be a final jet and remove it from the list. This procedure is iterated until no particles are left.

The jet Lorentz four-momentum is then reconstructed from the corrected energy and angles with respect to the primary event vertex.

Jet energy calibration The jet energy calibration relates the jet energy measured with the ATLAS calorimeter to the true energy of the corresponding jet of stable particles. To achieve this reference jets in Monte Carlo simulations (truth jets) are formed from simulated stable particles using the same jet algorithm.

The calibration procedure corrects for the detector effects that affect the jet energy measurement by using energy and η-dependent calibration factors, based on Monte Carlo simulation and collision-data. The following effects are taken into consideration:

- **Calorimeter non-compensation:** partial measurement of the energy deposited by hadrons.
- **Dead material:** energy losses in inactive regions of the detector.
- **Leakage:** energy of particles reaching outside the calorimeters.
- **Out of calorimeter jet cone:** energy deposits of particles inside the truth jet entering the detector that are not included in the reconstructed jet.
- **Noise thresholds and particle reconstruction efficiency:** signal losses in the calorimeter clustering and jet reconstruction.

The absolute calorimeter response to energy deposited via electromagnetic processes was validated in the hadronic calorimeters using muons, both from test-beams and produced in situ by cosmic rays.

Part III

Diphoton analysis

CHAPTER 6

Diphoton analysis overview

The main topic of this thesis is the search for spin-0 and spin-2 resonances in the diphoton invariant mass spectrum. The signal searched for are either RS gravitons or additional Higgs bosons as predicted by 2DHM model, the two BSM model taken into consideration are introduced in Chapter 2. In this chapter the main backgrounds for the analysis are introduced, then the MC samples for both signal and background used in the process are listed. Finally the optimization of the selection, the composition of the selected events and a brief overview of the analysis techniques are discussed.

Then in the following chapters the analysis strategy concerning signal model, background estimation and statistic treatment will be outlined. Public results for this analysis were released in December 2015 [8], in Moriond 2016 [10] with 3.2 fb^{-1} of data at $\sqrt{s} = 13$ TeV from 2015 and in ICHEP 2016 [11] with 3.2 fb^{-1} + 12.2 fb^{-1} of data at $\sqrt{s} = 13$ TeV respectively from 2015 and 2016 data taking. The same search was done by the CMS collaboration and can be seen in References [12, 13] for data at $\sqrt{s} = 13$ TeV from year 2015 and 2016 respectively.

6.1 Background composition

The main background sources in the diphoton channel can be divided into two categories: irreducible and reducible background.

- **Irreducible background** is due to SM production of real photon pairs. Events with two photons can be generated by the direct production of photons from quarks, by the radiative emission of photons from quarks and from fragmentation photons. The main irreducible background can be see in Figure 6.3.

More in detail three sources can be considered:

- The Born process $qq \to \gamma\gamma$, illustrated in Figure 6.3 (a). In terms of power counting in α, this tree level process is of $O(\alpha^2)$;
- The box process $gg \to \gamma\gamma$, of order $O(\alpha^2\alpha_s^2)$ (see Figure 6.3 (b)), enhanced by the gluon PDF

- The bremsstrahlung process $qg \to q\gamma\gamma$, of order $O(\alpha^2\alpha_s)$ (see Figure 6.3 (c)). In addition, photons produced in fragmentation processes are considered as prompt photons. Consequently the single photon-plus-jet, or the multi-jets processes, with respectively one or two partons fragmenting into high-p_T photon(s) are included in the irreducible background. Leading-order fragmentation diagrams are shown in Figure 6.3 (d) and (e).

The reducible background instead is:

- **Reducible background** includes events in which one or both of the reconstructed photon candidates result from a different physics object, usually a jet, faking the photon signature. The production processes of photon and jet events can be seen in Figure 6.2.

The relation between the cross section of di-photon, di-jet and photon-jet processes can be seen in Figure 6.1.

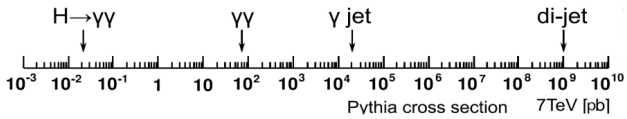

Figure 6.1: Scaling of the cross section between the production of di-jet, photon-jet and photon-photon events.

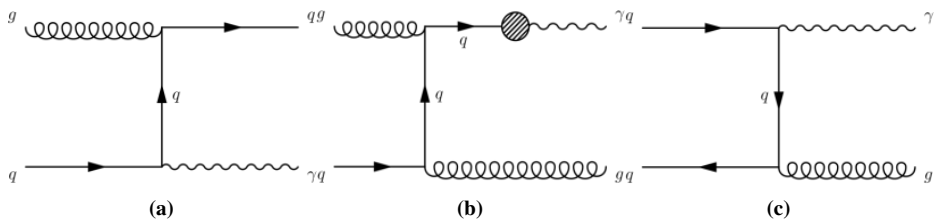

Figure 6.2: Reducible background sources from SM processes, only the processes with one photon and one jet are shown. (a) and (b) are Compton scattering and take ~ 90% of the phase space while (c) is the annihilation process and takes the remaining ~10% of the phase space.

Photons are reconstructed and identified in the ATLAS detector as seen in Section 5.4.4, furthermore a selection on the trasverse energy and on the isolation variable is applied as will be shown in Sections 6.3.3 and 6.3.4. The applied selection greatly reduces the reducible background coming from di-jet and γ-jet events whose cross section would be several order of magnitude higher than diphoton production processes (Figure 6.1).

After the identification and selection process the total background coming from di-jets and γ-jet is around 10 % of the selected number of events, as found with purity studies that will be introduced in Section 6.6.

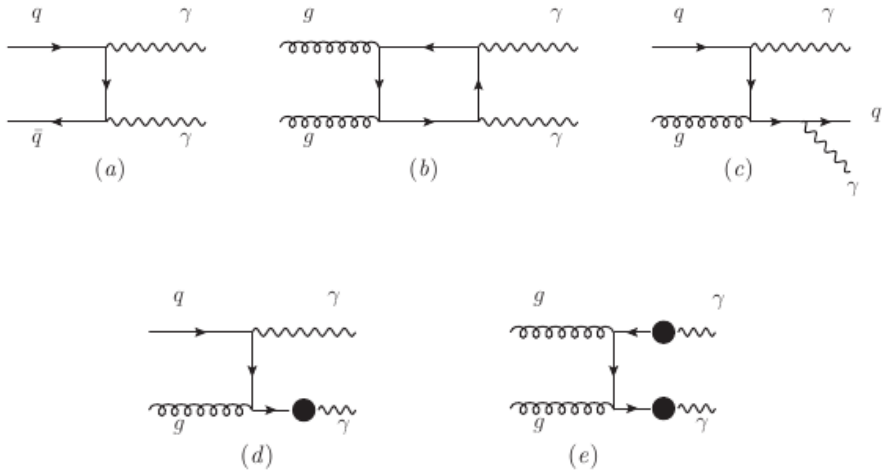

Figure 6.3: Irreducible background sources from SM processes. From left to right and top to bottom: direct production of two photons from quarks, production of photons via box-diagram from gluons, radiative emission of one photon from a quark, one fragmentation photon, two fragmentation photons.

6.2 Monte Carlo samples

As already stated in the previous chapters a reliable Monte Carlo simulation of the studied physics processes is crucial for any analysis at the LHC. In this section the Monte Carlo (MC) samples of signal and background will be listed. These samples are the starting point for the production of the signal and background models in Chapter 7 and Chapter 8 respectively.

6.2.1 Signal Monte Carlo samples

6.2.1.1 Spin-0

The scalar Higgs-like signal model is simulated using an Higgs boson production processes in pp collision at $\sqrt{s} = 13$ TeV followed by a decay to two photons. The MC samples are produced for different resonance mass hypothesis in the range [150 - 2000] GeV.

The width Γ_X of most of the MC samples is set to $\Gamma_X = 4.07$ MeV, corresponding to the width of a 125 GeV SM Higgs boson, regardless of the resonance mass (Narrow Width Approximation: NWA). The gluon-fusion (ggF) production mode is chosen as the baseline for optimization and signal parametrization studies. In this mode, the interference between the $gg \to X \to \gamma\gamma$ process and the continuous QCD diphoton production associated to the $gg \to \gamma\gamma$ process is estimated to be tiny for the NWA [113] and is neglected in the simulation.

Since the goal of the analysis is to perform a model-independent search, the properties of the signal shape are also studied for the other Higgs-like production modes, however their difference with the ggF production is negligible. For this reason only the gluon fusion process will be used

Process	Generator	Mass [GeV]	N_{events} ($\times 10^3$)
ggF	PowHeg+Pythia8	150-200-250-300-350 400-450-500-600-700	30
		800	100
		900-1000-1500-2000	30
VBF	PowHeg+Pythia8	200-300-400-500-600 800-1000-1500-2000	30
WH	Pythia8	200-300-400-500-600 800-1000-1500-2000	30
ZH	Pythia8	200-300-400-500-600 800-1000-1500-2000	30
ttH	Pythia8	200-300-400-500-600 800-1000-1500-2000	30

Table 6.1: MC samples of the different Higgs production modes used to study the signal shapes, with the available simulated mass values and the corresponding statistics.

and the other production are taken into account as a systematic variation.

The Higgs-boson-like signal samples produced via ggF and VBF are simulated with the Powheg [114, 115] generator interfaced to Pythia8 for showering and hadronization. The WH, ZH and ttH samples are simulated with Pythia8 only. A summary of the generated NWA samples can be found in Table 6.1.

The search covers signals with instrinsic widths of the resonance ranging up to $\Gamma_X/m_X = 0.10$. Since it is impractical to generate signal samples for various values of both m_X and Γ_X, the signal shapes for the non-NWA cases are described using convolutions of the NWA shape with Breit-Wigner distributions. Large-width samples are, however, generated for several values of Γ_X at selected m_X points in order to validate these techniques. These samples are listed in Table 6.2.

6.2.1.2 Spin-2

The spin-2 signal model is obtained from Randall-Sundrum (RS) graviton production in pp collision at $\sqrt{s} = 13$ TeV followed by a decay in two photons. Only the effect of the first KK excitation is simulated. Multiple samples were produced with Pythia8 for different values of the coupling $k/\overline{M}_{\text{Pl}}$ and mass of the Graviton M_X. The width of the generated samples is proportional to the $k/\overline{M}_{\text{Pl}}$ following the relation $\Gamma_{G^*} = 1.44 \cdot (k/\overline{M}_{\text{Pl}})^2 M_X$. The available samples have $k/\overline{M}_{\text{Pl}}$ and M_X ranging between $0.01 < k/\overline{M}_{\text{Pl}} < 0.25$ and $500 < M_X < 5500$ GeV. Samples where produced in the mass range [500, 1000] GeV with 50 GeV steps while in the range [1000, 5500] with 500 GeV steps. A summary of the graviton samples used is presented in Table 6.3.

In addition to the single mass and width samples a so-called 'flat mass' sample is produced with high statistics. The flat mass sample is simulated starting from a sample with 5 TeV mass and

Process	Generator	Mass [GeV]	Width/Mass [%]	N_{events} ($\times 10^3$)
ggF	PowHeg+Pythia8	400	5	30
			7	30
			10	100
		800	5	30
			7	30
			10	100
		1500	5	30
			7	30
			10	100

Table 6.2: MC samples of different mass and width values that are simulated to validate the shape of a large width resonance.

Generator	Mass [GeV]	$k/\overline{M}_{\text{Pl}}$	N_{events} ($\times 10^3$)
Pythia8	500-1000 GeV (50 GeV step)	0.01-0.05-0.1-0.15-0.2-0.25	20
Pythia8	1000-5500 GeV (500 GeV step)	0.01-0.05-0.1	20
Pythia8	5000 GeV (Flat)	0.1 (Flat)	1500

Table 6.3: MC samples of different $M_X$and $k/\overline{M}_{\text{Pl}}$values for a Graviton resonance simulation.

$k/\overline{M}_{\text{Pl}} = 0.1$ RS graviton, where the effect of the Breit-Wigner term is removed. Once the flat graviton mass spectrum has been generated and analyzed, re-weighting to any mass and coupling is achieved by reversing this procedure on an event by event basis. The flat sample re-weighting procedure has been validated for a $k/\overline{M}_{\text{Pl}}$ and M_X interval by producing, starting from the flat sample, RS graviton samples for a wide range of the M_X and $k/\overline{M}_{\text{Pl}}$ parameters, which are then compared to simulated samples for a single mass and width using the same parameter values. The limit of the validity of this procedure is reached when the values of M_X and $k/\overline{M}_{\text{Pl}}$ are both small at the same time. For this reason for $k/\overline{M}_{\text{Pl}} \leq 0.05$ Randall-Sundrum signal samples are generated for each mass point.

6.2.2 Background Monte Carlo samples

6.2.2.1 Samples with full detector simulation

The irreducible SM background of events with two prompt photons are simulated using the Sherpa version 2.1 event generator [116] with up to 2 additional two partons in the final state with the CT10 PDF. The generated events are filtered by requiring the presence of two photons with a transverse energy larger then 20 GeV in the final state. In order to maximize the available statistics over the mass range of interest, the simulation is separately performed in exclusive slices of diphoton invariant mass $m_{\gamma\gamma}$. Table 6.4 lists the properties of these prompt diphoton samples, including the

Generator	$m_{\gamma\gamma}$ range [GeV]	Cross section [pb]	Filter efficiency	N_{events}
Sherpa	100 – 160	$3.9722 \cdot 10^{+1}$	$4.9729 \cdot 10^{-1}$	999200
	160 – 250	$1.1981 \cdot 10^{+1}$	$4.7858 \cdot 10^{-1}$	497200
	250 – 400	3.7119	$4.3236 \cdot 10^{-1}$	499800
	400 – 650	1.0114	$3.5116 \cdot 10^{-1}$	500000
	650 – 1000	$2.3480 \cdot 10^{-1}$	$2.5150 \cdot 10^{-1}$	499000
	1000 – 1500	$6.0455 \cdot 10^{-2}$	$1.6727 \cdot 10^{-1}$	499400
	1500 – 2000	$1.2409 \cdot 10^{-2}$	$1.1035 \cdot 10^{-1}$	499500
	2000 – 2500	$3.3581 \cdot 10^{-3}$	$8.0306 \cdot 10^{-2}$	499500
	2500 – 3000	$1.0460 \cdot 10^{-3}$	$6.1888 \cdot 10^{-2}$	99000
	3000 – 3500	$3.5256 \cdot 10^{-4}$	$5.0045 \cdot 10^{-2}$	99800
	3500 – 4000	$1.2396 \cdot 10^{-4}$	$4.1190 \cdot 10^{-2}$	99800
	4000 – 4500	$4.4474 \cdot 10^{-5}$	$3.5153 \cdot 10^{-2}$	99400
	4500 – 5000	$1.6024 \cdot 10^{-5}$	$3.0293 \cdot 10^{-2}$	99600
	5000 – ∞	$8.6793 \cdot 10^{-6}$	$2.4712 \cdot 10^{-2}$	99200

Table 6.4: MC samples with two prompt photons. In the columns are shown the corresponding cross section, the efficiency of the applied filter, and the corresponding number of generated events.

corresponding cross section, the efficiency of the applied filter, and the corresponding number of events before the selection.

6.2.2.2 Reducible background

Monte Carlo samples for reducible background were used in the optimization of the analysis selection. Single photon samples of Pythia8 and Sherpa with the CT10 PDF and p_{T} of the photon ranging from 20 GeV to 4 TeV were used.

6.3 Analysis selection optimization

In this section the optimization of the kinematic and isolation selection cuts will be explained. Furthermore the calculation of the relevant kinematic variables for the analysis will be introduced.

6.3.1 The diphoton invariant mass

The most important kinematic variable used in the diphoton channel is the invariant mass of the two photon. This quantity depends on the energy of the two photons and on the angle between them. The uncertainty on this quantity depends on the photon energy reconstruction, calibration and on the measurement of the photons direction. The invariant mass is calculated as:

$$m_{\gamma\gamma} = \sqrt{2E_1E_2(1-cos(\theta))} \tag{6.1}$$

where E_1 and E_2 the energies of the leading and subleading photons and θ the angle between the two photons. A particle produced in the pp collisions and decaying in two photons would be observed as a deviation from the Standard Model background diphoton invariant mass distribution.

6.3.2 cosθ^*

Spin information of a hypothetic particle decaying in two photons can be extracted from the distribution of the absolute value of the cosine of the polar angle θ^* (cosθ^*) of the photons with respect to the z-axis of the Collins-Soper (CS) frame. This kinematic variable depends on the angular distribution of the two photons in the final state.

The CS frame is constructed by boosting to the produced particle rest frame, and then rotating in such a way that measured variables remain sensitive to spin. This choice minimizes the effects from initial state radiation and results in better discriminating power than other options such as the beam axis or boost direction of the produced particle.

cosθ^* can be defined in two ways, one is depending on the energy and the p_Z of the two photons and the other is explicitly depending on the $\Delta\eta$ between the two photons:

$$\cos\theta^* = \frac{\left(E^{\gamma 2}+p_Z^{\gamma 2}\right)\cdot\left(E^{\gamma 1}-p_Z^{\gamma 1}\right)-\left(E^{\gamma 1}+p_Z^{\gamma 1}\right)\cdot\left(E^{\gamma 2}-p_Z^{\gamma 2}\right)}{m_{\gamma\gamma}\cdot\sqrt{m_{\gamma\gamma}^2+\left(p_T^{\gamma\gamma}\right)^2}} \tag{6.2}$$

$$\cos\theta^* = \frac{\sinh\left(\eta_{\gamma 1}-\eta_{\gamma 2}\right)}{\sqrt{1+\left(p_T^{\gamma\gamma}/m_{\gamma\gamma}\right)^2}}\cdot\frac{2p_T^{\gamma 1}p_T^{\gamma 2}}{m_{\gamma\gamma}^2} \tag{6.3}$$

The distribution of this variable would be different in case of a spin-0 particle and a spin-2 particle as seen in Figure 6.4, left. In case of a discovery, it is a crucial kinematic variable for distinguishing between a spin-0 or a spin-2 resonance. cosθ^* was already used in run-I for the SM Higgs spin measurement [117].

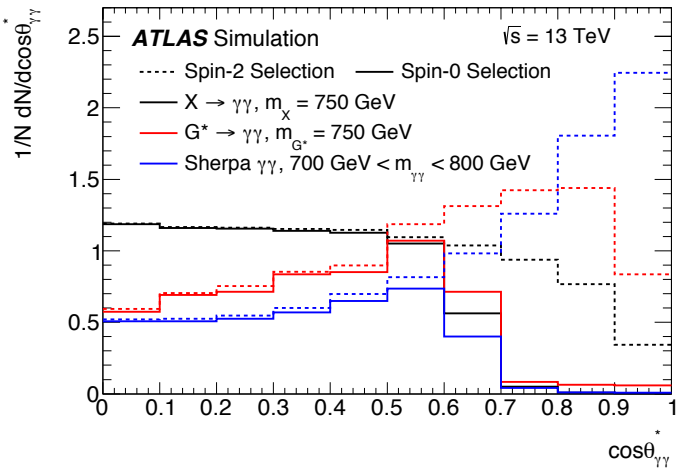

Figure 6.4: Effect of the selection on $\cos\theta^*$ distribution for signal and background samples. For the relative (spin-0) and absolute (spin-2) selection [10].

6.3.3 Kinematic selection

As already said the kinematic selection in the two analyses is different, however in the pre-selection a preliminary absolute cut of 40 GeV and 30 GeV is already applied in both analyses. In the spin-2 selection the transverse energy of each photon is required to satisfy $E_T > 55$ GeV, while in the spin-0 selection a relative selection on the E_T of the two photons is applied. This spin-0 relative selection was optimized using simulated background and signal MC samples. For the evaluation of the sensitivity simulated MC sample of $\gamma\gamma$, γ-jet and jet-jet were used.

Given the isotropic distribution of the decay of a spin-0 particle, the average transverse energy of the two photons is expected to be higher than that of photons from background processes at the same invariant mass. This is why relative cuts are applied for the spin-0 analysis. For a given value of $m_{\gamma\gamma}$, the transverse energy is required to be $E_T > 0.4m_{\gamma\gamma}$ for the leading photon and $E_T > 0.3m_{\gamma\gamma}$ for the subleading photon. This selection improves the expected sensitivity by more than 20% for hypothetical Higgs boson masses larger than 600 GeV with respect to the initial selection (Figure 6.5, left). However if the relative cut selection is applied to a benchmark spin-2 signal no improvement is found (Figure 6.5, right), for this reason an absolute cut was decided for the spin-2 analysis. Relative selection is directly affecting the angular distribution of the selected events, the effect on $\cos\theta^*$ can be seen in Figure 6.4.

The value of 55 GeV for the p_T selection in the spin-2 analysis was chosen to have a less model dependent selection while avoiding distortion on the invariant mass distribution due to a threshold effect with the trigger selection. This was because the requested trigger at the beginning was `2g50_loose` (two `loose` photons with p_T of 50 GeV) since it was supposed to be the lowest unprescaled diphoton trigger for the whole 2016, then it was lately changed to the `g35_g25_loose` trigger.

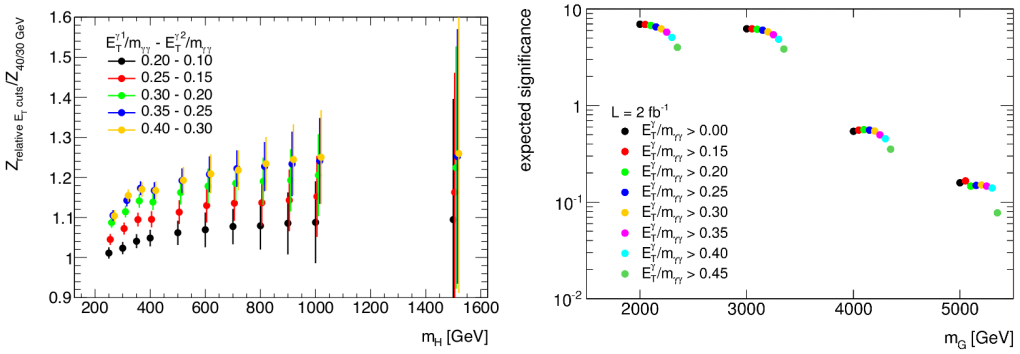

Figure 6.5: Effect of the relative cuts on significance (signal/ $\sqrt{\text{background}}$) for spin-0 signal samples (left) and spin-2 signal samples (right). For a spin-0 signal there is an improvement of 10-20% while for a spin-2 signal no improvement is seen.

6.3.4 Isolation selection

A selection on the isolation variable is crucial in the photon selection for further rejecting the background due to jets faking photons. The isolation, as already introduced in Section 5.6, can be computed in the calorimeter or in the inner detector using tracks. A selection on both types of isolation was used for the two analyses and the values of the cuts were optimized using MC samples of spin-0,2 signal and MC samples of diphoton and photon jet background.

Since the Standard Model background decreases with p_{T}, and since analyses searching new phenomena at high p_{T} need to have a very high efficiency, the isolation cuts need to be loosened with increasing p_{T}. This is particularly true in the case of the calorimeter isolation, where the leakage correction becomes large at high p_{T}: since this is only an averaged correction, and known to not agree well between data and Monte Carlo, the isolation cut needs to be particularly loosened to avoid any unwanted efficiency loss. For these reasons the selection is implemented cutting on the relative isolation, *i.e.* isolation divided by p_{T}.

FixedCutTight and FixedCutTightCaloOnly. The photon isolation working points were optimized for high p_T photons. For the `FixedCutTight` working point a selection is applied both on calorimetric isolation (cone $\Delta R = 0.40$) and on track isolation $\Delta R = 0.20$, while for the `FixedCutTightCaloOnly` a selection is applied only on the calorimetric isolation (cone $\Delta R = 0.40$). The main motivation to use relative cuts is that more rejection is needed at lower p_T, where the rate of background is higher. At high p_T the selection is set to to have an efficiency on signal samples > 98 %.

The selection on calorimetric and track isolation is of the form $< X * p_T + Y$. The values of X and Y where optimized to the values see in Table 6.5 looking at the signal efficiency of Graviton

and Higgs samples in diphoton and the rejection of background modelized using Sherpa diphoton and photon jet samples. The jet-jet background component was considered negligible for these studies. The fraction of diphoton and photon jet used in this study was chosen to emulate Run-I purity before isolation (~70% for $\gamma\gamma$, ~30% for γ-jet).

Studies for the developing of the WPs can be seen in Figure 6.6. The signal efficiency, background efficiency and significance can be seen in Figure 6.7 for spin-2 selection, the Run-I isolation selection (TopoEtcone40 < 7 GeV) is shown as a reference. The same plots for spin-0 selection are in Figure 6.8. The significance was evaluated as signal efficiency on the square root of background efficiency: $s = s_{eff} / \sqrt{b_{eff}}$.

The FixedCutTight working point was chosen for both the spin-0 and spin-2 analyses.

WP	Calo selection	Track selection
FixedCutTight	topoetcone40 < 0.022 * p_T + 2.45 [GeV]	topoetcone20 < 0.05 * p_T
FixedCutTightCaloOnly	topoetcone40 < 0.022 * p_T + 2.45 [GeV]	-

Table 6.5: FixedCutTight and FixedCutTightCaloOnly working points

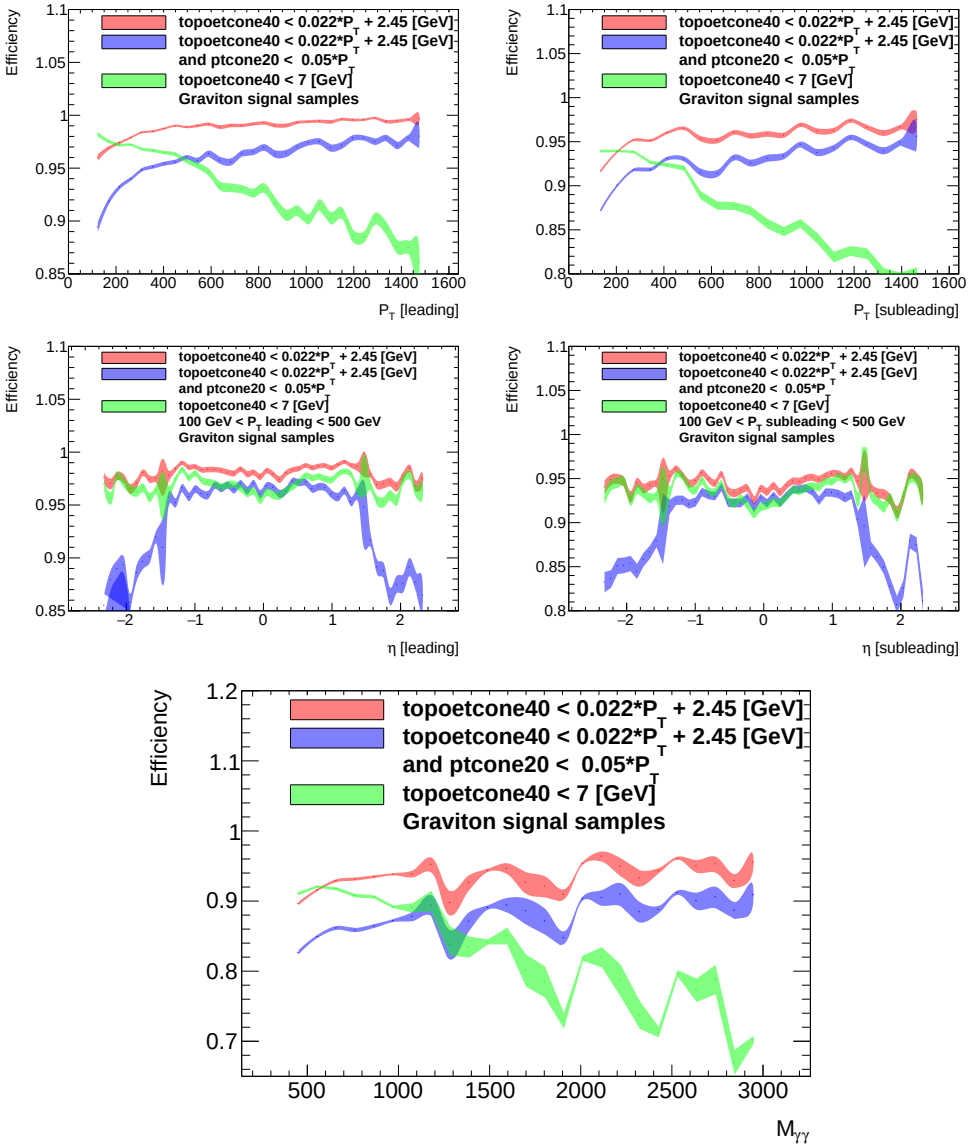

Figure 6.6: Single photon efficiency of isolation selections on top of tight identification as a function of P_T and η of the leading and subleading photon. The selections are the two WP already introduced plus the old graviton selection: fixed cut of 7 GeV. In the lowest plot the selection is applied on both photon and the efficiency is in function of $M_{\gamma\gamma}$.

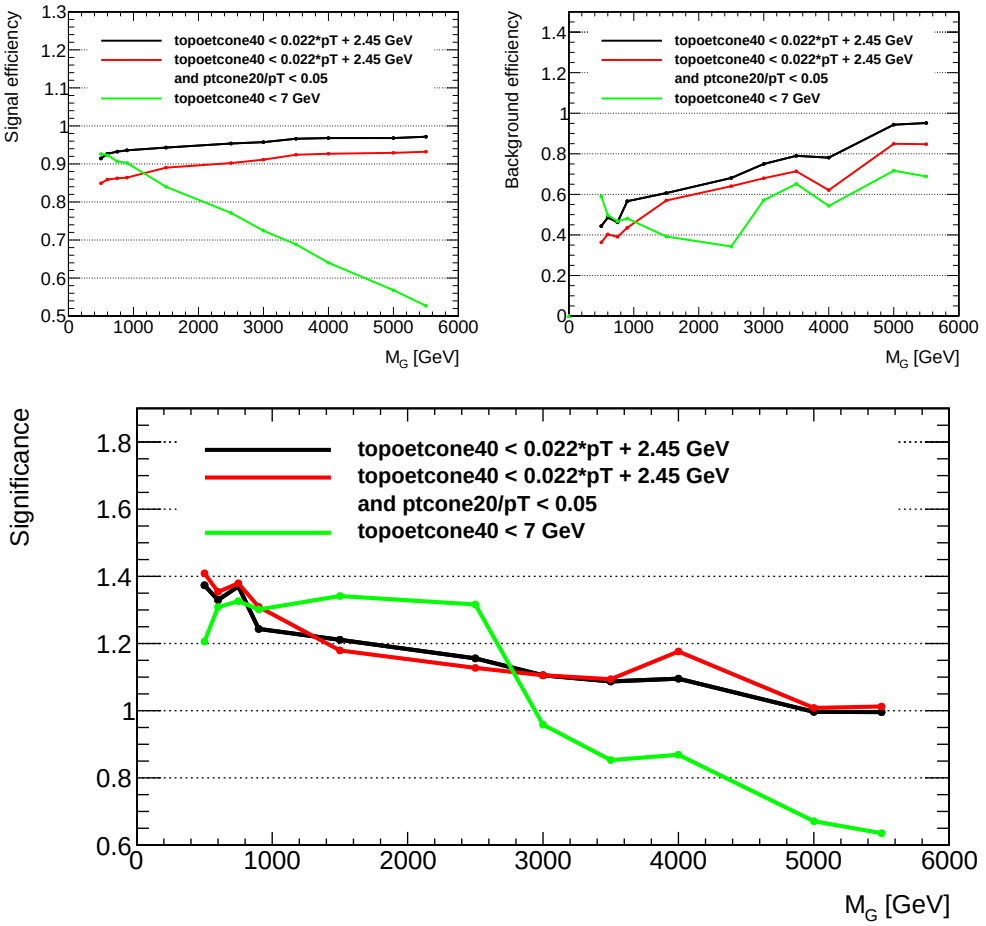

Figure 6.7: Signal efficiency (left), background effiency (right) and significance (bottom) of the isolation cut on top the graviton selection (2 tight photons of $p_T > 55$ GeV) for Graviton samples of several masses. The significance is evaluated as eff(signal)/ $\sqrt{\text{eff(background)}}$ with MC background samples of two photons and photon jet.

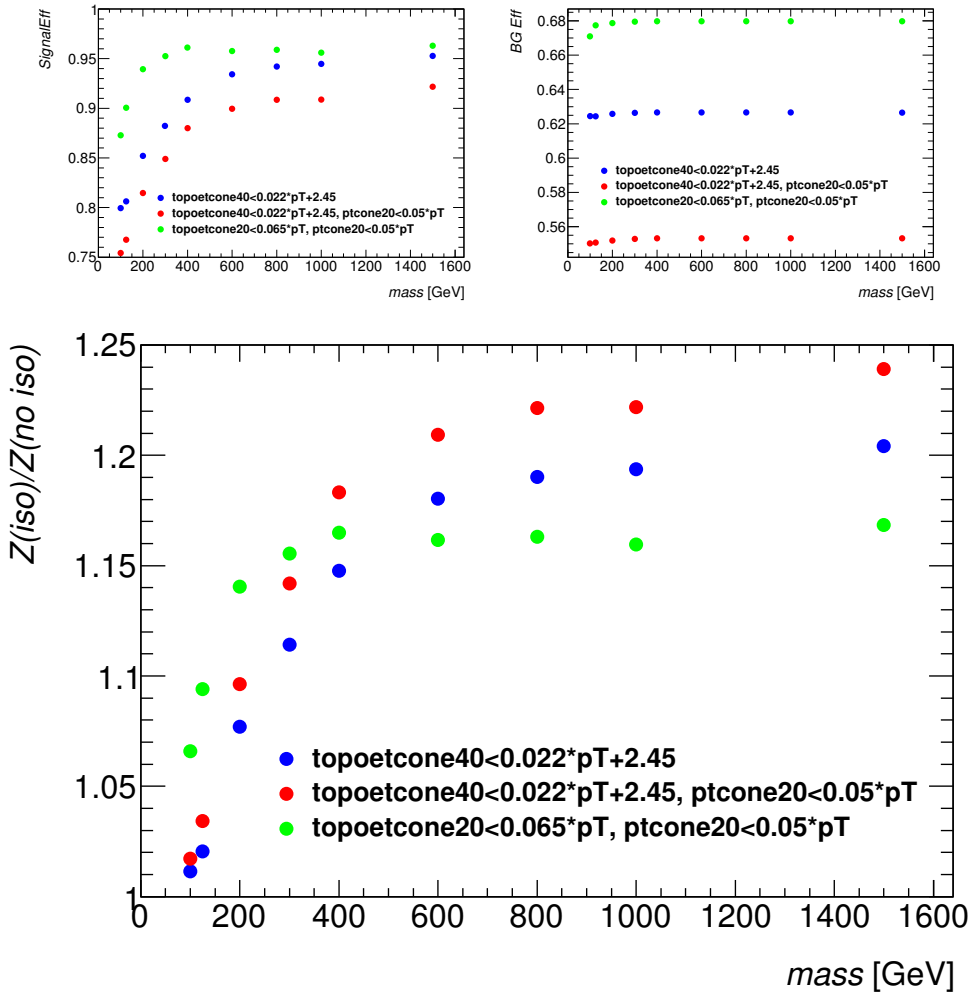

Figure 6.8: Efficiency of isolation selections on top of all the other cuts as a function of $M_{\gamma\gamma}$, for (a) signal samples, (b) background samples, as described in the text. Efficiencies are computed after applying all analysis cuts (2 tight photons with 0.3, 0.2 cuts applyed on $p_T / M_{\gamma\gamma}$) except the isolation cuts themselves. Last plot is the relative improvement on the expected significance as a function of $M_{\gamma\gamma}$.

6.4 Summary of event selection

In this section the complete analysis selection will be introduced, the optimization of the single cuts of the selection were discussed in details in the previous sections.

6.4.1 Analyzed data

Data taken from the ATLAS detector during run-II operations of 2015 and 2016 were analyzed. The total integrated luminosity corresponds to 3.2 fb^{-1} + 33.9 fb^{-1} respectively from 2015 and 2016 data. The following selection is applied on the complete dataset of the two years. The introduced Monte Carlo simulated samples of signal and background were also analyzed in the same way.

The μ distribution in data for the years 2015 and 2016 is shown in Figure 3.2. As can be seen, the number of interactions per bunch crossing is higher in 2016.

6.4.2 Event selection

Only events passing a on-line ATLAS trigger selection are taken into consideration. The trigger used is called `g35_g25_loose`, which requires two photon passing loose identification with E_{T} at trigger level (calibrated with an older version of the MVA-calibration than the reconstruction level one without the crack calibration and α_i corrections) of at least 35 GeV (leading) and 25 GeV (sub-leading). This trigger was run unprescaled in the whole dataset, and has a signal efficiency larger than $99.9\%^{+0.027}_{-0.26}\text{stat} \pm 0.05\text{syst}$ for events fulfilling the two analyses. This first selection is made on-line during data taking.

On the events passing the trigger selection an additional pre-selection that requires calibrated E_{T} (with MVA methods as explained in section 5.5.3) above 40 GeV and 30 GeV and the `loose` identification criteria of the ATLAS photon ID explained in section 5.4.4 is applied. Furthermore an angular selection is applied to both photon: $|\eta_\gamma| < 2.37$, also photons in the crack region between EM calorimeter barrel and end-cap defined as $1.37 < |\eta_\gamma| < 1.52$ are removed. The photons passing the pre-selection are then ordered as a function of p_{T} and the two most energetic photons are taken into consideration. These two photons will be referred as the leading (most energetic) photon and subleading (second most energetic) photon.

After the pre-selection on both photons the `tight` identification criteria is applied (explained in section 5.4.4). Then the primary vertex corresponding to the pp collision that produced the diphoton candidate is identified as explained in section 6.4.3. The primary vertex position influences the direction (η, ϕ) of the two photons and the invariant mass calculation. In addition, the calorimeter-based and track-based isolation requirements are applied to further reduce the background from jets misidentified as photons, thus increasing the expected sensitivity of the analyses. The isolation selection applied is the FixedCutTight working point explained in section 6.3.4.

Different additional selections are then applied for the spin-2 and spin-0 resonance searches. In the spin-2 selection the transverse energy of each photon is required to satisfy $E_{\text{T}} > 55$ GeV. While in spin-0 selection the transverse energy is required to be $E_{\text{T}} > 0.4 m_{\gamma\gamma}$ for the leading photon and

Selection	$M_{\gamma\gamma}$ cut	3.2 fb^{-1} of data 2015	33.9 fb^{-1} of data 2016
Spin-0	$M_{\gamma\gamma} > 180$ GeV	2992	29430
Spin-2	$M_{\gamma\gamma} > 200$ GeV	5327	52030

Table 6.6: Number of selected events in years 2015 and 2016 for spin-0 and spin-2 selections.

$E_{\mathrm{T}} > 0.3 m_{\gamma\gamma}$ for the subleading photon. The optimization of the kinematic cut is explained in section 6.3.3.

Invariant mass of the selected events for 38 fb^{-1} of data 2015 and 2016 can be seen in Figure 6.9 The efficiency of the selection goes from 50% to 65% for spin-2 selection on a spin-2 MC signal as seen in Figure 6.14 and from 25% to 45% for spin-0 selection on a spin-0 MC signal. The number of selected events in years 2015 and 2016 for both selections can be found in Table 6.6. Kinematic variables distributions of the spin-0 and spin-2 signals after the respective selections can be found in Figure 6.10 and Figure 6.11.

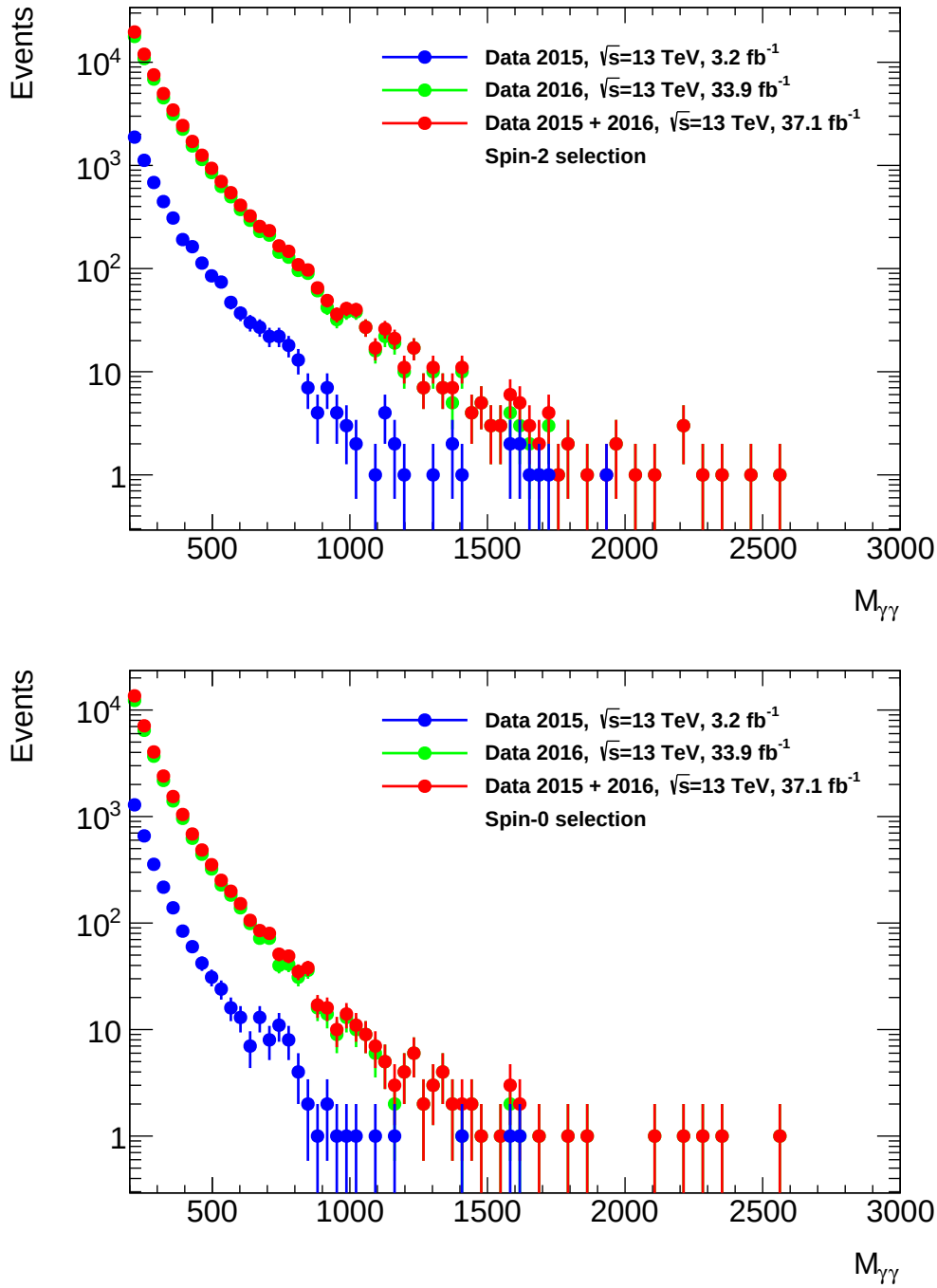

Figure 6.9: Invariant mass distribution for the spin-2 (top) and spin-0 (bottom) selections for data 2015 (3.2 fb^{-1}), 2016 (33.9 fb^{-1}) and combined (37.1 fb^{-1}).

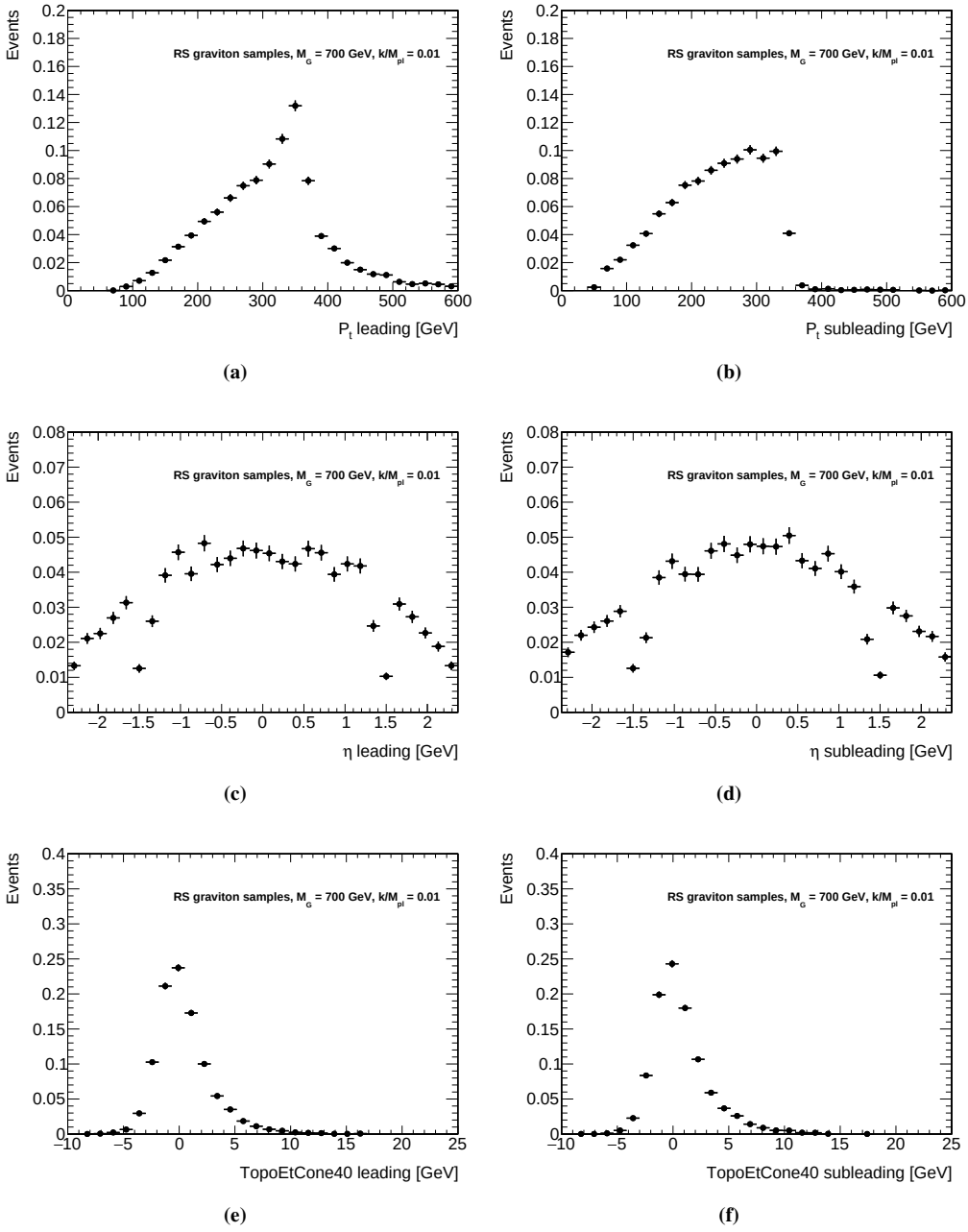

Figure 6.10: Kinematic variables for a spin-2 signal simulation Monte Carlo sample. The spin-2 selection is applied.

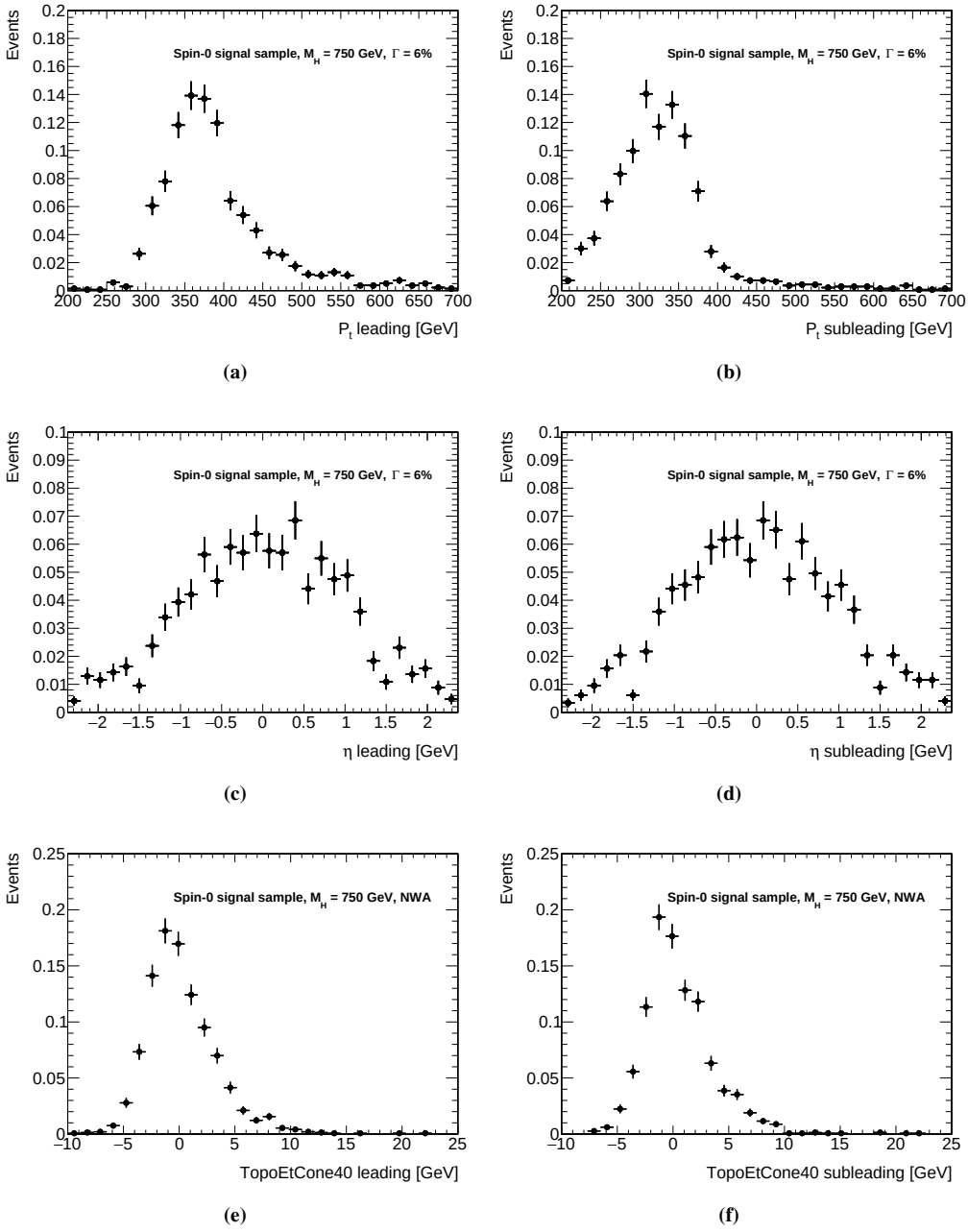

Figure 6.11: Kinematic variables for a spin-0 signal simulation Monte Carlo sample. The spin-0 selection is applied.

6.4.3 Primary vertex definition

The primary interaction point is an input to calculate the photon direction and the diphoton invariant mass. Discriminating against additional interactions occurring in the same bunch crossing (in-time pileup) is a requirement when applying track isolation criteria and jet-to-vertex tagging algorithms.

An algorithm that combines information from the longitudinal segmentation of the calorimeter ("pointing"), tracks from photon conversions and the ones used in the primary vertex reconstruction has been developed for LHC Run-I results [118] and adapted for Run-II. Artificial neural networks were trained in simulated samples of $gg \to H \to \gamma\gamma$ to separate the reconstructed primary vertices within 0.3 mm from the true interaction point from pileup vertices (beyond 2 mm) using the following inputs:

- $(z_{\text{common}} - z_{\text{vertex}})/\sigma_z$ where z_{vertex} is the position of the primary vertex, z_{common} is the weighted mean of the intersections of the extrapolated photon trajectories given by the calorimeter "pointing" with a constraint from the beam spot position; σ_z is the associated error.
- $\sum p_{\text{T}}$and $\sum p_{\text{T}}^2$, the scalar sum of p_{T} and p_{T}^2 of the tracks associated to the vertex
- $\Delta\phi(\gamma\gamma, \text{vertex})$: the azimuthal angle between the diphoton system and system defined by the vector sum of the tracks associated to the vertex.

The selected vertex in each event is the one that maximises the output value of the discriminants. The efficiency for selecting the correct vertex in graviton samples with $k/\overline{M}_{\text{Pl}} = 0.1$ varies typically between 70% and 100% depending on the number of primary vertices in the event, as shown in Fig. 6.12b. Without applying any weights to correct for the beam spread ("z-vertex") or the pileup distributions in data, the overall efficiency is about 90% for a benchmark RS graviton signal with mass of $m_{G^*} = 2$ TeV and 80% for $m_{G^*} = 4$ TeV.

As a result, the invariant mass resolution is improved with respect to the hardest vertex in the event (Fig. 6.12c). Using the interquartile range as estimator for the resolution, the improvement with respect to using the nominal primary vertex is about 7%, and only within 1% of the result obtained using the true production point. For smaller values of $k/\overline{M}_{\text{Pl}}$, one expects larger improvements due to the decrease of the natural width of the resonance.

6.5 Signal efficiency and cross-section

The expected number of signal events, also called signal yield, is the product of three terms: the cross section of the production process times branching ratio to two photons, the efficiency of the selection cuts (kinematic selection, reconstruction and identification) and, in the spin-0 analysis, the acceptance of the kinematic requirements (in E_{T}, η and truth-level isolation). The acceptance is calculated as the fraction of decays satisfying the fiducial acceptance at the generator level.

To make the spin-0 analysis independent from the production process of the scalar resonance, the measured signal is interpreted as a fiducial cross-section measured within a fiducial volume

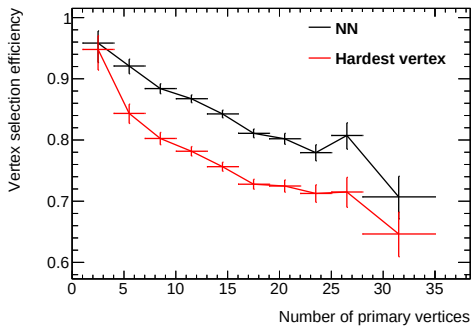

(a)

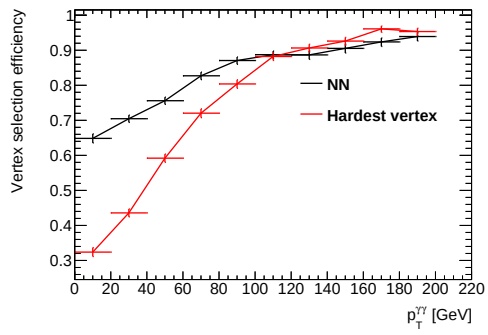

(b)

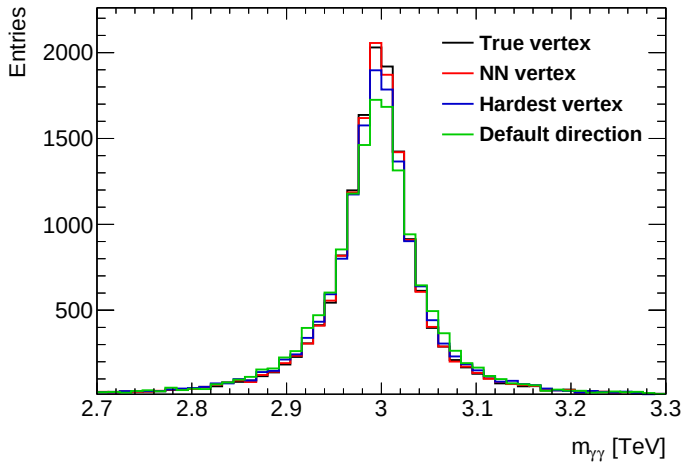

(c)

Figure 6.12: Efficiency for selecting the correct vertex within 0.3 mm using the hardest vertex in the event or the NN algorithm as a function of the number of reconstructed primary vertexes (a) and as a function of $P_T^{\gamma\gamma}$ (b). (c) Diphoton invariant mass spectrum using different primary vertex choices for $m_{G^*} = 3$ TeV and $k/\overline{M}_{\rm Pl} = 0.1$.

chosen to minimize the model-dependence of the result. To do so a C_X correction factor defined in the following section is applied to the production cross section.

While the spin-2 analysis is performed in the context of a single model, so a simple cross-section for to the total RS graviton production is corrected by the total efficiency of the analysis.

6.5.1 Spin-0 C_X factors

To extract the fiducial cross-section the number of fitted signal events in data must be corrected for detector effects: reconstruction, identification and selection efficiencies. The correction factor is defined as:

$$C_X = \frac{N_{\text{selection}}}{N_{\text{fiducial}}}, \tag{6.4}$$

where $N_{\text{selection}}$ is the number of reconstructed signal events passing all the analysis cuts, and N_{fiducial} is the number of truth signal events generated within the fiducial volume explained in the following (both numbers are evaluated with signal MC samples).

In order to minimize the model-dependence of the result, the fiducial acceptance defined at truth level must closely match the experimental acceptance of the measurement. The fiducial volume is therefore defined by kinematic cuts applied on the truth photon variables so as to mimic the ones used at the reconstruction level. Acceptance cuts are applied at MC generation level on E_{T}, η and on the particle level isolation of the photons[1]. The definition of the fiducial volume was studied using Higgs boson Monte Carlo samples from different production modes (ttH, VBF, WH, ZH and ggF). The truth level calorimeter isolation cut applied at the generator level of the Monte Carlo sample is truth-topoetcone40 < 0.05 * p_T + 2.45 [GeV].

The C_X factor is computed with MC samples at several M_X from Eq. 6.4, applying the analysis cuts to obtain the numerator and the fiducial cuts to obtain the denominator. Because the results must be provided in finer mass steps than provided by the MC samples, an interpolation between these points is necessary. The mass-dependence is fitted using the functional form $C_X(M_X) = a_0 + a_1 \exp(a_2 M_X)$. The results are illustrated in Fig. 6.13.

The identification/isolation efficiency ranges from 52% to 62% in the mass range from 200 GeV to 700 GeV for a Higgs boson produced by gluon fusion and is almost constant above 700 GeV. The gluon fusion production mode is used to compute the value of the kinematic selection efficiency, which ranges from 65% for a particle of mass 200 GeV to 71% at 700 GeV (almost constant above 700 GeV). After the truth level fiducial volume selection different Higgs boson production modes yield differences in selection efficiency values of at most ±3%, which is taken as an uncertainty. In the case of a decay width larger than the detector resolution, the correction factor for kinematic selection efficiency varies by up to ±5% depending on the assumed decay width, this variation is taken as an additional uncertainty.

[1] The particle isolation is defined as the transverse energy of the vector sum of all stable particles (except muons and neutrinos) found within the $\Delta R = 0.4$ cone around the photon.

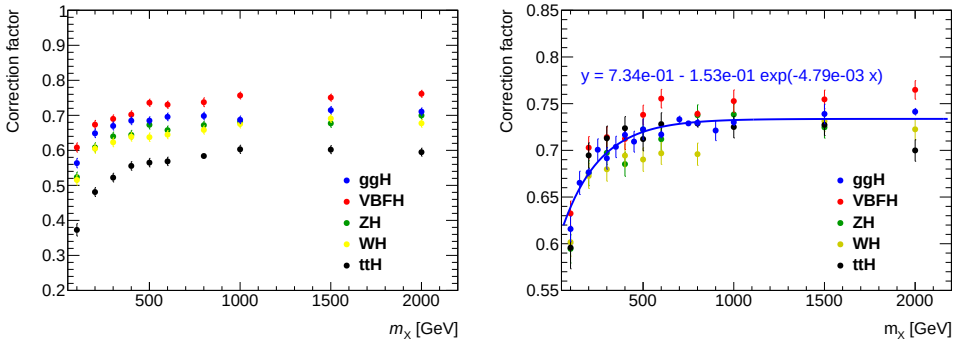

Figure 6.13: C_X factors computed for five different Higgs production modes, as a function of m_X. On the left plots (a), the fiducial volume is defined using all selection criteria except the particle-level isolation. On the right plot (b), a p_T-dependent isolation cut is also applied at the particle level.

6.5.2 Spin-2 efficiency factors

For the spin-2 resonance search, the efficiency for the benchmark RS graviton model can be simply defined as:

$$\epsilon_{ff,G} = \frac{N_{\text{passing}}}{N_{\text{total}}} \tag{6.5}$$

where N_{total} is the total number of events corresponding to given values of m_{G^*} and $k/\overline{M}_{\text{Pl}}$, and N_{passing} counts those events among N_{total} producing a photon pair that gets reconstructed and passes all selections. The acceptance varies from 66% at a mass of 500 GeV, to 91% at a mass of 5000 GeV. The identification/isolation efficiency is almost constant at 68% in this mass range. The total efficiency of the selection thus ranges from 50% to 65% for masses between 500 GeV and 5000 GeV with a small dependence on the width (Figure 6.14). To obtain a smooth parameterization from the single point measured by the MC the efficiency corrections are fitted with a single functional form of the kind: $\epsilon_{ff,G}(M_G) = a_1 - a_2 e^{-b_1 M_G} - a_3 e^{-b_2 M_G}$.

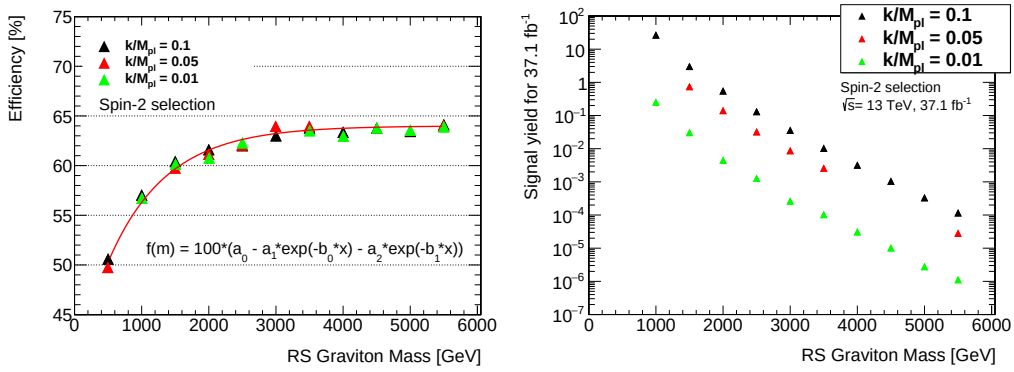

(a) **(b)**

Figure 6.14: Left: efficiency in % of the spin-2 selection for spin-2 signals MC samples at different mass of the graviton and different couplings. Right: Expected signal yield (using Sherpa LO cross-section) for 36.1 fb^{-1} (corresponding to data 2015 and 2016) for spin-2 signal for different $k/\overline{M}_{\mathrm{Pl}}$ (widths).

6.6 Composition of the selected sample

The selected events mainly come from diphoton production (around 90%), followed by photon+jet production, with one jet misidentified as a photon, and dijet production with two jets misidentified as photons. Events coming from from Drell–Yan, $W\gamma$ or $Z\gamma$ production, with either one or two isolated electrons misidentified as photons, are negligible.

A precise estimate of the background composition is required for the background estimation in the spin-2 resonance search. It is also used in the studies for the choice of background function in the spin-0 resonance search. Two methods are used to estimate the relative contribution of the various sources of background directly from data, these methods are based on control regions built from events failing the isolation requirement and/or some of the tight photon identification requirements.

2×2 sidebands method. In the first method, which is the 2×2 sidebands method, four regions for each photon candidate are constructed. The first region, where candidates pass isolation and identification requirements, corresponds to the signal region. The other regions correspond to candidates failing the isolation requirement only, failing part of the tight identification requirement only or failing both. The method allows the simultaneous extraction of the numbers of genuine diphoton events, photon+jet, jet+photon and dijet background events. Furthermore the efficiencies of the tight identification and isolation requirements for photon candidates from misidentified jets are calculated. A detailed explanation of this method can be found in Ref. [119].

Matrix method. The second method, called the matrix method, classifies the diphoton candidates passing tight identification requirements into four categories depending on whether both, only the

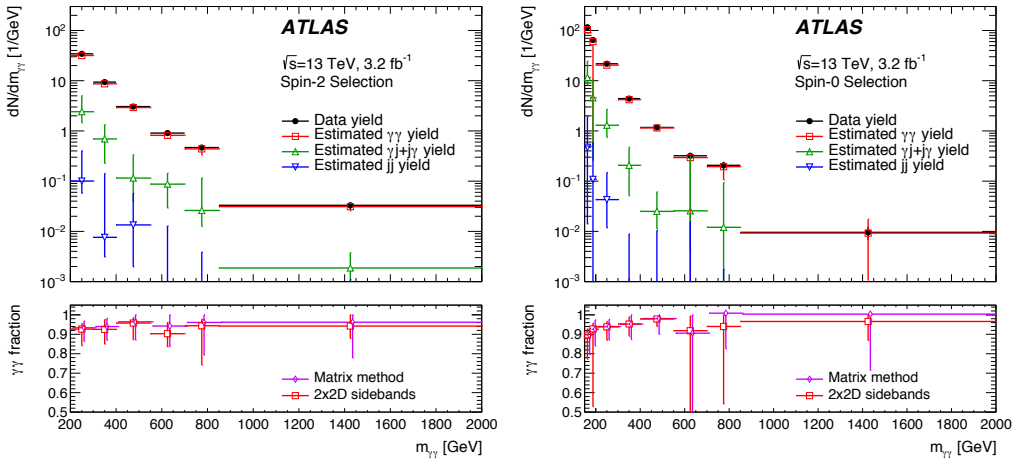

Figure 6.15: The diphoton invariant mass distributions (upper panels) of the data for the spin-2 and spin-0 selections and their decomposition into contributions from genuine diphoton, photon+jet plus jet+photon and jet+jet events, determined as described in the text. The bottom panels show the purity of diphoton events as determined from the two methods. The total uncertainties are shown, including statistical and systematic components [10].

leading, only the sub-leading or none of the photons pass the isolation selection. The numbers of observed events in data in these categories are related to the numbers of genuine diphoton, photon+jet, jet+photon and dijet events. However the number of events has to be re-scaled through isolation efficiencies for signal and background. The efficiency for background is estimated in control regions of the data, using events failing a subset of the tight identification requirements. A detailed explanation of this method can be found in Ref. [120].

Systematic uncertainties. The main systematic effect on the purity estimation in both methods comes from the definition of the identification control regions. To evaluate the systematic uncertainty the anti-tight control region was modified relaxing the tight identification, this was done removing some of the shower shape cuts. The modified control regions are made with LoosePrime2, LoosePrime3, LoosePrime4, LoosePrime5 where LoosePrimeX means X cuts removed from the identification requirements, for further explanation on LoosePrime see Section 8.1. The variation of the purity using the loosePrime control region is taken as systematic variation.

Then an uncertainty was evaluated on the isolation, both changing the isolation control region definition and taking into account the isolation variable difference between data and MC simulation. Furthermore the uncertainty on the photon identification efficiency is taken into account. An uncertainty was also associated on the MC generator, using the Pythia generator instead of Sherpa and taking the difference as systematic uncertainty. The estimate of these uncertainties is sensitive

to the small number of events in some of the control regions.

Purity estimation. The purity is defined in both selections as the ratio of diphoton events to the total number of events in the sample. Both methods can either be applied over the full selected kinematic range, or in bins of $m_{\gamma\gamma}$. In this way inclusive as well as differential yields can be provided. The two cited method are applied and Figure 6.15 shows the decomposition of the selected data sample into the contributions from diphoton, photon+jet or jet+photon, and dijet events for both selections and the corresponding purities. The purity is $(94^{+3}_{-7})\%$ for the spin-2 selection and $(93^{+3}_{-8})\%$ for the spin-0 selection. The two methods give consistent results within their uncertainties. The purity observed in data 2016 is compatible with the one showed for data 2015.

6.7 Analysis strategy

In this section a brief overview of the signal and background modeling techniques used in the analysis can be found. Furthermore a brief introduction to the statistic tools will be given. A more detailed explanation of these topics can be found in the next chapters.

6.7.1 Signal modeling overview

The signal distribution is expected to peak near the assumed mass of the new particle, with an observed width that is the convolution of its intrinsic decay width with the experimental resolution. For both the spin-0 and spin-2, the experimental resolution of the invariant mass is modelled with a double-sided Crystal Ball (DSCB) function. Interference effects between signal and background are ignored. The diphoton invariant mass resolution for a narrow resonance, as measured by the σ_{CB} parameter, varies from about 2 GeV at a mass of 200 GeV to about 13 GeV at a mass of 2000 GeV.

For samples with small decay width, the σ_{CB} of the DSCB Gaussian core parameterizes the entire effect of the experimental invariant mass resolution. While the signal mass distribution for any value of the mass and large width is obtained in both analyses by a convolution of the intrinsic detector resolution, modelled by a DSCB function, with the predicted distribution of the mass line-shape at generator level.

6.7.2 Background modeling overview

To estimate the SM background contribution in the $m_{\gamma\gamma}$spectrum two different methods are used in the spin-0 and spin-2 analysis. The first approach is based on using a smooth functional form, with fully data-driven parameters to model the total background. In this approach, used for the spin-0 resonance search, the mass distribution from data is fitted in the range above 150 GeV and the search range for the signal is 200–2500 GeV, in which there are enough data events. To choose the appropriate functional form a spurious signal test was conducted on a family of function, then

the need for additional degrees of freedom is tested with an F-test on data. The spurious signal is the small bias on the number of fitted signal events introduced by the studied function.

The spin-2 search aims to reach masses up to 5000 GeV and the small number of data events at high masses is not sufficient to well constrain a functional form fit. The shape of the invariant mass distribution of the main SM diphoton background is thus predicted using the next-to-leading (NLO) order in QCD DIPHOX [121] computation. Then the background from photon+jet and dijet production is evaluated using control samples from the data. To get the complete background model the components are summed with fractions calculated with a data-driven estimation.

6.7.3 Statistic strategy

The signal plus background model is fitted with maximum-likelihood fits on the $m_{\gamma\gamma}$ distribution of the selected events, for (m_X, $k/\overline{M}_{\rm Pl}$) hypotheses where a spin-2 resonance from the benchmark RS model is probed, or for (m_X, α) hypotheses where the presence of a spin-0 resonance of mass m_X and width $\Gamma = \alpha \cdot m_X$ is probed. Each fit allows for a single signal component. The function used to describe the data can be written as

$$N_{\rm S} f_{\rm S}(m_{\gamma\gamma}) + N_{\rm B} f_{\rm B}(m_{\gamma\gamma}), \tag{6.6}$$

where $N_{\rm S}$ is the fitted number of signal events, $f_{\rm S}(m_{\gamma\gamma})$ is the normalized invariant mass distribution for a given signal hypothesis, $N_{\rm B}$ is the fitted number of background events and $f_{\rm B}(m_{\gamma\gamma})$ is the normalized invariant mass distribution of the background events. Uncertainties in the signal parameterization, the acceptance and detector efficiency correction factors for the signal and in the description of the background shape are included in the fit via nuisance parameters.

The local p-value (p_0) for the compatibility with the background-only hypothesis when testing a given signal hypothesis (m_X, α) is based on scanning the $q_0(m_X, \alpha)$ test statistic as explained in Appendix A.

Global significance values are computed to account for the look-elsewhere effect. The methods used to produce the results in this thesis is based on a large number of pseudo-experiments. Also a second method, used as cross-check, is based on the techniques described in Refs. [122–124].

The expected and observed 95% confidence level (CL) exclusion limits are computed using a modified frequentist approach CL_s with the asymptotic approximation as explained in Appendix A.

CHAPTER 7

Signal model

In this chapter the signal modeling technique adopted in both the spin-0 and the spin-2 analyses will be presented. In both analyses, the signal is described using the numerical convolution of two analytical shapes:

- A double-sided Crystal Ball function (DSCB) that parameterizes the response function of the detector.
- A true lineshape of the resonance that is parameterized as the product of a Breit-Wigner (BW) distribution, a mass-dependent factor accounting for the parton luminosity and the matrix elements for the $gg \to \gamma\gamma$ process.

The resolution function has to be parameterized as a function of the mass of the hypothetical signal using narrow width MC samples. The intrinsic width (either $k/\overline{M}_{\mathrm{Pl}}$ for spin-2 or α for spin-0) dependence is obtained through the convolution with the true lineshape.

7.1 Resolution function

The reconstructed invariant mass $m_{\gamma\gamma}$ distribution of a resonant signal could be asymmetric even for a narrow signal (i.e. with intrinsic width smaller than the detector resolution), because of photon energy resolution effects. The functional form used to describe it is the double-sided Crystal Ball function (DSCB), which consists of a Gaussian core extended by power-law tails above and below the peak. More precisely it is defined by the expression

$$N \cdot \begin{cases} e^{-t^2/2} & \text{if } -\alpha_{\mathrm{low}} \le t \le \alpha_{\mathrm{high}} \\ \dfrac{e^{-0.5\alpha_{\mathrm{low}}^2}}{\left[\frac{\alpha_{\mathrm{low}}}{n_{\mathrm{low}}}\left(\frac{n_{\mathrm{low}}}{\alpha_{\mathrm{low}}} - \alpha_{\mathrm{low}} - t\right)\right]^{n_{\mathrm{low}}}} & \text{if } t < -\alpha_{\mathrm{low}} \\ \dfrac{e^{-0.5\alpha_{\mathrm{high}}^2}}{\left[\frac{\alpha_{\mathrm{high}}}{n_{\mathrm{high}}}\left(\frac{n_{\mathrm{high}}}{\alpha_{\mathrm{high}}} - \alpha_{\mathrm{high}} + t\right)\right]^{n_{\mathrm{high}}}} & \text{if } t > \alpha_{\mathrm{high}}, \end{cases} \tag{7.1}$$

where $t = (m_{\gamma\gamma} - \mu_{CB})/\sigma_{CB}$ with μ_{CB} the peak of the Gaussian distribution and σ_{CB} the width of the Gaussian part of the function; N is a normalization parameter; α_{low} (α_{high}) is the position of the junction between the Gaussian and power law on the low (high) mass side in units of t; and

n_{low} (n_{high}) is the exponent of this power law. The parameter $\Delta M_X = \mu_{CB} - M_X$ (where M_X is the mass of the hypothetical expected signal) is defined as the difference between the peak of the Gaussian and the reference mass value. An illustrative drawing of the double-sided Crystal Ball function is provided in Figure 7.1.

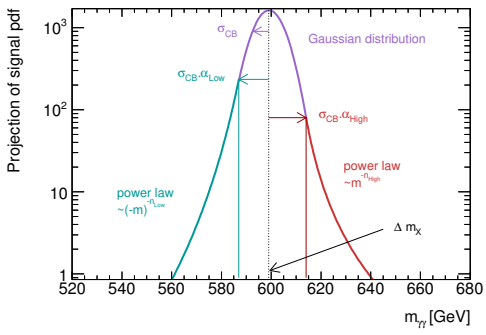

Figure 7.1: Description of the double-sided Crystal Ball function parameters, for a signal mass $m_X = 600$ GeV. μ_{CB} is the peak of the Gaussian distribution and σ_{CB} represents the width of the Gaussian part of the function; α_{low} (α_{high}) is the position of the junction between the Gaussian and power law on the low (high) mass side in units of t; and n_{low} (n_{high}) is the exponent of this power law. $\Delta M_X = \mu_{CB} - M_X$ (where M_X is the mass of the hypothetical expected signal) is defined as the difference between the peak of the Gaussian and the reference mass value.

The parameterization of the DSCB has to cover wide ranges of expected signal masses, to do so the DSCB parameters are expressed as analytical functions of M_X. The parameterization is determined in two steps. The DSCB shape is first fitted to signal distributions for each hypothetical mass of the expected signal. Analytical functions are then chosen to describe the evolution of these DSCB parameters with M_X. The functional forms used are either linear or quadratic functions of M_X. Afterwards a complete model that is depending on M_X is initialized with the fitted values. The model is then used to obtain the actual values of the coefficients from a simultaneous multi-dimensional fit to signal samples at several M_X.

The resolution function is the same in the two analyses and it is fitted on the small width MC signal samples (listed in Section 6.2.1.1.). For the spin-0 analysis, the NW ggF signal samples at M_X= 200, 400, 700, 750, 800, 1000, 1200, 1600, 2000 and 2400 GeV are used. While for the spin-2 analysis, the $k/\overline{M}_{\text{Pl}}$= 0.01 samples at m_{G^*}= 500-5000 GeV (with 50 GeV between 500 GeV and 1000 GeV and 500 GeV step between 1000 GeV and 5000 GeV) are used.

7.2 Spin-0 model

The scalar signal is parameterized as a function of both the mass M_X of the resonance and its relative width $\alpha_X = \Gamma / M_X$. In case of narrow width (NW) parameterization the line-shapes are directly described by DSCB functions. While the chosen approach to describe the large width (LW) shape is to built a model by convolving the resolution function described in the previous Section with the lineshape of the studied resonance. In this model the parameters have values that are functions of both M_X and width.

The truth lineshape is taken from the `Madgraph` 5 next-to leading orded generator. The

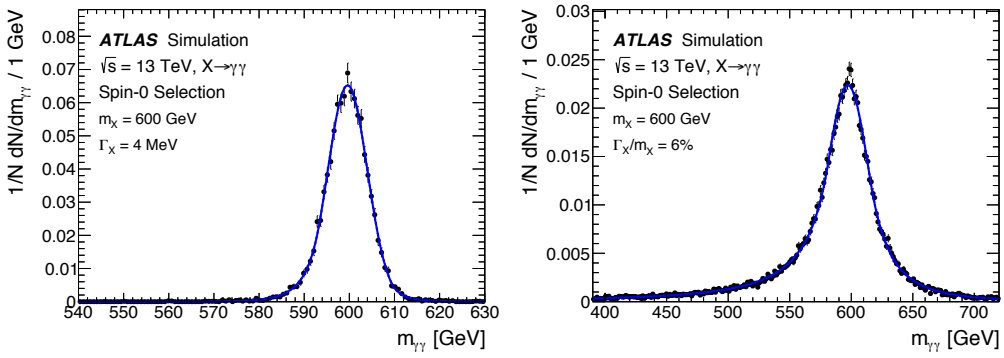

(a) (b)

Figure 7.2: The $m_{\gamma\gamma}$ distributions for different signal hypotheses for a scalar resonance with a mass of 600 GeV and (a) a narrow decay width and (b) with $\Gamma/m = 0.06$. The resolution DSCB fit is superimposed in (a), while in (b) the convolution of the truth lineshape with the DSCB resolution fit is shown [10].

`Madgraph` generated lineshape was found to be well-modelled by the following formula:

$$\frac{d\sigma_{EFT}}{dm_{\gamma\gamma}} \propto \mathcal{L}_{gg}.BW.m_{\gamma\gamma}^{7}. \tag{7.2}$$

where $\mathcal{L}_{gg}$ is the gluon luminosity, $m_{\gamma\gamma}$ is the diphoton invariant mass, and BW is a modified Breit-Wigner distribution (assumed by `PowHeg` to model off-shell behavior):

$$BW \equiv \frac{1}{\pi} \frac{\hat{s}\Gamma_X/M_X}{(\hat{s} - M_X^2)^2 + (\hat{s}\Gamma_X/M_X)^2}, \tag{7.3}$$

The convolution itself is implemented in RooFit exploiting the fast Fourier transform. The parameterized shape is compared with MC samples in Figure 7.2 for the scalar hypothesis, showing reasonable agreement. Parameters as a function of m_X can be see in Figure 7.3.

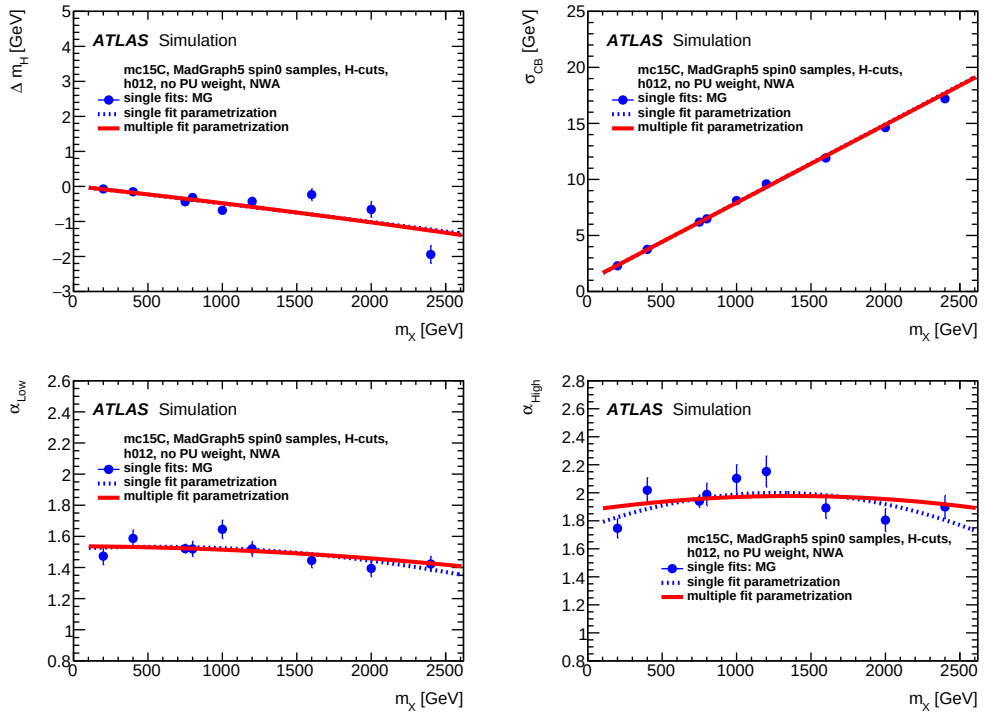

Figure 7.3: Comparison of the multiple mass fit parameterization (red line) to the output parameters of the single mass point fits (blue points) and to the parameterization of the single mass point fit parameters (blue dashed line) for the scalar model. The parameters are given as a function of m_X for the gluon gluon fusion simulation samples: $\Delta m_X = \mu_{CB} - m_X$ (top left), σ_{CB} (top right), α_{low} (bottom left), α_{high} (bottom right). For Δm_X few points deviate from the fit but that has no effect [10].

7.3 Spin-2 model

The search for a RS graviton resonances is performed for resonance masses 500 GeV $< m_{G^*} <$ 3.5 TeV. The width of the resonance is given by the $k/\overline{M}_{\rm Pl}$ parameter, for which the range $0.01 < k/\overline{M}_{\rm Pl} < 0.3$ is considered, since for higher and lower values of $k/\overline{M}_{\rm Pl}$ the model in consideration becomes unphysical. Signal parameterizations are determined as a function of both M_G and $k/\overline{M}_{\rm Pl}$. For large values of $k/\overline{M}_{\rm Pl}$ the graviton line-shape exhibits a relative large high-mass tail (see Figure 7.4), due to the strong m_{G^*}-dependence of all partial widths, and an overall factor of s^2 in the expression for the production cross section [125].

Following the approach used to model the scalar line shape for large width, the graviton theoretical line-shape corresponding to $k/\overline{M}_{\rm Pl}$ is expressed by the product of a Breit-Wigner term with mass m_G and width $\Gamma_{G^*} = 1.44 \cdot (k/\overline{M}_{\rm Pl})^2 M_X$, a parton luminosity term and a term corresponding to the squared matrix element of the production process. In order to calculate the theoretical graviton line-shape, the product of the parton luminosity and squared matrix element terms is obtained from the graviton MC sample by removing the Breit-Wigner term, and parameterized as a 6-order polynomial function as done when generating the graviton flat sample discussed in Section 6.2.1.2. Figure 7.4 shows the parameterization of the product of the parton luminosy and squared matrix element terms as a function of $m_{\gamma\gamma}$ as obtained from Pythia, as well as a few examples of the predicted theoretical lineshapes for various values of m_{G^*} and $k/\overline{M}_{\rm Pl}$.

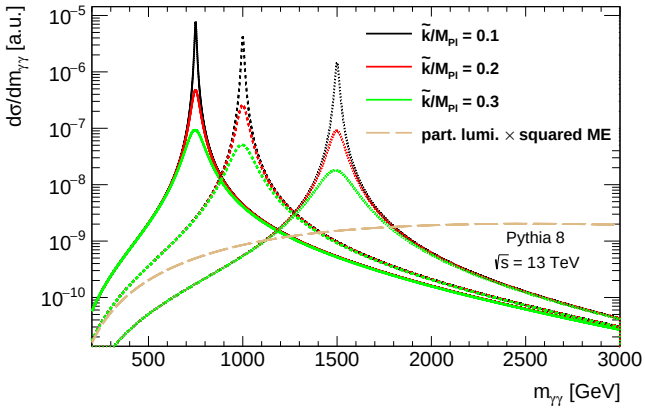

Figure 7.4: Examples of the theoretical RS graviton line-shapes as predicted by Pythia for various values of m_{G^*} and $k/\overline{M}_{\rm Pl}$, and the corresponding parameterization of the product of the parton luminosity and squared matrix element terms once the Breit-Wigner term has been removed.

The effects of the experimental selections and detector response are parameterized from DSCB fits of narrow graviton MC samples ($k/\overline{M}_{\rm Pl}$=0.01, or $\Gamma_{G^*}/m_{G^*} = 1.44 \cdot 10^{-4}$). The DSCB $n_{\rm low}$ and $n_{\rm high}$ parameters are respectively fixed to 6 and 3. The other parameters μ_{CB}, σ_{CB}, $\alpha_{\rm low}$ and $\alpha_{\rm high}$ are parameterized as second order polynomials of the graviton truth mass m_{G^*}. The parameters of these second order polynomials are fitted with the values from the individual fits.

In order to obtain the complete graviton signal lineshape at the detector level after all analysis selections for given m_{G^*} and $k/\overline{M}_{\rm Pl}$ values, the NW graviton signal shape parameterised by the DSCB discussed above are numerically convoluted using a Fast Fourier Transform with the product of the theoretical BW(m_{G^*},$k/\overline{M}_{\rm Pl}$) lineshape term with the parton luminosity and squared matrix

element. The parameterized graviton shape is compared with MC samples at several masses and widths, showing reasonable agreement. An example is shown in Figure 7.6. Parameters as a function of m_G can be see in Figure 7.5.

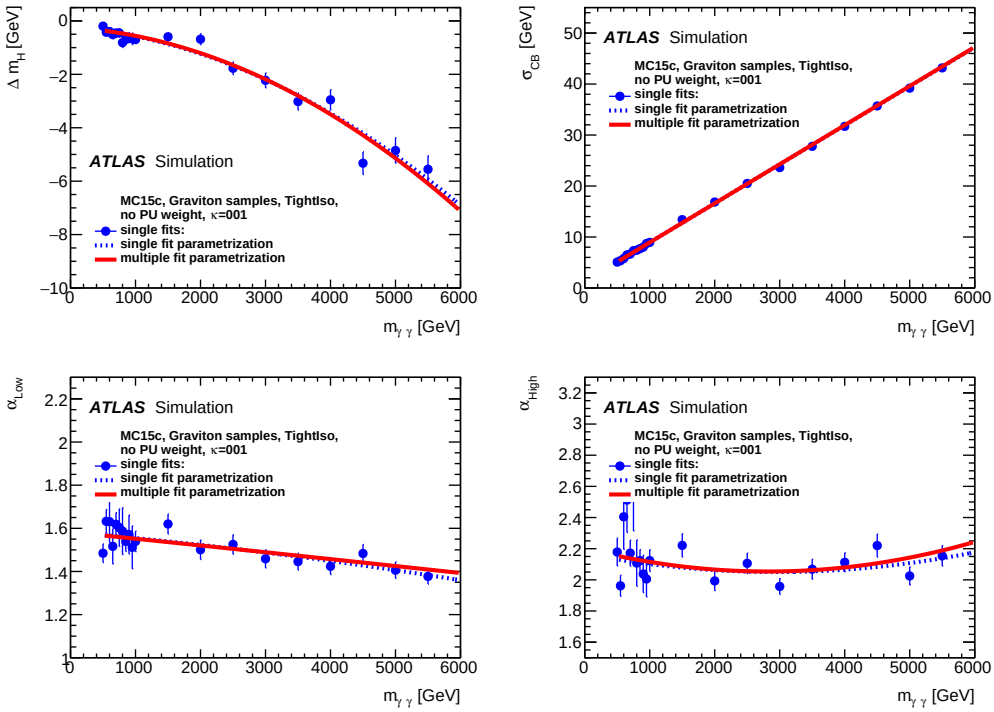

Figure 7.5: Comparison of the multiple mass fit parameterization (red line) to the output parameters of the single mass point fits (blue points) and to the parameterization of the single mass point fit parameters (blue dashed line) for the scalar model. The parameters are given as a function of m_G for the spin-2 signal simulation samples: $\Delta m_G = \mu_{CB} - m_G$ (top left), σ_{CB} (top right), α_{low} (bottom left), α_{high} (bottom right). For Δm_G few points deviate from the fit but that has no effect [10].

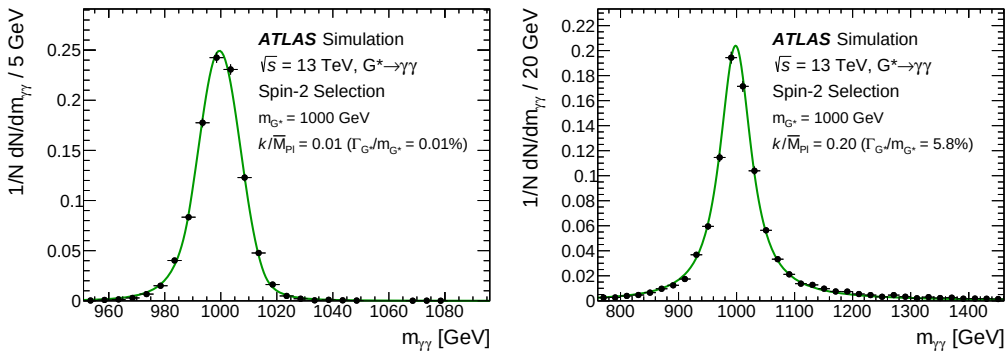

(a) **(b)**

Figure 7.6: The $m_{\gamma\gamma}$ distributions for different signal hypotheses for an RS graviton with a mass of 1000 GeV and (a) $k/\overline{M}_{\mathrm{Pl}} = 0.01$, (b) $k/\overline{M}_{\mathrm{Pl}} = 0.2$. A fit is superimposed using the convolution of the graviton mass line-shape with the detector resolution for the graviton signal [10].

7.4 Signal model with morphing

Other than the two methods cited above an alternative signal parameterization technique for the graviton signal was explored. This techniques exploits a morphing algorithm to build a complete signal model starting from a finite set of simulated samples. The procedure is the following: first a PDF distribution is built for each one of the simulated samples then the PDFs for the intermediate values of mass and width are extrapolated with morphing.

The PDF can be directly shaped from the histograms of the distributions, however in order to start from smooth PDFs at each dataset is associated a kernel density estimation [126] (KDE). KDE is a data smoothing technique where a gaussian kernel is drawn for each one of the points in a dataset, then the distribution is built summing all the kernels with a smoothening factor.

In the morphing procedure, described in more detail in Reference [127], the moments of the PDFs are calculated from the simulated samples as follows:

$$E[X^n] = \int_{-\infty}^{\infty} x^n f(x) dx \tag{7.4}$$

where $f(x)$ is the starting PDF and $E[X^n]$ is the n_{th} moment of the PDF. Then the moments $E[X^n]$ are interpolated either with a linear of polynomial function in the moments space. To evaluate the PDF for an interpolated point of the phase space the procedure is reversed.

$$f(x) = \int_{-\infty}^{\infty} e^{j2\pi xs} \left(\sum_{n=0}^{\infty} \frac{(-js2\pi)^2}{n!} E'[X^n] \right) ds \tag{7.5}$$

where the $E'[X^n]$ are the interpolated value of the moments.

Thanks to this technique from the finite set of signal mass distributions described in section 6.2.1.2 a signal template for any intermediate mass can be easily obtained. The interpolation

in case of more than one morphing parameter is made with a grid of signals and the interpolation is made from the grid of the moments. An explicative plot of 2-D morphing can be found in Figure 7.7. In the case of this analysis 3-way morphing was developed: on the mass of the

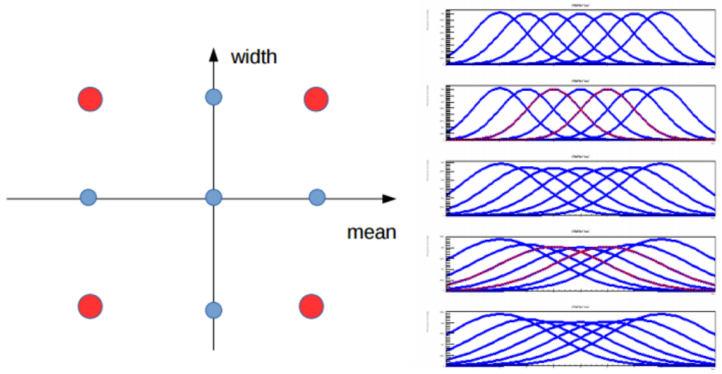

Figure 7.7: Moment morphing of gaussians, starting from 4 gaussian of 2 masses and 2 widths (red lines, points) other gaussian with in-between parameters can be interpolated (blue lines, points).

resonance, on the width and on the resolution systematic. To morph on the resolution simulated samples were prepared with the resolution systematic at $\pm 1, 2, 3\sigma$. Example inputs for RS signal are shown in Figure 7.8.

In order to validate the method the same morphing procedure is performed but excluding one single mass sample from the input, then the distribution for that sample is predicted and compared with the original. In Figure 7.9 left plot is the starting distribution and on the right plot the morphed distribution in blue is compared with the original distribution in red.

Morphing can be applied to any kind of signal shape as long a sufficient number of simulated samples is provided. The advantage of this technique is that no analytical modelization is necessary and it can be applied even when it's impossible to use an analytical parameterization, one example is the ADD graviton signal introduced in Section 2.3.1.

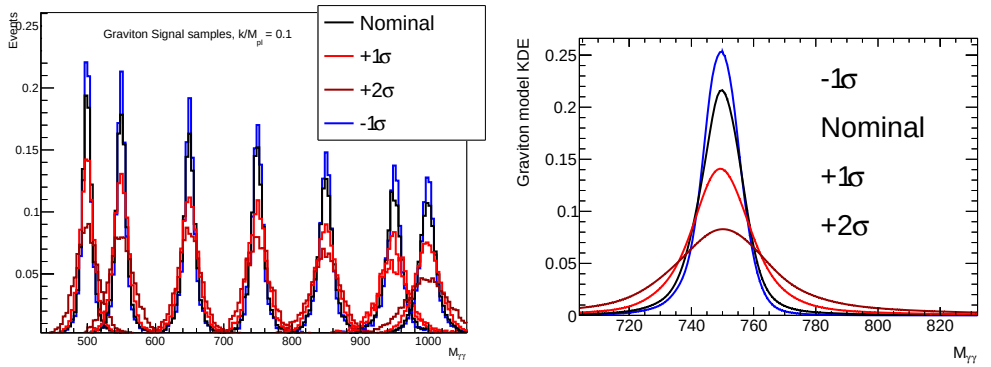

Figure 7.8: Inputs for signal morphing for RS graviton signal. Left: starting histograms for $k/\overline{M}_{\mathrm{Pl}} = 0.1$ and several masses, shown are the resolution systematic variations (positive σ in red, negative σ in blue). Right: KDE distribution of several resolution variations for one mass and width.

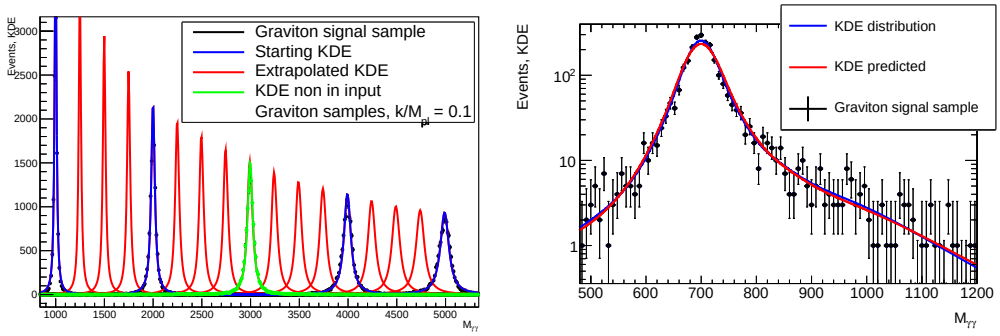

Figure 7.9: Left plot: distribution of simulated samples and KDEs, one distribution (in green) is removed from the inputs and predicted. Right plot: the morphed distribution in blue is compared with the original distribution in red.

CHAPTER 8

Background model

As explained in Section 6.1 there are two main components of SM background: the irreducible ($\gamma\gamma$) from the diphoton QCD production and reducible (γ-jet, jet-γ, jet-jet) from jets mis-identified as photons. The technique to model the background is different in the spin-2 and spin-0 analyses. The irreducible background mass distribution in the spin-2 analysis is obtained from MC simulations while the shape of the reducible background is determined using data-driven methods. Then the different background contributions are mixed according to the relative fractions measured in data in a low mass control region.

In the spin-0 analysis the background estimation is based on a functional form fit that is used to describe the sum of all the background components. However a similar technique to spin-2 background estimation is used to build a complete model to evaluate the bias introduced by the analytical functions choices.

The reducible background estimation for the spin-2 background model and the spin-0 background model to test the spurious signal is done in the same way for the two selection. The irreducible bacgkround component however is done slightly differently in the two analyses: for the spin-2 estimation additional NLO corrections are applied from the diphox generator to the diphoton Sherpa simulation.

Both methods returns a PDF that is then fitted on data, the two methods were proven to be compatible with each other (Section 8.5). It was proven that in both cases the background model well describes data. This was done evaluating the χ^2 distribution of a background only fit on data, the $\frac{\Sigma\chi^2}{N_f}$, where N_f is the number of degrees of freedom, is around 1 for both methods (Section 8.4). The background estimation of the two methods are consistent within errors. For values of $M_{\gamma\gamma} > 2$ TeV the MC-driven background estimation has a lower shape uncertainty than the analytic function fit.

8.1 Reducible background estimation

To determine the shape of the diphoton invariant mass spectrum of the reducible backgrounds, different background-enriched data control samples are defined. In all control samples, the two photon candidates are required to pass the isolation cut as well as the same kinematical selections.

Definition	Relaxed cuts
LoosePrime 2	$w_{\eta,1}$, F_{side}
LoosePrime 3	$w_{\eta,1}$, F_{side}, ΔE
LoosePrime 4	$w_{\eta,1}$, F_{side}, ΔE, E_{ratio}
LoosePrime 5	$w_{\eta,1}$, F_{side}, ΔE, E_{ratio}, $w_{s,\text{tot}}$

Table 8.1: The definitions of the LoosePrime control regions. E.g. LoosePrime 2 means that the tight identification criteria is applied with the exception of the two shower shapes mentioned.

To build the control samples the photon ID selection criteria are partially inverted. To achieve the partial inversion the single cuts on the shower shapes are removed, creating intermediate photon ID criteria called LoosePrime. Four different types of LoosePrime are used, their definition and the corresponding shower shapes whose cut was removed can be found in Table 8.1. The definition of the different shower shape variables used in the LoosePrime definitions can be found in Section 5.4.4.

The first set of control samples, named Tight-AntiTight, contain those events where the leading photon candidate passes the photon-ID requirement applied for the signal selection. However, the second photon candidate is required to fail the Tight photon identification requirement, but to pass the Loose (or LoosePrime) requirement; the latter restriction is applied since the trigger required two Loose photons. The Tight-AntiTight samples are enriched in γ+jet events, where the photon passes Tight and a jet passes Loose (LoosePrime) but not Tight and is reconstructed as a fake photon.
The second set of control samples, named AntiTight-Tight contain events where the leading photon candidate is required to pass Loose (LoosePrime) and fail the Tight requirement whereas the second photon candidate is required to pass the Tight requirement. This second sample is enriched in jet+γ events.
In terms of the reducible background from jet+jet events, the shape of the mass distribution of this background is determined using the AntiTight-AntiTight data control samples, in analogy to the other control samples discussed above, where we require both of the two photon to pass Loose (LoosePrime) and fail the Tight requirement.

In order to smooth the distributions obtained in the different background control regions, an analytic function is used to fit to the mass spectra. The fit functions considered are of the form:

$$f_{k_1,k_2} = x^{k_1(1-\log(x))} \times x^{k_2 \times \log(x)} \tag{8.1}$$

$$f_{k_1,k_2,k_3,k_4} = x^{k_1(1-\log(x))} \times x^{k_2 \times \log(x)} \times \left(1 - \frac{1}{1+e^{(x-k_3)/k_4}}\right) \tag{8.2}$$

$$f_{k_1,k_2,k_3,k_4,k_5,k_6} = x^{k_1(1-\log(x))} \times x^{k_2 \times 1-\log(x)} \tag{8.3}$$

$$\times \left(1 - \frac{1}{1+e^{(x-k_3)/k_4}}\right) \times \left(1 - \frac{1}{1+e^{(x-k_5)/k_6}}\right) \tag{8.4}$$

where the k_i are the free parameters determined by the fit. Unbinned negative log-likelihood (NLL) fits are performed in the mass range [150-3000] GeV. The final choice of the functional form is driven by the maximum likelihood values for the different candidate functions. If the difference of the maximum likelihood value is within 0.5, the function with the lowest number of degrees of freedom is chosen.

The reducible background estimation was made with the combination of 2015 and 2016 data to benefit from the higher statistics. A study was conducted on the reducible background estimation obtained from the 2015 and 2016 data and good agreement was found for the background shapes between the two data-sets.

In terms of the typical properties among those regions, the Loose control region is the loosest one from all control regions listed in Table 8.1. Therefore it will have a high statistics and a high fake background fraction. However, the fake background in this region might not be representative for the fake background in the signal region. The LoosePrime 2 control region is the tightest one and therefore is expected to best represent the background in the signal region. However, this control region contains a large fraction of true photons and low statistic.

Taking into account possible correlations between the shower shape variables and the mass distribution, contaminations due to real photons, as well as the need for reasonable statistics in the control background samples, the LoosePrime4 (failing the Tight criteria but passing the LoosePrime4 criteria) cut is chosen for the nominal region of the background shape estimation of γ+jet and jet+γ components, while the Loose (failing the Tight criteria but passing the Loose criteria) is used for the nominal region of the background shape estimation of jet+jet components. In order to assess the systematics of the reducible background shape in this method, possible variations were studied in the extrapolated fit functions from different background control regions.

For the γ+jet and jet+γ component estimation, the LoosePrime 4 is used as baseline and all other LoosePrime variations (LoosePrime 5 to LoosePrime 2) and Loose are used to assign the systematic uncertainty. However, for the jet+jet component estimation, Loose is used as baseline and only LoosePrime 4 and LoosePrime 5 will be used to assign the systematic uncertainty. Figures 8.1, 8.3 show the results of the nominal fit while Figures 8.2, 8.4 show the result of the fit with the LoosePrime variations.

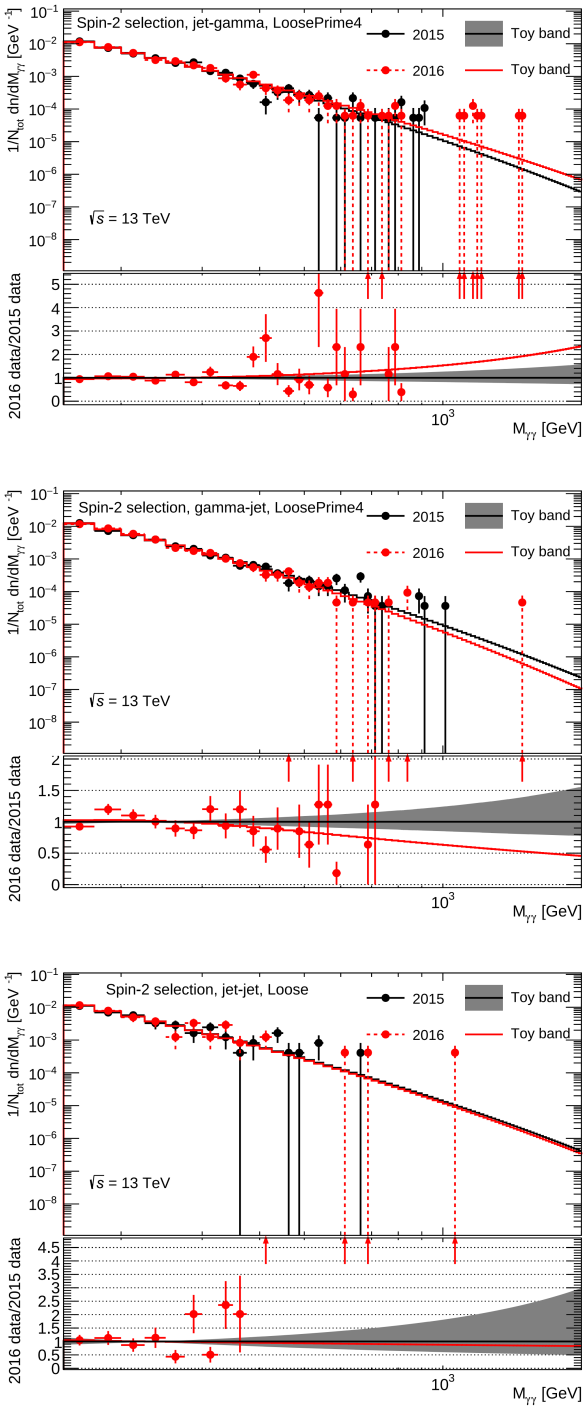

Figure 8.1: Spin-2 selection reducible background fit of (from top to bottom): jet-γ with LoosePrime4, γ-jet using LoosePrime4, jet-jet using Loose.

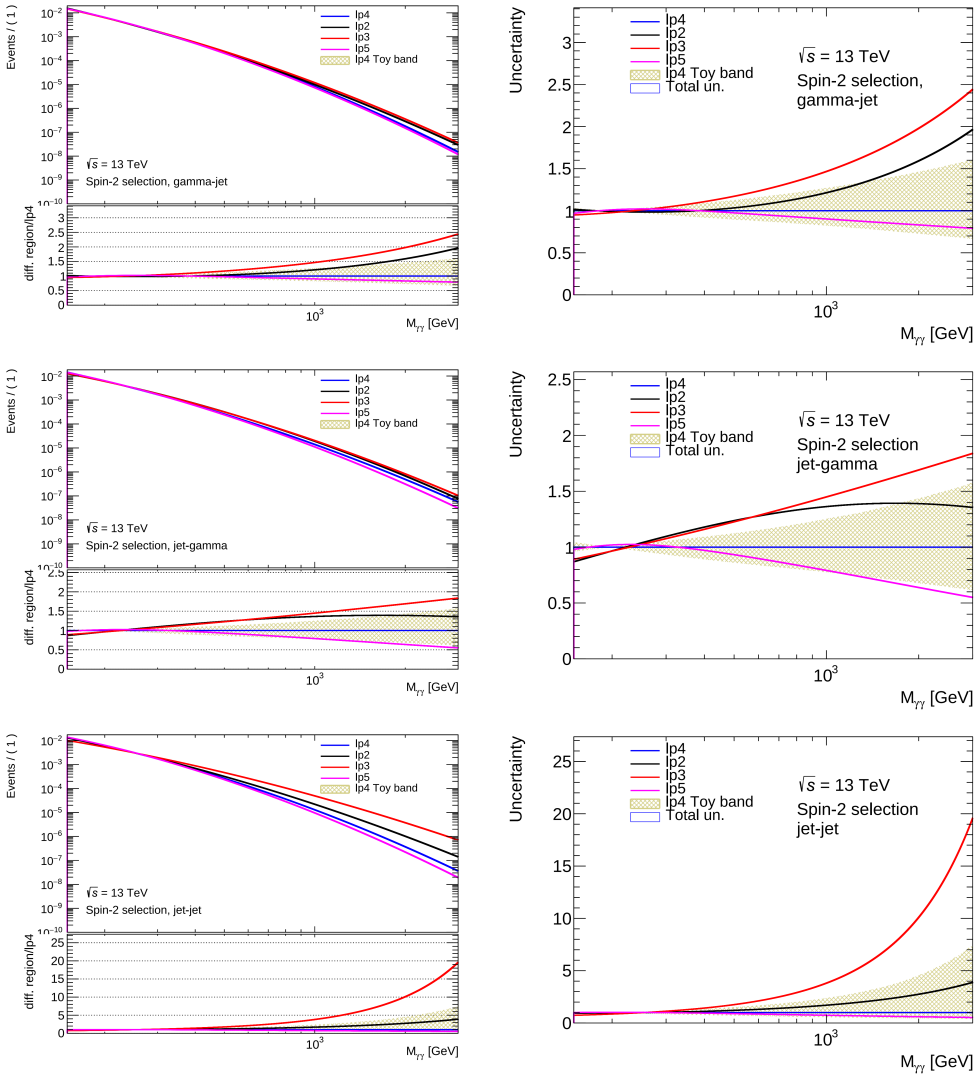

Figure 8.2: Spin-2 selection reducible background fit (left) and relative uncertainty (right) of from top to bottom: γ-jet (nominal is LoosePrime4), jet-γ (nominal is LoosePrime4), jet-jet (nominal is Loose).

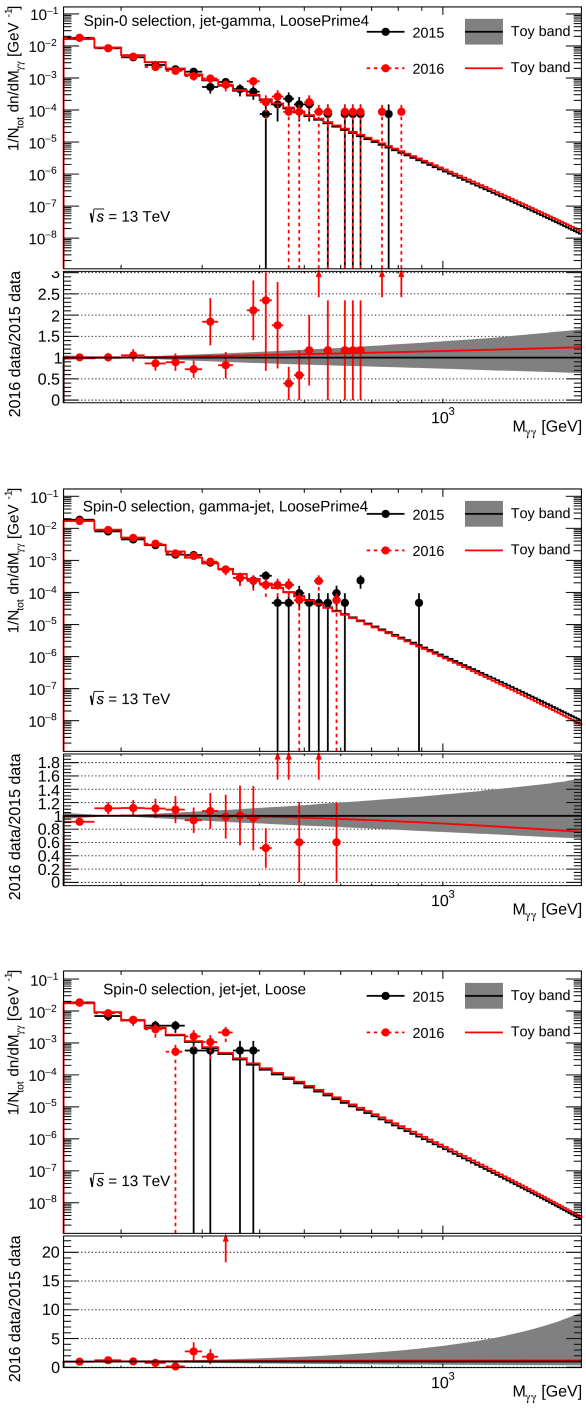

Figure 8.3: Spin-0 selection reducible background fit of (from top to bottom): jet-γ with LoosePrime4, γ-jet using LoosePrime4, jet-jet using Loose.

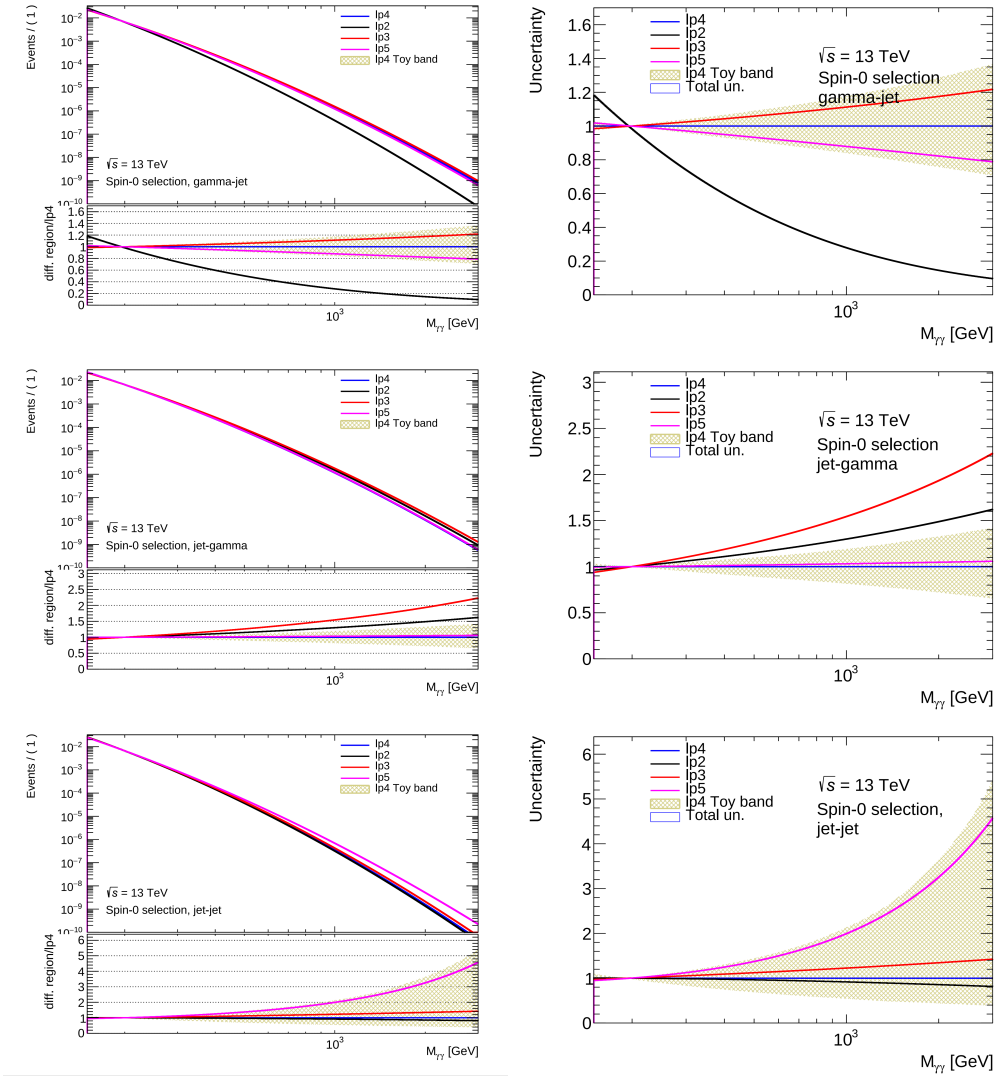

Figure 8.4: Spin-0 selection reducible background fit (left) and relative uncertainty (right) of from top to bottom: γ-jet (nominal is LoosePrime4), jet-γ (nominal is LoosePrime4), jet-jet (nominal is Loose).

8.2 Spin-2 analysis background estimation

The estimation of the background in the graviton analysis proceeds in two steps: first the shape of the $m_{\gamma\gamma}$ spectrum for the irreducible $\gamma\gamma$ background and three reducible background components (γj, $j\gamma$ and jj) is produced from Monte Carlo. Then the four contributions are summed with fractions measured in data from a data-driven technique. The determination of the shape of the irreducible background is discussed in Section 8.2.1 and the determination of the shapes of the reducible backgrounds has been discussed in Section 8.1.

8.2.1 Parton-level simulations for the irreducible background estimation

The MC samples for the irreducible diphoton background cited in Section 6.2.2.1 have been generated using a generator (Sherpa) that employs a combination of fixed-order matrix elements, parton showers and/or final state radiation to describe the SM diphoton production processes. For the background prediction in the spin-2 analysis, the DIPHOX generator was used to refine the prediction of the invariant mass spectrum. DIPHOX [121] is a fixed-order program of Matrix Element calculation with the capability of handling NLO calculation of all the processes, including the fragmentation into a leading photon of one or two final-state partons. Its treatment of fragmentation is particularly accurate. Despite the absence of treatment of the soft emission, which may imply discontinuities in the description of physical observables, DIPHOX provides accurate high-p_T differential cross sections. Diphox NLO prediction was used to refine the prediction obtained with Sherpa parton shower generator by reweighting with k-factors, at the generator level, their $m_{\gamma\gamma}$ distribution to the one obtained using DIPHOX.

The default setup for DIPHOX event generation uses the CTEQ66M PDF set which has been obtained using NLO calculations. The fragmentation, factorisation and renormalisation scales are set to the mass of the diphoton system. The generator-level photon isolation cut in DIPHOX has been adjusted to mimick the effect of the reco-level photon isolation cut (Table 8.2). The theory systematic uncertainty is then obtained by considering a number of parameters variations, resulting in a $m_{\gamma\gamma}$ shape variation. This will be described in Section 9.3.2.

In order to avoid statistical fluctuations, large DIPHOX samples have been generated, yielding an accurate correction up to $m_{\gamma\gamma}$=5 TeV. The correction is then parameterised with the following 9th grade polynomial fit function:

$$f(m_{\gamma\gamma}) = \begin{cases} \sum_{i=0}^{9} p_i \times m_{\gamma\gamma}^i & \text{if } m_{\gamma\gamma} \leq 4000 \text{ GeV}, \\ f(4000 \text{ GeV}) & \text{if } m_{\gamma\gamma} > 4000 \text{ GeV}, \end{cases} \tag{8.5}$$

where the p_i are the free parameters. The corrections in function of $m_{\gamma\gamma}$ to the Sherpa inviarant mass distribution can be seen in Figure 8.5.

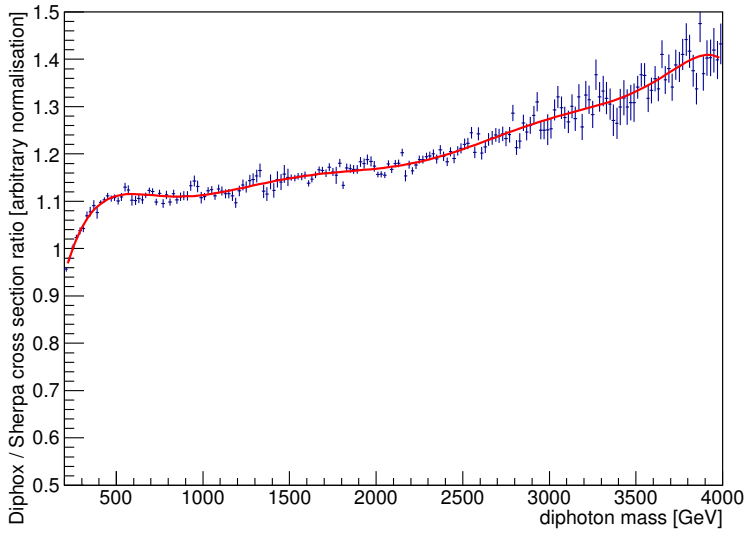

Figure 8.5: Effective k-factor correction as a function of diphoton mass obtained from the ratio DIPHOX/SHERPA at truth levelfor the spin-2 selection. This is only a shape comparison. Specifically, the histogram has been normalised in such a way that that the ingeral of the ratio in the region [200,300] GeV is equal to one. The solid line represents the result of a fit to a smooth function.

Scenario	Isolation requirement
Reco-level cut (for reference)	$E_{\mathrm{T}}^{\mathrm{iso}} < 0.022 \times E_{\mathrm{T}}^{\gamma} + 2.45$ GeVand $ptvarcone20 < 0.05 \times E_{\mathrm{T}}^{\gamma}$
"Up" variation of generator-level cut	$E_{\mathrm{T}}^{\mathrm{truth,parton}} < 0.022 \times E_{\mathrm{T}}^{\gamma,truth} + 12$ GeVand $E_{\mathrm{T}}^{\mathrm{truth,parton,cone0.2}} < 0.05 \times E_{\mathrm{T}}^{\gamma,truth}$
"Central" estimate of generator-level cut	$E_{\mathrm{T}}^{\mathrm{truth,parton}} < 0.022 \times E_{\mathrm{T}}^{\gamma,truth} + 5$ GeVand $E_{\mathrm{T}}^{\mathrm{truth,parton,cone0.2}} < 0.05 \times E_{\mathrm{T}}^{\gamma,truth}$
"Down" variation of generator-level cut	$E_{\mathrm{T}}^{\mathrm{truth,parton}} < 0.022 \times E_{\mathrm{T}}^{\gamma,truth} + 3.5$ GeVand $E_{\mathrm{T}}^{\mathrm{truth,parton,cone0.2}} < 0.05 \times E_{\mathrm{T}}^{\gamma,truth}$

Table 8.2: Tune of the generator-level cut used to mimic the tight reco-level isolation cuts on both the calorimetric and tracking isolations of the Spin-2 analysis.

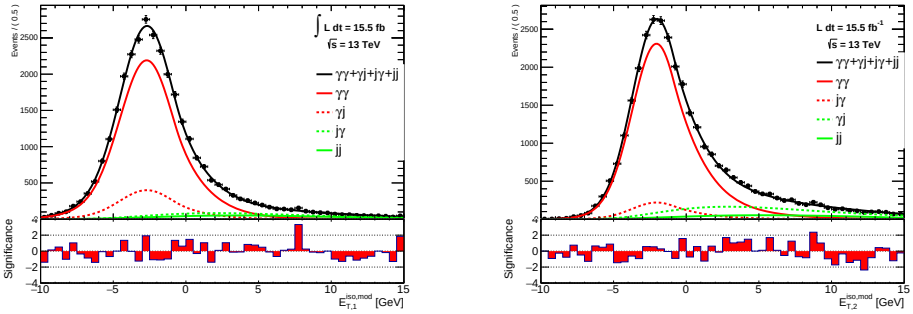

Figure 8.6: (Shifted) Isolation energies measured for the leading (left) and subleading (right) photon candidate for events selected in the low-mass control region and with a relaxed isolation cut $E_T^{iso} < 15$ GeV. The result of the 2D template fit is superimposed in black. The green lines show the contributions of the different jet components. The red lines show the contributions of the different photon components.

8.2.2 Background decomposition

The background composition is studied in a low-mass control region $[200, 514.3]$ GeV. The upper limit has been chosen to coincide with the first bin boundary above 500 GeV in the binned statistical analysis that will be discussed in the following sections. To determine the contribution of the four different background sources considered, a two-dimensional template fit method was used with the calorimetric isolation energies of the two photons in the low-mass control region.

This method, known as the isolation template fit method, determines the background components with an extended maximum likelihood fit to the two-dimensional isolation distribution of the Tight diphoton candidates. It has been developed for the purpose of Standard Model diphoton cross section measurement [119, 128]. The probability density function (PDF) is defined as follows:

$$P(E_{T,1}^{iso}, E_{T,2}^{iso}) = N_{\gamma\gamma} P(E_{T,1}^{iso}) P(E_{T,2}^{iso}) + N_{\gamma j} P(E_{T,1}^{iso}) J(E_{T,2}^{iso}) + \quad (8.6)$$

$$N_{j\gamma} J(E_{T,1}^{iso}) P(E_{T,2}^{iso}) + N_{jj} J(E_{T,1}^{iso}, E_{T,2}^{iso}) \quad (8.7)$$

The coefficients $N_{\gamma\gamma}, N_{\gamma j}, N_{j\gamma}, N_{jj}$ of the four 2D probability density functions are the yields of the different components in the sample where the two photons pass the Tight selection (Tight-Tight sample). $E_{T,i}^{iso}$ is the calorimetric isolation variable for the leading (if i=1) or subleading (if i=2) photon candidate. $P(E_{T,i}^{iso})$ and $J(E_{T,i}^{iso})$ are the true photon and fake photon isolation probability density functions (PDFs), while $J(E_{T,1}^{iso}, E_{T,2}^{iso})$ is the global PDF for dijet background. The reason why the jj PDF is not factorised as the product of the leading and sub-leading object PDFs is that the correlation of two fake candidates isolation variables has been shown to be non-negligible (see Reference [119] for more information).

For the purpose of this fit a very loose selection on the isolation energy is used, namely $E_T^{iso} < 15$ GeV. This is done to provide the fit with a control region that is enriched in background. The fit results, i.e. the values of $N_{\gamma\gamma}, N_{\gamma j}, N_{j\gamma}, N_{jj}$ represent the sample composition with this loose isolation cut. However the final isolation cut used in this search is more tight, and the values

of $N_{\gamma\gamma}, N_{\gamma j}, N_{j\gamma}, N_{jj}$ need to be adjusted to take into account the tighter cut. The adjustment is non trivial since a p_T^γ-dependent isolation cut is applied, namely $E_T^{iso} < 0.022 \times p_T^\gamma + 2.45$ GeV. To address this issue, the isolation fit was performed using a modified isolation observable: E_T^{iso} was replaced with with $E_T^{iso} - 0.022 \times p_T^\gamma$. In the following, the notation E_T^{iso} is used to denote the modified isolation energy.

True and fake photon isolation shapes are extracted directly from data. For the purpose of the determination of the isolation template for fake photons, a diphoton sample is selected by requiring both photons to pass the LoosePrime4 identification criteria. The fake photon templates $J(E_{T,i}^{iso})$ are extracted from a control sample where the photon candidate i fails the Tight criteria. Namely, the $J(E_{T,1}^{iso})$ is taken from the AntiTight-Tight region, $J(E_{T,2}^{iso})$ from the Tight-AntiTight region and $J(E_{T,1}^{iso}, E_{T,2}^{iso})$ from the AntiTight-AntiTight region. The PDFs are smoothed by fitting Novosibirsk functions to the isolation distributions. The Novosibirsk function is defined as:

$$f(E_T^{Iso}) = A_S \exp(-0.5\ln^2[1 + \Lambda\tau \cdot (E_T^{Iso} - E_0)]/\tau^2 + \tau^2), \tag{8.8}$$

where $\Lambda = \sinh(\tau\sqrt{\ln 4})/(\sigma\tau\sqrt{\ln 4})$, the peak position is m_0, the width is σ, and τ is the tail parameter.

The true photon templates $P(E_{T,i}^{iso})$ are obtained by subtracting the normalised isolation distribution for photons failing Tight criteria from the distribution of photons from the Tight-Tight sample. The template for fake photons is normalised to the Tight-Tight sample at $E_{T,i}^{iso} > 10$ GeV where the fakes are known to dominate the distribution of isolation energy. In this way $P(E_{T,i}^{iso})$, which is described by the sum of a Crystal Ball function and a gaussian (with the same mean as the Crystal Ball function), can be determined. It has been shown that this functional form describes well the shape for true photons in the simulation. Finally a smoothed KDE distribution built from the 2D histogram of the control sample where both candidates fail the Tight criteria is used for $J(E_{T,1}^{iso}, E_{T,2}^{iso})$.

Once the PDFs have been extracted from the control samples described above, a fit to the selected Tight-Tight photon sample is performed with the PDF described in Equation 8.6, with all parameters fixed except the normalisations. The result of this 2D isolation is shown in Fig. 8.6. Integrating the PDF up to the 2.45 GeV isolation cut allows to determine the different background components in the low mass control region.

Systematic uncertainties due to the correlation between the isolation and identification cuts and the quantity of true photons contaminating the jet templates are assessed by varying the LoosePrime sample. Having determined both the shapes and the normalisations of the irreducible and reducible background contributions in the low-mass control region, the background prediction is extrapolated to the whole invariant mass range, the prediction superimposed with data can be seen in Figure 8.11 (a). The comparison of the purity obtained with the background decomposition technique with the other methods introduced in Section 6.6 can be seen in Figure 8.7.

selection	inclusive purity			
	2x2DSB method	matrix method	2D fit (XY)	2D fit (TM)
spin-0 (2015)	$0.901 \pm 0.006^{+0.015}_{-0.094}$	$0.909 \pm 0.004^{+0.022}_{-0.083}$	$0.918 \pm 0.011 \pm 0.033$	$0.909 \pm 0.020 \pm 0.091$
spin-0 (2016)	$0.902 \pm 0.003^{+0.019}_{-0.097}$	$0.904 \pm 0.002^{+0.025}_{-0.086}$	$0.912 \pm 0.007 \pm 0.036$	$0.867 \pm 0.010 \pm 0.087$
spin-0 (2015+2016)	$0.901 \pm 0.003^{+0.018}_{-0.096}$	$0.906 \pm 0.002^{+0.025}_{-0.086}$	$0.914 \pm 0.006 \pm 0.035$	$0.866 \pm 0.008 \pm 0.087$
spin-2 (2015)	$0.907 \pm 0.007^{+0.015}_{-0.090}$	$0.921 \pm 0.004^{+0.014}_{-0.080}$	$0.915 \pm 0.013 \pm 0.034$	$0.889 \pm 0.015 \pm 0.089$
spin-2 (2016)	$0.905 \pm 0.004^{+0.018}_{-0.087}$	$0.916 \pm 0.002^{+0.020}_{-0.070}$	$0.904 \pm 0.008 \pm 0.034$	$0.895 \pm 0.013 \pm 0.090$
spin-2 (2015+2016)	$0.905 \pm 0.003^{+0.017}_{-0.088}$	$0.918 \pm 0.002^{+0.020}_{-0.072}$	$0.907 \pm 0.007 \pm 0.034$	$0.893 \pm 0.010 \pm 0.089$

Figure 8.7: Comparison of the inclusive purity in data 2015, 2016 and combined obtained with the three methods introduced in Section 6.6 (first three columns) and the method to obtain the background modelization for the spin-2 analysis (last column). Agreement between all methods is at 1-2% level.

8.3 Spin-0 analysis background estimation

In the spin-0 analysis a data-driven estimate is used for the background SM contribution. The $m_{\gamma\gamma}$ background shape is modeled by a smooth functional form. In order to be able to search to the largest possible value of m_X, a functional form capable to describe the background over a large mass range is desirable, however with the lowest number of degrees of freedom and withouth introducing a large signal bias. The properties of the fitting function will be constrained by the data statistics on the lower end of the $m_{\gamma\gamma}$ spectrum, and would allow to perform a stable signal-plus-background fit until the end of the studied $m_{\gamma\gamma}$ spectrum.

8.3.1 Spurious signal

In order to validate a functional form to describe the $m_{\gamma\gamma}$ spectrum a "*spurious signal*" validation is used. The candidate function is used to perform a signal-plus-background fit for several signal mass hypothesis m_X on a background-only high statistics MC sample. The statistic uncertainties of this MC sample must be negligible with respect to local modulation of the predicted $m_{\gamma\gamma}$ spectrum: the scope of this test is not to fit the local statistical fluctuation, but to evaluate how a given functional form can adapt to the true expected background shape. The candidate functions are tested using the available diphoton SHERPA $\gamma\gamma$ MC sample mixed with the data driven $\gamma + jet$ component obtained as described in Section 8.1. The mixture is based on the expected components fractions from data driven methods seen in Section 6.6.

The number of fitted signal events for a given signal mass hypothesis m_X (called spurious signal $N_{spurious}(m_X)$) is evaluated in the range of interest in steps of 10 GeV. The largest value of $N_{spurious}(m_X)$ in the fitted range is chosen as the maximum spurious signal $N^{max}_{spurious}(m_X)$. A function passes the spurious signal test if it does not generate a value of $N^{max}_{spurious}(m_X)$ larger than a small fraction of the expected background statistical uncertainty, this value is traditionally set to 30%. Among different validated functions, that with the smallest number of free parameters is chosen as the baseline.

Afterwards $N_{spurious}(m_X)$ is parameterized with a functional form, however since the raw $N_{spurious}(m_X)$ distribution has large variations (Figure 8.8) the following procedure was developed to produce an envelope of the maximum values of $N_{spurious}(m_X)$. First the distribution is splitted

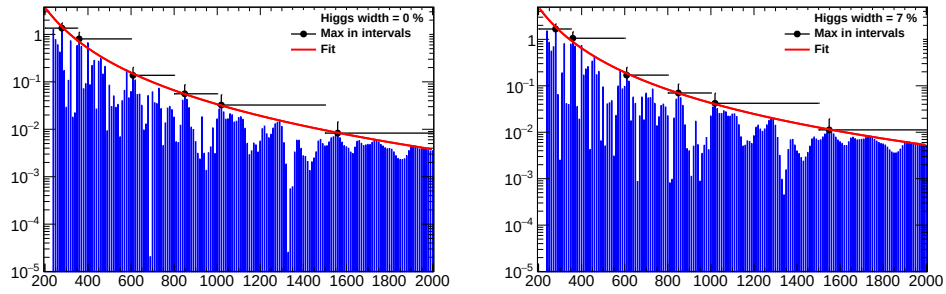

(a) (b)

Figure 8.8: Spurious signal for the NWA case (left) and $\alpha_X = 7\%$ case (right). The blue histogram represents the $N_{spurious}(m_X)$ and the red line is the parametrization.

in large bins, then the maximum value of $N_{spurious}(m_X)$ is evaluated for each bin. An analytical function is fitted to the maximum points, if the fit fails the first time the procedure is re-iterated with larger error bars. The output of the procedure can be seen in Figure 8.8. The parameterized value of $N_{spurious}(m_X)$ for the chosen function is used in the statistical modeling as a nuisance parameter on the signal yield to account for background modeling uncertainty.

In case of the large–width signal the values of $N_{spurious}(m_X)$ are separately obtained for signal hypotesis with $\alpha_X = 0, 0.02, 0.04, 0.06, 0.08$ and 0.10, and a linear interpolation is used to obtain the uncertainty for arbitrary values of α_X in the range $0 \leq \alpha_X \leq 0.10$.

8.3.2 Background modeling functions

The $m_{\gamma\gamma}$ spectrum is fitted in the mass range [180, 3000] GeV (however the search range for the analysis is [200, 2500] GeV) with functional forms of the nested[1] family [129] that passed the spurious signal test:

$$f_{k;d}(x;b,\{a_k\}) = (1-x^d)^b x^{\sum_{j=0}^{k} a_j \log(x)^j}, \tag{8.9}$$

where $x = \frac{m_{\gamma\gamma}}{\sqrt{s}}$, the a_k, b are the free parameters and the d parameter is usually set in the range [0,1].

The fit range was chosen looking at the spurious signal ($N^{max}_{spurious}(m_X)$ should not be larger than 30% of the expected background statistical uncertainty) and the expected sensitivity of a signal at high $m_{\gamma\gamma}$ (>700 GeV).

To choose the appropriate value of the d functions with $d = [0, 1]$ are tested with the spurious signal test. The value $d = 1/3$ passed the spurious signal test with the statistic of data from 2015, while with the statistic of the full 2016 dataset the parameter d had to be modified to $d = 1/2$ to

[1] Two statistical models are nested if the first model can be transformed into the second model by imposing constraints on the parameters of the first model. In this case the k-1 function is equal to the k function with $a_k = 0$.

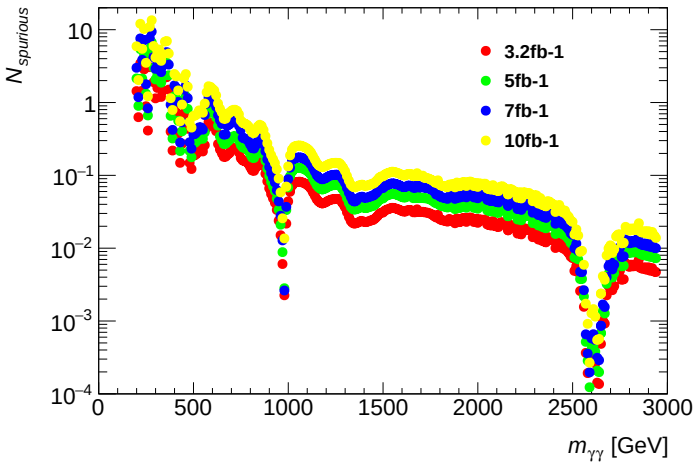

Figure 8.9: Spurious signal distribution for spin-0 analysis assuming different total luminosity.

pass the spurious signal test. The different value of d between the two years is explained by the different total number of events: the spurious signal shape remains the same increasing lineraly with N (Figure 8.9) but the expected background statistical uncertainty diminishes (going as $\sqrt{N}$) thus lowering the maximum threshold of $N^{max}_{spurious}(m_X)$.

In both years the number of degrees of freedom is initially chosen as 2 then the need for additional parameters is tested using the F-Test described in the following section.

8.3.3 F-Tests on data

The need for additional degrees of freedom was tested on data, starting from the functional forms selected on Monte Carlo with the spurious signal test. To do so a F-test [130] was conducted exploiting the nested property of the chosen family of functions. A double sided p_0 test was perfomed with an additional degree of freedom, practically an unbinned fit was done on data using the functions with 3 and the 2 free parameters. The additional parameter would be useful if its addition would result in a 2σ improvement in p_0 for the background only fit. Using 2015 and 2016 data separately, no need for an additional degree of freedom with respect to the baseline function with 2 parameters was observed. Examples fit can be found in Figure 8.10.

8.3.4 Chosen functional form

The chosen functional from for 3.2 fb^{-1} of 2015 data is:

$$f(x;b,a) = (1-x^{1/3})^b x^a, \tag{8.10}$$

while for 33.9 fb^{-1} of 2016 data is:

$$f(x;b,a) = (1-x^{1/2})^b x^a, \tag{8.11}$$

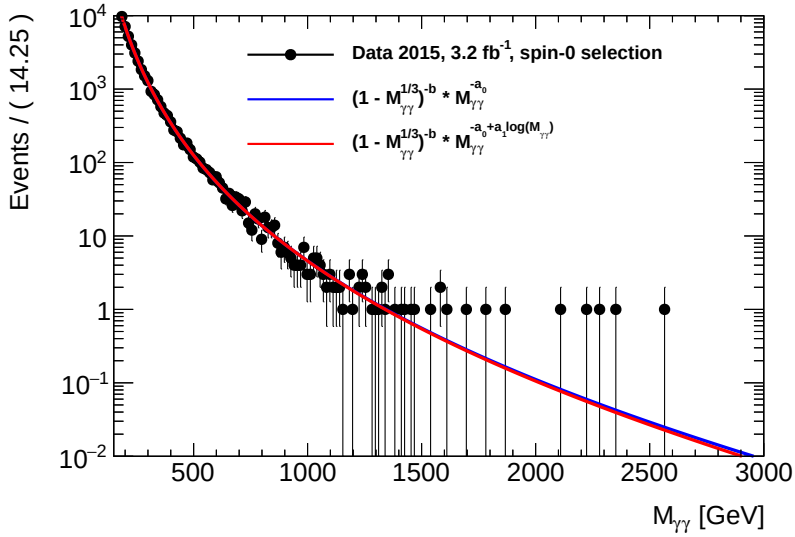

(a)

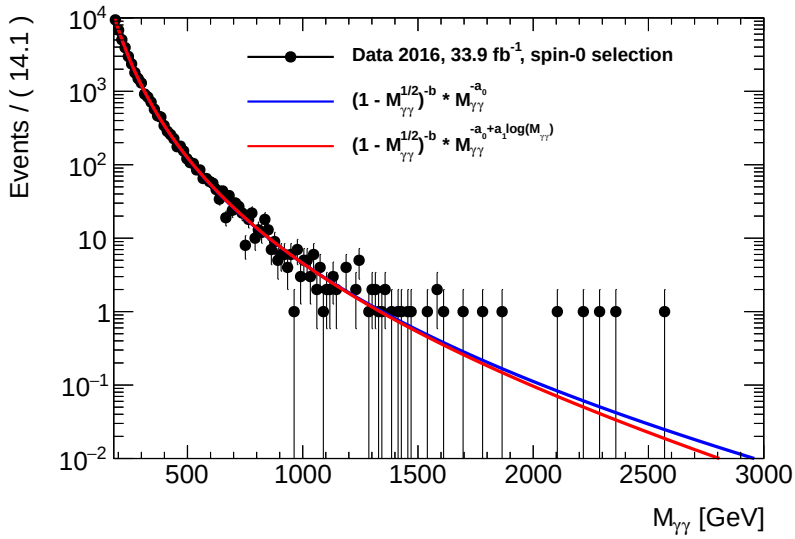

(b)

Figure 8.10: $m_{\gamma\gamma}$ spectrum of data from (a) 2015 and (b) 2016, superimposed is the background-only fit for two functional form with 2 and 3 degrees of freedom. It can be seen that the additional degree of freedom do not improve the quality of background-only fit.

8.4 Background goodness of fit

Once the background model is built in the two analyses (template for spin-2 and analytic function for spin-0) it is necessary to estimate if the model describes the data in a satisfying way. The goodness of the background-only fit to data was evaluated to test the background models. The dataset from year 2016 was used for these studies.

The following method was applied: a background-only fit is performed fixing the signal component at zero, however the systematic variation on the background are allowed to vary. Then the number of events for data and model are calculated in bins such that the number of events is never less than 10. In these bins the χ^2 is evaluated as $(N_{\texttt{data}} - N_{\texttt{model}})^2 / N_{\texttt{data}}$. The χ^2 for each bin is then summed and divided by the total number of bins. The study shows that $\chi^2 \sim 1$ for both methods, indicating that in both cases the background estimation well-describes the data. Results can be seen in Figure 8.11.

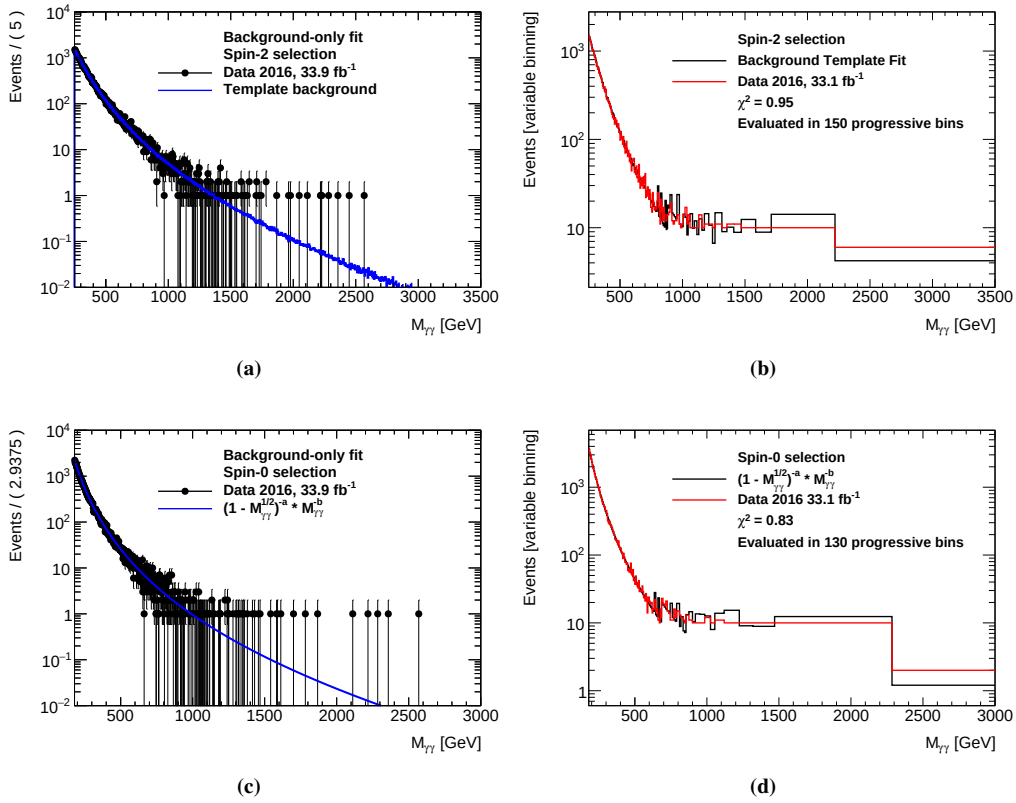

Figure 8.11: Goodness of fit for spin-2 (top) and spin-0 bottom. The left plots show the background-only fit on data 2016, the right plots show the number of events in variable bins used to evaluate the χ^2.

8.5 Comparison of background models

To ensure a robust background modelization the two methods of background estimation for the two analyses have been cross-checked one with the other. To do so an analytical function was studied to be used in the spin-2 analysis and a Monte Carlo template was built for the spin-0 analysis as described in Section 8.2. The comparison was done fitting the two background models to the dataset from year 2016.

The same procedure described in Section 8.3 was applied to find an analytical function from the spin-2 analysis, the chosen function for data 2016 is:

$$f(x;b,a) = (1-x)^{-a} x^{-b+c*\log(x)} \tag{8.12}$$

The comparison of the background only fit for the two methods can be seen for the two analyses in Figure 8.12. Tables 8.3 and 8.4 (spin-0 and spin-2 respectively) show the predicted number of events for the two methods in large bins of $m_{\gamma\gamma}$ compared with data 2016.

$m_{\gamma\gamma}$ interval [GeV]	MC template	Analytical fit	Data
[200.0 – 500.0]	28274	28260	28244
[500.0 – 1000.0]	1090	1102	1115
[1000.0 – 2000.0]	64	73	66
[2000.0 – 3500.0]	2	3	5

Table 8.3: Number of events in large bins predicted by the Monte Carlo template and analytical fit background models, spin-0 selection.

$m_{\gamma\gamma}$ interval [GeV]	MC template	Analytical fit	Data
[250.0 – 500.0]	25672	25929	25488
[500.0 – 1000.0]	3126	3244	3180
[1000.0 – 2000.0]	224	226	227
[2000.0 – 3500.0]	8	8	9

Table 8.4: Number of events in large bins predicted by the Monte Carlo template and analytical fit background models, spin-2 selection.

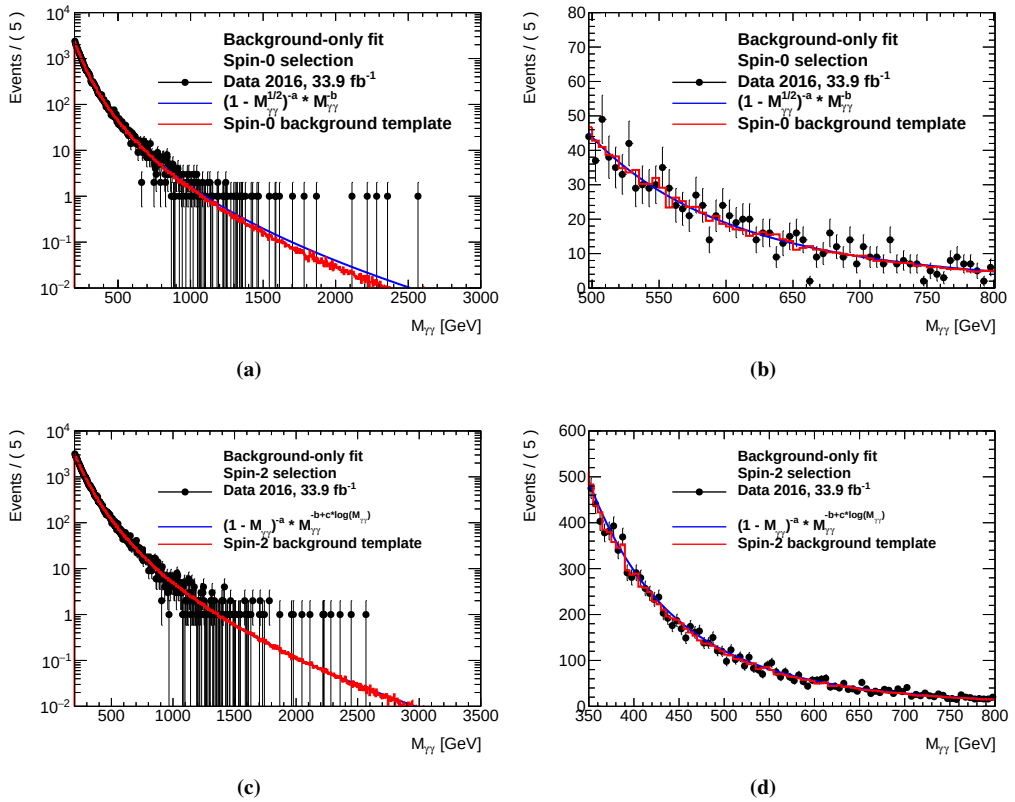

Figure 8.12: Comparison of a backround-only fit to data 2016 of the Monte Carlo template and analytical fit background models. For spin-0 (top) and spin-2 (bottom) selection, left plots show the whole $m_{\gamma\gamma}$ range, right plots show a smaller interval.

CHAPTER 9

Systematic uncertainties

In order to obtain a correct final result from the statistic studies the model has to include accurate systematic uncertainties. These uncertainties are included in the statistic modeling as nuisance parameters as explained in Chapter 10. In this chapter the systematic uncertainties on the signal and background estimation will be reviewed. A summary of the values of the systematic uncertainties can be found in Table 9.5. The correlation of the nuisance parameters between 2015 and 2016 data is discussed in Section 10.4. The uncertainties can be grouped in three types: uncertainties on the signal shape, uncertainties on the signal yield and uncertainties on the background shape.

The only systematic uncertainty on the signal model shape is energy resolution uncertainty as explained in Section 9.1.1. On the signal yield the main uncertainties (Section 9.2) are on photon identification, isolation selection and model-dependence uncertainties on the cross section. The uncertainties on the background estimation are different in the case of the MC-template technique used in the spin-2 analysis (Section 9.3.2) and in the functional form fit used in the spin-0 analysis (Section 9.3.1).

9.1 Systematic uncertainties on the signal shape

The only source of systematic variation that is taken into account for the signal shape is the photon energy resolution. The resolution affects the σ_{CB} parameter allowing the signal to be broader or narrower of the tested width. This systematic is important to assess the compatibility with the narrow width approximation. The photon energy scale systematic only affects the center value of the signal shape (M_X), with the effect of broadening the likelihood distribution around the tested signal mass. Uncertainties on photon identification and isolation selection have no effect on the final shape of the tested signal resonance. The effect of the energy resolution and scale uncertainties can be seen in Figure 9.1 for graviton samples of $k/\overline{M}_{\mathrm{Pl}}$ 0.01 and 0.1. Note that the effect of the resolution uncertainty is large for a narrow signal and small for a signal with large intrinsic width.

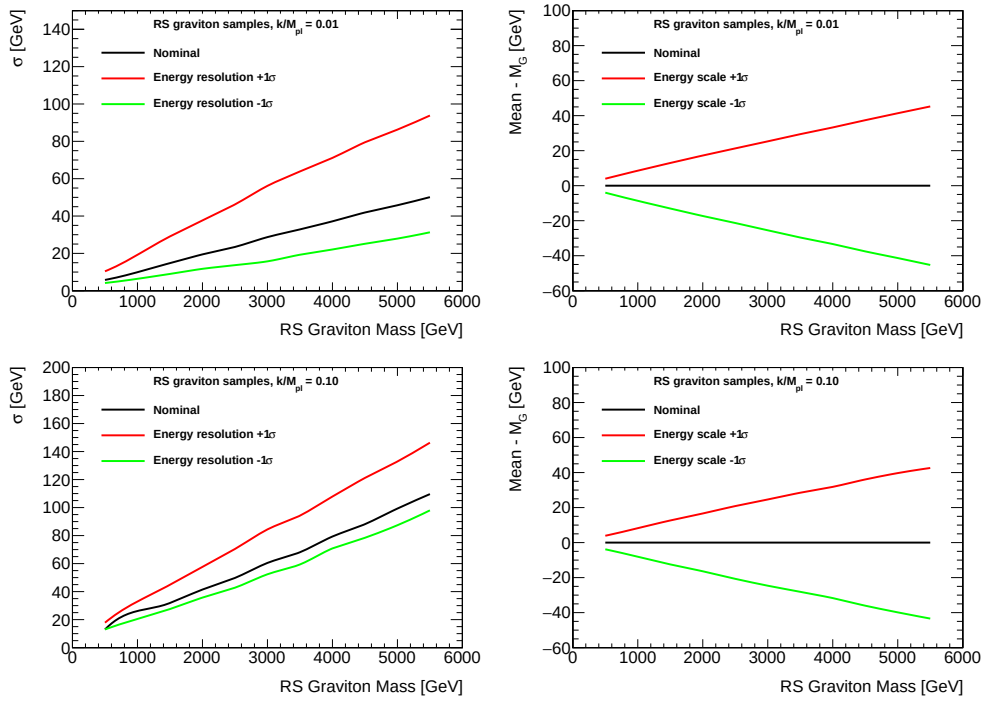

Figure 9.1: Left: variation of the σ_{RMS} due to up/down shift of the calorimeter resolution parameters, as a function of M_X, for the graviton $k/\overline{M}_{\mathrm{Pl}} = 0.01$ and $k/\overline{M}_{\mathrm{Pl}} = 0.1$ samples. Left: variation of the mean of the distribution due to up/down shift of the calorimeter scale parameters, as a function of M_X, for the graviton $k/\overline{M}_{\mathrm{Pl}} = 0.1$ and $k/\overline{M}_{\mathrm{Pl}} = 0.1$ samples.

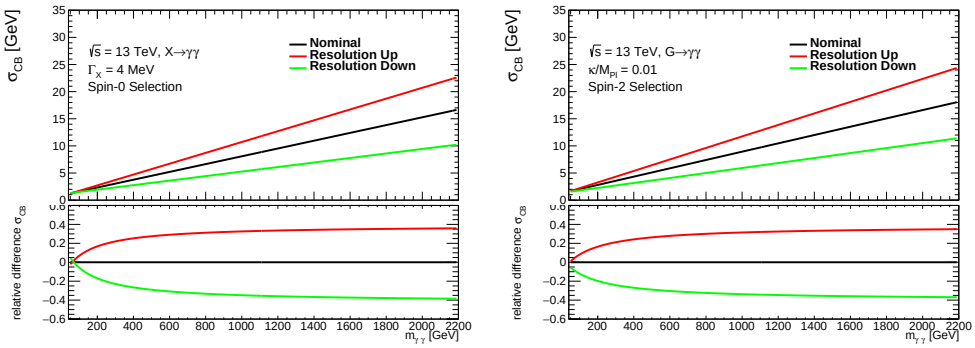

Figure 9.2: Variation of the σ_{CB} parameter due to up/down shift of the calorimeter resolution parameters, as a function of M_X, for the nominal NW scalar samples (left) and the graviton $k/\overline{M}_{\mathrm{Pl}} = 0.01$ samples (right). The bottom insets show the relative difference between the shifted samples and the nominal sample.

	Scalar	Graviton
200	2.33 GeV $^{+17\%}_{-17\%}$	-
500	4.49 GeV $^{+27\%}_{-29\%}$	5.10 GeV $^{+26\%}_{-29\%}$
700	6.28 GeV $^{+31\%}_{-33\%}$	7.02 GeV $^{+30\%}_{-32\%}$
2000	15.27 GeV $^{+36\%}_{-38\%}$	16.60 GeV $^{+35\%}_{-37\%}$

Table 9.1: Examples of DSCB σ_{CB} parameter for the Narrow width spin-0 ($\Gamma = 4$ MeV) and spin-2 ($k/\overline{M}_{\mathrm{Pl}} = 0.01$) samples, and the associated uncertainty.

9.1.1 Photon energy resolution

The uncertainty on the photon energy resolution is applied consistently on the two (leading and subleading) photons in the signal MC samples and propagated to the invariant mass distribution. The signal $m_{\gamma\gamma}$ distribution is broader for positive variation and narrower for negative variation of this systematic uncertainty. The resulting $m_{\gamma\gamma}$ distributions are then fitted using the multiple mass point fit method to extract new signal parameterisation parameters for both the up and down variations of the resolution systematic.

The change in the resolution parameter values mainly impact the σ_{CB} parameter: Figure 9.2 shows the fitted σ_{CB} values for the up and down shifts, compared to the nominal value as a function of M_X. The bottom plot shows the relative difference between the modified samples and the nominal samples. The systematic on σ_{CB} is taken into account in the statistic model as a single nuisance parameter, its value is parameterized by interpolating between the nominal and shifted values of σ_{CB}.

In Table 9.1 some values of the DSCB σ_{CB} parameter and its uncertainties both for narrow samples of spin-0 and spin-2 are reported. The uncertainties are relative to the corresponding nominal value of σ_{CB} at the same mass.

9.2 Systematic uncertainties on the signal yield

The sources of systematic uncertainties taken into account for the number of expected signal events are the photon identification, isolation selection and model-dependence uncertainties. Uncertainties on photon energy scale and resolution have no effect on the selected number of signal events. Other than the analysis-related systematic uncertainties an uncertainty on the integrated luminosity is included. This systematic is different for data collected in 2015 and in 2016.

9.2.1 Photon identification uncertainty

The uncertainty on the photon identification selection is based on the comparison of the signal efficiency obtained using Monte Carlo samples before and after applying shifts (accounting for the difference between data and simulation) on the shower shape distributions used in the identification selection (identification explained in Section 5.4.4). The shifts on the shower shape distribution are applied on both photons consistently and propagated to the final signal yield. Scale factors are calculated with this procedure as the ratio between the signal efficiencies with and without the shifts. Then the scale factor (with and without the shifts) are applied as a weight to photons resulting in an uncertainty on the efficiency of around 2%. These scale factors were calculated with data from the first part of 2015.

The relation of the photon identification uncertainty on the diphoton yield as a function of M_X is mostly flat as seen in Figure 9.3, however a small dependency is found. The uncertainty is parameterized as

$$\sigma_{ID}(M_X) = (a_0^{ID} + a_1^{ID} M_X)[1 + \exp(a_2^{ID} M_X)], \tag{9.1}$$

with values of the parameters for the scalar and graviton cases shown in Table 9.2. This parameterization is valid for all production modes and width values considered in the search.

	Spin-0	Spin-2
a_0^{ID}	0.0226	0.0262
a_1^{ID}	$1.72\,10^{-4}$ GeV^{-1}	$1.53\,10^{-4}$ GeV^{-1}
a_2^{ID}	-0.091 GeV^{-1}	-0.0411 GeV^{-1}

Table 9.2: Values of the parameters describing the photon ID uncertainty as described in the text.

9.2.2 Photon isolation selection uncertainty

The isolation uncertainty has two contributions: one from the calorimeter isolation selection and one from the tracking isolation selection. This uncertainty is completely different from the isolation matching uncertainty on the spin-2 background estimation that will be explained in the following section: this one is on the data/simulation difference between the isolation selection at reconstruction level, the other one is on the truth level/reconstruction level isolation selection difference in the simulation. The impact of the isolation uncertainty on the signal shape is

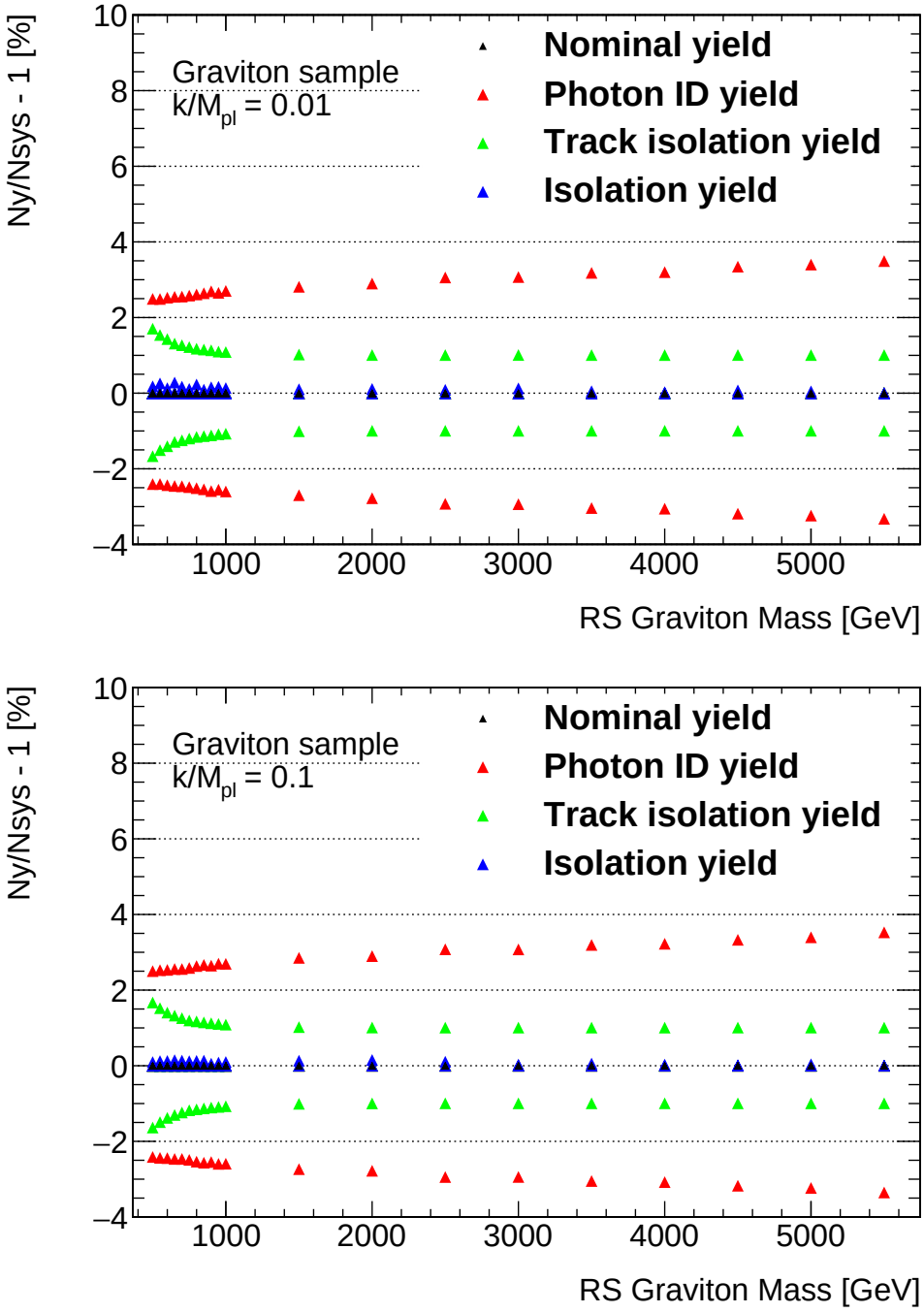

Figure 9.3: Systematic uncertainties associated with the photon identification, isolation and track isolation as a function of M_X for k/M$_{pl}$ = 0.01 (top) and k/M$_{pl}$ = 0.1 (bottom), for spin-2 MC signal samples. Signal samples of graviton at several masses were used.

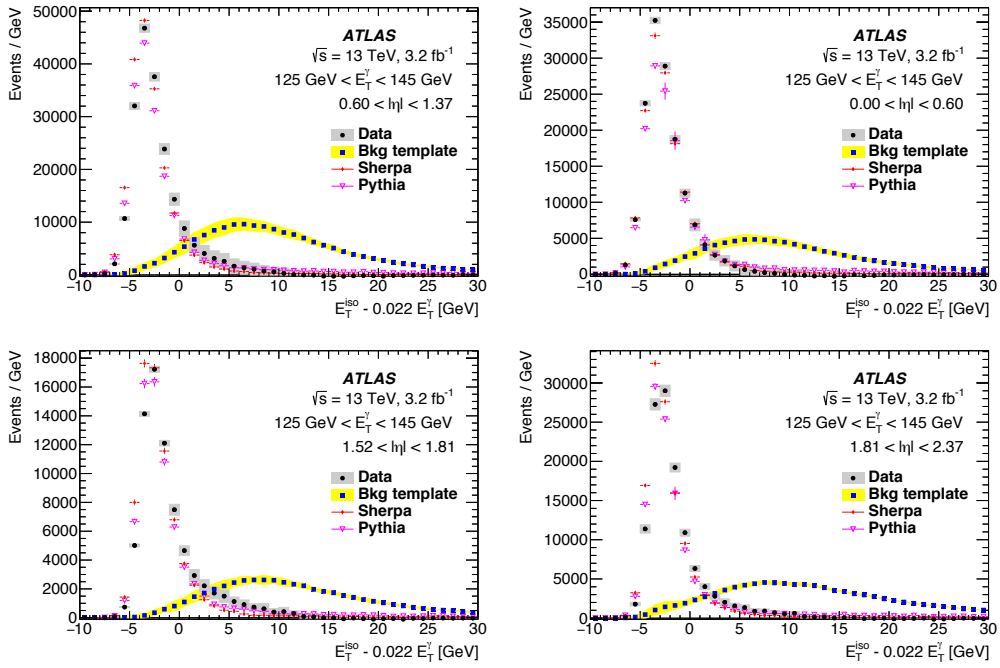

Figure 9.4: Distributions of the calorimeter isolation variable ($E_T^{iso} - 0.022E_T(\gamma)$) for photon candidates fulfilling the tight identification criteria for 125 GeV < E_T <145 GeV and four η regions. The background contribution to the data, shown as "Bkg template", has been subtracted. It has been determined using a control sample with a subset of the identification requirements inverted and normalized to the data in the region $E_T^{iso} - 0.022E_T(\gamma) > 12$ GeV. The data distributions are compared to predictions from simulation using either Sherpa or textscPythia8 to generate inclusive photon events. The error bars represent the statistical uncertainties. The bands around the background and the subtracted data distributions represent the estimate of the systematic uncertainties on the background estimate. The calorimeter isolation requirement corresponds to a cut at 2.45 GeV on this variable [10].

considered to be negligible. However the impact of the expected number of events is sizeable and is derived as follows (Figure 9.3 and Figure 9.5).

For the calorimeter-based selection, a data-driven shift, measured evaluating the isolation variable central value difference between MC and data (Figure 9.4), is applied to the isolation energy of the photons in MC simulation. The size of the shift is up to 2 GeV in the endcap region. The difference between the nominal selection and the selection on the corrected calorimeter isolation is used to estimate the associated systematic uncertainty. The corresponding uncertainty on the event yield is evaluated for several M_X values. The calorimeter-based isolation uncertainty is parameterized as

$$\sigma_{iso,calo}(M_X) = 0.01 \exp(a_0^{calo} M_X), \tag{9.2}$$

For the track-based requirement, a data-driven correction is applied to account for the imperfect modeling of the track isolation momentum of photons in MC simulation. A scale factor on the

	Spin-0	Spin-2
a_0^{calo}	$-1.08\,10^{-3}$ GeV^{-1}	$-6.26\,10^{-4}$ GeV^{-1}
a_0^{trk}	4.318	1034
a_1^{trk}	-3.321 GeV^{-1}	-1033 GeV^{-1}
a_2^{trk}	0.0061 GeV^{-1}	$7.825\,10^{-4}$ GeV^{-1}
a_3^{trk}	181.7 GeV	-2584

Table 9.3: Values of the parameters describing the isolation uncertainties as decribed in the text.

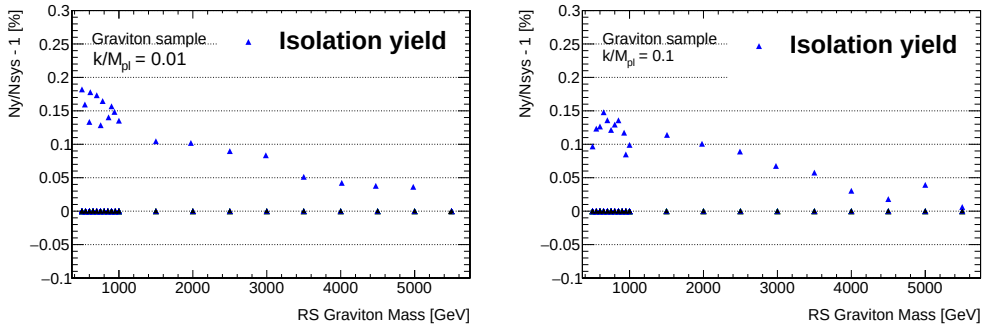

Figure 9.5: Systematic uncertainties associated with the photon isolation (zoomed version of Figure 9.3) as a function of $M_X$for k/M$_{pl}$ = 0.01 (left) and k/M$_{pl}$ = 0.1 (right), for spin-2 MC signal samples. Signal samples of graviton at several masses were used.

efficiency is calculated and the difference between the isolation efficiency of photons in MC simulation with and without this correction is taken as an uncertainty associated with this selection. The track-based isolation uncertainty is parameterized as

$$\sigma_{iso,trk}(M_X) = a_0^{trk} + a_1^{trk}\mathrm{erf}[a_2^{trk}(M_X - a_3^{trk})]. \tag{9.3}$$

The values of the parameters in these expressions for the scalar and graviton cases are shown in Table 9.3. In both cases, the parameterizations are valid for all width values considered in the search. The total uncertainty associated with photon isolation is obtained by adding these two uncertainties in quadrature.

9.2.3 Model dependence uncertainties for the scalar model

For the spin-0 model, an uncertainty is included to account for the efficiency dependence of the production modes for the new resonance. The reason for this uncertainty is that new physics doesn't necessarily follow the relative fraction of the production modes predicted by the SM, and each production mode provides a slightly different value of the C_X correction factor on the number of signal events. Then the residual differences from the production process dependency is treated as systematics uncertainty.

The C_X factors are evaluated for the five main production modes. The uncertainty is taken to be half the difference between the maximum and the minimum value at a given mass point. A fit to a constant distribution is performed to smooth out statistical fluctuations leading to a final value of ±2.1%.

In case of a large width signal, there is an additional 1.9% uncertainty assigned due to the small differences between C_X factors computed at different widths. This uncertainty is combined in quadrature with the production mode uncertainty to obtain a theory uncertainty of 2.8% on the C_X factor in the large width case. For the narrow width case, only the production mode uncertainty is used.

9.2.4 Luminosity and trigger uncertainty

An additional uncertainty on the luminosity [131] calculation is applied on the signal yield. This uncertainty is the only one that is different and un-correlated between year 2015 and 2016. Furthermore an uncertainty on the on-line trigger efficiency [132] is applied on the signal yield. The values of the systematics can be found in Table 9.5.

9.3 Systematic uncertainties on the background estimation

As explained in detail in Chapter 8, the background estimation is done with two different methods in the spin-0 and spin-2 analysis. The systematic uncertainties associated to the two different approaches are of different nature and are evaluated in different ways. For the spin-0 analysis the only source of uncertainty is the spurious signal. While for the MC-template method several systematic uncertainties on the shape of the MC spectrum are taken into account and will be explained in the following.

9.3.1 Systematic uncertainty on the functional form background shape

For the spin-0 analysis background modelization the main source of systematic uncertainty is the spurious signal. From the parameterization discussed in Section 8.3.1 the number of spurious signal events for a given signal hypothesis (M_X, α_X) is extracted. The spurious signal is then introduced in the model as a nuisance parameter on the signal yield centered at 0 and with a $\pm 1\sigma$ standard deviation equal to the number of spurious signal events.

9.3.2 Systematic uncertainties the MC template background model

As described in Chapter 8, the estimation of the background in the spin-2 analysis proceeds in two steps: determination of the shape of the irreducible and reducible background spectra and combination of the background shapes in the low-mass control region ($m_{\gamma\gamma}$<500 GeV). The systematic uncertainty sources for this model are from the theoretical uncertainties on the irreducible background shape uncertainties, from the reducible background estimation, from the uncertainty on the background fractions and from the statistical fluctuation of the LO MC (Sherpa).

Irreducible background. As described in the previous section, the shape of the $\gamma\gamma$ irreducible background is taken from Sherpa simulation corrected using a k-factor obtained from a NLO calculation (DIPHOX). To take into account theoretical uncertainties, several physical parameters are varied to estimate the impact on the correction. The relative difference from the central value of the k-factor is then taken as systematic uncertainty on the $\gamma\gamma$ background. The considered variations are the following: parton density functions (PDF) uncertainties, choice of PDF set, photon isolation at generator level, as well as fragmentation, factorisation and renormalisation scales.

More specifically, the variations used to assess the PDF uncertainties are the 44 variation sets for the 22 eigenvectors that are provided with the CTEQ66M PDF set, plus the difference between the central values of the (default) CTEQ66M and the (alternative) MSTW2008 NLO PDF set. Each of the fragmentation, factorisation and renormalisation scales is first varied separately by a factor 0.5 and 2; correlated variations (by the same amount) of all three scales are also considered. As several variations are considered for each source of uncertainty, the upward and downward uncertainties are respectively obtained as:

$$\Delta\sigma^{+} = \sqrt{\sum_{i\in\text{variations}} max(\sigma_i^{+} - \sigma_0, \sigma_i^{-} - \sigma_0, 0)}, \tag{9.4}$$

$$\Delta\sigma^{-} = \sqrt{\sum_{i\in\text{variations}} max(\sigma_0 - \sigma_i^{+}, \sigma_0 - \sigma_i^{-}, 0)} \tag{9.5}$$

with $\sigma_i^{\pm}$ being a variation for a given systematic source i and σ^0 the nominal value. A fit to the average of upward and downward variations $(\Delta\sigma^{+} + \Delta\sigma^{+})/2$ is used to smoothen and symmetrise the effect for each contribution.

Isolation matching. To evaluate the DIPHOX (Section 8.2.1) NLO corrections it is needed to use a parton-level isolation cut to mimic the effect of the reco-level isolation cut on the full simulation Monte Carlo. In order to evaluate the matching, a sample is needed in which both the parton-level isolation and the reco-level are available. For these studies the Sherpa samples from Section 6.2.2.1 are used. Sherpa can be used because it's an event generator that simulates all individual final state particles interfaced to the full simulation of the detector.

Diphoton events with $m_{\gamma\gamma} > 200$ GeV are selected using the same kinematic and photon ID requirements as in the spin-2 analysis. Each reconstructed photon is matched to the corresponding generator-level photon. For each generator-level photon the generator-level parton isolation (sum of the transverse energies of all partons inside a cone of $\Delta R < 0.4$ around the generator-level photon) is calculated. Then a corresponding selection is calculated on the generator-level to mimic the reco-level isolation cut of the analysis.

Finally "up" and "down" variations have been chosen such that a deviation of a few percent from the exact matching is covered in all pseudorapidity regions. This variation is then taken into account as a systematic uncertainty on the irreducible background shape as isolation matching uncertainty. The definition of the generator level cut and variations can be found in Table 9.4.

Scenario	Isolation requirement
Reco-level cut (for reference)	$E_{\mathrm{T}}^{\mathrm{iso},0.4} < 0.022 \times E_{\mathrm{T}}^{\gamma} + 2.45$ GeVand $E_{T,\mathrm{track}}^{\mathrm{iso},0.2} < 0.05 \times E_{\mathrm{T}}^{\gamma}$
"Up" variation of generator-level cut	$E_{\mathrm{T}}^{\mathrm{truth,parton},0.4} < 0.022 \times E_{\mathrm{T}}^{\gamma,truth} + 12$ GeVand $E_{\mathrm{T}}^{\mathrm{truth,parton},0.2} < 0.05 \times E_{\mathrm{T}}^{\gamma,truth}$
"Central" estimate of generator-level cut	$E_{\mathrm{T}}^{\mathrm{truth,parton},0.4} < 0.022 \times E_{\mathrm{T}}^{\gamma,truth} + 5$ GeVand $E_{\mathrm{T}}^{\mathrm{truth,parton},0.2} < 0.05 \times E_{\mathrm{T}}^{\gamma,truth}$
"Down" variation of generator-level cut	$E_{\mathrm{T}}^{\mathrm{truth,parton},0.4} < 0.022 \times E_{\mathrm{T}}^{\gamma,truth} + 3.5$ GeVand $E_{\mathrm{T}}^{\mathrm{truth,parton},0.2} < 0.05 \times E_{\mathrm{T}}^{\gamma,truth}$

Table 9.4: Tune of the generator-level cut used to mimic the tight reco-level isolation cuts on both the calorimetric and tracking isolations.

Reducible background. The assessment of the systematic uncertainties on the shape of the mass distributions of the reducible background components was performed studying the possible variations in the extrapolation fit function, as was already discussed in Section 8.1. The systematic is evaluated by fitting the $m_{\gamma\gamma}$ distributions in background control regions defined by changing LoosePrime definition: i.e. LoosePrime 5, LoosePrime3, LoosePrime 2 and Loose (LoosePrime 4 in case of jet-jet control region) instead of LoosePrime 4 (Loose in case of jet-jet). The goal of this check is to estimate the impact of the correlation between the diphoton invariant mass and the identification criteria. The systematic uncertainty is conservatively calculated as the difference between the AntiTight-LoosePrime4 (AntiTight-Loose in case of jet-jet) definition, and the largest deviating LoosePrime definition.

Background decomposition. In addition to the shape uncertainties, a smaller systematic uncertainty arises from the background decomposition technique. This uncertainty is computed by comparing the total background prediction using the yield estimates from different LoosePrime definitions. Then the uncertainty is propagated to the background model with the variation of the composition on the low mass control region.

Total systematic uncertainty on the MC-template. Furthermore the statistic uncertainty of the LO MC used for the irreducible background determination is taken into account. To do so a systematic uncertainty is associated to each bin in the final template PDF allowing it to change within the statistical error of the MC for that bin of $m_{\gamma\gamma}$. This source of systematic variation is completely un-correlated to the $m_{\gamma\gamma}$ variable, each bin can vary independently. The discontinuities seen in the red line of Figure 9.8 correspond to the mass slices that have been used in the event simulation. The effect of the statistic systematics can be seen in Figure 9.6. However the procedure dramatically increase the number of free parameters in the final statistical analysis, adding a few hundreds of nuisance parameter to the fit.

The shape and statistic uncertainties in the prediction of the total background (using the

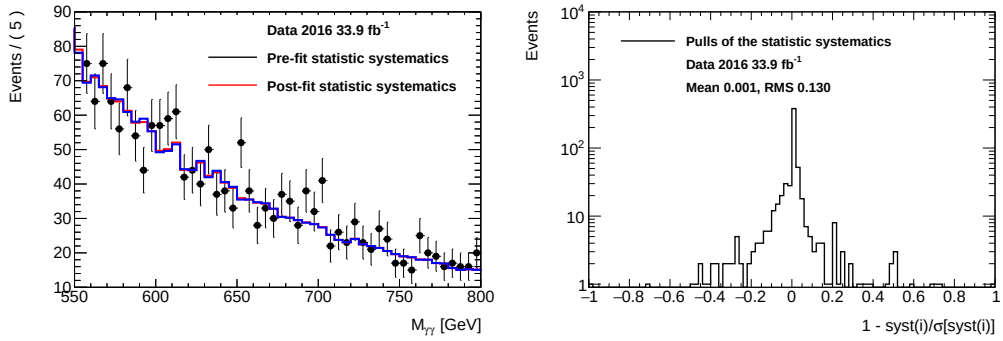

(a) **(b)**

Figure 9.6: Left: effect of the statistic systematic shown in a small interval of $m_{\gamma\gamma}$Ṙight: distribution of the post-fit (background-only fit to data 2016) pulls of the statistic systematics over the whole $m_{\gamma\gamma}$ range.

graviton selection) are summarised in Fig. 9.8 as a function of $m_{\gamma\gamma}$. The shape of the irreducible background uncertainty is the largest contributor to the total uncertainty for $m_{\gamma\gamma}$ higher that 2 TeV, while the isolation selection systematic uncertainty dominates for lower $m_{\gamma\gamma}$. The post-fit pulls of the background systematics can be seen for the two years in Figure 9.7.

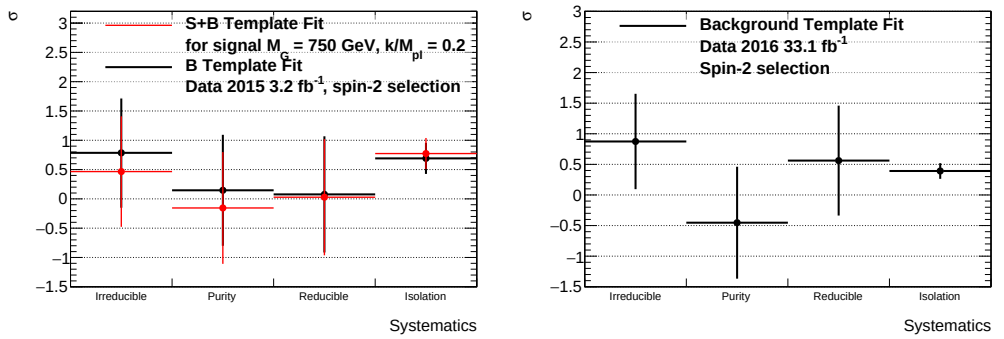

Figure 9.7: Post-fit pulls of the background systematic for the spin-2 selection for 2015 (left) and 2016 (right). For data 2016 the pulls for the background-only fit is shown, while for data 2015 the pulls for the background-only and the signal plus background fit (with the signal in the excess region) are shown.

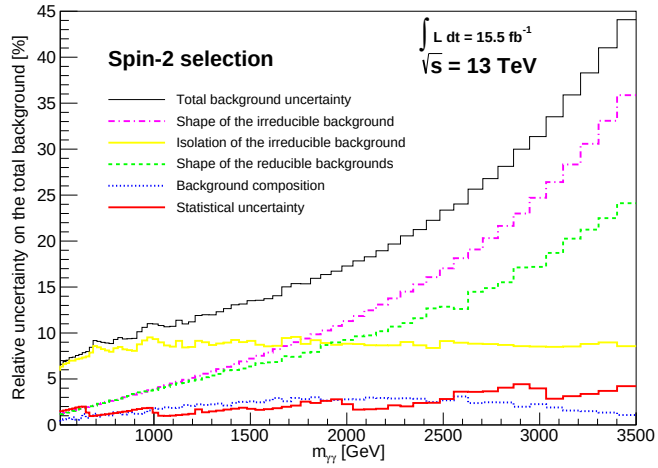

Figure 9.8: Uncertainty in the total background estimate as a function of $m_{\gamma\gamma}$ for the spin 2 analysis. The contributions due to the PDF variations, isolation matching, reducible background and decomposition are shown. The contribution labelled "statistical uncertainty" refers to the uncertainty due to the finite number of SM $\gamma\gamma$ background events simulated using Sherpa MC simulation.

Source	Uncertainty (spin-0)	Uncertainty (spin-2)	Reference
	Signal yield		
Luminosity	±2.1% (2015), ±3.7% (2016)	±2.1% (2015), ±3.7% (2016)	Ref. [131]
Trigger	±0.5%	±0.5%	Ref. [132]
Photon identification	±2 – 3%, mass-dependent	±2 – 3%, mass-dependent	Section 9.2.1
Isolation efficiency	±1 – 4%	±1 – 2%	Section 9.2.2
Scalar production process	±2.8%	-	Section 9.2.3
Photon energy scale	negligible	negligible	Section 9.2.3
Photon energy resolution	negligible	negligible	Section 9.2.3
	Signal modeling (on σ_{CB})		
Photon energy resolution	$^{+17\%}_{-17\%}$ ($M_X = 200$ GeV) $^{+36\%}_{-38\%}$ ($M_X = 2TeV$)	$^{+26\%}_{-29\%}$ ($M_X = 500$ GeV) $^{+35\%}_{-37\%}$ ($M_X = 2TeV$)	Section 9.1.1
	Background		
Spurious Signal for 2015 and 2016	0.11 – 19.9 events, NWA 0.36 – 117 events, LWA α= 10%	- -	Section 8.3.1
MC template uncertainties	-	Figure 9.8	Section 9.3.2

Table 9.5: Summary of the main sources of systematic uncertainty for the measurement of σ_{fiducial} for the spin-0 and spin-2 analyses. Unless written otherwise, numbers are mass independent.

CHAPTER 10

Statistical framework

In high-energy physics a well-defined statistical framework is crucial to claim a discovery or asses exclusion limits for a given model. In the following chapter the procedure specific to this analysis to calculate the statistic results will be explained. Results will be based on a frequentist approach based on a maximum profile likelihood fit using Wilks and Walds approximations as explained in detail in Appendix A. The signal parametrization is the one described in Chapter 7 and the background model is described in Chapter 8. The systematic uncertainties are listed in Chapter 9.

The signal plus background model used to describe data is a per-event PDF:

$$\begin{aligned}
&\mathcal{M}(m_{\gamma\gamma};\sigma_{fid},M_X,\alpha_X,N_{bkg},\boldsymbol{a},\boldsymbol{\theta_S}) = \\
&N_{sgn}(\sigma_{fid},M_X,\boldsymbol{\theta_S})f_{sgn}(m_{\gamma\gamma};M_X,\alpha_X,\theta_\sigma) + N_{bkg}f_{bkg}(m_{\gamma\gamma};\boldsymbol{a}) \\
&\mathcal{M}(m_{\gamma\gamma};\sigma_{RS},M_G,k/\overline{M}_{\mathrm{Pl}},N_{bkg},\boldsymbol{\theta_S},\boldsymbol{\theta_B}) = \\
&N_{sgn}(\sigma_{RS},M_G,\boldsymbol{\theta_S})f_{sgn}(m_{\gamma\gamma};M_X,k/\overline{M}_{\mathrm{Pl}},\theta_\sigma) + N_{bkg}f_{bkg}(m_{\gamma\gamma};\boldsymbol{\theta_B})
\end{aligned} \tag{10.1}$$

f_{sgn} and f_{bkg} are the signal and background PDFs. The quantities N_{sgn} and N_{bkg} are the number of signal events and the background components respectively. σ_{fid} is the fiducial production cross-section while σ_{RS} is the graviton production cross-section. The $\boldsymbol{a}$ are the background shape parameters for spin-0 analysis and $\boldsymbol{\theta_B}$ are the background nuisance parameters for the spin-2 analysis. More specifically the $\boldsymbol{\theta_B}$ include the fully correlated shape systematic (Diphox PDF and isolation matching, reducible background, background decomposition) and the statistic uncertainty from the Sherpa MC. The $\boldsymbol{\theta_S}$ collectively designates the nuisance parameters on the signal yield and θ_σ the nuisance parameter on the photon energy resolution.
As listed in Chapter 9 the nuisance parameters $\boldsymbol{\theta_S}$ on the signal yield are:

- θ_{lumi}: uncertainty on the integrated luminosity of the data sample. Different between year 2015 and year 2016.
- $\theta_{eff,X}$, $\theta_{isol,X}$: systematic uncertainties on photon identification and isolation selection efficiencies.
- θ_{Th}: model-dependance uncertainty on the cross section (spin-0 only).

- θ_{SS}: spurious signal (spin-0 only).

N_{bkg} is a free parameter in the fit, while N_{sgn} is parameterized in the spin-0 (Higgs) and spin-2 (RS graviton) cases as

$$\begin{aligned} N_{sgn,Higgs}(\sigma_{fid}, M_X, \boldsymbol{\theta}_{N_{sgn}}) &= \sigma_{fid}\, C_X \mathcal{L} \prod_{n=1}^{|\boldsymbol{\theta}_{N_{sgn}}|} K_i(\theta_{Si}) \\ N_{sgn,RS}(\sigma_{RS}, M_X, \boldsymbol{\theta}_{N_{sgn}}) &= \sigma_{RS}\, \epsilon_{ff,G} \mathcal{L} \prod_{n=1}^{|\boldsymbol{\theta}_{N_{sgn}}|} K_i(\theta_{Si}) \end{aligned} \tag{10.2}$$

Where $\mathcal{L}$ is the integrated luminosity of the sample, ϵ_{ff} is the efficiency of the selection for RS graviton, C_X is the spin-0 efficiency factor and the $K_i(\theta_{Si})$ factors parameterize the systematic uncertainties on the number of signal events. For these uncertainties the following expression is used:

$$K_i(\theta_{Si}) = e^{\log(1\pm\theta_{Si}\sigma_{Si})} \tag{10.3}$$

where the relative variations on N_{sgn} for the systematic uncertainty σ_{Si} is as listed in Table 9.5. This expression ensures that the modifications to the signal event yield for $\theta_{Si} = \pm 1$ are exactly equal to the $\pm 1\sigma_{Si}$ variations used to define the uncertainties and positive defined.
The final likelihood is then multiplied for the gaussian constrains of the nuisance parameters (comprehending the ones on the signal yield, on the resolution and on the background) with mean $\theta_{glob,k}$ and $\sigma = 1$:

$$C(\theta_k) = e^{-\frac{1}{2}(\theta_k - \theta_{glob,k})^2} \tag{10.4}$$

The overall likelihood, including extended and constraint terms, reads:

$$\begin{aligned} &\mathcal{M}_f(\sigma_{fid}, M_X, \alpha_X, N_{bkg}, \boldsymbol{a}) = \\ &e^{-\left(N_{sgn}+N_{bkg}\right)} \left[\prod_{i=1}^{n} \mathcal{L}(m_{\gamma\gamma_i}; \sigma_{fid}, M_X, \alpha_X, N_{bkg}, \boldsymbol{a})\right] \\ &\left[\prod_{k=1}^{\dim\boldsymbol{\theta}} \exp\left(-\tfrac{1}{2}\left(\theta_k - \theta_{glob,k}\right)^2\right)\right] \\ &\mathcal{M}_f(\sigma_{RS}, M_G, k/\overline{M}_{\mathrm{Pl}}, N_{bkg}, \boldsymbol{\theta_B}) = \\ &e^{-\left(N_{sgn}+N_{bkg}\right)} \left[\prod_{i=1}^{n} \mathcal{L}(m_{\gamma\gamma_i}; \sigma_{RS}, M_G, k/\overline{M}_{\mathrm{Pl}}, N_{bkg}, \boldsymbol{\theta_b})\right] \\ &\left[\prod_{k=1}^{\dim\boldsymbol{\theta}} \exp\left(-\tfrac{1}{2}\left(\theta_k - \theta_{glob,k}\right)^2\right)\right] \end{aligned} \tag{10.5}$$

where $\theta_{glob,k}$ is the set of auxiliary measurements used to constrain the systematic uncertainties. In the calculation of the significance the values of these variables is fixed at $\boldsymbol{\theta_{glob}} = \mathbf{0}$, however their value is randomly thrown in the generation of toy MC.

10.0.1 Specific spin-0

The region tested for a new signal in the spin-0 analysis is [200, 2500] GeV, then limits are evaluated in the region [200, 3500] GeV. In addition to the ones discussed above 2 new nuisance parameters are introduced:

- θ_{C_X}: production-mode uncertainty on the C_X factor.
- θ_{SS}: uncertainty from the spurious signal estimation.

In this analysis N_{sgn} is parameterized as:

$$N_{sgn}(\sigma_{fid}, M_X, \boldsymbol{\theta}_{N_{sgn}}, \theta_{SS}) = \sigma_{fid}\,\epsilon_{ff}\,\mathcal{L}\,C_X(M_X)\prod_{i=1}^{|\boldsymbol{\theta}_{N_{sgn}}|} K_i(\theta_i) + \sigma_{SS}\,\theta_{SS} \tag{10.6}$$

$C_X(M_X)$ the value of the C_X factor for the considered mass M_X. σ_{SS} and θ_{SS} the spurious signal uncertainty and its associated nuisance parameter. The statistical treatment is performed with an unbinned likelihood. The usual gaussian constraints are added for these 2 nuisance parameters to the likelihood.

10.0.2 Specific spin-2

The region tested for a new signal in the spin-2 analysis is [500, 2500] GeV, then limits are evaluated in the region [500, 3500] GeV. The uncertainties described in Section 9.3.2 are implemented in the model as four independent nuisance parameters with Gaussian constraints. The effect of the limited MC statistic is also included in the model by means of one nuisance parameter of a different value per bin of the template, again associated with a Gaussian constraint. To reduce the number of parameters of the fit the bin by bin uncertainties are dropped for masses above 1.5 TeV where their contribution is subdominant. The statistical treatment (p_0 and limits) is performed with the same methodology as used for the spin-0 analysis, however using a binned likelihood with 5 GeV bin size to avoid large computing time.

10.1 Local significance

In both analyses a signal of unknown mass M_X, width α_X (or coupling $k/\overline{M}_{\rm Pl}$, for simplicity from now on α_X will refer to width in both models), and signal strength μ is searched on top of a smooth background distribution described by nuisance parameters $\boldsymbol{\theta}$ (in the following N_{bkg} is considered a nuisance parameter). The signal strength which is a multiplier of the cross-section is the parameter of interest. The test of the background-only against the signal-plus-background with specified M_X, α_X is quantified with the q0 profile likelihood ratio test statistic (Section A.2):

$$q_0(M_X, \alpha_X) = -2\log \mathcal{L}(0, M_X, \alpha_X, \hat{\hat{\boldsymbol{\theta}}})/L(\hat{\mu}, M_X, \alpha_X, \hat{\boldsymbol{\theta}}) \tag{10.7}$$

where $\hat{\hat{\boldsymbol{\theta}}}$ are the parameters for best fit background-only model and $\hat{\mu}, \hat{\boldsymbol{\theta}}$ are the parameters for the best fit signal-plus-background model for a specified mass and width [133].

The local p0 is then computed for each pair of $q_0(M_X, \alpha_X)$, a 2-D scan is made in these two parameters. The "uncapped p-value" definition is used, so that $p_0 = 0.5$ corresponds to no signal, $p_0 < 0.5$ to positive signal, and $1 > p_0 > 0.5$ to negative signal. From the p0 the local significance $Z_0^{\rm local}$ (in σ) can be calculated as

$$Z = \Phi^{-1}(1 - p0) \tag{10.8}$$

where Φ^{-1} is the quantile (inverse of the cumulative distribution) of the standard Gaussian. Then the maximum significance $Z_{0,\,\rm max}^{\rm local}$ value is found for the (M_X, α_X) hypothesis that leads to the largest deviation from the background-only hypothesis, which corresponds to $q_{\rm max}$.

Conventionally in the particle physics field an observed phenomena is considered interesting if $Z > 3\sigma$ and very interesting if $Z > 5\sigma$. However when looking for a signal in a large range of the (M_X,α_X) parameter space the local significance is not the right quantity to look at. To understand the level of importance of an observation the global significance needs to be evaluated as explained in Section 10.2.

10.2 Global significance

10.2.1 Global significance

Statistical fluctuations of data leading to large Z_0^{local} are more common for searches than the corresponding p_0 probability would suggest. In a large searched phase space the probability to find anywhere in the search region a minimum as large or larger than the one singled out is increased, so the importance of the observed local significance is lower.

To take into account the phase space explored in the analysis a reduction of the maximum local significance, $Z_{0,\,\text{max}}^{\text{local}}$, is estimated and the "global" significance, Z_0^{global}, is evaluated. This reduction to the true "global" significance is referred to as the look-elsewhere effect.

Having two degrees of freedom in the search, specifically mass and width, provides a 2-D phase space to explore. So to evaluate the effect on Z_0^{global} the look-elsewhere effect for a 2-D phase space has to be considered. Two methods were exploited to evaluate it: one is based on pseudo-experiments, which is used for the baseline results, and one is based on a random-field estimation, which is used to cross-check the baseline results. The two methods will be explained in the next sections.

For the spin-0 analysis the range of parameters considered is $200 < M_X < 2500$ GeV and $0\% < \Gamma < 10\%$. While for the spin-2 analysis the range of parameters considered is $500 < M_X < 2500$ GeV and $0.01 < k/\overline{M}_{\text{Pl}} < 0.3$.

10.2.2 Global significance with pseudo-experiments

The relation between Z_0^{global} and Z_0^{local} is estimated using signal plus background fits to background-only pseudo-experiments. The pseudo-experiment are generated with the background model described above with the following procedure: a maximum-likelihood fit of the background-only PDF is performed on the observed data and the profiled values of the nuisance parameters are stored. Then, in the generation of each pseudo-experiment, the global observables $\boldsymbol{\theta_{glob}}$ are randomized according to a Gaussian constraint PDF with a mean value equal to the the profiled value of the corresponding nuisance parameters $\boldsymbol{\theta}$. Values of the experimental observables ($M_{\gamma\gamma}$, in this case) are randomly generated from the background-only PDF with a Poisson probability distribution.

Then the maximum Z_0^{local} must be determined for each one of the pseudo-experiments. One possible approach is to simply perform fits for every combination of (M_X,α_X) hypotheses, determine the Z_0^{local} value at each point and find the maximum value. This procedure is computationally

intensive, so an alternative was developed in which multiple fits with free (M_X, α_X, σ_{sgn}) are performed on each dataset. Prior to every fit, the initial values of the parameters of interest are randomized within the signal search range. The random starting values are chosen to be distant from each other to avoid to use the same starting point more than one time. Then for each fit the $Z_0^{\text{local,i}}$ is evaluated and the maximum value is taken as $Z_{0,\,\text{max}}^{\text{local,i}}$, this method has been proven to converge to the real $Z_{0,\,\text{max}}^{\text{local,i}}$ value with a modest number of free fits.

With a sufficient number of pseudo-experiments the statistical distribution of Z_0^{local} is built using the values of $Z_{0,\,\text{max}}^{\text{local,i}}$. Then the distribution is used as a statistical test to derive the value of Z_0^{global} from the Z_0^{local} measured in data. To calculate Z_0^{global} for a given $Z_{0,\text{observed}}^{\text{local}}$, the distribution of Z_0^{local}, represented by $H(Z_0^{\text{local}})$, is integrated from the observed value to infinity:

$$Z_{0,\text{observed}}^{\text{global}} = \int_{Z_{0,\text{observed}}^{\text{local}}}^{\infty} H(Z_0^{\text{local}}) dZ_0^{\text{local}} \tag{10.9}$$

In this way, a functional relation $Z_0^{\text{global}}(Z_0^{\text{local}})$ is determined. Binomial errors, based on the number of pseudo-experiments and the $p_{0,\text{observed}}^{\text{local}}$, are provided. The pseudo-experiment approach is generally more reliable than the random field method described in the next section, and it is used as the baseline approach to compute global significance.

10.2.3 Global significance from random fields

As a cross-check the global significance in data 2015 was also estimated with an alternative method using asymptotic distributions. This method was studied in the case of a one-dimensional mass scan in Reference [134] and generalized to multi-parameter scans in Reference [124]. In the case of the (M_X, α_X) signal scan the correction has the form

$$p_{\text{global}} \approx E[\phi(A_u)] = p_{\text{local}} + e^{-u/2}(N_1 + \sqrt{u}N_2) \,, \tag{10.10}$$

where u is a threshold on the $q_0(M_X, \alpha_X)$ test statistic, A_u is the set of parameter points (M_X, α_X) where $q_0(M_X, \alpha_X) \geq u$, $\phi[A_u]$ is the Euler characteristic of that set of points, and N_1 and N_2 are constants that characterize the signal and background distributions and must be determined from toy Monte Carlo. In order to estimate N_1 and N_2, around 20 background-only pseudo-datasets were generated, and for each a scan of $q_0(M_X, \alpha_X)$ is done. For each scan $\phi(A_u)$ is calculated for $u = 0.1$ and $u = 0.9$.

10.3 Exclusion limits

A 95% C.L. limit on the fiducial cross section for the spin-0 analysis and on the RS production cross section for the spin-2 analysis computed using the same $\tilde{q}_{\sigma_{\text{fid}}}$ estimator [133] as in the Standard Model $H \to \gamma\gamma$ search. The technique is based on the CL_s [135] with approximated distribution, more details can be seen in Appendix A.3. Both expected and observed limits are calculated using asymptotic formulae. The limit is evaluated every 5 GeV from $m_X = 200$ GeV (spin-0) or $m_X = 500$ GeV (spin-2) to $m_X = 2500$ GeV. Limits values as a function of M_X

are evaluated for several values of width of the signal resonance. The limit evaluated with the asymptotic formulae was compared in some points with the limit evaluated with MC Toys and the two methods were found in agreement in the mass region where sufficient data is available (at least a couple of events). At high $m_{\gamma\gamma}$ region where less than 3 events are present the asymptotic approximation does not work well and a discrepancy of $\sim 20-30\%$ was found.

10.4 Combination of 2015 and 2016 datasets

Data from year 2015 and year 2016 are considered two independent datasets, so they are treated in the statistical analysis as independent categories. The resulting categories are weighted with the integrated luminosity of the corresponding year: 3.2 fb^{-1} for 2015 and 12.2 fb^{-1} for 2016. However most of the inputs are taken to be identical for the two years:

- All nuisance parameters (systematic uncertainties) are fully correlated between the years, except for the luminosity uncertainty.
- The shape systematics are assumed to be identical.
- The luminosity central values are the integrated luminosities of each dataset, and the corresponding systematic uncertainty are different.
- The reducible background shape is obtained by combining the 2015 and 2016 data to benefit from the increased statistic since no significant discrepancy was observed between the two years.
- For the spin-0 analysis the background shape is parameterized using the same functional forms in both years. The shape parameters are also correlated across the two categories so that the background shape is identical in both.
- The background normalization in the two year is parameterized with independent parameters.

10.5 Compatibility between the 2015 and 2016 datasets

The compatibility between the 2015 and 2016 datasets is estimated using a modified version of the statistical model. Instead of having a single parameter for the signal cross section in 2015 and 2016, two cross-section parameters, one for each year, are used. For 2015, a free parameter σ_{2015} is used, while for 2016 the cross-section is expressed as $\sigma_{2016} = \Delta\sigma + \sigma_{2015}$, where $\Delta\sigma$ is a free parameter. A profile likelihood scan is then performed for the parameter $\Delta\sigma$. The compatibility significance is then computed as $\sqrt{\lambda(\Delta\sigma = 0)}$, where λ is the likelihood profile: $-2\log L$.

Part IV

Results

Chapter 11

Results

The statistical interpretation of the spin-0 and spin-2 analyses results are obtained using the functional form and the MC template technique respectively. In both cases 2-D scan of local significance is performed together with the assessment of the global significance. The compatibility between data from 2015 and data from 2016 is calculated. Then exclusion limits are provided as a function of M_X for several widths hypothesis using the combination of data 2015 and 2016. Tables summarizing the results can be found in Section 11.3.

The 2015 data have been reanalyzed since Reference [10] with improved photon reconstruction algorithms. These changes include new corrections for pileup in TRT detector, updated photon conversion reconstruction, updated training of the MVA energy in the crack region, new Z energy scale redone with data 2015+2016, better track removal in track isolation. The changes in local significance for both analyses are induced from migrations of various events in and out of the 700-800 GeV region.

In the spin-2 analysis, compared to the results in Reference [10], the highest local significance of the deviation from the background-only hypothesis with the 2015 dataset has decreased from 3.8 standard deviations to 3.27 standard deviations, the signal mass hypothesis corresponding to the largest excess is 730 GeV instead of 750 GeV with a $k/\overline{M}_{\mathrm{Pl}}$ value of 0.3 instead of 0.23.

The significance of the largest excess above the background-only hypothesis decreased from 3.9 standard deviations of Reference [10] to 3.41 standard deviations. The corresponding signal mass and width also changed, from a mass of 750 GeV and a relative width of 6% to a mass of 730 GeV and a relative width of 8%.

11.1 Spin-0 analysis results

Discovery p-value The two dimensional significance scan for the background-only hypothesis is shown in Figure 11.1 for data from 2016 and 2015 and in Figure 11.2 for the combined dataset. The p-values distributions can be seen in Figure 11.3 and Figure 11.4. In addition, one dimensional (as function of the mass m_X) p_0 plots are shown for benchmark values of α_X in Figure 11.5, separately 2015, 2016 and combined.

In the 2015 data, the most significant excess (with maximum local significance) was observed for $m_X \simeq 735$ GeVand a width of $\alpha_X = 8$ %, corresponding to 3.41 σ of local significance. In the

2016 data, for those mass and width values the local significance corresponds to 0.3 σ. The most significant excess in 2016 data is observed for $m_X \simeq 305$GeV for the narrow width hypothesis, corresponding to 2.01 σ local significance. Combining 2015 and 2016 data, the most significant excess is observed for $m_X \simeq 1595$GeV for the narrow width model, corresponding to 2.10 σ local significance.

Fits for maximum local significance The signal+background fit and background-only fit for the $[M_X, \alpha_X]$ signal parameters corresponding the most significance deviation can be seen in Figure 11.6 and in Figure 11.7 for 2015 and 2016 data respectively. In Figure 11.8 the fit for the combined 2015 and 2016 dataset is shown. The fits are for the mass and the width of the signal to the values of the most significant deviation from background in 2015 and 2016 data respectively. The goodness of the background-only fit is shown in Section 8.4.

Global significance The global significance was calculated using pseudo-experiments as explained in Section 10.2.2. For the maximum local significance of 2.10 σ in the spin-0 analysis for the combined 2015+2016 dataset, the global significance was found to be $(-0.14 \pm 0.03)\sigma$ (Figure 11.9). The negative significance means that for the median search in which only background is present the scan of local p_0 values across mass and width will identify at least one point with a deviation from the background hypothesis greater than or equal to 2.08 σ. This result can be interpreted as: the observed maximum local significance in the combined data from 2015 and 2016 is slightly lower than the one typically expected in a background-only dataset. The global significance of the excess in the 2015 dataset is estimated to be 1.4 σ (Figure 11.10).

Compatibility The compatibility between the results obtained with 2015 data and 2016 data is estimated to be 3.2 σ, following the method described in Section 10.5. The compatibility is calculated using the mass and width of the signal with maximum significance for spin-0 analysis in data from 2015. The profile likelihood ratio of $\Delta\sigma = \sigma_{2016} - \sigma_{2015}$ is shown in Figure 11.11.

The compatibility of the 2015 dataset at 13 TeV and the Run-I dataset at 8 TeV was estimated to be (Reference [10]): 1.2 σ for the gluon-gluon production scenario and 2.1 σ for the quark-antiquark production scenario. In Run-I a 2 σ significance was observed at 750 GeV in the spin-0 selection.

Limit on the fiducial cross-section A 95% C.L. limit on the parameter σ_{fid} is computed using the same $\tilde{q}_{\sigma_{\text{fid}}}$ estimator discussed in Section 10.3. Both expected and observed limits are produced based on the asymptotic formula to determine the cross-section value corresponding to 95% C.L. exclusion. The observed and expected limits with $\pm 1, 2\sigma$ deviation are evaluated every 10 GeV from $m_X = 200$ GeV to $m_X = 3500$ GeV. The results are shown for different values of α_X in Figure 11.12 for combined 2015 and 2016 data. In Figure 11.13 is shown the observed limit of year 2015, 2016 and the combination.

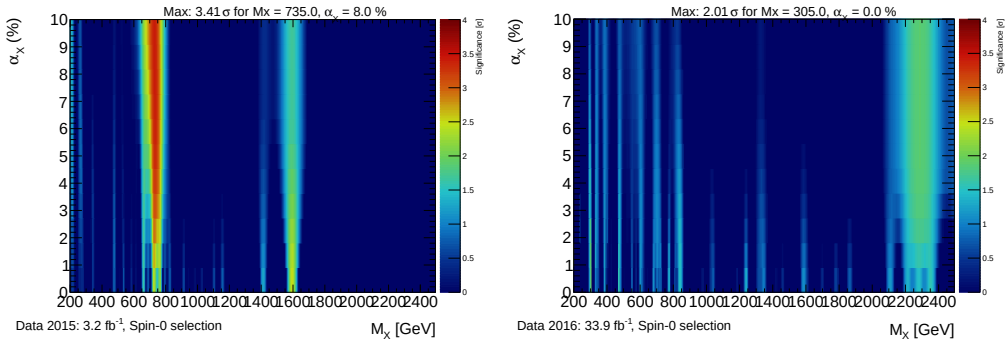

Figure 11.1: Observed 2-dimensional scan of the significance for the background-only hypothesis p_0, as a function of the probed resonance mass m_X and relative natural width α_X for 3.2 fb^{-1} of data 2015 (left) and 33.9 fb^{-1} of data 2016 (right).

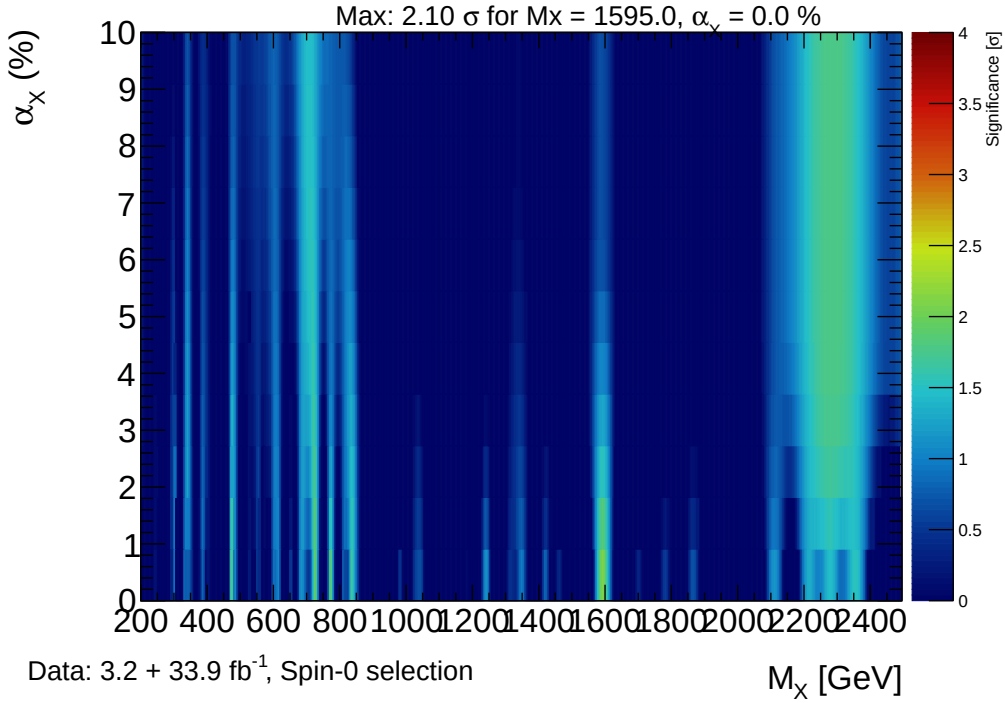

Figure 11.2: Observed 2-dimensional scan of the significance for the background-only hypothesis p_0, as a function of the probed resonance mass m_X and relative natural width α_X for 37.1 fb^{-1} of data 2015+2016.

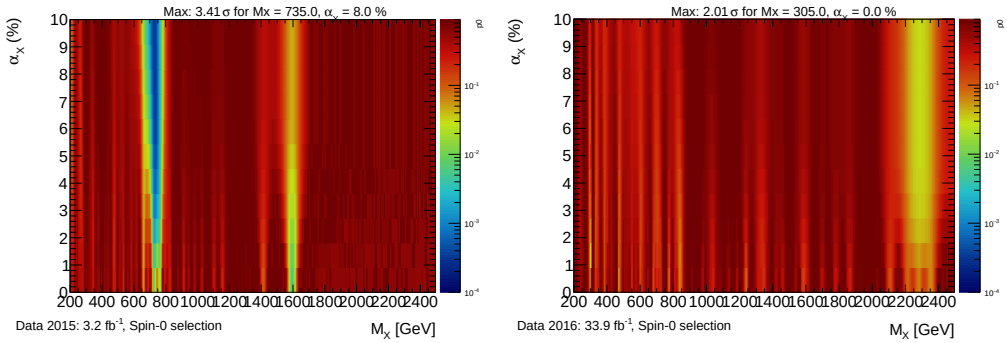

Figure 11.3: Observed 2-dimensional scan of the p-value for the background-only hypothesis p_0, as a function of the probed resonance mass m_X and relative natural width α_X for 3.2 fb^{-1} of data 2015 (left) and 33.9 fb^{-1} of data 2016 (right).

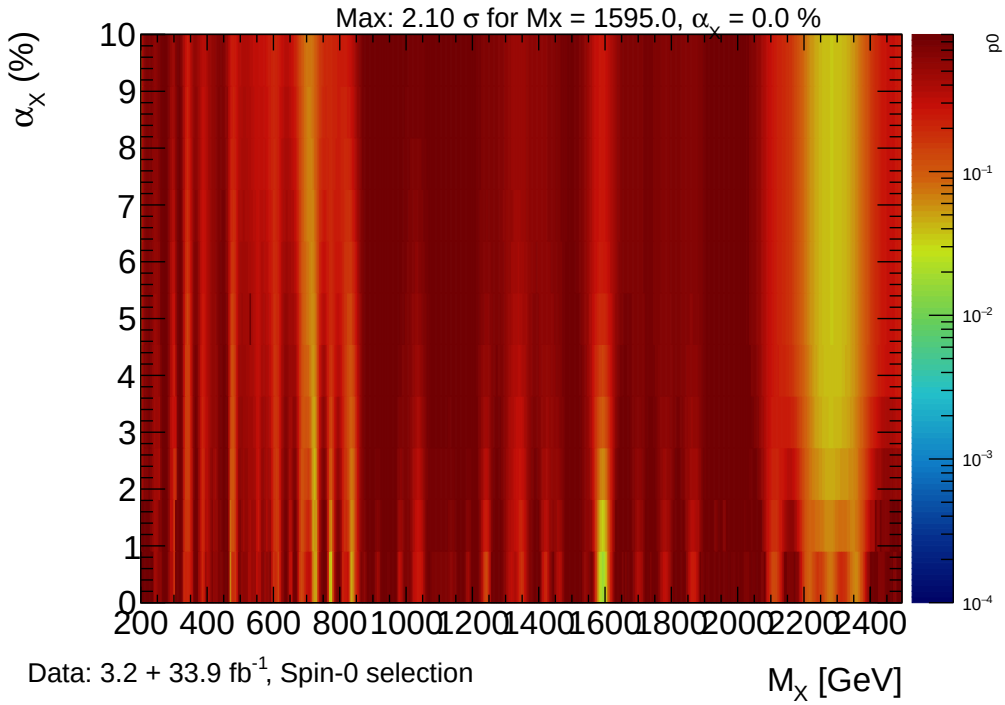

Figure 11.4: Observed 2-dimensional scan of the p-value for the background-only hypothesis p_0, as a function of the probed resonance mass m_X and relative natural width α_X for 37.1 fb^{-1} of data 2015+2016.

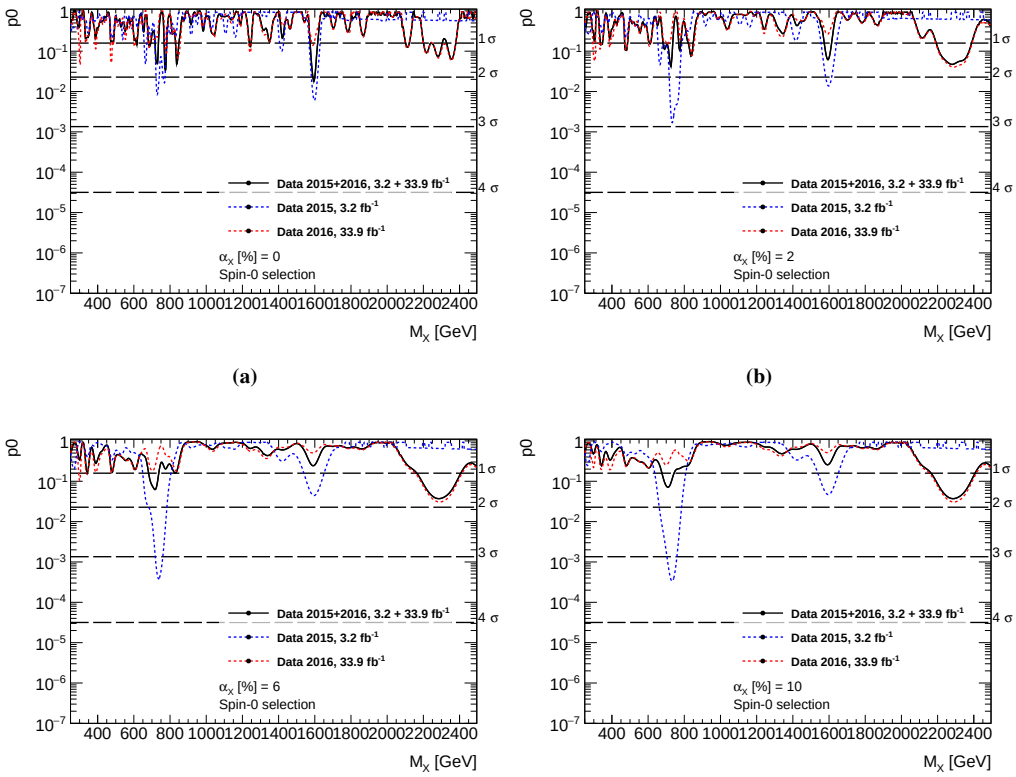

Figure 11.5: Observed scan of the significance for the background-only hypothesis as a function of the assumed mass, for various values of α_X. Results are shown for data from 2015 and 2016 data separately and for combined data of the two years.

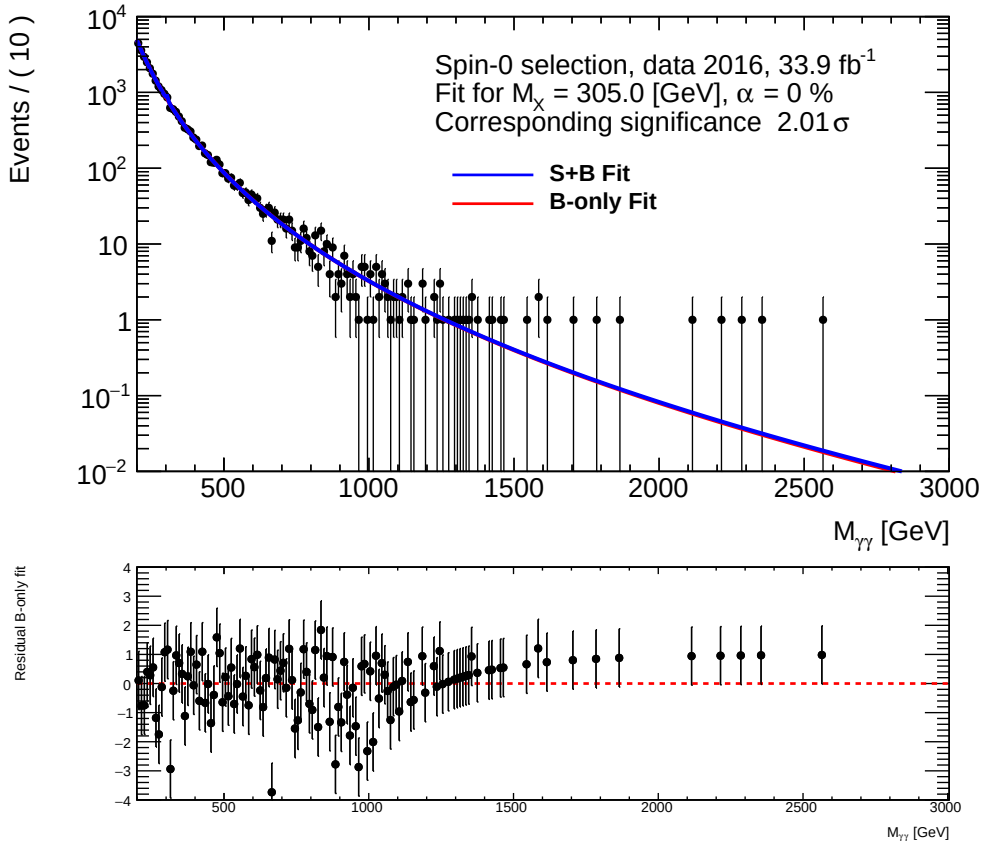

Figure 11.6: $m_{\gamma\gamma}$ spectrum from the diphoton candidates selected in a data-set corresponding to 33.9 fb^{-1} of 2016 data, with the signal+background fit and background-only fit superimposed. The subset plot shows the residual of the data with the background-only fit.

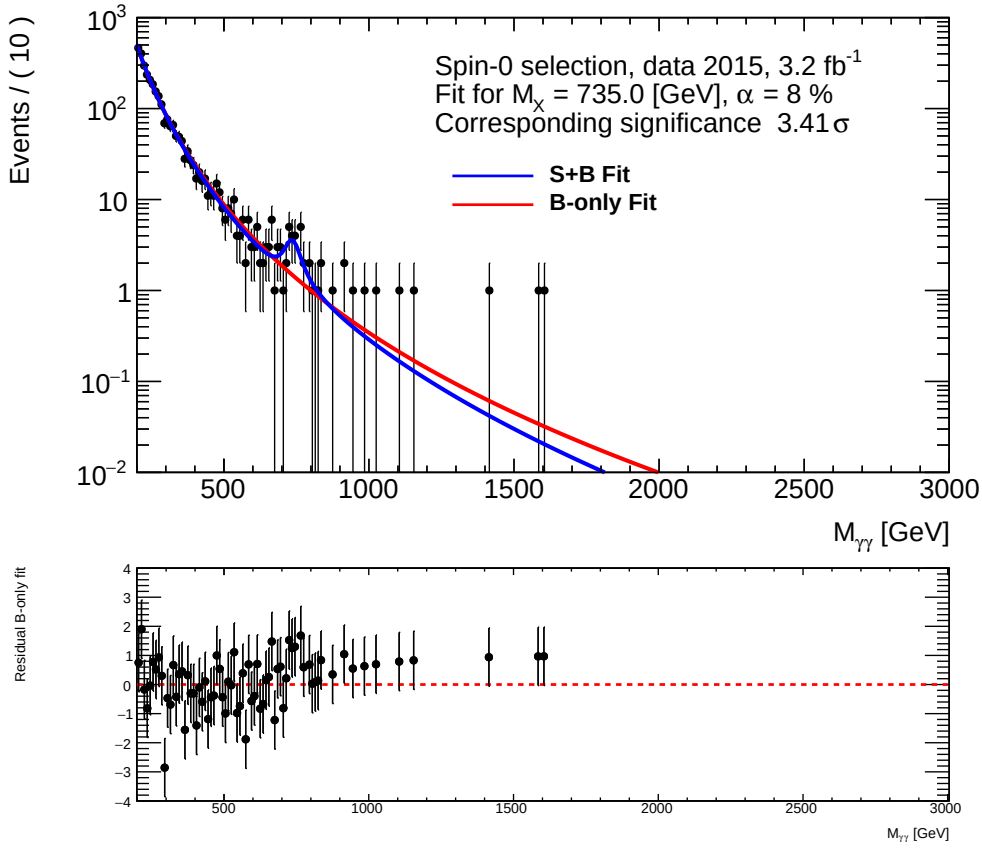

Figure 11.7: $m_{\gamma\gamma}$ spectrum from the diphoton candidates selected in a data-set corresponding to 3.2 fb^{-1} of 2015 data, with the signal+background fit and background-only fit superimposed. The subset plot shows the residual of the data with the background-only fit.

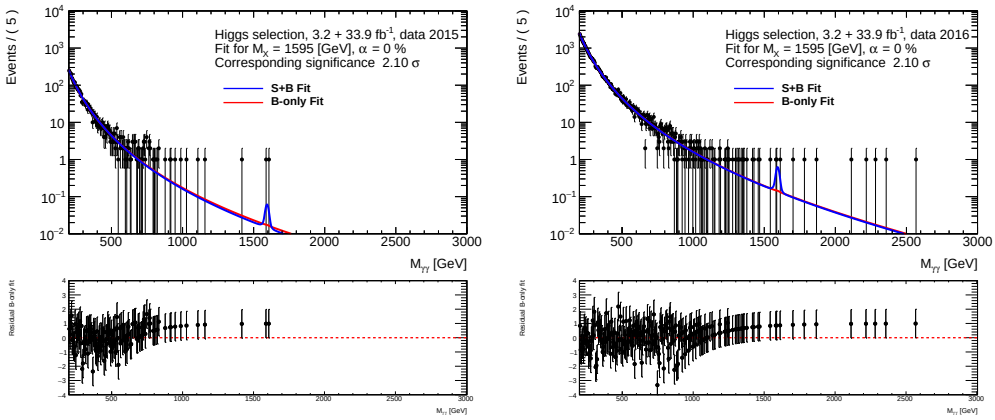

Figure 11.8: $m_{\gamma\gamma}$ spectrum from the diphoton candidates selected in a data-set corresponding to 3.2 fb^{-1} + 33.9 fb^{-1} of data projected in year 2015 (Left) and 2016 (Right), with the signal+background fit and background-only fit superimposed. The subset plot shows the residual of the data with the background-only fit.

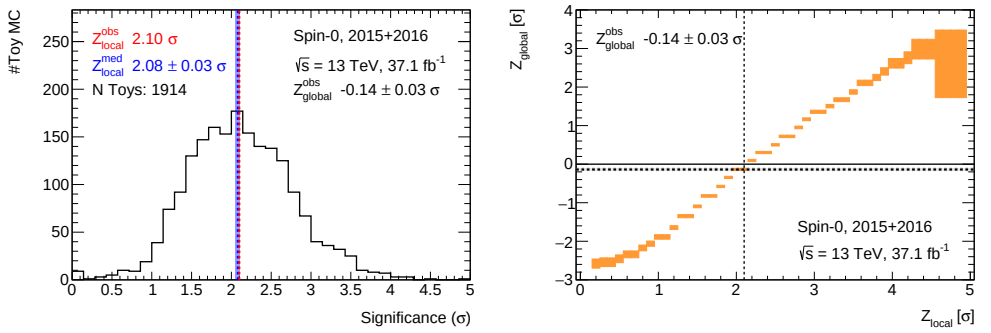

(a) **(b)**

Figure 11.9: Global significance for the spin-0 selection in the combined 2015+2016 dataset. Left: distribution of the local significances found in toys. Right: correspondence curve between local and global significance calculated from the toys.

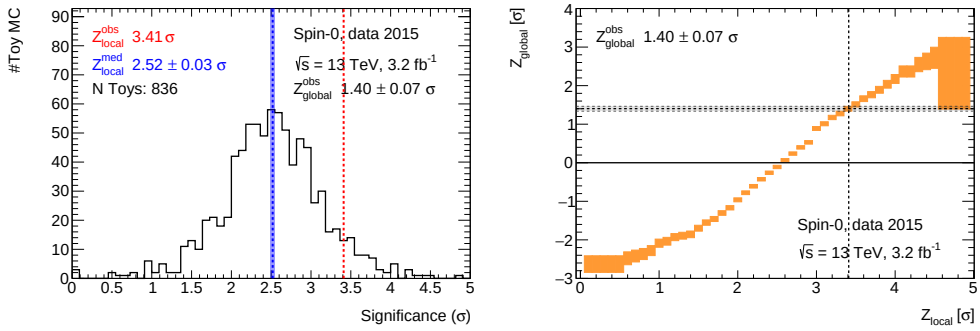

(a) **(b)**

Figure 11.10: Global significance for the spin-0 selection in data 2015. Left: distribution of the local significances found in toys. Right: correspondence curve between local and global significance calculated from the toys.

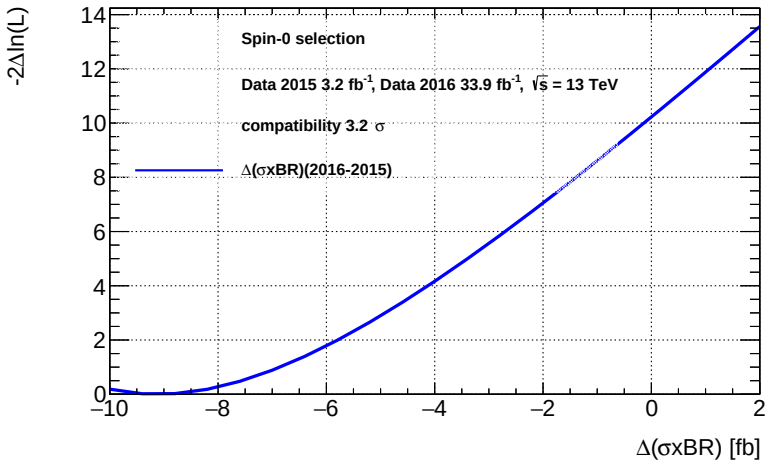

Figure 11.11: Profile likelihood ratio as a function of $\Delta\sigma = \sigma_{2016} - \sigma_{2015}$. The tested (M_X, α_X) point is the one with the maximum significance in data 2015.

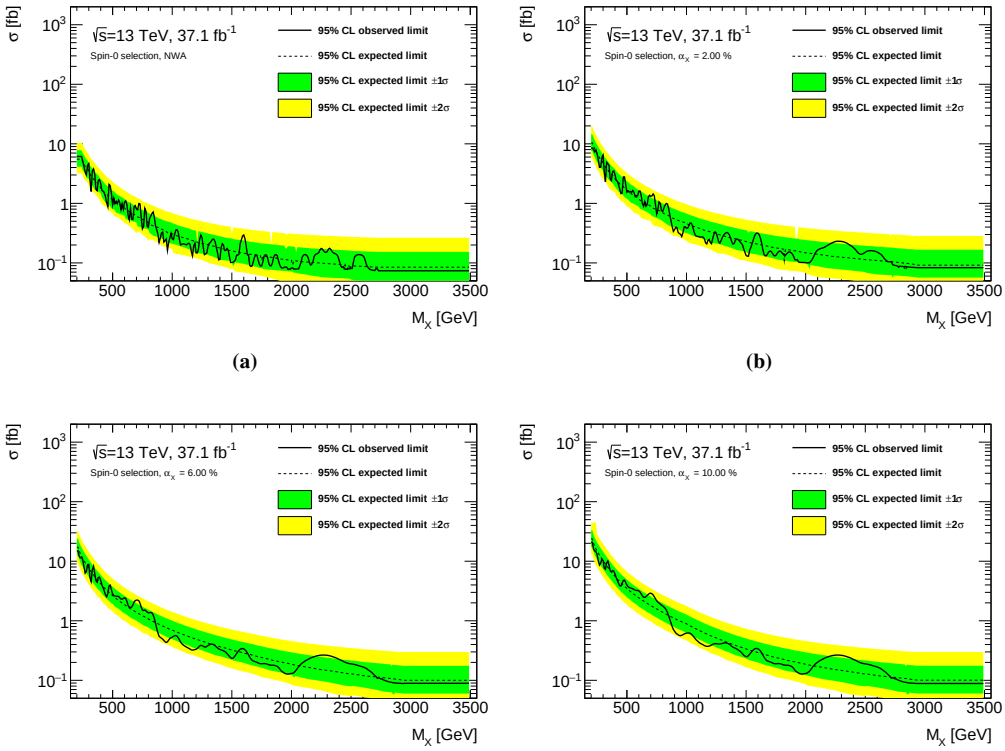

Figure 11.12: Expected and observed limit on the fiducial production cross-section limit σ_{fid} as a function of the resonance mass M_X, for various values of the signal width α for the combined 2015 and 2016 data-set.

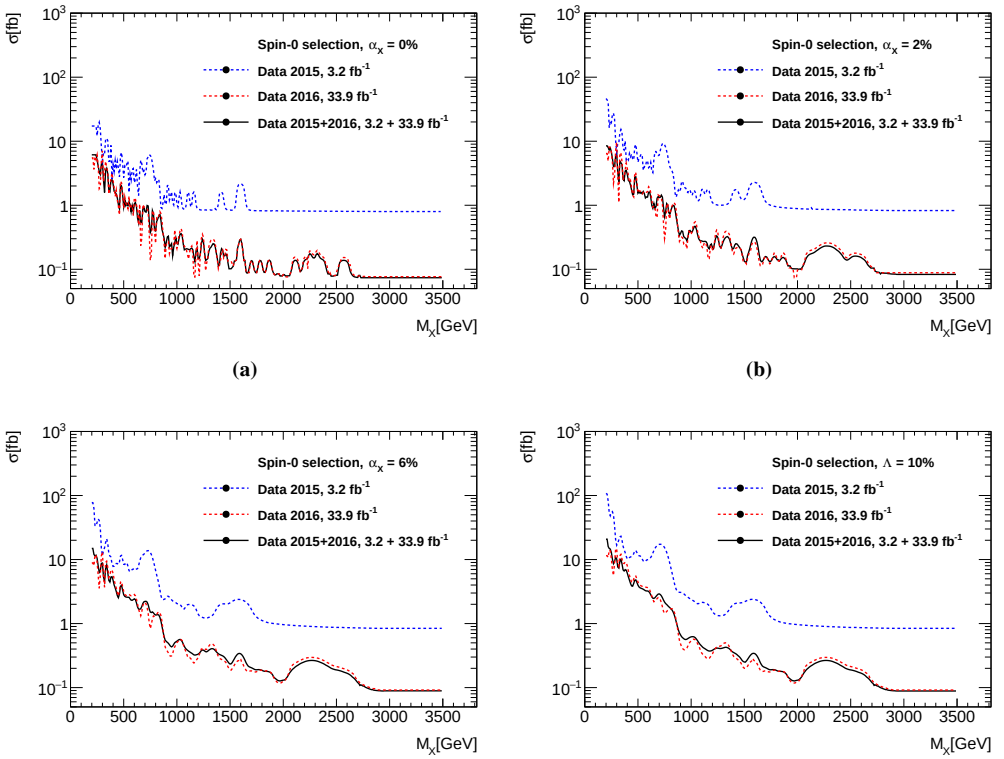

Figure 11.13: Observed limit on the fiducial production cross-section limit σ_{fid} as a function of the resonance mass M_X, for various values of the signal width α for the 2015, 2016 and combined data-set.

11.2 Spin-2 analysis results

Discovery p-value The two dimensional (allowing both the mass, m_X, and the coupling $k/\overline{M}_{\rm Pl}$ to float) significance is shown in Figure 11.1 for data from 2016 and 2015 and in Figure 11.15 for combined data from 2016 and 2015. The p-values distributions can be seen in Figure 11.16 and Figure 11.17. In addition, one dimensional (as function of the mass m_X) p_0 plots are shown for different values of $k/\overline{M}_{\rm Pl}$ in Fig. 11.18 (for separately 2015, 2016 and combined).

In the 2015 data, the most significant excess (maximum significance) was observed for $m_X \simeq$ 735 GeV and a coupling of $k/\overline{M}_{\rm Pl} = 0.3$, corresponding to 3.27 σ local significance. However in the 2016 data, for those mass and width values the local significance corresponds to 2 σ. The most significant excess in 2016 is observed for $m_X \simeq$ 700GeV and a coupling of $k/\overline{M}_{\rm Pl} = 0.25$, corresponding to 2.59 σ local significance. Combining 2015 and 2016 datasets, the most significant excess is observed for $m_X \simeq$ 705GeV and a coupling of $k/\overline{M}_{\rm Pl} = 0.3$, corresponding to 3 σ local significance.

Fits for maximum local significance The signal+background fit and background-only fit for the $[M_G, k/\overline{M}_{\rm Pl}]$ signal parameters corresponding the most significance deviation can be seen in Figure 11.19 and in Figure 11.20 for 2015 and 2016 data respectively. In Figure 11.21 the fit for the combined 2015 and 2016 dataset is shown. The fit are for the mass and the width of the signal to the values of the most significant deviation from background in 2015 and 2016 data respectively.

Global significance As in the spin-0 analysis the global significance was calculated using pseudo-experiments (Section 10.2.2). The most significant excess (3 σ at $m_X \simeq$ 705GeV, $k/\overline{M}_{\rm Pl} = 0.3$) corresponds to a global significance of $(1.07 \pm 0.06)\sigma$ (Figure 11.22). The global significance of the excess in the 2015 dataset is estimated to be 1.4 σ (Figure 11.23).

Compatibility The compatibility between the results obtained with 2015 data and 2016 data is estimated to be 2.2 σ, following the method described in Section 10.5. The compatibility is calculated using the mass and width of the signal with maximum significance for spin-2 analysis in data from 2015. The profile likelihood ratio of $\Delta\sigma = \sigma_{2016} - \sigma_{2015}$ is shown in Figure 11.24.

The compatibility of the 2015 dataset at 13 TeV and the Run-I dataset at 8 TeV was estimated to be (Reference [10]): 2.7 σ for the gluon-gluon production scenario and 3.3 σ for the quark-antiquark production scenario. In Run-I no excess was observed at 750 GeV in the spin-2 selection.

Limit on the total cross-section A 95% C.L. limit on the RS graviton production cross-section σ_{RS} is computed using the same $\tilde{q}_{\sigma_{\rm fid}}$ estimator discussed in Section 10.3. Both expected and observed limits are produced based on the asymptotic formula to determine the cross-section value corresponding to 95% C.L. exclusion. The observed and expected limit (expected with $\pm 1, 2\sigma$ deviation) is evaluated every 10 GeV from $m_X = 500$ GeV to $m_X = 3500$ GeV. The results are shown for different values of $k/\overline{M}_{\rm Pl}$ in Figure 11.25 for combined 2015 and 2016 data. In Figure 11.26 is shown the observed limit of year 2015, 2016 and combined.

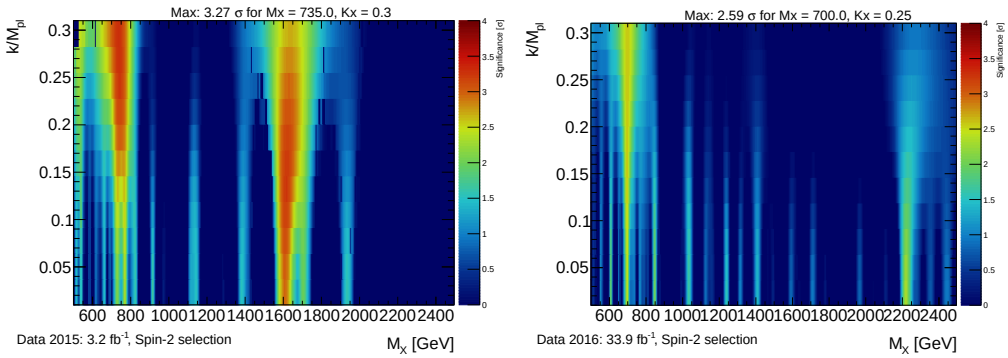

Figure 11.14: Observed 2-dimensional scan of the significance for the background-only hypothesis p_0, as a function of the probed resonance mass m_X and $k/\overline{M}_{\mathrm{Pl}}$ for 3.2 fb^{-1} of data 2015 (left) and 33.9 fb^{-1} of data 2016 (right).

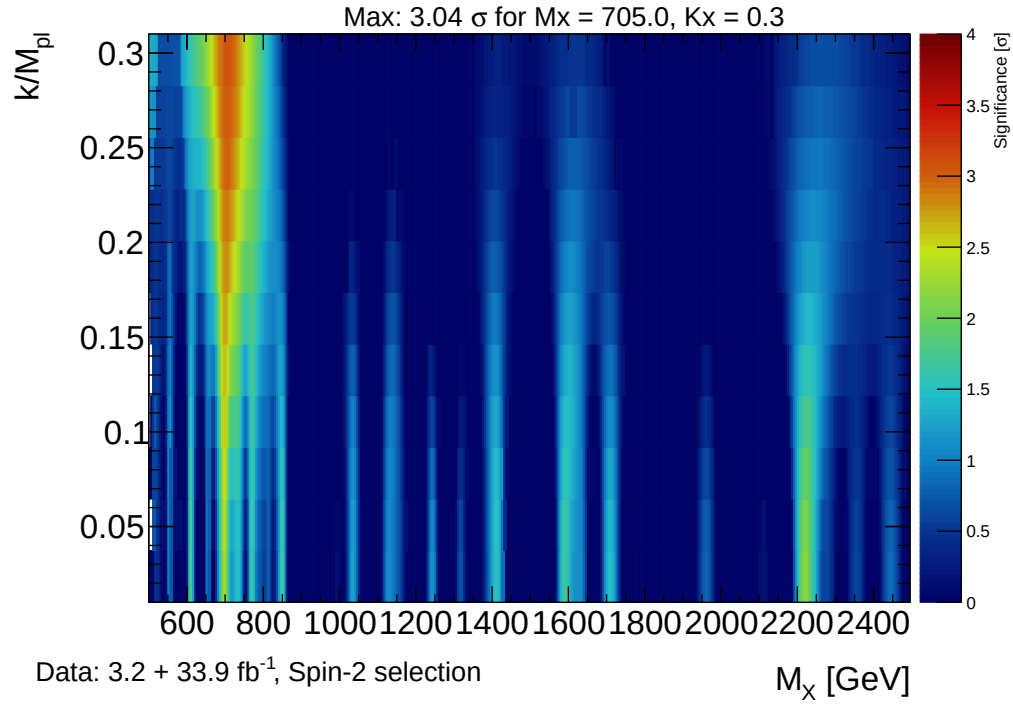

Figure 11.15: Observed 2-dimensional scan of the significance for the background-only hypothesis p_0, as a function of the probed resonance mass m_X and $k/\overline{M}_{\mathrm{Pl}}$ for 37.1 fb^{-1} of data 2015+2016.

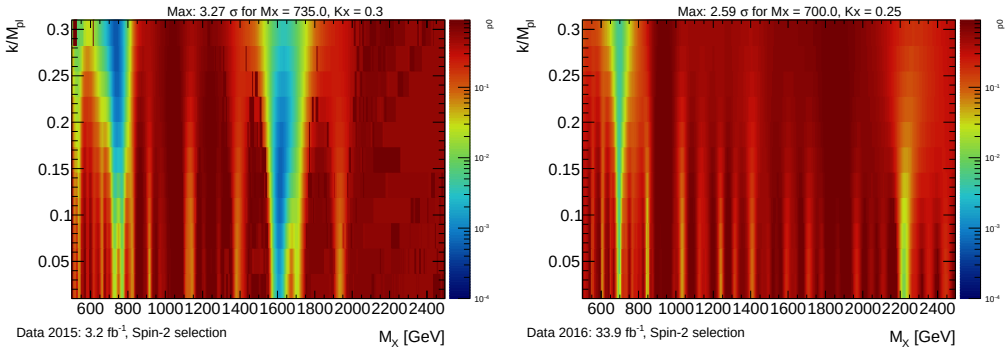

Figure 11.16: Observed 2-dimensional scan of the p-value for the background-only hypothesis p_0, as a function of the probed resonance mass m_X and $k/\overline{M}_{\mathrm{Pl}}$ for 3.2 fb^{-1} of data 2015 (left) and 33.9 fb^{-1} of data 2016 (right).

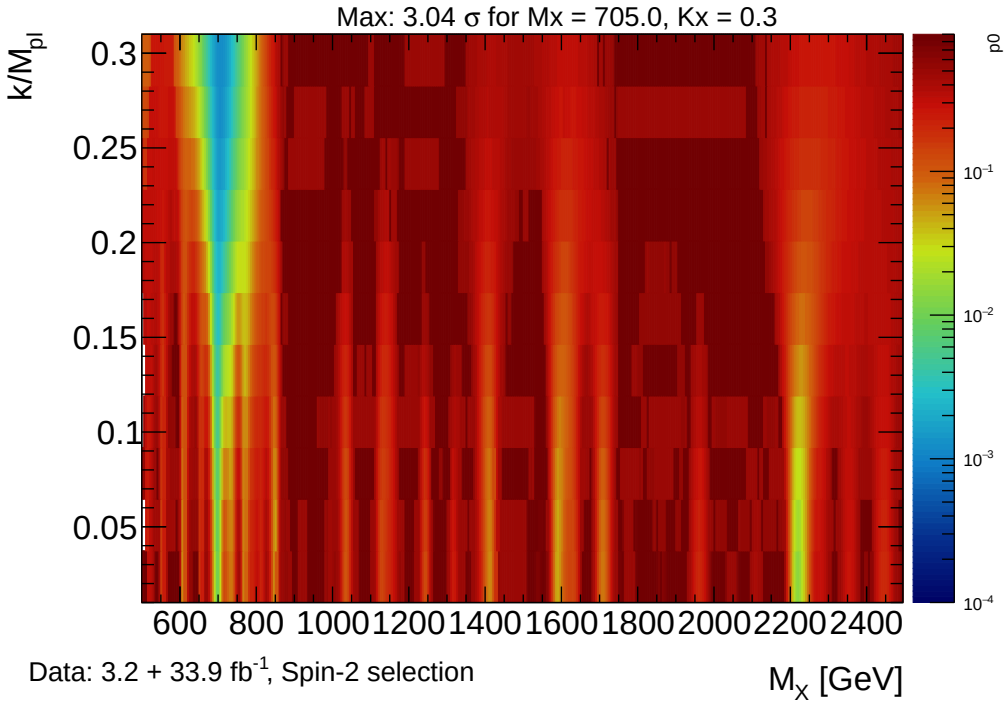

Figure 11.17: Observed 2-dimensional scan of the p-value for the background-only hypothesis p_0, as a function of the probed resonance mass m_X and $k/\overline{M}_{\mathrm{Pl}}$ for 37.1 fb^{-1} of data 2015+2016.

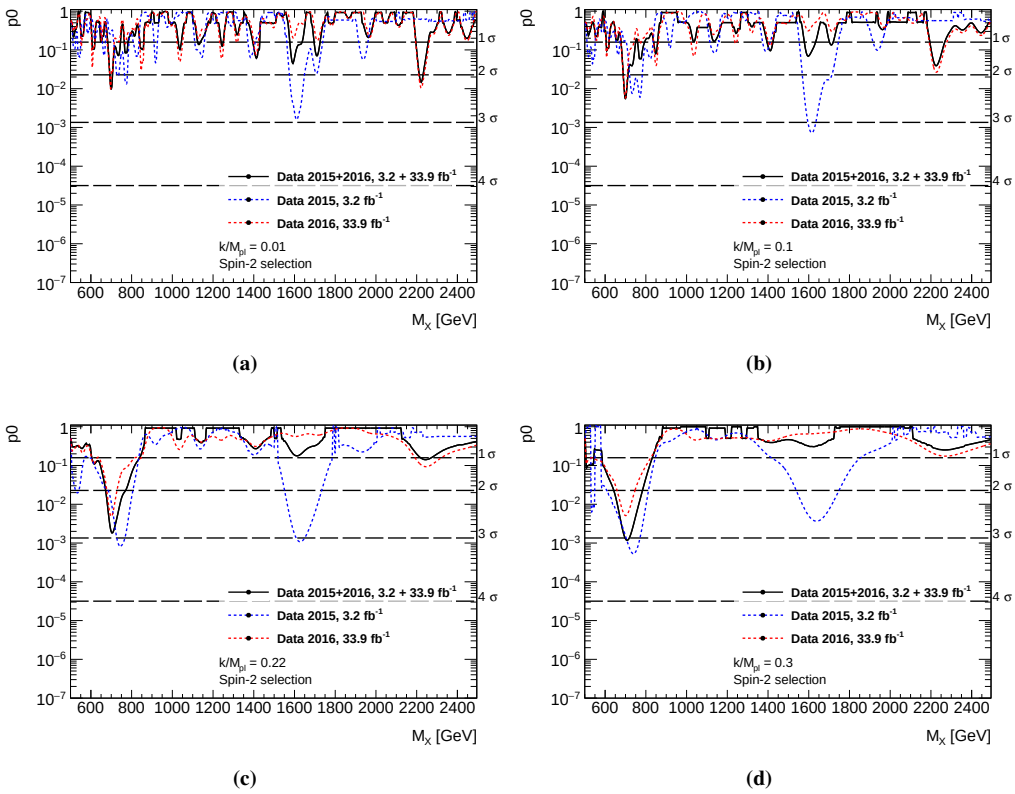

Figure 11.18: Observed scan of the p-value for the background-only hypothesis p_0 as a function of the assumed mass, for various values of $k/\overline{M}_{\mathrm{Pl}}$. Results for data 2015, 2016 and combination are shown separately.

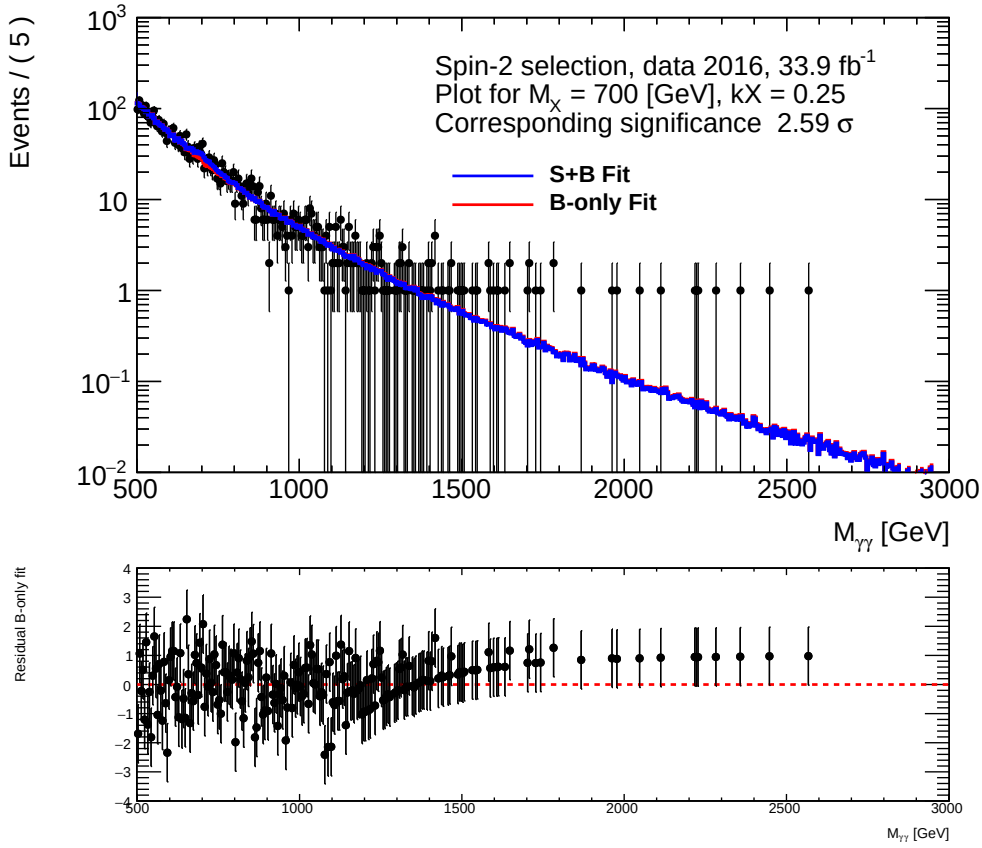

Figure 11.19: $m_{\gamma\gamma}$ spectrum from the diphoton candidates selected in a data-set corresponding to 33.9 fb^{-1} of 2016 data, with the signal+background fit and background-only fit superimposed. The subset plot shows the residual of the data with the background-only fit.

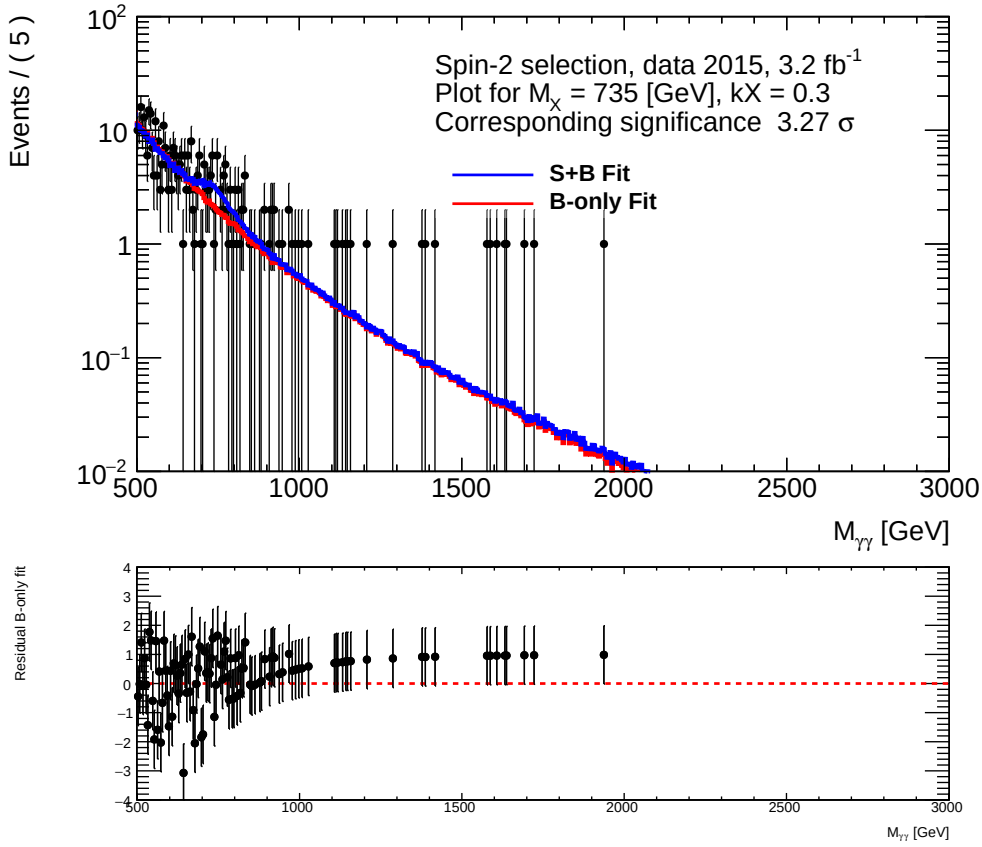

Figure 11.20: $m_{\gamma\gamma}$ spectrum from the diphoton candidates selected in a data-set corresponding to 3.2 fb^{-1} of 2015 data, with the signal+background fit and background-only fit superimposed. The subset plot shows the residual of the data with the background-only fit.

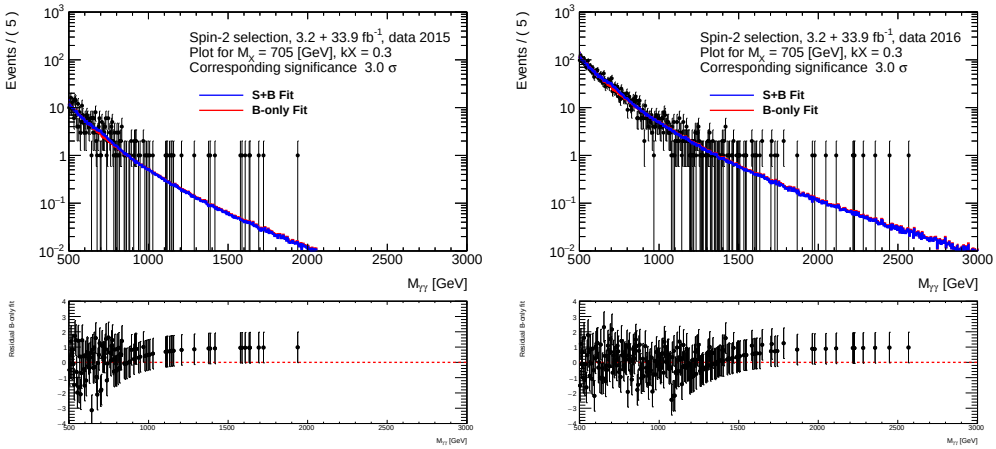

Figure 11.21: $m_{\gamma\gamma}$ spectrum from the diphoton candidates selected in a data-set corresponding to 3.2 fb^{-1} + 33.9 fb^{-1} of data projected in year 2015 (Left) and 2016 (Right), with the signal+background fit and background-only fit superimposed. The subset plot shows the residual of the data with the background-only fit.

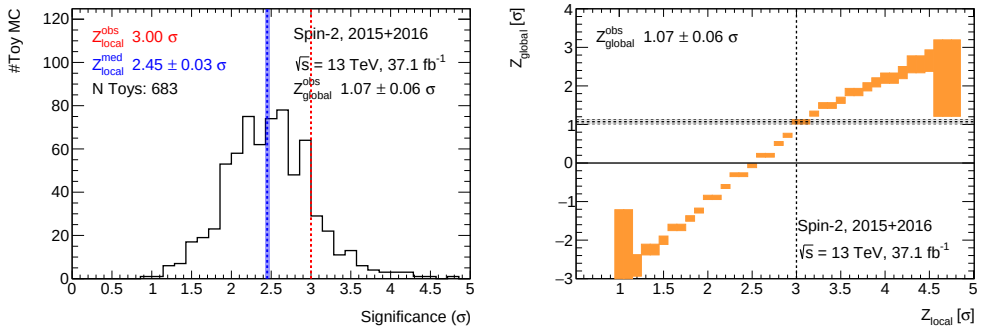

(a) **(b)**

Figure 11.22: Global significance for the spin-2 selection. Left: distribution of the local significances found in toys. Right: correspondence curve between local and global significance calculated from the toys.

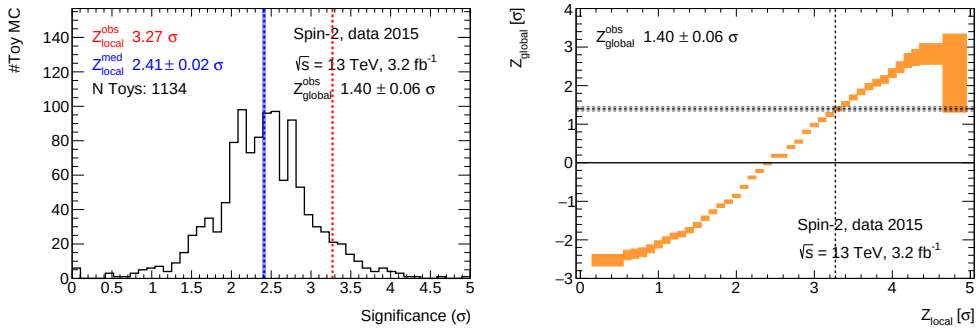

(a) **(b)**

Figure 11.23: Global significance for the spin-2 selection in data 2015. Left: distribution of the local significances found in toys. Right: correspondence curve between local and global significance calculated from the toys.

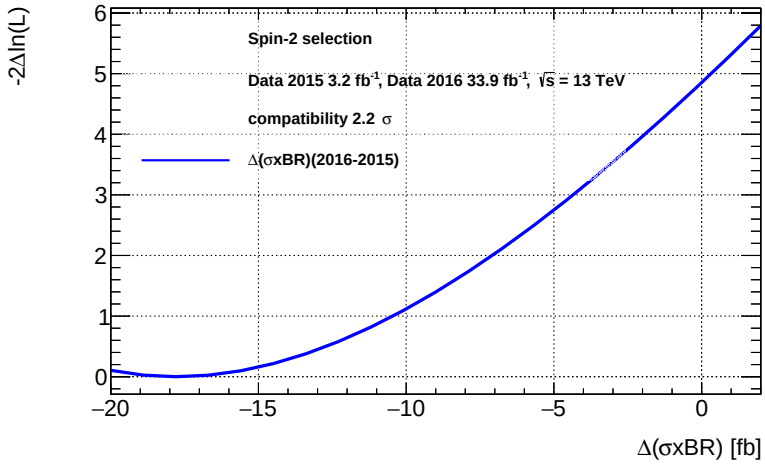

Figure 11.24: Profile likelihood ratio as a function of $\Delta\sigma = \sigma_{2016} - \sigma_{2015}$. The tested $(M_X, k/\overline{M}_{\mathrm{Pl}})$ point is the one with the maximum significance in data 2015.

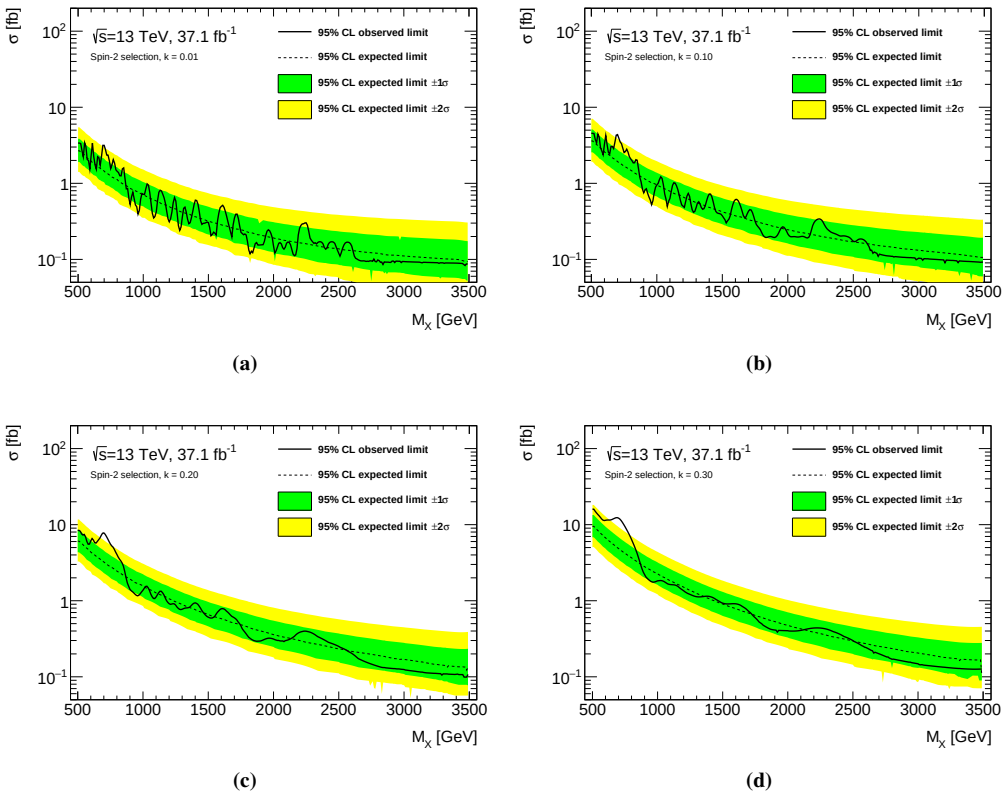

Figure 11.25: Expected and observed limit on the production cross-section limit σ_{RS} as a function of the resonance mass M_G for various values of $k/\overline{M}_{\mathrm{Pl}}$ for the combined 2015 and 2016 dataset. The theoretical cross-section σ_{RS} is shown as a function of M_G.

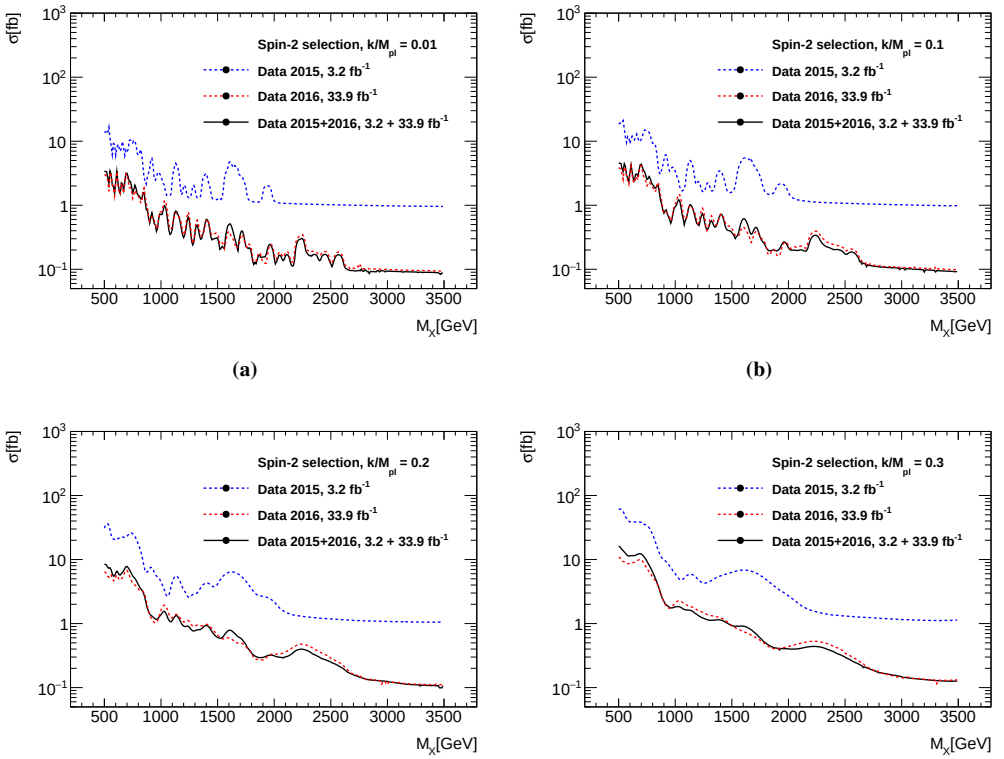

Figure 11.26: Observed limit on the production cross-section limit σ_{RS} as a function of the resonance mass M_G, for various values of $k/\overline{M}_{\mathrm{Pl}}$ for the 2015, 2016 and combined datasets.

11.3 Summary results table

A summary of the results for 2015, 2016 and their combination is shown in Table 11.1. Since the excess in data 2015 was found in the 700-800 GeV region Table 11.2 is dedicated for local maximums in that region.

Years	Scalar			Graviton		
	Z_{max}	Z_{glob}	(m_H, Γ)	Z_{max}	Z_{glob}	$(m_G, k/\overline{M}_{\rm Pl})$
2015	3.4 σ	1.4 σ	735 GeV, $\alpha = 8\%$	3.3 σ	1.4 σ	735 GeV, $\kappa = 0.3$
2016 (2015 max)	0.3σ	-	735 GeV, $\alpha = 8\%$	2 σ	-	735 GeV, $\kappa = 0.3$
2016	2 σ	-	305 GeV, NWA	2.6 σ	-	700 GeV, $\kappa = 0.25$
2015 + 2016	2.1 σ	0 σ	1595, NWA	3.0 σ	1 σ	705 GeV, $\kappa = 0.3$
Compatibility	3.2 σ	-	735 GeV, $\alpha = 8\%$	2.2 σ	-	735 GeV, $\kappa = 0.3$

Table 11.1: The highest local significance points (mass and width) for 2015 and 2016 dataset and combined.

Years	Scalar		Graviton	
	Z_{max}	(m_H, Γ)	Z_{max}	$(m_G, k/\overline{M}_{\rm Pl})$
2015	3.4 σ	735 GeV, $\alpha = 8\%$	3.3 σ	735 GeV, $\kappa = 0.3$
2016	1.3 σ	760 GeV, NWA	2.6 σ	700 GeV, $\kappa = 0.25$
2015 + 2016	1.9 σ	710, NWA	3.0 σ	705 GeV, $\kappa = 0.3$

Table 11.2: The highest local significance points (mass and width) for 2015 and 2016 dataset and combined, in the 700-800 GeV region.

11.4 Event displays

The event display for the two events with highest invariant mass can be seen in Fig. 11.28-Fig. 11.27, corresponding to $m_{\gamma\gamma}$=2.6 TeV and $m_{\gamma\gamma}$=2.45 TeV. In both displays a selection is applied on: the inner detector tracks of $P_T > 5$ GeV, on the EM calorimeter clusters of E > 1 GeV and in the Tile calorimeter of $|TileE_T| > 3$ GeV.

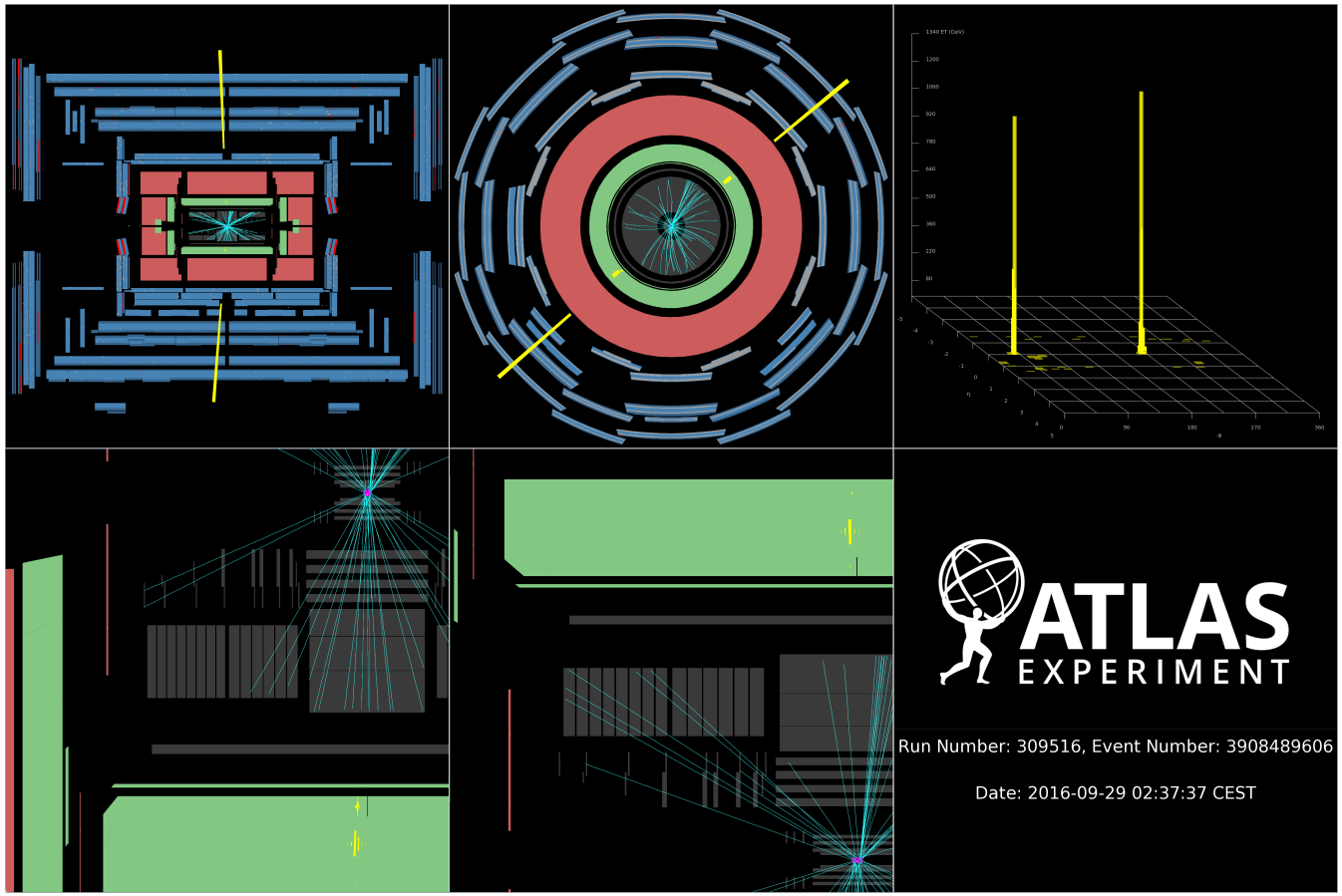

Figure 11.27: Event display of a di-photon event, both photons are unconverted and in the barrel. The event is the most energetic observed event and passes both selections. Event information: Run and event numbers = 309516, 3908489606. Invariant mass $m_{\gamma\gamma} = 2.6$ TeV.

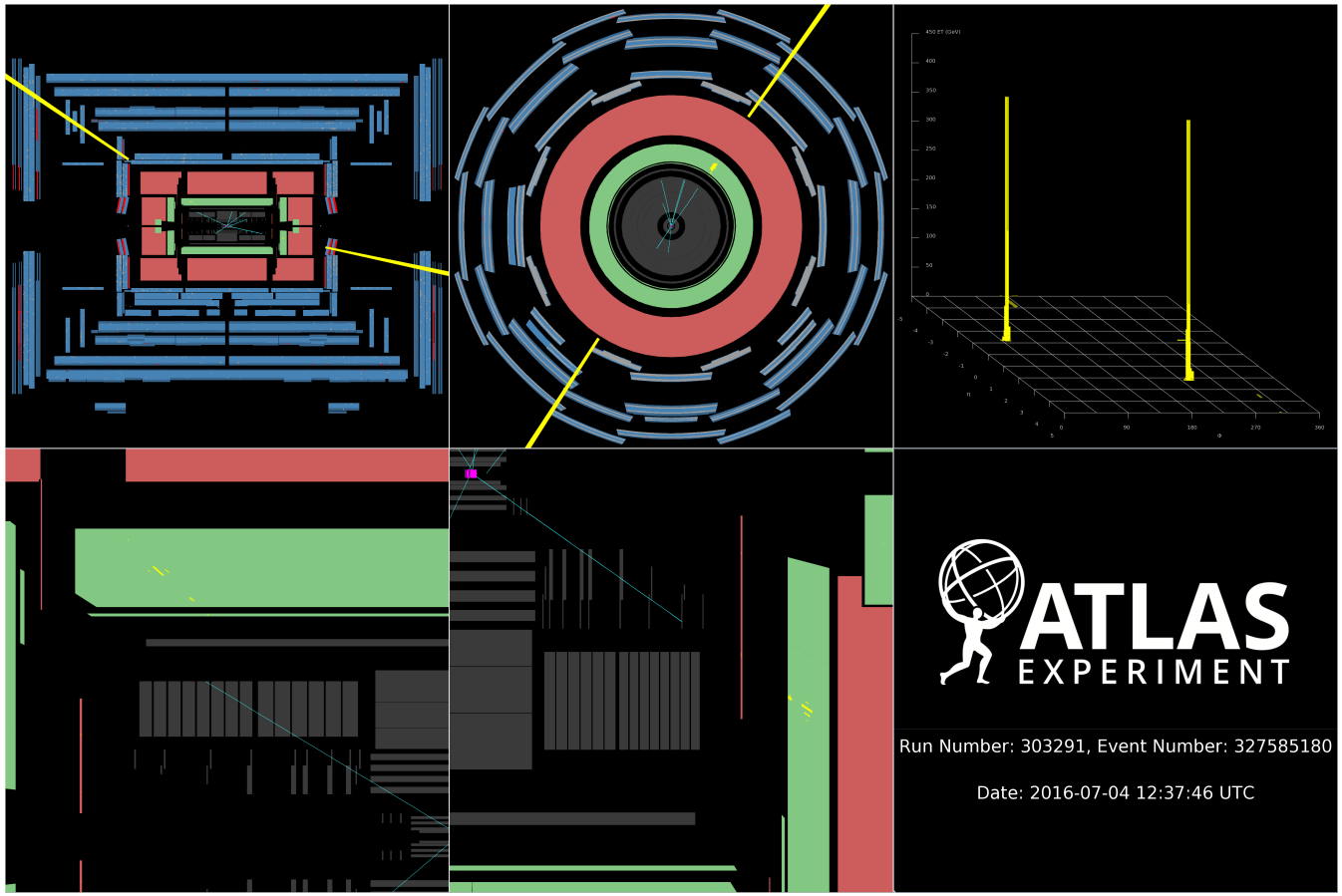

Figure 11.28: Event display of a di-photon event, both photon are converted, one photon is in the barrel the other one is in the end-cap. The event is the second most energetic observed event and passes only the spin-2 selection. Event information: Run and event numbers = 303291, 327585180. Invariant mass $m_{\gamma\gamma} = 2.45$ TeV.

11.5 Conclusions

Searches for new resonances decaying into two photons with the ATLAS experiment at the LHC have been presented. The pp collision data corresponding to an integrated luminosity of 3.2 fb^{-1} and 33.9 fb^{-1} that were recorded in years 2015 and 2016 respectively at a center-of-mass energy of $\sqrt{s} = 13$ TeV were analyzed. Two analyses were presented, one optimized for the search for spin-2 Randall-Sundrum graviton Kaluza-Klein towers with mass above 500 GeV and one for spin-0 resonances with mass above 200 GeV. The selection, the systematic uncertainties, the signal and the background models for the two cases were discussed.

Data 2015 The largest local significance observed in data 2015 for the spin-0 analysis was 3.4 σ for M_X=735 GeV and $\Lambda = 8$ %. While for the spin-2 analysis a 3.3 σ deviation was found for M_G=735 GeV and $k/\overline{M}_{\rm Pl} = 0.3$. However the global significance associated to the excess in both analyses was 1.4 standard deviations.

Data 2016 The largest local significance observed in data 2016 for the spin-0 analysis is around 2 σ for M_X=305 GeV and narrow signal. While for the spin-2 analysis a 2.6 σ deviation is found for M_G=700 GeV and $k/\overline{M}_{\rm Pl} = 0.25$. The observed local significance for the points of maximum significance in data 2015 is 0.3 σ and 2 σ respectively for the spin-0 and spin-2 analyses.

Data 2015+2016 In the combined 2015+2016 data at $\sqrt{s}$ =13 TeV with 37.1 fb^{-1} of integrated luminosity, the largest local significance for the spin-0 analysis is 2.1 σ at M_X=1595 GeV and narrow signal. For the spin-2 analysis the largest significance is 3 σ at M_G=705 GeV and $k/\overline{M}_{\rm Pl} = 0.3$. In the combined dataset the global significance associated to the maximum deviation from the background-only hypothesis is zero in the spin-0 analysis. While for the spin-2 analysis a global significance of 1 standard deviation is observed.

Compatibility The compatibility between year 2015 results and year 2016 results is 3.2 σ for the spin-0 analysis and 2.2 σ for the spin-2 analysis. This value is evaluated in the [M_X,α_X] of maximum local deviation from the background hypothesis in data 2015.

Summary A summary of the significance results for 2015, 2016 and their combination can be seen in Table 11.1. The expected and observed 95% CL upper limits can be found in Figure 11.12 and Figure 11.25.

Conclusions A very promising excess was found in the 2015 dataset and presented in December of year 2015 [8] and at the Moriond conference of year 2016 [10], although the observation was still compatible with the background-only hypothesis since the global significance was around 2 σ. The same study was conducted on the combined dataset from year 2015 and 2016 with 10 times the available statistic but the excess around 735 GeV, where the largest deviations from the background-only hypothesis was observed in the 2015 dataset, was not confirmed.

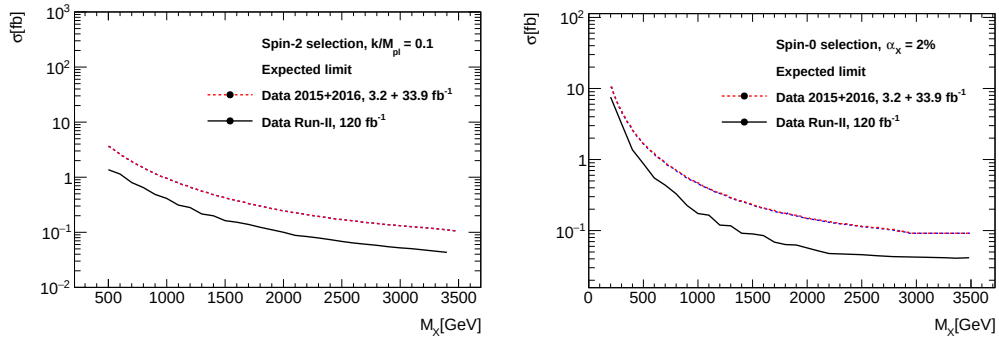

(a) **(b)**

Figure 11.29: Expected limit on the production cross-section σ_{RS} and σ_{fid} as a function of the resonance mass M_G, for $k/\overline{M}_{\mathrm{Pl}}$=0.1 and $\alpha_X = 2\%$. Limits are for the expected statistic of the Run-II dataset.

Data are consistent within 1 standard deviation with the Standard Model background-only hypothesis in the scanned parameter space for both analyses. Exclusion limits at 95% of confidence level are evaluated as a function of mass and width of the resonance, upper limits are set on the fiducial cross-section for the spin-0 analysis and on the Randall-Sundrum production cross-section for the spin-2 analysis.

Perspectives The search for spin-0 and spin-2 resonances will be conducted on the full dataset provided by ATLAS in the next two years (until the end of 2018) that should reach up between 100-120 fb^{-1}of available statistic. Prospect of exclusion on the σ_{RS} and σ_{fid} can be seen in Figure 11.29.

Part V

Appendices

APPENDIX A

Frequentist statistic analysis introduction

A well-defined statistical environment is crucial to assert statements both in term of discovery, exclusion or measurement. With a statistic study is possible to establish the statistic significance of a discrepancy from the expected background or, in case of agreement, to evaluate the excluded cross-section of the sought after signal. Furthermore it is also possible to measure the properties (such as mass, width or cross-section) of a know process by profiling the likelihood function and evaluate the minimum. This process can be done for single parameters or for more than one parameter combined.

In case of searches and exclusions other than the observation on data it is also useful to characterize the sensitivity of an experiment by reporting the expected (e.g., mean or median) significance that one would obtain for a variety of signal hypotheses. However finding both the significance for a specific data set and the expected significance can involve Monte Carlo calculations that are computationally expensive. For this reason approximate methods will be used in some cases. Those methods are based on results due to Wilks [136] and Wald [137] by which one can obtain both the significance for given data as well as the full sampling distribution of the significance under the hypothesis of different signal models, all without recourse to Monte Carlo. In this chapter the frequentist statistical test will be briefly introduced [138, 139]. To simplify the explanation a search for a resonant in the diphoton channel will be used as example case.

A.1 Formalism

In this section the general procedure used to search for a new phenomenon in the context of a frequentist statistical test will be outlined. For purposes of discovering a new signal process, one defines the null hypothesis, H_0, as describing only known processes, here designated as background, in this case the background is composed of Standard Model processes without the presence of an unforseen signal. This is to be tested against the alternative H_1, which includes both background as well as the sought after signal.

To summarize the outcome of such a search one quantifies the level of agreement of the observed data with a given hypothesis H by computing a p-value, i.e., a probability, under assumption of H, of finding data (in an experiment) of equal or greater incompatibility with the

predictions of H. One can regard the hypothesis as excluded if its p-value is observed below a specified threshold. In particle physics one usually converts the p-value into an equivalent significance, Z, defined such that a Gaussian distributed variable found Z standard deviations above its mean has an upper-tail probability equal to p. That is,

$$Z = \Phi^{-1}(1-p) \tag{A.1}$$

where Φ^{-1} is the quantile (inverse of the cumulative distribution) of the standard Gaussian.

For the discovery a new signal, the particle physics community has tended to regard rejection of the background hypothesis with a significance of at least $Z = 5\ \sigma$ (corresponding to $p = 2.87 \cdot 10^{-7}$) as an appropriate level to constitute a discovery. However rejecting the background only hypotesys is only the first step to the discovery of something completely new. Much more studies are required to verify the presence and the nature of new physics.

Instead for the purpose of excluding a signal hypothesis, a threshold p-value of 0.05 (i.e., 95% confidence level, which corresponds to $Z = 2\ \sigma$) is often used.

A widely used procedure to establish discovery (or exclusion) in particle physics is based on a frequentist significance test using a likelihood ratio as a test statistic. In addition to parameters of interest such as the rate (cross section) of the signal process, the signal and background models will contain also nuisance parameters corresponding to systematic errors.

A.1.1 Signal and background

In the following section the calculation of the likelihood ratio PDF [1] will be shown, to do so the search for deviation from the background in the invariant mass spectrum will be used as example.

For each event we measure invariant mass, the expectation value of every bin of the invariant mass histogram is $E[n_i] = \mu s_i + b_i$ where i runs on all the bins of the histogram, s_i and b_i are the signal and background expected values for the bin i:

$$\begin{aligned} s_i &= s_{tot} \int_{bin,i} f_s(x;\theta_s)dx, \\ b_i &= b_{tot} \int_{bin,i} f_b(x;\theta_b)dx, \end{aligned} \tag{A.2}$$

μ is the strenght of the signal process, $\mu = 0$ is for a background only model and $\mu = 1$ is for the expected nominal signal process. The functions $f_s(x;\theta_s)$ and $f_b(x;\theta_b)$ represent the signal and the background respectively (they represent the ideal distribution of signal and background in an experiment with very high statistic). θ_s and θ_b represent parameters that characterize the shapes of PDFs where we include the systematic uncertainties. The quantities s_{tot} and b_{tot} are the total mean numbers of signal and background events. The likelihood function is the product of Poisson

[1] Probability Distribution Function

probabilities for all bins:

$$L(\mu,\theta) = \prod_{j=1}^{N} \frac{(\mu s_j + b_j)^{n_j}}{n_j!} e^{-(\mu s_j + b_j)} \tag{A.3}$$

To test a hypothesized value of μ we consider the profile likelihood ratio

$$\lambda(\mu) = \frac{L(\mu,\hat{\hat{\theta}})}{L(\hat{\mu},\hat{\theta})} \tag{A.4}$$

Here $\hat{\hat{\theta}}$ in the numerator denotes the value of θ that maximizes L for the specified μ, i.e., it is the conditional maximum-likelihood (ML) estimator of θ (and thus is a function of μ). The denominator is the maximized (unconditional) likelihood function, i.e., $\hat{\mu}$ and $\hat{\theta}$ are their ML estimators. The presence of the nuisance parameters broadens the profile likelihood as a function of μ relative to what one would have if their values were fixed. This reflects the loss of information about μ due to the systematic uncertainties.

A.1.2 Test statistic and p-value

From the definition of $\lambda(\mu)$, one can see that $0 \leq \lambda(\mu) \leq 1$, with $\lambda(\mu)$ near 1 implying good agreement between the data and the hypothesized value of μ. Equivalently it is convenient to use the statistic

$$t_\mu = -2ln\lambda(\mu) \tag{A.5}$$

as the basis of a statistical test. Higher values of t_μ thus correspond to increasing incompatibility between the data and μ. We may then define a test of a hypothesized value of μ by using the statistic t_μ directly as measure of discrepancy between the data and the hypothesis, with higher values of t_μ correspond to increasing disagreement. To quantify the level of disagreement we compute the p-value,

$$p_\mu = \int_{t_\mu,obs}^{\infty} f(t_\mu|\mu)dt_\mu \tag{A.6}$$

where t_μ, obs is the value of the statistic t_μ observed from the data and $f(t_\mu|\mu)$ denotes the pdf of t_μ under the assumption of the signal strength μ. When using the statistic t_μ, a data set may result in a low p-value in two distinct ways: the estimated signal strength $\hat{\mu}$ may be found greater or less than the hypothesized value μ. As a result, the set of μ values that are rejected because their p-values are found below a specified threshold α may lie to either side of those values not rejected, i.e., one may obtain a two-sided confidence interval for μ. The relation between the p-value and the observed t_μ and also with the significance Z are illustrated in Figure A.1.

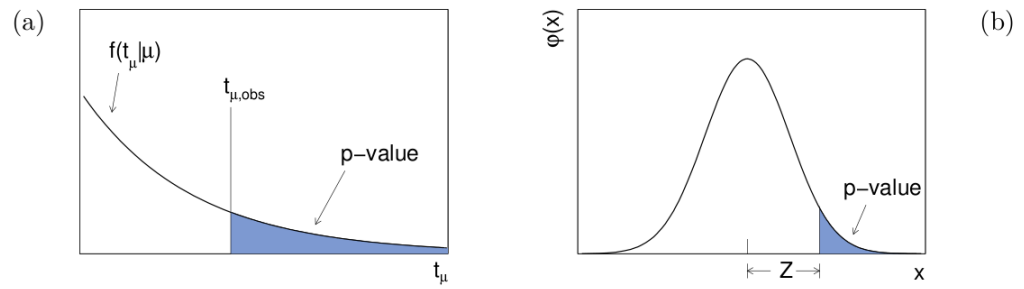

Figure A.1: (a) Illustration of the relation between the p-value obtained from an observed value of the test statistic t_μ. (b) The standard normal distribution $\phi(x) = \left(1/\sqrt{2\pi}\right) e^{-(x^2/2)}$ showing the relation between the significance Z and the p-value.

A.2 Test statistic for discovery of a positive signal

Often it is assumed that the presence of a new signal can only increase the mean event rate beyond what is expected from background alone. That is, the signal process necessarily has $\mu \geq 0$, and to take this into account we define an alternative test statistic below called $\tilde{t}_\mu$. We can then define $\tilde{\lambda}(\mu)$ for data with $\mu < 0$

$$\tilde{\lambda}(\mu) = \begin{cases} \frac{L(\mu,\hat{\hat{\theta}}(\mu))}{L(\hat{\mu},\hat{\theta})} & \hat{\mu} \geq 0 \\ \frac{L(\mu,\hat{\hat{\theta}}(\mu))}{L(0,\hat{\hat{\theta}}(0))} & \hat{\mu} < 0 \end{cases} \tag{A.7}$$

Here $\hat{\hat{\theta}}(0)$ and $\hat{\hat{\theta}}(\mu)$ refer to the conditional ML estimators of θ given a strength parameter of 0 or μ, respectively. We can denote $\tilde{t}_\mu$ as

$$\tilde{t}_\mu = -2ln\tilde{\lambda}(\mu) = \begin{cases} -2ln\frac{L(\mu,\hat{\hat{\theta}}(\mu))}{L(\hat{\mu},\hat{\theta})} & \hat{\mu} \geq 0 \\ -2ln\frac{L(\mu,\hat{\hat{\theta}}(\mu))}{L(0,\hat{\hat{\theta}}(0))} & \hat{\mu} < 0 \end{cases} \tag{A.8}$$

As was done with the statistic t_μ, one can quantify the level of disagreement between the data and the hypothesized value of μ with the p-value. For this one needs the distribution of $\tilde{t}_\mu$. Also similar to the case of t_μ, values of μ both above and below $\hat{\mu}$ may be excluded by a given data set, one may obtain either a one-sided or two-sided confidence interval for μ.

A.2.1 Test statistic for p_0

An important special case of the statistic $\tilde{t}_\mu$ described above is used to test $\mu = 0$ in a class of model where we assume $\mu \geq 0$. Rejecting the $\mu = 0$ hypothesis effectively leads to the discovery

of a new signal. For this important case we use the special notation $q_0 = \tilde{t}_0$. Substituting in equation A.8 we obtain

$$q_0 = \begin{cases} -2ln\lambda(0) & \hat{\mu} \geq 0 \\ 0 & \hat{\mu} < 0 \end{cases} \tag{A.9}$$

where $\lambda(0)$ is the profile likelihood ratio for $\mu = 0$ as defined in Equation A.4. We may contrast this to the statistic t_0. In that case one may reject the $\mu = 0$ hypothesis for either an upward or downward fluctuation of the data. This is appropriate if the presence of a new phenomenon could lead to an increase or decrease in the number of events found. In an experiment looking for neutrino oscillations, for example, the signal hypothesis may predict a greater or lower event rate than the no oscillation hypothesis. With q_0 however we consider the data to lack agreement with the background only model only for $\hat{\mu} > 0$. A value of $\hat{\mu}$ below zero however would also point in the invalidation of the background only model. To quantify the level of disagreement between the data and the hypothesis of $\mu = 0$ using the observed value of q_0 we compute the p-value in the same manner as done with p_0 namely,

$$p_0 = \int_{q_0,obs}^{\infty} f(q_0|0)dq_0 \tag{A.10}$$

Here $f(q_0|0)$ denotes the pdf of the statistic q_0 under assumption of the background only, with no signal, $(\mu = 0)$ hypothesis.

A.3 Test statistic for upper limits

In this section we will define the q_μ value to establish an upper limit on the strength parameter μ. q_μ is defined as

$$q_\mu = \begin{cases} -2ln\lambda(\mu) & \hat{\mu} \leq \mu \\ 0 & \hat{\mu} > \mu \end{cases} \tag{A.11}$$

We set $q_\mu = 0$ for values of $\hat{\mu} > \mu$ because, when setting an upper limit, we would not regard data with $\hat{\mu} > \mu$. Such data would represent less compatibility with μ than the data obtained, and therefore this is not taken as part of the rejection region of the test. Higher values of q_μ represent greater incompatibility between the data and the hypothesized value of μ. As with the case of discovery, one quantifies the level of agreement between the data and hypothesized μ with p-value. For an observed value q_0, obs one has

$$p_\mu = \int_{q_\mu,obs}^{\infty} f(q_\mu|\mu)dq_\mu \tag{A.12}$$

A.4 Approximate distributions

In order to find the p-values described above we are required to know the sampling distribution $f(q_\mu|\mu)$ for the test statistic. It can be obtained either throwing toy Monte Carlo or using asymptotic approximations. However using a toy Monte Carlo to build a sufficiently smooth distribution in the tail would result in a lot of time spent in generation and analysis of the samples. In case of approximate distribution of the profile likelihood ratio we can expand the term $ln\lambda$ as

$$-2ln\lambda = \frac{(\mu-\hat{\mu})^2}{\sigma^2} + O(1/\sqrt{N}) \tag{A.13}$$

Here $\hat{\mu}$ follows a Gaussian distribution with a mean μ' and standard deviation σ, and N represents the data sample size. The standard deviation σ of $\hat{\mu}$ is obtained from the covariance matrix of the estimators for all the parameters $V_{ij} = -E\partial^2 lnL/\partial\theta_i\partial\theta_j$ where $\theta_0 = \mu$. We can use this approximation to evaluate $f(t_\mu;\Lambda)$

$$f(t_\mu;\Lambda) = \frac{1}{2\sqrt{t_\mu 2\pi}}\left[e^{-(\sqrt{t_\mu}+\sqrt{\Lambda})^2/2} + e^{-(\sqrt{t_\mu}-\sqrt{\Lambda})^2/2}\right] \tag{A.14}$$

with Λ representing the number of standard deviations

$$\Lambda = \frac{(\mu-\mu')^2}{\sigma^2} \tag{A.15}$$

We can generalize the result for more than one parameter of interest θ_r, giving the possibility to define more than one nuisance parameter in the analysis. Some of the formulae given require the standard deviation σ of μ, which is assumed to follow a Gaussian distribution with a mean of μ'. To estimate σ we relate to a special artificial data set that we call the *Asimov data set* [133]. We define the Asimov data set such that when one uses it to evaluate the estimators for all parameters, one obtains the true parameter values. We can then define the parameters for λ with values representing those implied by the assumed distribution of the data. In practice, these are the values that would be estimated from the Monte Carlo model using a very large data sample. We can use the Asimov data set to evaluate the *Asimov likelihood* L_A and the corresponding profile likelihood ratio λ_A. In practice one could, for example, evaluate the the derivatives of $ln(L_A)$ numerically, use this to find the inverse covariance matrix, and then invert and extract the variance of μ. That is, from the Asimov data set one obtains an estimate of the non centrality parameter Λ that characterizes the distribution $f(q_\mu|\mu')$.

We can define the cumulative distribution of t_μ where ϕ is the cumulative distribution of the standard (zero mean, unit variance) Gaussian

$$F(t_\mu|\mu') = \Phi\left(\sqrt{t_\mu} + \frac{\mu-\mu'}{\sigma^2}\right) + \Phi\left(\sqrt{t_\mu} - \frac{\mu-\mu'}{\sigma^2}\right) - 1 \tag{A.16}$$

For the special case of $\mu = \mu'$ $F(t_\mu|\mu)$ is therefore

$$F(t_\mu|\mu) = 2\Phi\left(\sqrt{t_\mu}\right) - 1 \tag{A.17}$$

The p-value and the significance are

$$p_\mu = 1 - F(t_\mu|\mu) = 2\left(1 - \Phi\left(\sqrt{t_\mu}\right)\right) \tag{A.18}$$

$$Z_0 = \Phi^{-1}(1 - p_\mu) \tag{A.19}$$

If the p-value is found below a specified threshold α (often one takes $\alpha = 0.05$), then the value of μ is said to be excluded at a confidence level (CL) of $1 - \alpha$. The set of points not excluded form a confidence interval with CL$= 1 - \alpha$. Here the endpoints of the interval can be obtained simply by setting $p_\mu = \alpha$ and solving for μ. Assuming the approximation we find

$$\mu_{Up/lo} = \hat{\mu} \pm \sigma\phi^{-1}(1 - \alpha/2) \tag{A.20}$$

One subtlety with this formula is that σ itself depends at some level on μ. In practice to find the upper and lower limits one can simply solve numerically to find those values of μ that satisfy $p_\mu = \alpha$.

A.4.1 Approximate value for p_0

We can then evaluate approximated value for λ as we did before. The resulting σ for the zero signal hypothesis ($\mu' = 0$) is $\sigma_A^2 = \frac{\mu^2}{-2ln\lambda_A(\mu)}$. The resulting q_0 for the approximate value, where $\hat{\mu}$ follows a Gaussian distribution with mean μ' and standard deviation σ is

$$q_0 = \begin{cases} \hat{\mu}^2/\sigma^2 & \hat{\mu} \geq 0 \\ 0 & \hat{\mu} < 0 \end{cases} \tag{A.21}$$

From this one can show that the pdf of q_0 has the form

$$f(q_0|\mu') = \left(1 - \Phi\left(\frac{\mu'}{\sigma}\right)\right)\delta(q_0) + \frac{1}{2\sqrt{2q_0\pi}} e^{-\frac{1}{2}\left(\sqrt{q_0} - \frac{\mu'}{\sigma}\right)^2} \tag{A.22}$$

and in the special $\mu' = 0$

$$f(q_0|\mu') = \frac{1}{2}\delta(q_0) + \frac{1}{2\sqrt{2q_0\pi}} e^{-\frac{q_0}{2}} \tag{A.23}$$

That is, one finds a mixture of a delta function at zero and a chi-square distribution for one degree of freedom, with each term having a weight of 1/2. In the following we will refer to this mixture

as a half chi-square distribution or $\frac{1}{2}\chi^2_1$. The corresponding cumulative distribution for the case $\mu' = 0$ is found to be

$$F(q_0|0) = \Phi\left(\sqrt{q_0}\right) \tag{A.24}$$

and the p-value for the $\mu = 0$ hypothesis is

$$p_0 = 1 - F(q_0|0) = 1 - \Phi\left(\sqrt{q_0}\right) \tag{A.25}$$

and the significance is

$$Z_0 = \Phi^{-1}(1 - p_0) = \sqrt{q_0} \tag{A.26}$$

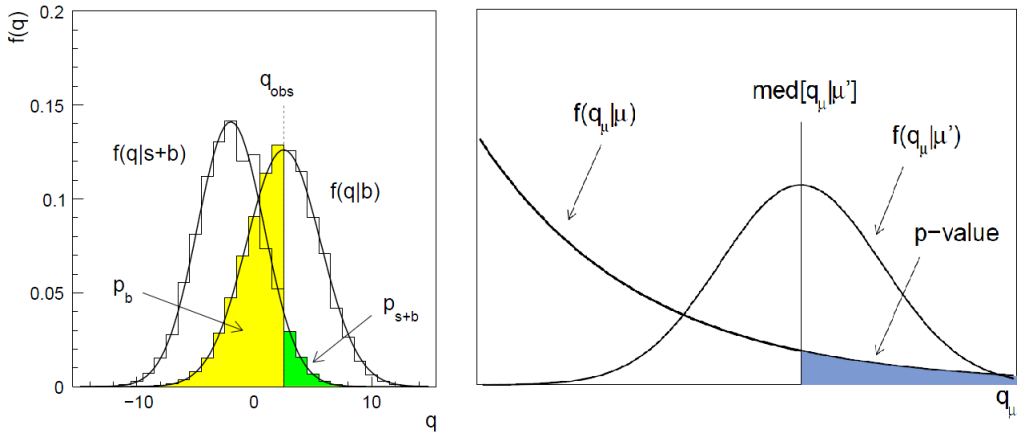

Figure A.2: Left: Illustration of the the p-value corresponding to the median of q_μ assuming a strength parameter μ'. Right: The distribution of the statistic $q = -2ln(L_{s+b}/L_b)$ under the hypotheses of $\mu = 0$ and $\mu = 1$ for a binned dataset.

A.4.2 Approximate value for exclusion

Assuming the validity of the approximation we can write the test statistic for q_μ as

$$q_\mu = \begin{cases} (\mu - \hat{\mu})^2/\sigma^2 & \hat{\mu} < \mu \\ 0 & \hat{\mu} > \mu \end{cases} \tag{A.27}$$

where $\hat{\mu}$ as before follows a Gaussian centered about μ' with a standard deviation σ. From this one can show that the pdf of q_0 has the form

$$f(q_\mu|\mu') = \Phi\left(\frac{\mu' - \mu}{\sigma}\right)\delta(q_\mu) + \frac{1}{2\sqrt{2q_\mu\pi}} e^{-\frac{1}{2}\left(\sqrt{q_\mu} - \frac{\mu'-\mu}{\sigma}\right)^2} \tag{A.28}$$

so that the special case $\mu = \mu'$ is a half-chi-square distribution:

$$f(q_0|\mu') = \frac{1}{2}\delta(q_\mu) + \frac{1}{2\sqrt{2q_\mu\pi}}e^{-\frac{q_\mu}{2}} \tag{A.29}$$

The corresponding cumulative distribution for this special case with $\mu = \mu'$ is found to be

$$F(q_\mu|\mu') = \Phi\left(\sqrt{q_\mu}\right) \tag{A.30}$$

and the p-value for the hypothesized μ is

$$p_\mu = 1 - F(q_\mu|\mu) = 1 - \Phi\left(\sqrt{q_\mu}\right) \tag{A.31}$$

therefore the corresponding significance is

$$Z_\mu = \Phi^{-1}(1 - p_\mu) = \sqrt{q_\mu} \tag{A.32}$$

As with the statistic t_μ above, if the p-value is found below a specified threshold α (often one takes $\alpha = 0.05$), then the value of μ is said to be excluded at a confidence level (CL) of $1 - \alpha$. The upper limit on μ is the largest μ with $p_\mu \leq \alpha$. Here this can be obtained simply by setting $p_\mu = \alpha$ and solving for $p_\mu = \alpha$. We find that

$$\mu_{Up} = \hat{\mu} + \sigma\phi^{-1}(1 - \alpha) \tag{A.33}$$

σ depends in general on the hypothesized μ, so the upper limit is found numerically as the value of μ for $p_\mu = \alpha$.

A.4.3 CLs

When the b and s+b hypotheses are well separated (as in Figure A.2 (left)) , there is a high probability of excluding the s+b hypothesis ($p_{s+b} < 0.05$) if in fact the data contain background only. In this case the power of test of s+b relative to the alternative b is high.

But if the two distributions are close to each other there is a non-negligible probability of rejecting s+b even though the sensitivity is low. In this other case the power of the s+b test is low relatively to the b alternative. In the limit case of no sensitivity, the distributions coincide and the probability of exclusion is equal to 0.05. However a model should not be excluded by a test that holds no sensitivity to it.

To enhance the sensitivity the CL_s solution was introduced. In this procedure the test is not based on the usual p-value ($CL_{s+b} = p_{s+b}$), but it is based on CL_s. The CL_s p-value is equal to CL_{s+b} divided by CL_b, which is one minus the b-only hypothesis:

$$CL_s = \frac{CL_{s+b}}{CL_b} = \frac{p_{s+b}}{1 - p_b} \tag{A.34}$$

where p_{s+b} and p_b are the integrals of the p-value distributions shown in Figure A.2 (left). The s+b hypothesis is then rejected if $CL_s \leq 0.05$. This procedure effectively reduces the p-value to:

$$p_\mu = \frac{p_\mu}{1 - p_b} \tag{A.35}$$

Preventing the exclusion when the s+b and b distributions become close and the sensitivity is low.

APPENDIX B

ATLAS DCS and High voltage system of the LAr calorimeter

B.1 Contribute given

During my PhD I contributed to the ATLAS data taking doing several shifts as hardware expert on call for the Liquid Argon (LAr) calorimeter. I also developed parts of the LAr calorimeter high voltage control system and took care of the operations in the rack cavern USA15 where the high voltage modules are. For example I developed the WinCCoA panel to control the High-Voltage and another panel to calculate the mean current in all HV cannels (Figure B.3). I also created a database stored in the Tier-0 with the information of the nominal voltages in the calorimeter.

B.2 DCS and DAQ

In parallel to the trigger system of ATLAS, two other independent systems are responsible for the data taking and control the experiment infrastructure: the data acquisition system (DAQ), and the Detector Control System (DCS). The former is in charge of controlling the hardware and software elements of the detectors and the elements associated with High-Level-Trigger and data storage. This enables diagnostic and error recovery, with the capability of removing or re-enabling individual parts without stopping the full acquisition.

The DCS, on the other hand, ensures coherent and safe operation. It handles the control of the detector equipment and related infrastructure, monitoring the operational parameters such as temperature and power-supply voltages. Both systems are capable of taking corrective actions and additionally provide a human interface for the full control of ATLAS and its sub-detectors. Among other parts of the detector the high voltage (HV) system of the ATLAS electromagnetic calorimeter is controlled by the DCS system. The following sections will focus on a brief introduction of the WinCCOA SCADA system and the control of the LAr HV system.

In the following a short introduction to the LAr calorimeter readout system and calibration will also be presented. For an extensive explanation of the LAr electronics and performance please refer to the LAr calorimeter TDR [84].

B.3 SCADA systems

The DCS of ATLAS is a SCADA system, which means Supervisory Control And Data Acquisition. The term SCADA usually refers to centralized systems which monitor and control entire sites, or complexes of systems spread out over large areas. It is a system for remote monitoring and control that operates with coded signals over communication channels. The control system may be combined with a data acquisition system by adding the use of coded signals over communication channels to acquire information about the status of the remote equipment for display or for recording functions. This system is similar to an industrial control system, however SCADA systems distinguish themselves by being large-scale processes that can include multiple sites, which is the case of the LHC or ATLAS. The ATLAS DCS has a similar structure such as industrial processes, civil defense siren systems, space stations, monitor and control heating, ventilation, and air conditioning.

A human–machine interface (HMI) is the input-output device through which the human operator controls the process, and which presents process data to a human operator. HMI is usually linked to the SCADA system's databases and software programs, to provide trending, diagnostic data, and management information such as scheduled maintenance procedures, logistic information, detailed schematics for a particular sensor or machine, and expert-system troubleshooting guides.

SCADA systems typically implement a distributed database, commonly referred to as a tag database, which contains data elements called tags or points. A point represents a single input or output value monitored or controlled by the system. In Cern's facilities a ORACLE database that is located in the Tier-0 facility is exploited for this function.

An important part of most SCADA implementations is alarm handling. The system monitors whether certain alarm conditions are satisfied, to determine when an alarm event has occurred. Once an alarm event has been detected, one or more actions are taken. In many cases, a SCADA operator may have to acknowledge the alarm event; this may deactivate some alarm indicators, whereas other indicators remain active until the alarm conditions are cleared. Usually several alarm level can be used in respect of the gravity of the situation, such as: WARNING/ERROR/FATAL.

B.3.1 WinCCOA

In Cern's facilities the SCADA system and HMI in use is the Siemens WinCC Open Architecture (WinCCOA). It is written for the Microsoft Windows operating system and it uses Microsoft SQL Server for logging and comes with a VBScript and ANSI C application programming interface. WinCCOA works on a scattered system, so it is scalable, redundant and accessible from everywhere. An example WinCCOA scheme can be seen in Figure B.1. The control systems of main experiments at LHC (ATLAS, CMS, ALICE, LHCb) run on WinCCOA. Between the experiments there is a joint project, called "Joint Controls Project" (JCOP), that aims to reduce the overall manpower cost required to produce and run the experiment control systems.

Regarding the LAr sub-detector and in particular the HV system, WinCCOA runs on eight linux machines in USA 15 cavern of the ATLAS experiment, on each machine the server controlling the

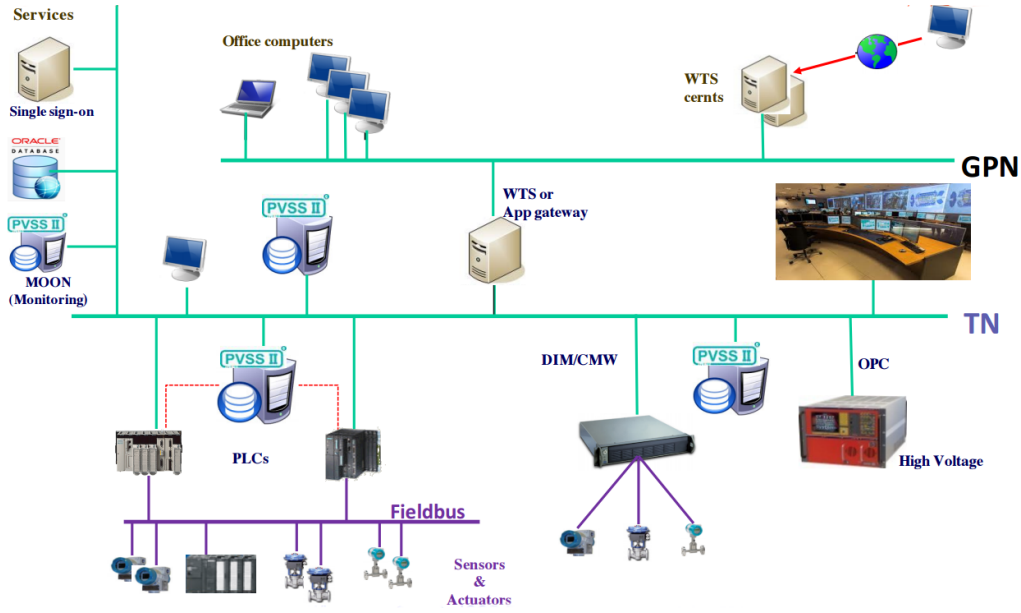

Figure B.1: WinCCOA example working scheme.

hardware is running on a windows virtual machine.

B.4 Finite state machines

A finite-state machine (FSM) is a mathematical model of computation used to design both computer programs and sequential logic circuits. It is conceived as an abstract machine that can be in one of a finite number of states. The machine is in only one state at a time; the state it is in at any given time is called the current state. It can change from one state to another when initiated by a triggering event or condition; this is called a transition. A particular FSM is defined by a list of its states, its initial state, and the triggering condition for each transition.

ATLAS control system is based on a finite state machine structure, it is divided in partitions (e.g. sub-detectors as the LAr calorimeter), and sub-partitions (e.g. the barrel/endcap sections of the calorimeter) down to the single components (e.g. the HV channels). The commands given by a user trickle down from more general partition to the single components, so if the command to switch off ATLAS is given all sub-detectors will communicate to the single components the switch off command. In the same way the status of a single component will influence the status of the complete machine, so if there is an ERROR in one component it will be brought up to the ATLAS partition. A scheme of the ATLAS and LAr calorimeter FSM can be seen in Figure B.2.

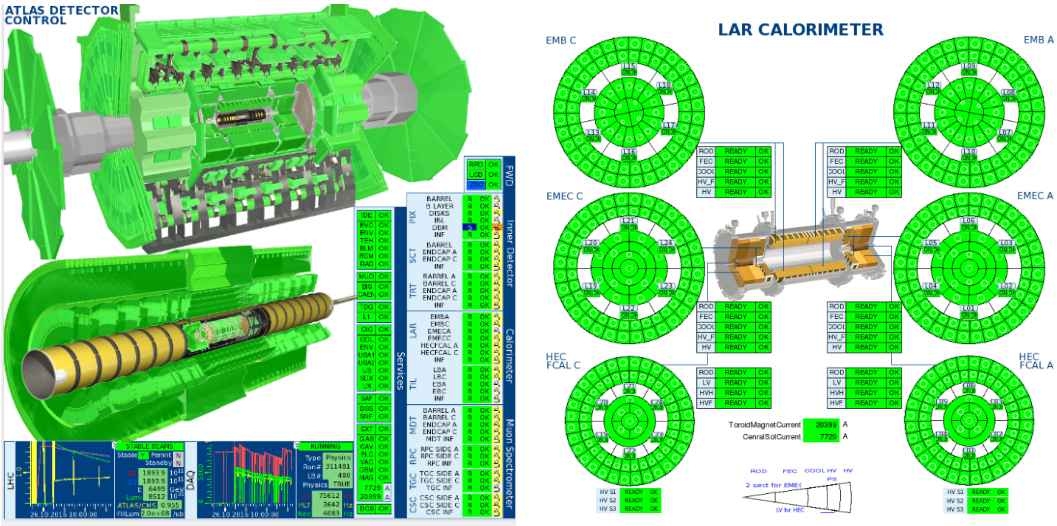

Figure B.2: Finite state machine of the ATLAS detector (left) and the LAr calorimeter (right). The LAr calorimeter FSM is in fact a part of the ATLAS FSM.

B.5 LAr HV control system

As already stated the control system of the LAr sub-detector HV system runs on eight linux machines in USA 15 cavern. The system is divided in four partitions: EMB (electromagnetic barrel), EMEC (electromagnetic endcap), HEC (hadronic endcap), FCAL (forward calorimeter) plus the presamplers of electromagnetic barrel and endcap. Each system is then divided in two sides A and C. Furthermore a purity system is installed in the calorimeter to evaluate the luminosity. The actual high voltage is supplied by ISEG 16 or 32 channels HV modules that are installed in crates placed in the USA 15 cavern.

The readout from each channel is composed by the voltage, the current and a bitmask representing the status of the channel. While the control operations that can be exerted on HV channels are ramping up and down the voltage and change the thresholds of the alarms. Operations on the voltage of the HV system can be made with the DCS FSM directly, however one channel at a time, or with specific panels developed by the LAr group to change the settings of several modules at the same time. Example panels can be seen in Figure B.3.

The current should be zero during the normal operation of the channel and go to a limited value in presence of collisions because of the passing through particles. However some of the HV channels are in short circuit and a non-zero current is always present, sometimes these short circuits come and go, an example can be seen in Figure B.4. If the short circuit is stable usually the voltage of the channel is lowered to lower the current to a manageable level. The lowering of the voltage has an effect on the energy reading of the cells, however this effect can be corrected in later phase.

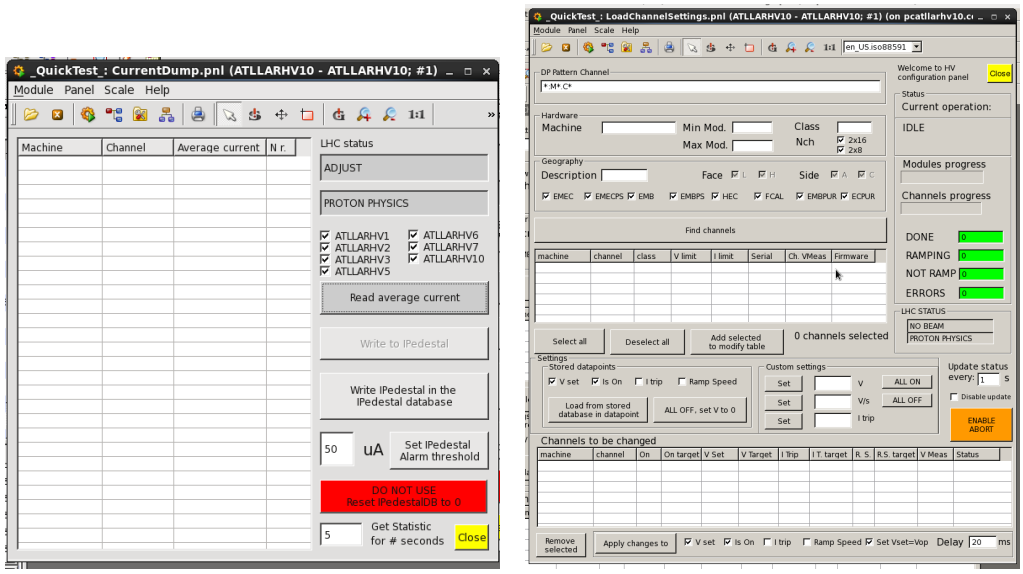

Figure B.3: Example voltage control panels. Left: panel to read the average current in all HV channels during the interfill. Right: panel to control the voltage of several modules at the same time.

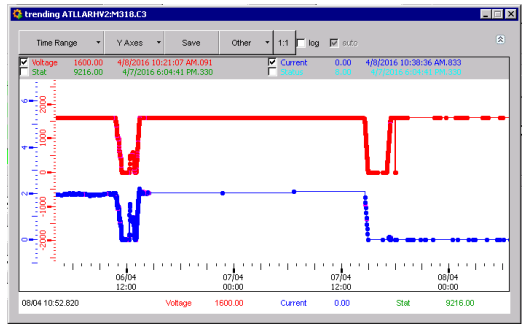

Figure B.4: Example current (blue) and voltage (red) readings for one HV channel. It can be seen that this channel was in short circuit with non zero current but after a reset of the voltage the short circuit disappeared.

B.6 HV trips

An HV channel should remain at the operational voltage since it is connected to a capacitor, however due to imperfections in the calorimeter, in the cables and in the modules itself sometimes trips can occur. A trip is a traumatic event, usually triggered by current spike, where the voltage quickly goes to zero, however the exact cause of a trip is not always clear. An example trip can be seen in Figure B.5. For the modules in the electromagnetic barrel and endcap an autorecovery procedure is implemented to avoid reaching zero voltage, if this option is activated the HV channel will start the to ramp up the voltage immediately after the trip. However the autorecovery procedure can fail, in this case and for channels where the autorecovery is not active the voltage has to be

operated manually. Usually one electrode in the calorimeter is connected to two HV channels, one for each face. Thanks to this double connection if one channel trips the other face of the electrode is still operational and at least half of the reading can be registered, otherwise there would be a hole in the detector. The halved energy reading is corrected in a later phase.

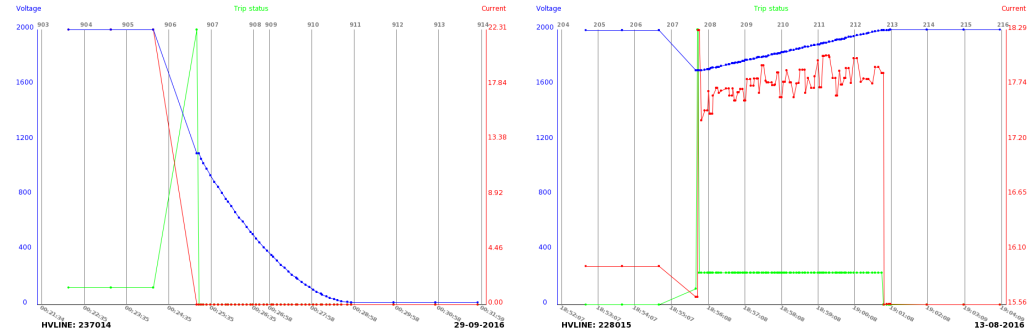

Figure B.5: Example voltage (blue) and current (red) readings during trip events of one high voltage channel. Left plot: trip without autorecovery, right plot: trip with successfull autorecovery.

B.7 Liquid argon temperature and impurities

During operation the LAr temperature and purity are continuously monitored in order to ensure accurate energy measurements. A change in temperature of the order of 1 K induces a 2% change in the energy measurement due to the changes in the drift time and the LAr density. For this reason there are 508 PT100 probes in the LAr calorimeter to monitor the temperature which remains at approximately 88.5 K. Impurities within the liquid argon, such as O_2 can also degrade the signal. For this reason 30 purity monitors, immersed in the LAr, are read out every 10 to 15 minutes.

B.8 LAr calorimeter readout system

When charged particles in the calorimeter shower cross the liquid argon gaps, they ionize the argon along their tracks. The applied high-voltage separates the electrons and the ions; they drift to the electrodes. During their drift, the electrons induce an electrical signal that is read out.

The resulting ionization current signal has a triangular shape, as shown in Figure B.6, and a drift time of 450-600 ns in the barrel. Since this drift time spans 18-24 LHC bunch crossings, the signal must be shaped and contracted in order to mitigate the effects of overlapping interactions. The 1524 front-end boards (FEBs), located concentrically around the LAr calorimeter, shape the signal in such a way that the area of the positive and negative lobes of the pulse are summed to zero. The shaping is performed in three different gains in order to meet the large dynamic energy range expected for physics signals.

The readout chain is schematically represented in Figure B.6. After the signal is shaped, it is transmitted through two paths, an analog path which leads to the Level 1 (LVL1) calorimeter

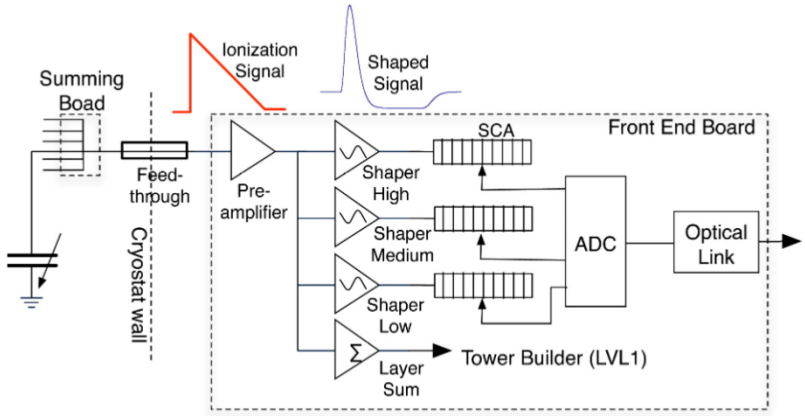

Figure B.6: The LAr readout chain showing the amplifiers and bi-polar shapers that shape the triangular ionization pulse on the FEBs.

trigger system and a digitizing chain. In the analog path a sum is performed over approximately 60 readout cells creating energy collections called trigger towers. The summed analog pulses are then analyzed by the hardware based LVL1 electronics which takes 2.5 μs to decide whether to retain or discard a particular event. In the digitizing path, shaped analog signals are stored in a switched capacitor array (SCA) and digitized with 12-bit analog-to-digital converters (ADC). For each triggered event, 5 ADC samples are sent out.

The signal amplitude is reconstructed on-line (in digital signal processors) using an optimal filtering technique. In addition, a quality factor is computed that measures how well the actual pulse shape matches the reference pulse shape. The optimal filtering coefficients are derived from the predicted pulse shape and the noise auto-correlation.

The pulse shape as well as the pedestal and the amplification of the readout chain can be measured using an electronic calibration system. The calibration of the LAr readout system is explained in more detail in the next section.

B.9 LAr calorimeter calibration system

In the following section a short overview of the LAr calorimeter calibration system will be presented. The main characteristic of the ATLAS electromagnetic calorimeter is the absence of active components inside the cryostat where they are exposed to high radiation flux. Since the liquid Argon is not expected to change its properties over time only the electronic readout has to be calibrated. A schematic diagram of the calibration system is presented in Figure B.7.

A voltage pulse, which simulates the ionization signal, is applied across an injection resistor R_{Inj} directly on the electrodes in the cryostat. The advantage of using resistance is the possibility to obtain 0.1% accuracy with little sensitivity to stray capacitances. These resistors are located on mother boards that are connected to the electrodes through summing boards, which group together

the signal of consecutive gaps to achieve the ϕ granularity.

The pulse produced by the calibration board is distributed to groups of nearby channels with little or no cross-talk in the detector. The calibration pulse sent inside the cryostat is an exponential voltage signal built from a precise DC current I_p using an inductor (L). It produces a fast voltage pulse with an exponential decay: $-R_0 I_p \exp(-t/\tau)$ on a 50 Ω termination with $\tau = R_0/(2L)$. This signal is propagated inside the calorimeter with a cable of impedance $Z_C = R_0$ terminated on a per mil impedance equivalent to R_0, in order to reduce any reflection of the signal. This impedance is made of the parallel association of R_{Inj} and the resistance R_a, different for each layer to ensure a correct 50 Ω termination.

To summarize, the accuracy on the amplitude of the calibration signal delivered to the detector is determined by the accuracy on the amplitude at the output of the calibration board, by the precision resistors in the cryostat and by the cable characteristics. The sum of these three contributions leads to 0.25% uniformity across all channels. In addition, a 0.1% stability of the amplitude is required.

B.9.1 LAr calorimeter readout calibration

The calibration process is divided in three different types of calibration runs which are usually taken during the interfill phase of LHC: pedestal, ramp and delay.

- **Pedestal run:** it consists of reading the detector with no input signal. It provides pedestal information from the average, noise from the RMS and noise autocorrelation from the timing correlation of the samples.
- **Ramp run:** during this process different input current signals (DAC) are injected. The gain slope of the calorimeter cells is extracted from a fit of the DAC versus ADC curve with a first order polynomial.
- **Delay run:** in this calibration one single signal amplitude is used. The calibration pulse is shifted by steps of 1.04 ns along 25 ns in order to reconstruct the pulse shape.

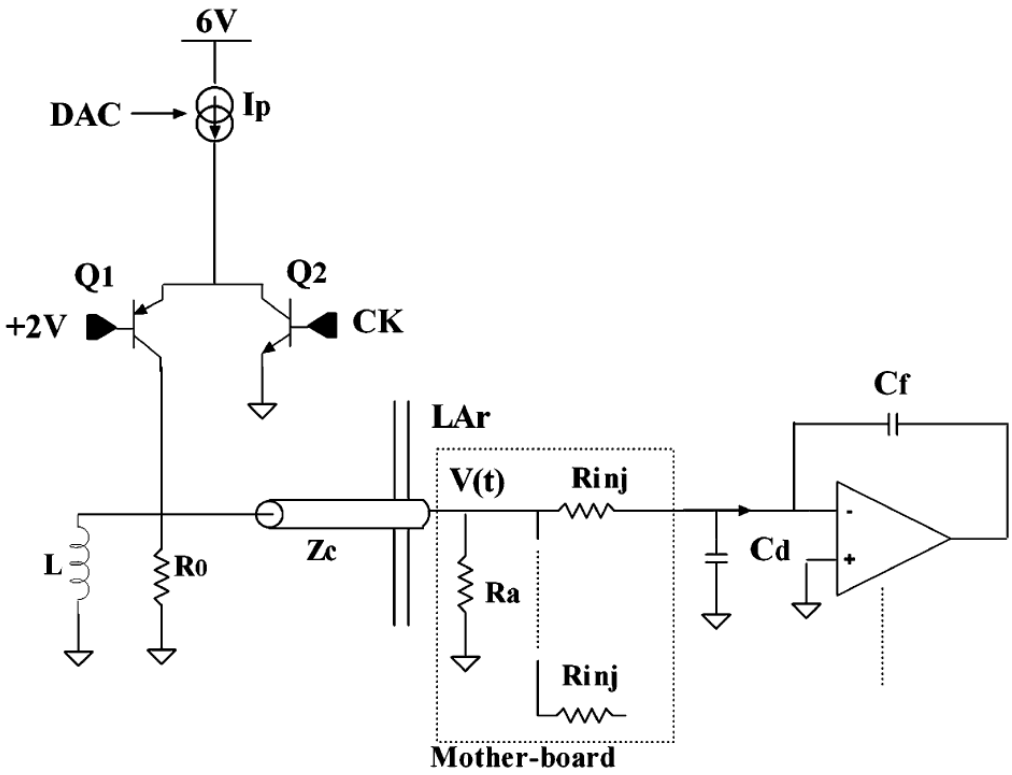

Figure B.7: Schematic diagram of the LAr calibration system. Left part of the diagram is located on the electronics calibration board at warm, while the right part corresponds to the distribution of the signal to the calorimeter cells, done with precision resistors in the liquid argon.

Appendix C

Studies of the properties of the excess region

The ATLAS Collaboration in December of the year 2015 was looking at an unforeseen excess in the diphoton invariant mass distribution. The observed excess was a resonance with mass around 750 GeV and width around 6 % of the mass. It was observed with data taken during 2015 and its significance was too high to be considered at first sight a simple statistical fluctuation. Surprisingly the invariant mass region of the excess was already studied in run-I and no striking feature was observed in the 8 TeV data. For the spin-2 analysis no excess was observed in run-I, while for the spin-0 analysis a small ($\sim 2\sigma$) excess was observed at the same invariant mass. Since this excess was not expected several studies were conducted to detect any source of systematic effect at detector, reconstruction or analysis level. These tests can be summarized in:

- Compare the distribution of kinematic variables in data with Monte Carlo of reducible and irreducible background samples.
- Compare the distribution of kinematic variables in data in the excess region with nearby regions of invariant mass.
- Study the time-distribution in the data taking of the events in the excess region.
- Study the detector-level properties of the observed photons.
- Study the effect of the energy calibration of the photons.

Many quantities are compared in different mass region, in particular between the excess region and the control region at lower and higher diphoton invariant mass. Three regions based on $m_{\gamma\gamma}$ are defined as:

Left side-band: $(600 \leq m_{\gamma\gamma} < 700)$ GeV

Excess region: $(700 \leq m_{\gamma\gamma} < 840)$ GeV in data 2015, $(650 \leq m_{\gamma\gamma} < 800)$ GeV in data 2016.

Right side-band: $(m_{\gamma\gamma} \geq 840)$ GeV in data 2015, $(m_{\gamma\gamma} \geq 800)$ GeV in data 2016.

C.1 Monte Carlo samples

The Monte Carlo samples used to describe the properties of the irreducible background are the same used in the main analysis stream seen in Section 6.2.2.1. Furthermore Monte Carlo samples with one photon and one jet, simulated with the Sherpa Monte Carlo and produced in slices of p_{T} of the simulated photon, were used to describe the reducible background. The reducible background distribution had a limited statistic especially for the high mass region, so no conclusive evidence can be derived with the comparison with data. Di-jet contribution was neglected since the contribution was small and the existing MC samples had insufficient statistic in the interesting region. In the following studies the two background sources were not summed as in other parts of the analysis; the normalized distribution of the kinematic variables were compared directly with data.

C.2 Techniques

In the following sections the technique exploited to identify the differences between data and MC, or data in the excess region and in the sideband region.

C.2.1 Statistic tests

Many distributions of reconstructed variables are compared. The variables are plotted after normalizing the sum of the content of each bin (excluding underflow and overflow) to unity. Since in some region of data the number of entries is quite small the error bands are not from the gaussian approximation, using the Poissonian standard deviation (symmetric $\pm\sqrt{n}$ where n is the entries in one bin). Instead asymmetric error bands are implemented. Precisely, the error bands represent confidence interval at 68% using the Neyman construction. The interval is central unless this does not enclose the point estimate n (i.e., for small n) in which case the interval is adjusted to start at n. Since the events from simulations are weighted, the error for each bin is equal to $\sqrt{\sum w_i}$, where w_i is the weight for one event.

To calculate the compatibility between two distributions (data-MC or data-data) two different statistic tests are exploited. A simple t-test was used to check the compatibility of the mean of the distributions, this is only applicable to a subset of the variables, for example isolation, but not to all of them, for example radius of conversion, since the mean is not a clear property of some distribution.

Instead a Kolmogorov-Smirnov (KS) test was used to compare the shape of the kinematic variable distributions. The KS test is a nonparametric test of the equality of continuous, one-dimensional probability distributions that can be used to compare a sample with a reference probability distribution, or to compare two samples. The latter case is applicable in these studies. This test statistic quantifies the distance between the distribution functions of the two tested samples. The null distribution of this statistic is calculated under the null hypothesis that the two samples are drawn from the same distribution.

For data the KS test has been computed with two equivalent methods ("KS test p-value" and "root p-value" in the figures) using the unbinned distributions. However, since simulations are weighted, when comparing data and simulations a modified KS test for binned distributions is used.

C.2.2 KDE distributions

For some of the kinematic distribution in data 2015 the number of events was low and it was impossible to compare the data distribution with the MC distributions. To estimate a rough comparison the Kernel Density Estimation [126] (KDE) of the distribution was calculated. KDE is a data smoothing technique that allows to make inferences about a finite data sample. The distribution is built as follows: a kernel of chosen shape is drawn for each one of the points in a dataset, then all the kernels are summed to build a smooth distribution. A tunable smoothing factor is used to avoid too many fluctuations in the distribution, this factor weights the single kernels in the sum with the density of the distribution around the kernel. In these studies a gaussian kernel of chosen width was chosen. Example of these distributions can be seen in Figure C.1 for data 2015.

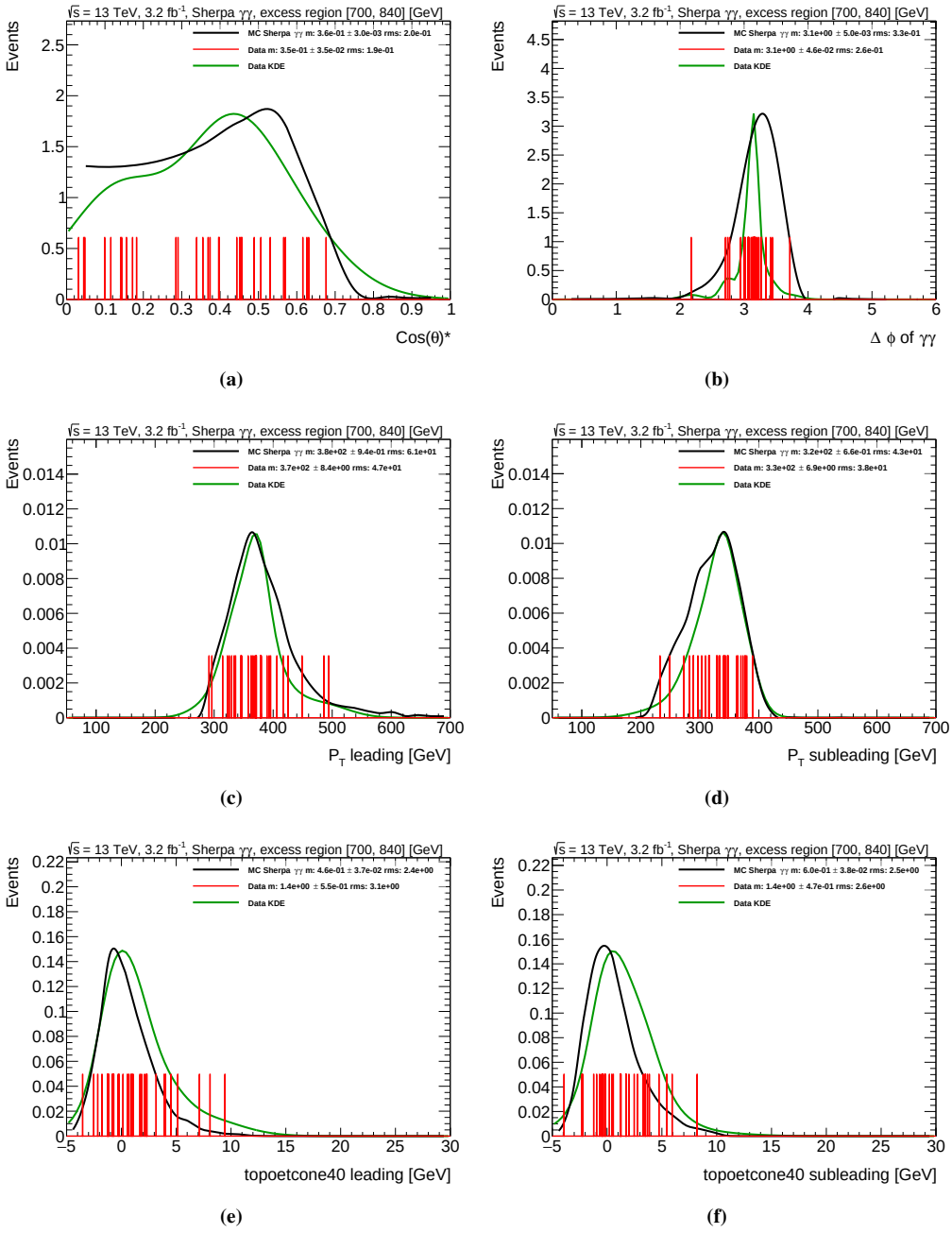

Figure C.1: KDE plots of several quantities for data 2015, distributions are for events selected by the spin-0 selection in the excess invariant mass region. Red lines represent the single events, black line is the KDE distribution for MC and green line is the KDE distribution build from the red lines.

C.2.3 S-plots

To study the properties of a signal one possibility is to compare the events in the excess region with the events in the sidebands region as already stated. However a more refined technique can be used to produce S-plots. With this technique is possible to have an estimate distribution of signal and background events. To produce S-plots the same signal-plus-background model used for the calculation of p_0 is exploited, the model is first fitted to data with mass and width of the resonance free (however with values starting around the studied excess). Then weights are calculated for each event as a function of the observable $m_{\gamma\gamma}$ using the signal and background fraction from the fitted model. This result in two weighted dataset: one weighted as signal and one weighted as background. Distributions are then plotted for the two weighted datasets, resulting in approximate distribution of kinematic variables for signal events and background events. This technique however requires that the studied distribution is uncorrelated with the observable used in the model, in this case $m_{\gamma\gamma}$. Example of these distributions can be seen in Figure C.2 for data 2015 (excess around 735 GeV) and in Figure C.3 for data 2016 (excess around 700 GeV).

The biggest difference between the excess proprieties and the background proprieties is observed in the η distribution of the photons, in the $\cos\theta^*$ distribution and in the $\Delta\eta$ between the photons.

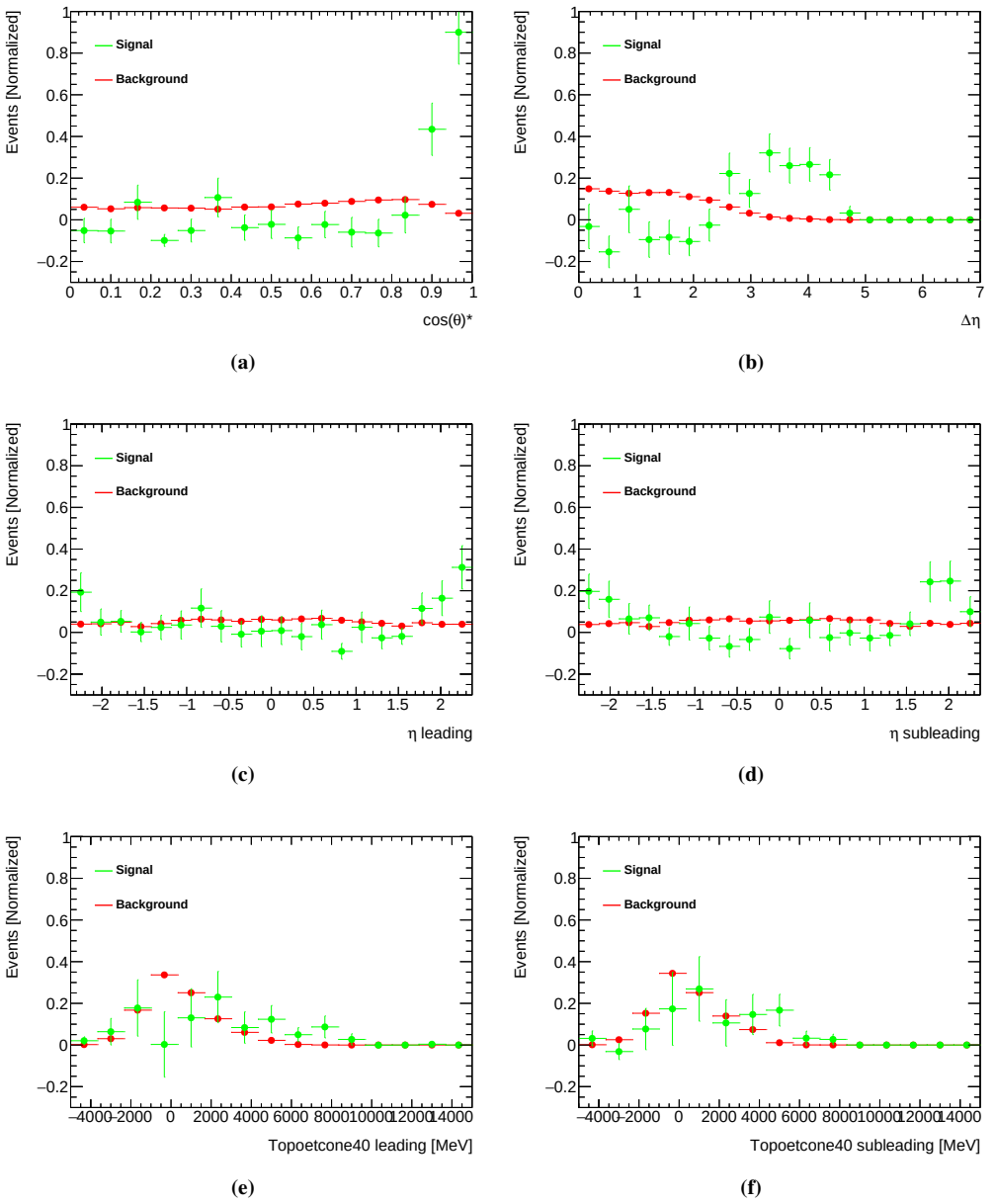

Figure C.2: S-plots of several quantities for data 2015, distributions are for events selected by the spin-2 selection over the entire mass range. Green lines are for signal distributions and red lines are for background distributions.

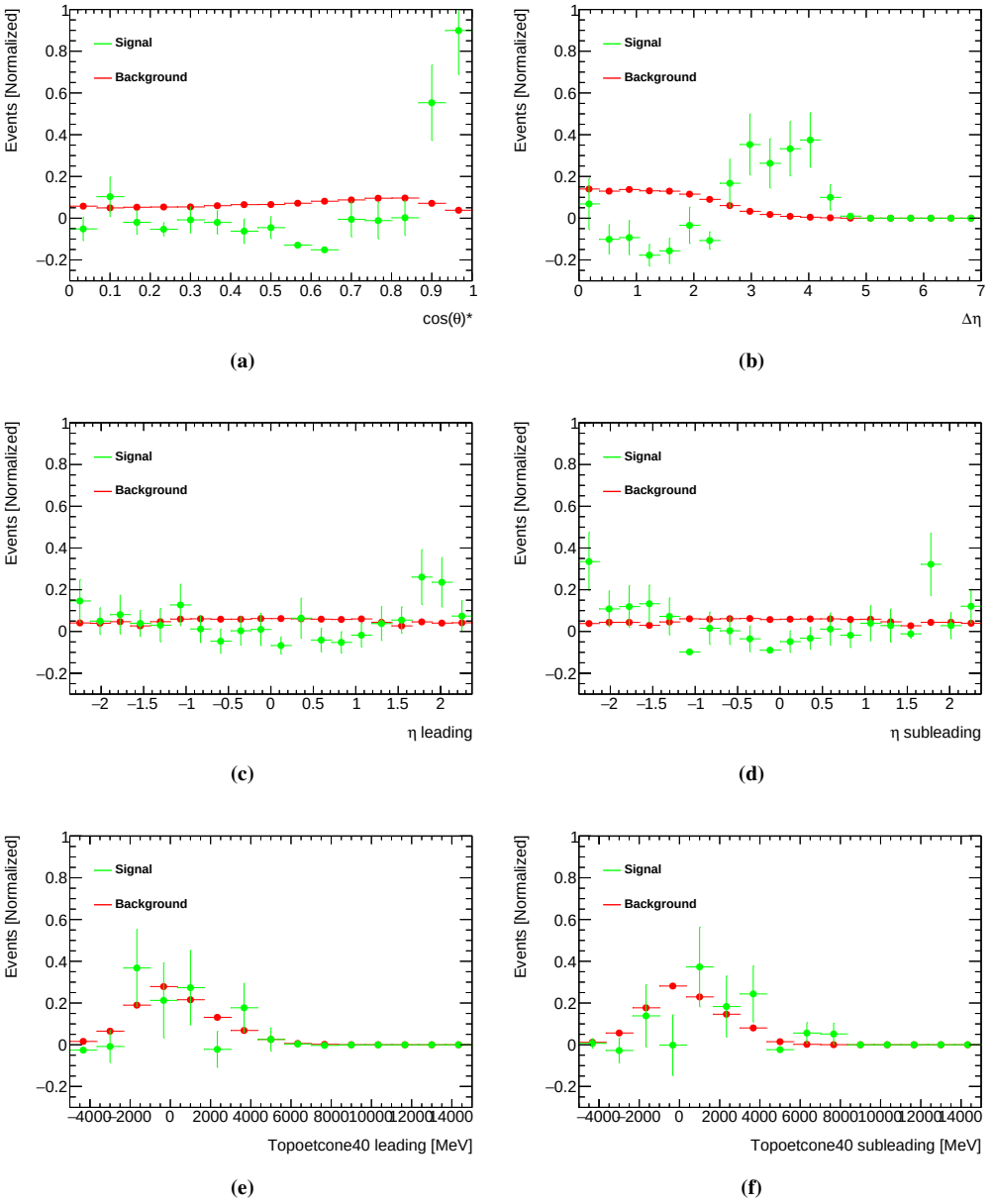

Figure C.3: S-plots of several quantities for data 2016, distributions are for events selected by the spin-2 selection over the entire mass range. Green lines are for signal distributions and red lines are for background distributions.

C.3 Kinematic variables

In the following sections several studies on kinematic variables will be shown for data 2015 and data 2016. The plots are comparison of data-MC and data-data using the techniques introduced in the previous section. In the following pages will be shown the comparison with Monte Carlo in the $m_{\gamma\gamma}$ excess region for spin-0 selection in Figures C.4 and C.5 for the years 2015 and 2016. Same comparison for the spin-2 selection is in Figures C.6 and C.7 for the years 2015 and 2016. Then the comparison of data in the $m_{\gamma\gamma}$ excess region versus data in the sideband regions is shown in Figures C.8, C.9 for spin-0 selection and respectively for both years. The comparison of data from 2015 and data from 2016 is also shows in Figures C.10, C.11 for both selections.

The tested variables are the proprieties of the photons: η, p_{T}, several shower shapes and isolation. Furthermore event-level variables are compared: ΔR between the photons and pileup distribution. Overall no striking difference is observed between kinematic variables in data and Monte Carlo and between the two years (only the pileup distribution is different as expected). Other than the one shown several other kinematic variables were tested but no strange behavior was observed.

C.3.1 Comparison with MC

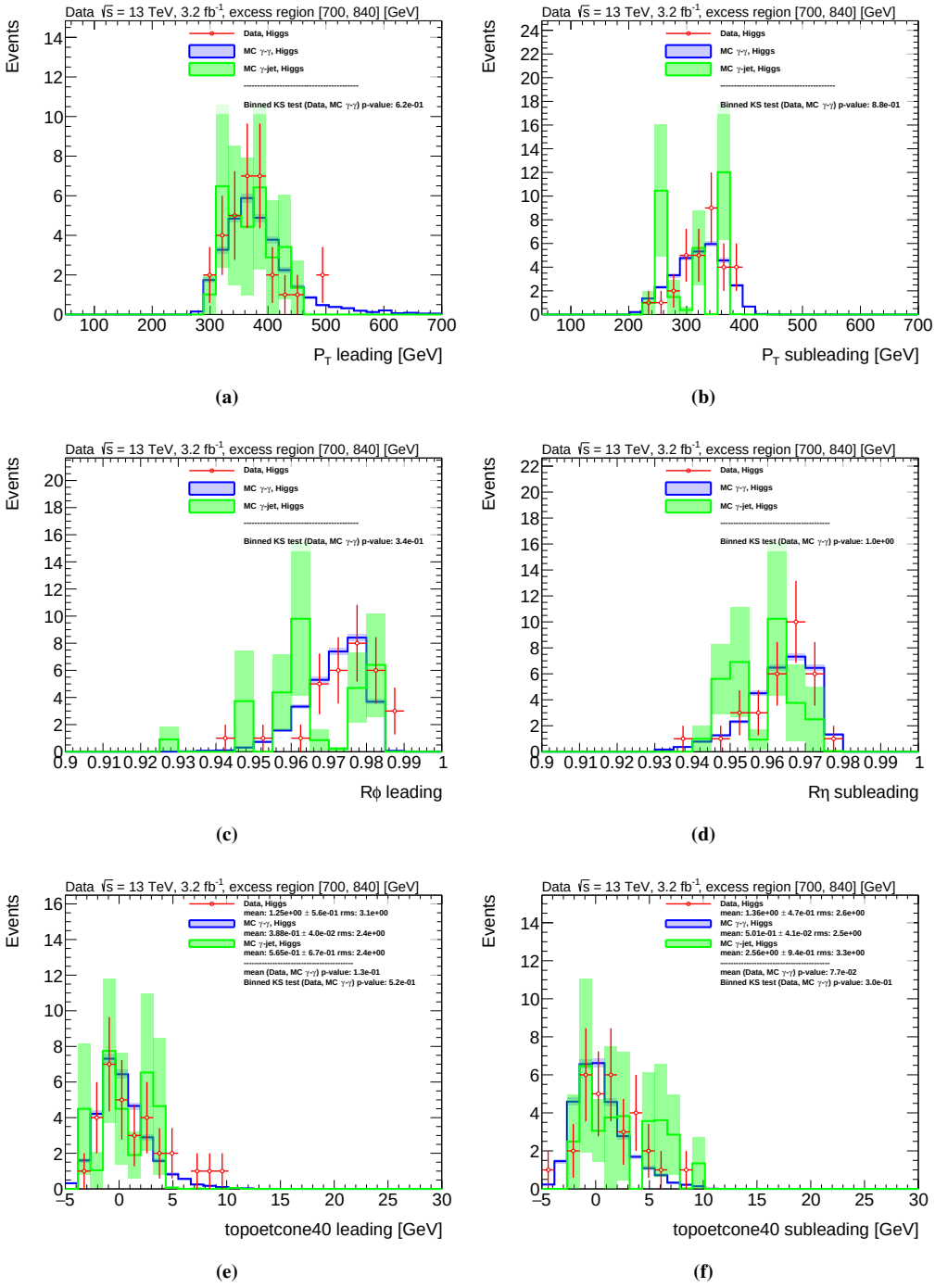

Figure C.4: Plots of several quantities for data 2015 versus Monte Carlo, distributions are for events selected by the spin-0 selection in the excess invariant mass region.

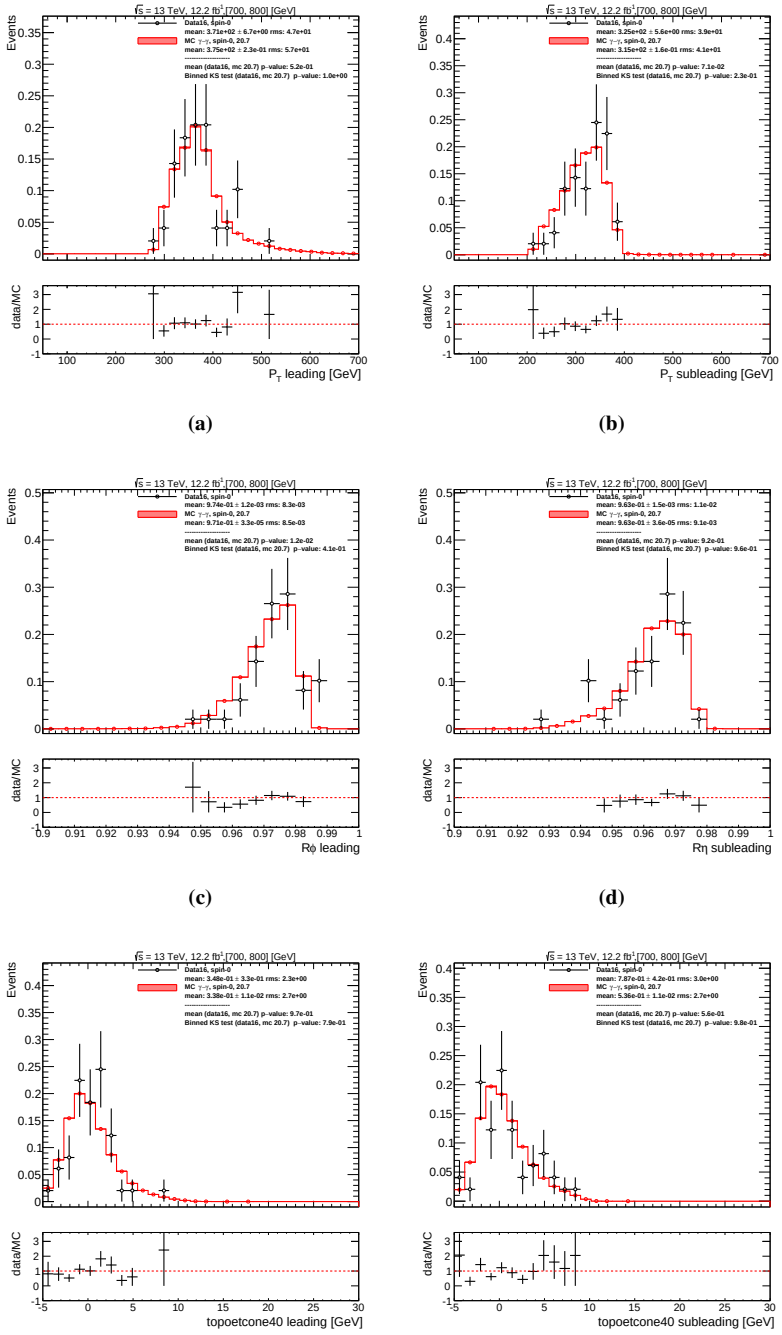

Figure C.5: Plots of several quantities for data 2016 versus Monte Carlo, distributions are for events selected by the spin-0 selection in the invariant mass region of the 2015 excess.

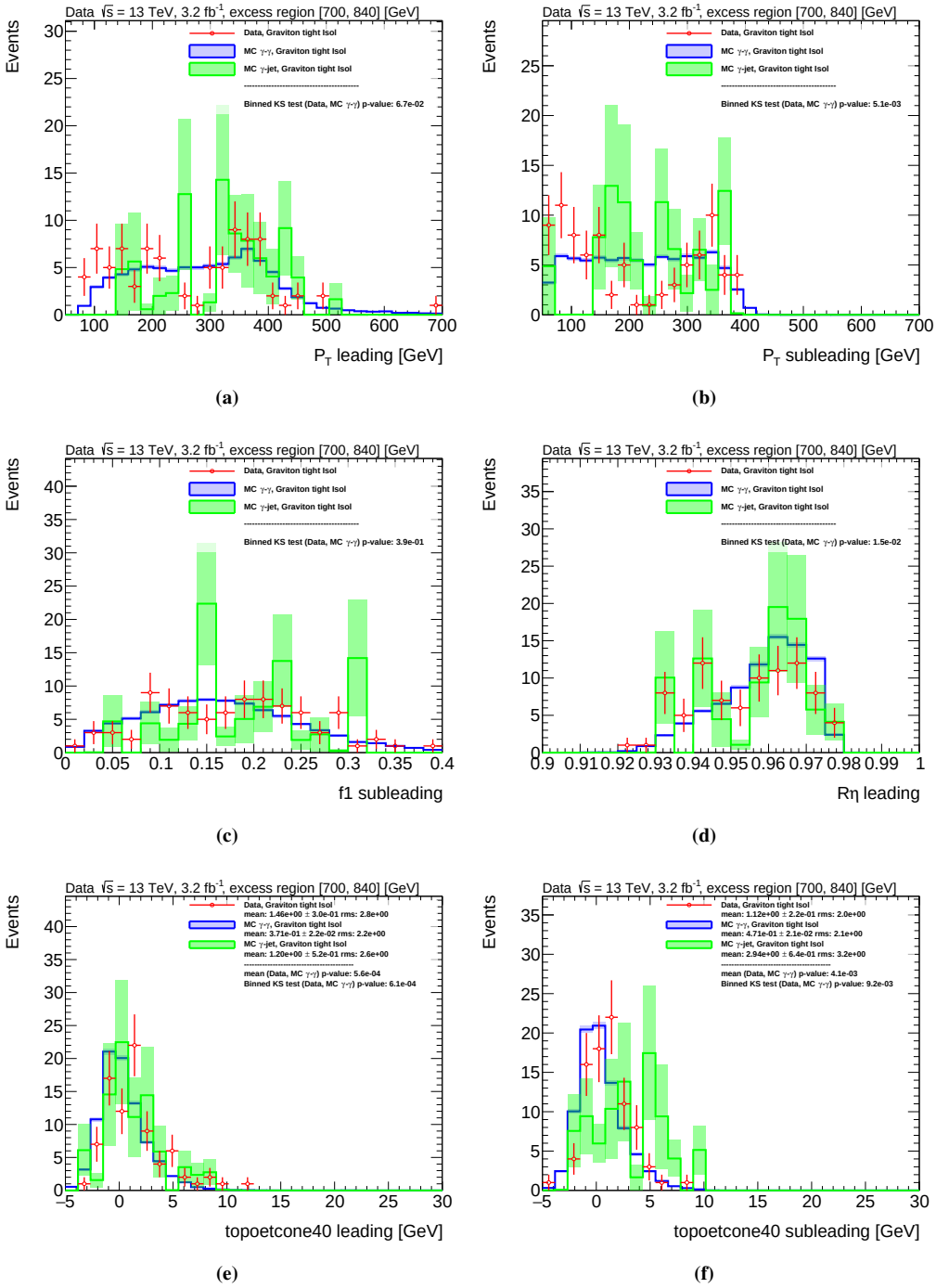

Figure C.6: Plots of several quantities for data 2015 versus Monte Carlo, distributions are for events selected by the spin-2 selection in the excess invariant mass region.

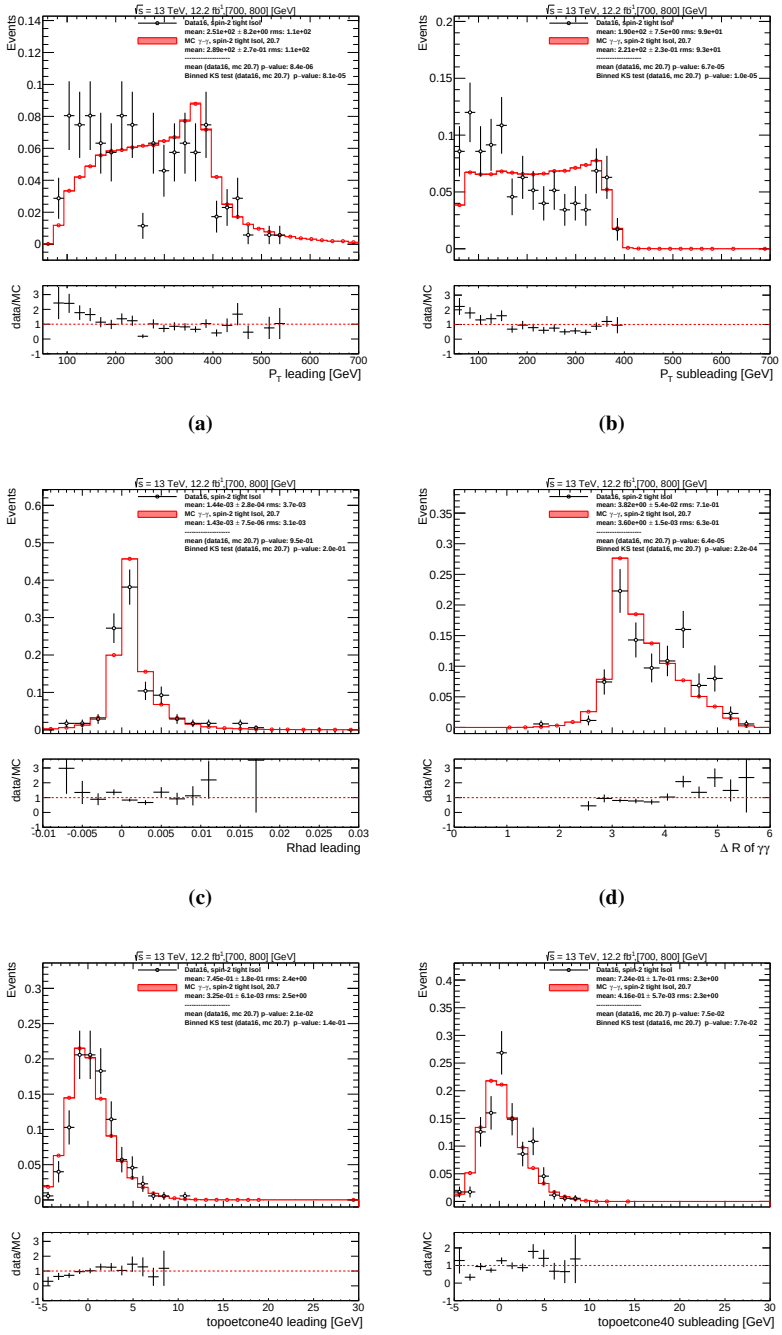

Figure C.7: Plots of several quantities for data 2016 versus Monte Carlo, distributions are for events selected by the spin-2 selection in the invariant mass region of the 2015 excess.

C.3.2 Comparison with data

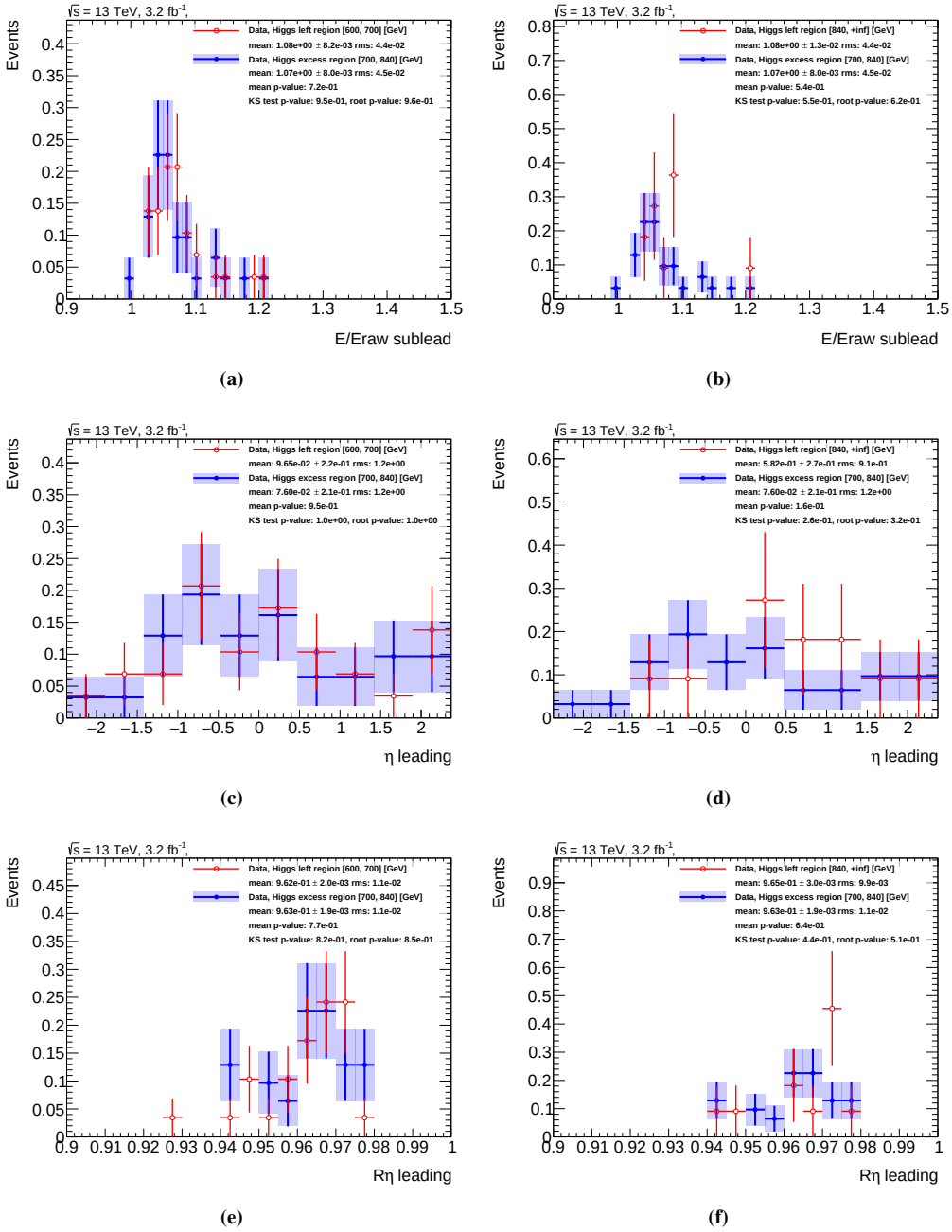

Figure C.8: Plots of several quantities for data 2015, distributions are for events selected by the spin-0 selection in the excess invariant mass region versus other region in invariant mass.

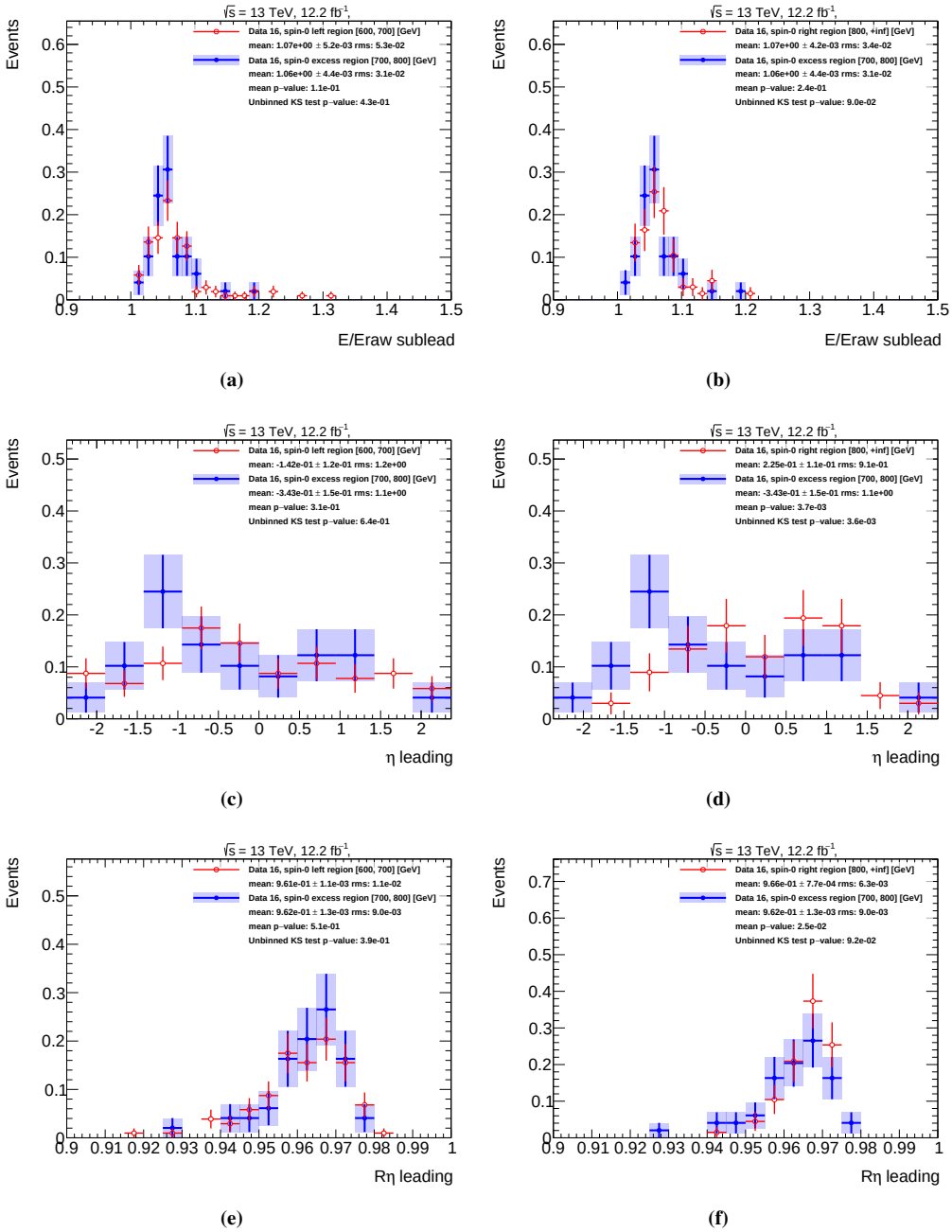

Figure C.9: Plots of several quantities for data 2016, distributions are for events selected by the spin-0 selection in the invariant mass region of the 2015 excess versus other region in invariant mass.

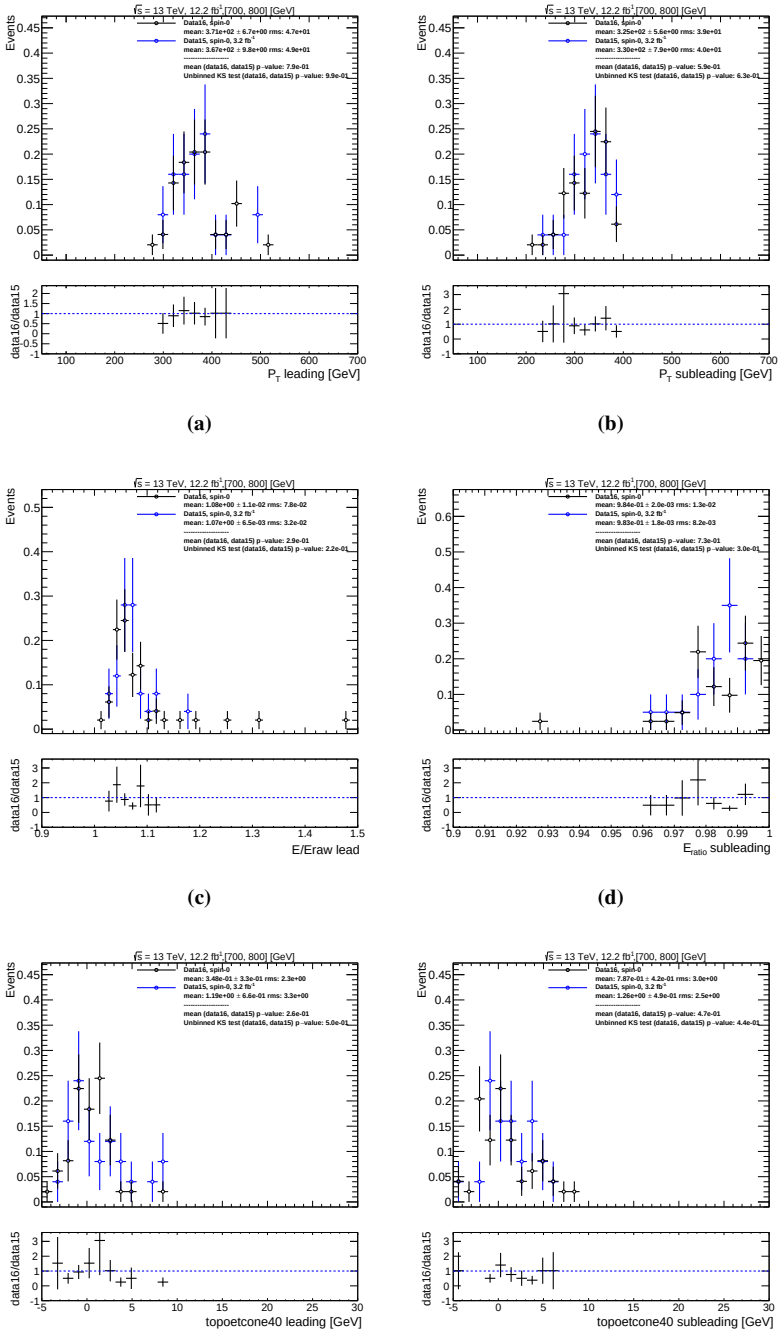

Figure C.10: Plots of several quantities for data 2015 versus data 2016, distributions are for events selected by the spin-0 selection in the invariant mass region of the 2015 excess.

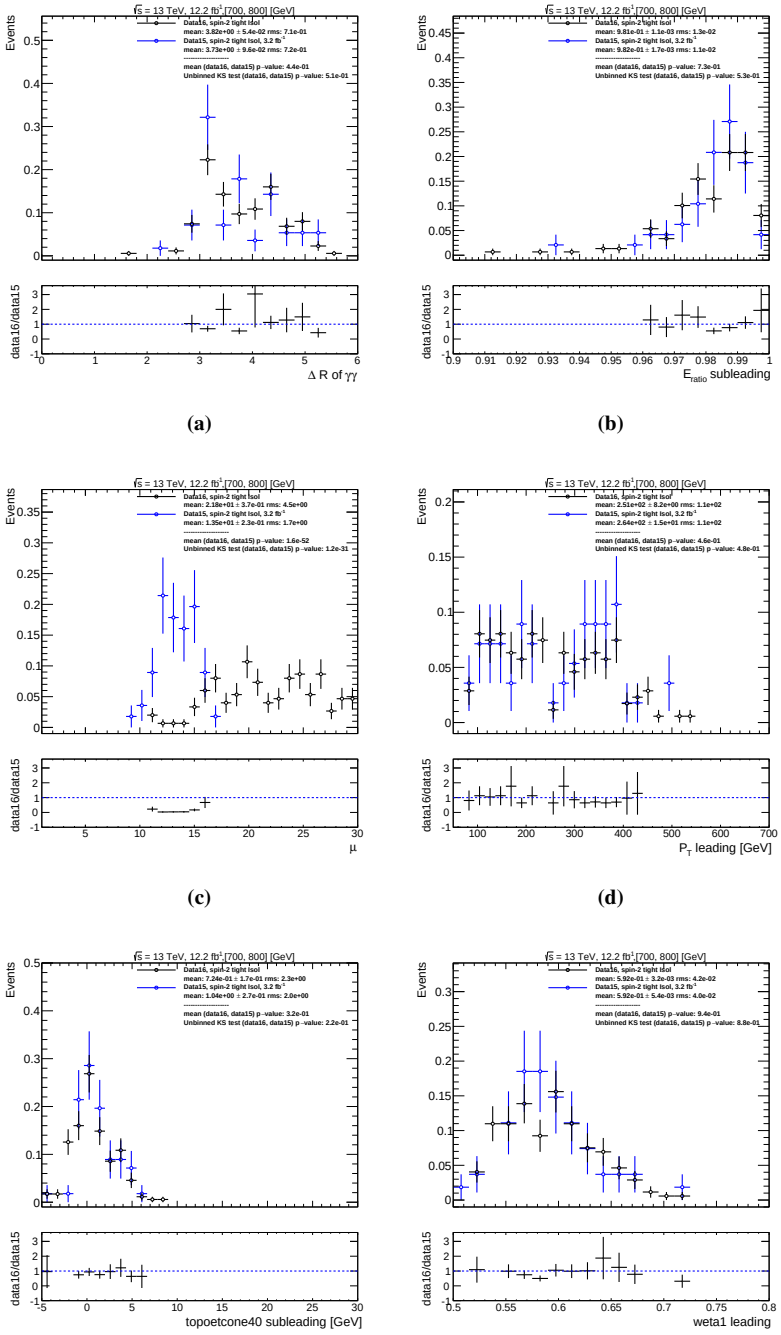

Figure C.11: Plots of several quantities for data 2015 versus data 2016, distributions are for events selected by the spin-2 selection in the invariant mass region of the 2015 excess.

C.4 Studies on Calibrations

In the following section effect of the energy calibration on photons will be studied. To do so the modified invariant mass spectrum was studied. The distribution was built using the MVA-only calibrated energy or the raw (non-calibrated) energy of the photons. The distribution of E/E_{RAW} where E and E_{RAW} are respectively the calibrated energy and the raw energy of the photons can be seen in Figures C.12 aC.13 for spin-0 and spin-2 selections. The study shows that the excess seen in 2015 was not an artifact of the calibration.

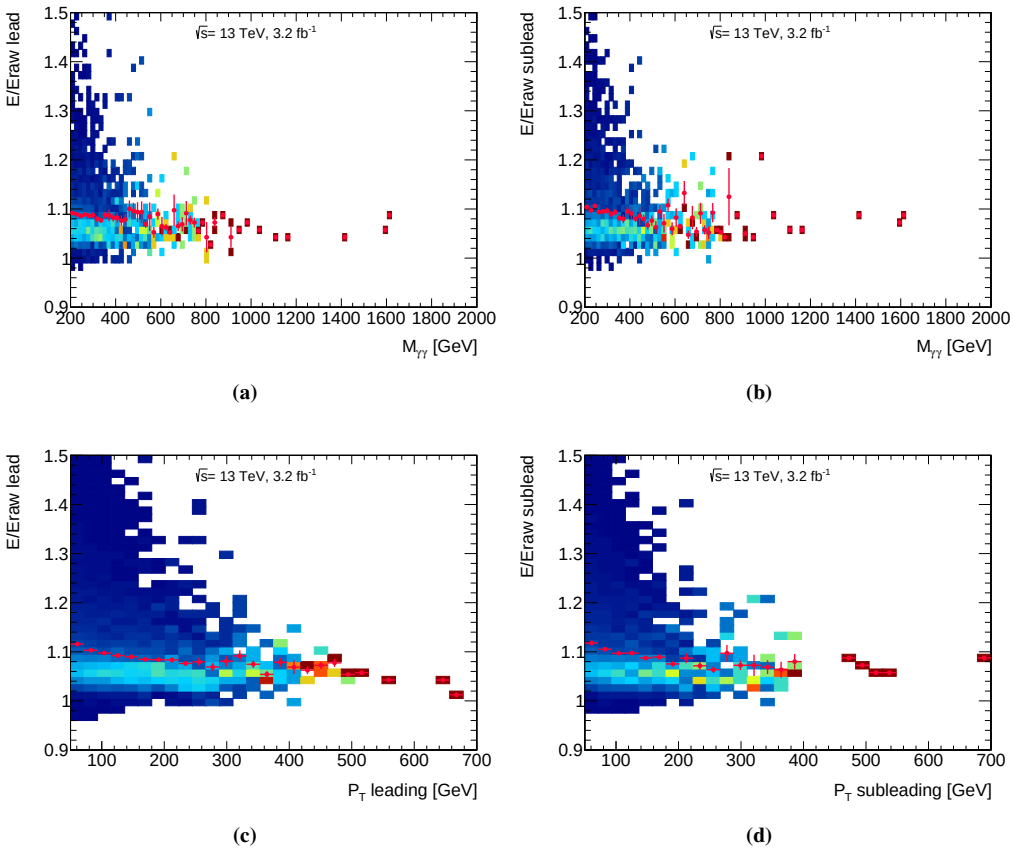

Figure C.12: 2-D plots for data 2015, distributions are for events selected by the spin-0 selection. The trend of E/E_{RAW} over p_{T} and $m_{\gamma\gamma}$ is shown. The red line is the profile of the 2-D distribution.

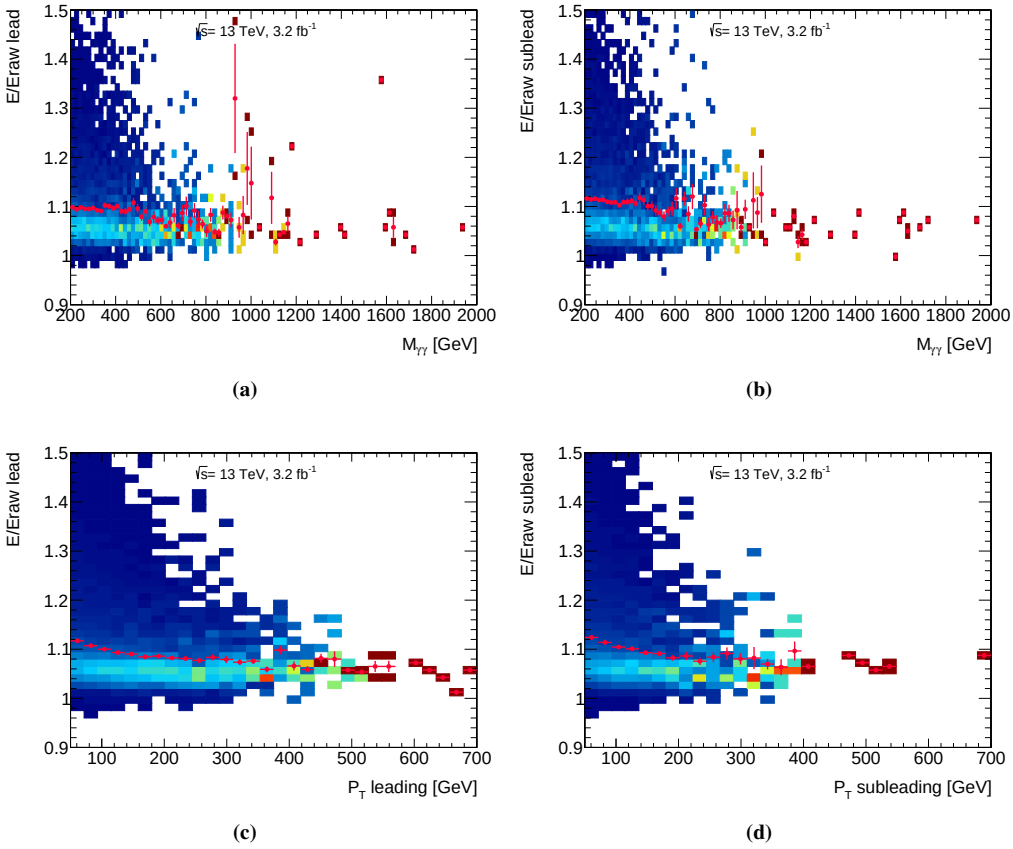

Figure C.13: 2-D plots for data 2015, distributions are for events selected by the spin-2 selection. The trend of E/E_{RAW} over p_{T} and $m_{\gamma\gamma}$ is shown. The red line is the profile of the 2-D distribution.

C.5 Detector level properties

In this section the properties of the calorimeter cell associated to the photons will be studied. The cells in the electromagnetic calorimeter have three different reading gain setting: high, medium and low. This study shows that there is no correlation between the excess in 2015 and the change in gain of the electromagnetic calorimeter. Furthermore the time reading of the cells in respect of event time was studied to understand if there is a possible contamination of events from other colliding bunches. No anomaly from out of time pileup is shown. The 2-D distribution of these quantities can be found in Figure C.14.

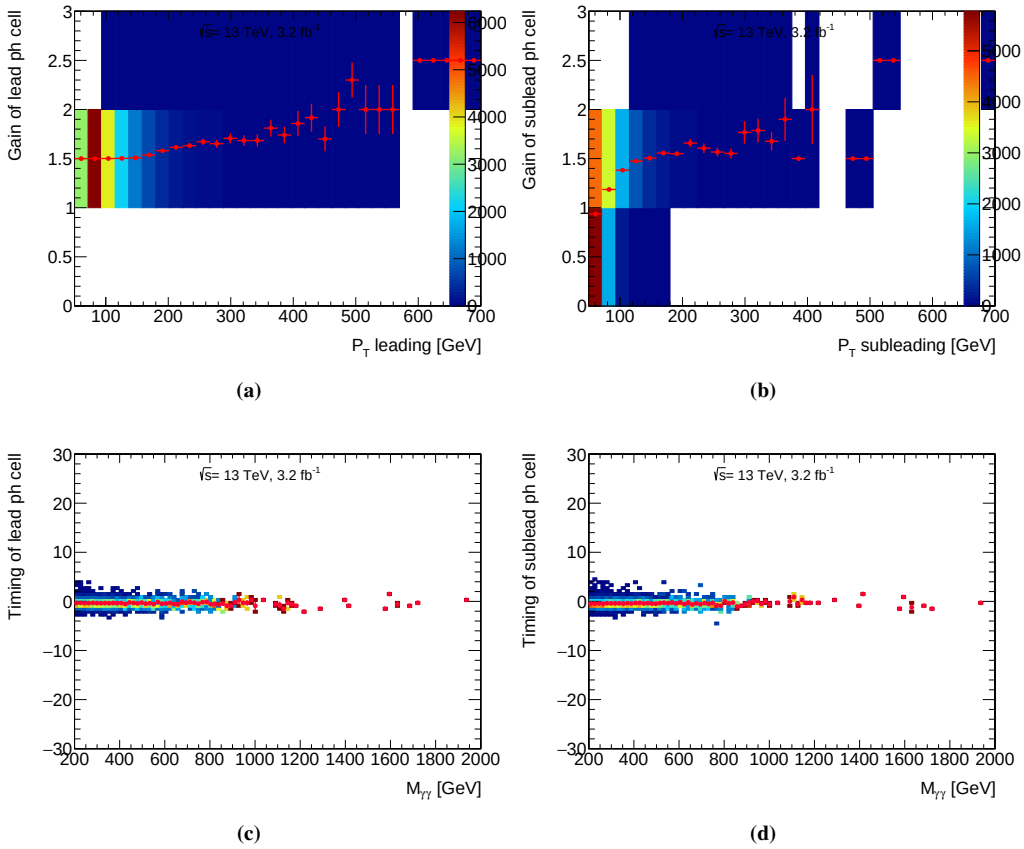

Figure C.14: Trend of cell gain and timing over p_{T} and $m_{\gamma\gamma}$ for data 2015, distributions are for events selected by the spin-2 selection. The red line is the profile of the 2-D distribution.

C.6 Pointing and vertex

The calorimeter pointing for the Z variable (along the beam axis) of the photons is calculated extrapolating the photon's deposited clusters in the calorimeter. This distribution was studied to check if an excess of events from beam background was present, meaning particles coming directly from the colliding beam and not from hard-collisions. The Z pointing distributions for year 2015 and 2016 can be found in Figures C.15 and C.16. The study shows no beam background excess.

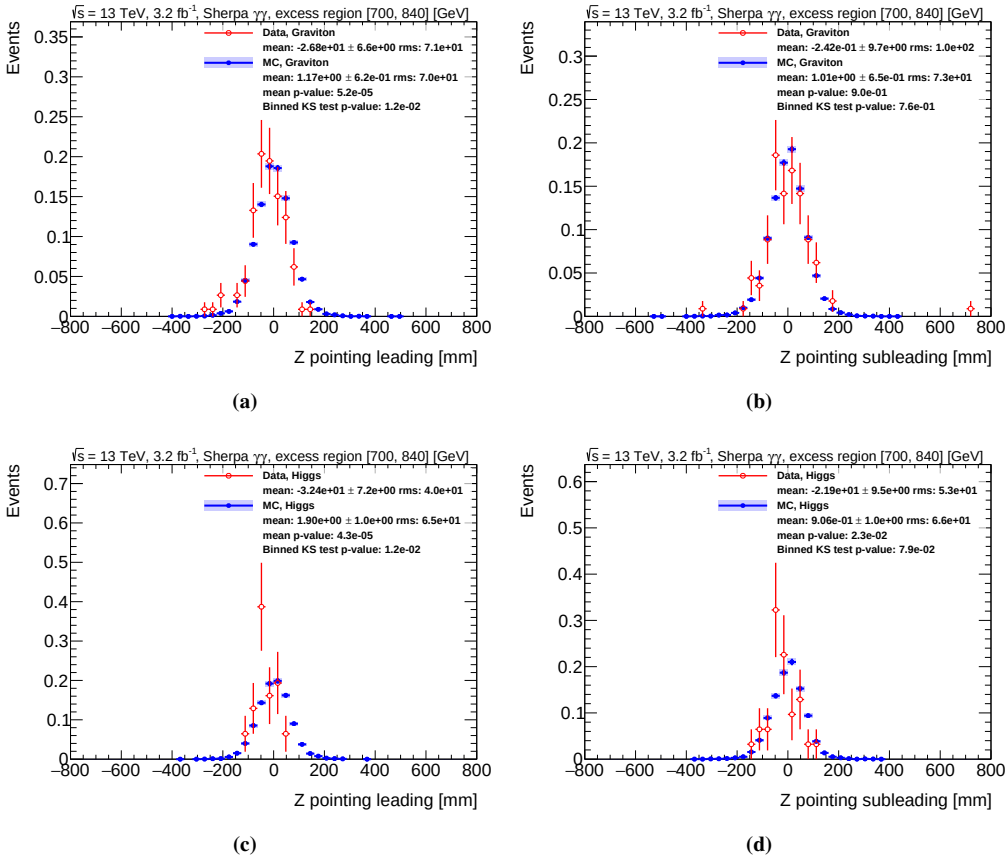

Figure C.15: Z pointing for data 2015, distributions are for events selected by the spin-0 and spin-2 selection in the excess invariant mass region.

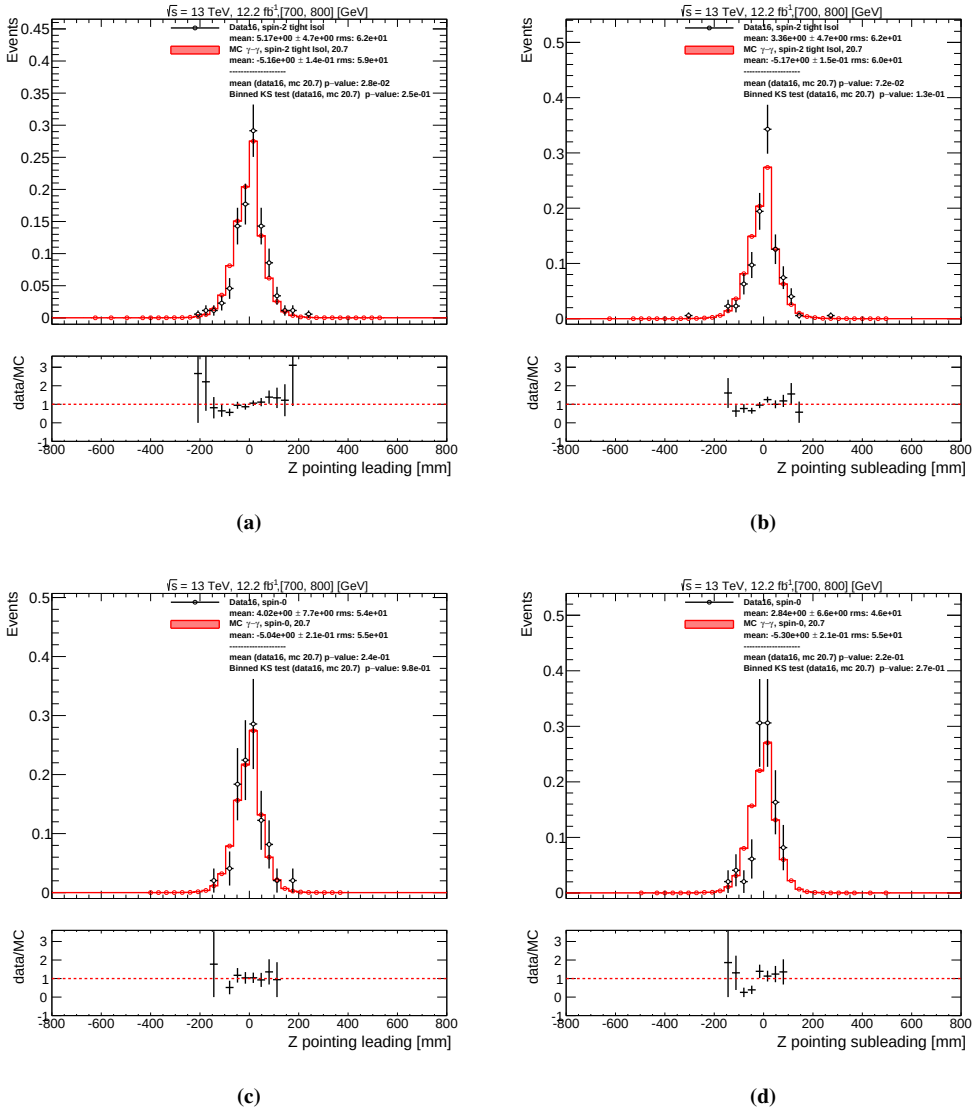

Figure C.16: Z pointing for data 2016, distributions are for events selected by the spin-0 and spin-2 selection in the invariant mass region of the 2015 excess.

Bibliography

[1] S. M. Mazza. "Search for a SM Higgs boson in the diphoton plus E_T^{MISS} channel". In: *Nuovo Cim.* C037.04 (2014), pp. 19–29. DOI: 10.1393/ncc/i2014-11786-2 (cit. on p. i).

[2] G. Aad et al. "Measurement of the Higgs boson mass from the $H \to \gamma\gamma$ and $H \to ZZ^* \to 4\ell$ channels with the ATLAS detector using 25 fb^{-1} of pp collision data". In: *Phys.Rev.* D90.5 (2014), p. 052004. DOI: 10.1103/PhysRevD.90.052004. arXiv: 1406.3827 [hep-ex] (cit. on p. i).

[3] E. Vilucchi et al. "PROOF-based analysis on the ATLAS Grid facilities: first experience with the PoD/PanDa plugin". In: *J.Phys.Conf.Ser.* 513 (2014), p. 032102. DOI: 10.1088/1742-6596/513/3/032102 (cit. on p. i).

[4] L. Randall and R. Sundrum. "An Alternative to compactification". In: *Phys.Rev.Lett.* 83 (1999), pp. 4690–4693. DOI: 10.1103/PhysRevLett.83.4690. arXiv: hep-th/9906064 [hep-th] (cit. on pp. ii, 21, 26).

[5] L. Randall and R. Sundrum. "A Large mass hierarchy from a small extra dimension". In: *Phys.Rev.Lett.* 83 (1999), pp. 3370–3373. DOI: 10.1103/PhysRevLett.83.3370. arXiv: hep-ph/9905221 [hep-ph] (cit. on pp. ii, 21, 26).

[6] "Search for Extra Dimensions in the Diphoton Final State using 20.3 fb^{-1} of pp Collisions at 8 TeV recorded by the ATLAS detector at the LHC". In: EXOT-2012-19 (2014) (cit. on p. ii).

[7] G. Aad et al. "Search for Scalar Diphoton Resonances in the Mass Range 65 – 600 GeV with the ATLAS Detector in pp Collision Data at $\sqrt{s} = 8\ TeV$". In: *Phys.Rev.Lett.* 113.17 (2014), p. 171801. DOI: 10.1103/PhysRevLett.113.171801. arXiv: 1407.6583 [hep-ex] (cit. on pp. ii, v, 34, 38).

[8] *Search for resonances decaying to photon pairs in 3.2 fb^{-1} of pp collisions at $\sqrt{s}$ = 13 TeV with the ATLAS detector*. Tech. rep. ATLAS-CONF-2015-081. Geneva: CERN, 2015. URL: http://cds.cern.ch/record/2114853 (cit. on pp. ii, 109, 209).

[9] "The ATLAS Experiment at the CERN Large Hadron Collider". In: *Journal of Instrumentation* 3.08 (2008), S08003. URL: http://stacks.iop.org/1748-0221/3/i=08/a=S08003 (cit. on pp. ii, 58, 65).

[10] M. Aaboud et al. "Search for resonances in diphoton events at $\sqrt{s}$=13 TeV with the ATLAS detector". In: *JHEP* 09 (2016), p. 001. DOI: 10.1007/JHEP09(2016)001. arXiv: 1606.03833 [hep-ex] (cit. on pp. ii, 109, 116, 132, 137, 138, 140, 141, 168, 185, 186, 196, 209).

[11] *Search for scalar diphoton resonances with 15.4 fb^{-1} of data collected at $\sqrt{s}$=13 TeV in 2015 and 2016 with the ATLAS detector*. Tech. rep. ATLAS-CONF-2016-059. Geneva: CERN, 2016. URL: https://cds.cern.ch/record/2206154 (cit. on pp. ii, 109).

[12] V. Khachatryan et al. "Search for Resonant Production of High-Mass Photon Pairs in Proton-Proton Collisions at $\sqrt{s}$ =8 and 13 TeV". In: *Phys. Rev. Lett.* 117.5 (2016), p. 051802. DOI: 10.1103/PhysRevLett.117.051802. arXiv: 1606.04093 [hep-ex] (cit. on pp. iii, 109).

[13] V. Khachatryan et al. "Search for high-mass diphoton resonances in proton-proton collisions at 13 TeV and combination with 8 TeV search". In: (2016). arXiv: 1609.02507 [hep-ex] (cit. on pp. iii, 109).

[14] H. Davoudiasl, J. L. Hewett, and T. G. Rizzo. "Phenomenology of the Randall-Sundrum Gauge Hierarchy Model". In: *Phys. Rev. Lett.* 84 (10 2000), pp. 2080–2083. DOI: 10.1103/PhysRevLett.84.2080. URL: http://link.aps.org/doi/10.1103/PhysRevLett.84.2080 (cit. on pp. iii, 26).

[15] G. F. Giudice, R. Rattazzi, and J. D. Wells. "Quantum gravity and extra dimensions at high-energy colliders". In: *Nuclear Physics B* 544.12 (1999), pp. 3 –38. ISSN: 0550-3213. DOI: http://dx.doi.org/10.1016/S0550-3213(99)00044-9. URL: http://www.sciencedirect.com/science/article/pii/S0550321399000449 (cit. on pp. iii, 23).

[16] N. Arkani-Hamed, S. Dimopoulos, and G. Dvali. "The Hierarchy problem and new dimensions at a millimeter". In: *Phys.Lett.* B429 (1998), pp. 263–272. DOI: 10.1016/S0370-2693(98)00466-3. arXiv: hep-ph/9803315 [hep-ph] (cit. on pp. iii, 21).

[17] "Search for extra dimensions using diphoton events in 7 TeV proton proton collisions with the ATLAS detector". In: *Physics Letters B* 710.45 (2012), pp. 538 –556. ISSN: 0370-2693. DOI: http://dx.doi.org/10.1016/j.physletb.2012.03.022. URL: http://www.sciencedirect.com/science/article/pii/S0370269312002869 (cit. on pp. iii, iv, 38).

[18] ATLAS Collaboration. "Search for high-mass diphoton resonances in pp collisions at $\sqrt{s}$ = 8 TeV with the ATLAS detector". In: *Phys. Rev. D* 92.3 (2015), p. 032004. DOI: 10.1103/PhysRevD.92.032004. arXiv: 1504.05511 [hep-ex] (cit. on pp. iii, 34, 38).

[19] S. e. a. Chatrchyan. "Search for Signatures of Extra Dimensions in the Diphoton Mass Spectrum at the Large Hadron Collider". In: *Phys. Rev. Lett.* 108 (11 2012), p. 111801. DOI: 10.1103/PhysRevLett.108.111801. URL: http://link.aps.org/doi/10.1103/PhysRevLett.108.111801 (cit. on pp. iii, 38).

[20] A. Hill and J.J. van der Bij. "Strongly interacting singlet - doublet Higgs model". In: *Phys. Rev. D* 36 (1987), p. 3463. DOI: 10.1103/PhysRevD.36.3463 (cit. on pp. v, 30).

[21] M. J. G. Veltman and F. J. Yndurain. "Radiative correction to *WW* scattering". In: *NPB* 325 (1989), p. 1. DOI: 10.1016/0550-3213(89)90369-6 (cit. on pp. v, 30).

[22] T. Binoth and J.J. van der Bij. "Influence of strongly coupled, hidden scalars on Higgs signals". In: *Z. Physics. C* 75 (1997), p. 17. DOI: 10.1007/s002880050442. arXiv: hep-ph/9608245 (cit. on pp. v, 30).

[23] R. Schabinger and J. D. Wells. "A minimal spontaneously broken hidden sector and its impact on Higgs boson physics at the CERN Large Hadron Collider". In: *Phys. Rev. D* 72 (2005), p. 093007. DOI: 10.1103/PhysRevD.72.093007. arXiv: hep-ph/0509209 (cit. on pp. v, 30).

[24] B. Patt and F. Wilczek. "Higgs-field portal into hidden sectors". In: (2006). arXiv: hep-ph/0605188 (cit. on pp. v, 30).

[25] G. M. Pruna and T. Robens. "Higgs singlet extension parameter space in the light of the LHC discovery". In: *Phys. Rev. D* 88 (2013), p. 115012. DOI: 10.1103/PhysRevD.88.115012. arXiv: 1303.1150 [hep-ph] (cit. on pp. v, 30).

[26] T. D. Lee. "A theory of spontaneous T violation". In: *Phys. Rev. D* 8 (1973), p. 1226. DOI: 10.1103/PhysRevD.8.1226 (cit. on pp. v, 30).

[27] CMS Collaboration. "Search for diphoton resonances in the mass range from 150 to 850 GeV in pp collisions at $\sqrt{s} = 8$ TeV". In: *PLB* 750 (2015), pp. 494–519. DOI: 10.1016/j.physletb.2015.09.062. arXiv: 1506.02301 [hep-ex] (cit. on pp. v, 34, 38).

[28] M. Peskin and D. Schroeder. *An Introduction to Quantum Field Theory*. Addison-Wesley Advanced Book Program, 1995 (cit. on pp. 3, 7).

[29] C. N. Yang and R. L. Mills. "Conservation of Isotopic Spin and Isotopic Gauge Invariance". In: *Phys. Rev.* 96 (1 1954), pp. 191–195. DOI: 10.1103/PhysRev.96.191. URL: http://link.aps.org/doi/10.1103/PhysRev.96.191 (cit. on p. 5).

[30] E. D. Bloom et al. "High-Energy Inelastic $e-p$ Scattering at 6° and 10°". In: *Phys. Rev. Lett.* 23 (16 1969), pp. 930–934. DOI: 10.1103/PhysRevLett.23.930. URL: http://link.aps.org/doi/10.1103/PhysRevLett.23.930 (cit. on p. 6).

[31] M. Breidenbach et al. "Observed Behavior of Highly Inelastic Electron-Proton Scattering". In: *Phys. Rev. Lett.* 23 (16 1969), pp. 935–939. DOI: 10.1103/PhysRevLett.23.935. URL: http://link.aps.org/doi/10.1103/PhysRevLett.23.935 (cit. on p. 6).

[32] F. Englert and R. Brout. "Broken Symmetry and the Mass of Gauge Vector Mesons". In: *Phys. Rev. Lett.* 13 (9 1964), pp. 321–323. DOI: 10.1103/PhysRevLett.13.321. URL: http://link.aps.org/doi/10.1103/PhysRevLett.13.321 (cit. on p. 9).

[33] P. W. Higgs. "Broken Symmetries and the Masses of Gauge Bosons". In: *Phys. Rev. Lett.* 13 (16 1964), pp. 508–509. DOI: 10.1103/PhysRevLett.13.508. URL: http://link.aps.org/doi/10.1103/PhysRevLett.13.508 (cit. on p. 9).

[34] G. S. Guralnik, C. R. Hagen, and T. W. B. Kibble. "Global Conservation Laws and Massless Particles". In: *Phys. Rev. Lett.* 13 (20 1964), pp. 585–587. DOI: 10.1103/PhysRevLett.13.585. URL: http://link.aps.org/doi/10.1103/PhysRevLett.13.585 (cit. on p. 9).

[35] T. Hahn et al. "SM and MSSM Higgs boson production cross-sections at the Tevatron and the LHC". In: (2006). arXiv: hep-ph/0607308 [hep-ph] (cit. on p. 12).

[36] LHC Higgs Cross Section Working Group et al. "Handbook of LHC Higgs Cross Sections: 1. Inclusive Observables". In: *CERN-2011-002* (CERN, Geneva, 2011). DOI: 10.5170/CERN-2011-002. arXiv: 1101.0593 [hep-ph] (cit. on p. 14).

[37] LHC Higgs Cross Section Working Group et al. "Handbook of LHC Higgs Cross Sections: 2. Differential Distributions". In: *CERN-2012-002* (CERN, Geneva, 2012). DOI: 10.5170/CERN-2012-002. arXiv: 1201.3084 [hep-ph] (cit. on p. 14).

[38] LHC Higgs Cross Section Working Group et al. "Handbook of LHC Higgs Cross Sections: 3. Higgs Properties". In: *CERN-2013-004* (CERN, Geneva, 2013). DOI: 10.5170/CERN-2013-004. arXiv: 1307.1347 [hep-ph] (cit. on p. 14).

[39] G. Aad et al. "Observation of a new particle in the search for the Standard Model Higgs boson with the ATLAS detector at the LHC". In: *Phys.Lett.* B716 (2012), pp. 1–29. DOI: 10.1016/j.physletb.2012.08.020. arXiv: 1207.7214 [hep-ex] (cit. on pp. 14, 16, 17).

[40] S. Chatrchyan et al. "Observation of a new boson at a mass of 125 GeV with the CMS experiment at the LHC". In: *Phys.Lett.* B716 (2012), pp. 30–61. DOI: 10.1016/j.physletb.2012.08.021. arXiv: 1207.7235 [hep-ex] (cit. on pp. 14, 16, 17).

[41] G. Aad et al. "Combined Measurement of the Higgs Boson Mass in pp Collisions at $\sqrt{s} = 7$ and 8 TeV with the ATLAS and CMS Experiments". In: *Phys. Rev. Lett.* 114 (2015), p. 191803. DOI: 10.1103/PhysRevLett.114.191803. arXiv: 1503.07589 [hep-ex] (cit. on pp. 14, 17).

[42] G. Aad et al. "Measurements of the Higgs boson production and decay rates and constraints on its couplings from a combined ATLAS and CMS analysis of the LHC pp collision data at $\sqrt{s} = 7$ and 8 TeV". In: *JHEP* 08 (2016), p. 045. DOI: 10.1007/JHEP08(2016)045. arXiv: 1606.02266 [hep-ex] (cit. on p. 15).

[43] *Measurement of fiducial, differential and production cross sections in the $H \to \gamma\gamma$ decay channel with 13.3 fb^{-1} of 13 TeV proton-proton collision data with the ATLAS detector*. Tech. rep. ATLAS-CONF-2016-067. Geneva: CERN, 2016. URL: http://cds.cern.ch/record/2206210 (cit. on p. 15).

[44] *Study of the Higgs boson properties and search for high-mass scalar resonances in the $H \to ZZ^* \to 4\ell$ decay channel at $\sqrt{s}$ = 13 TeV with the ATLAS detector*. Tech. rep. ATLAS-CONF-2016-079. Geneva: CERN, 2016. URL: http://cds.cern.ch/record/2206253 (cit. on p. 15).

[45] *Combined measurements of the Higgs boson production and decay rates in $H \to ZZ^* \to 4\ell$ and $H \to \gamma\gamma$ final states using pp collision data at $\sqrt{s} = 13$ TeV in the ATLAS experiment*. Tech. rep. ATLAS-CONF-2016-081. Geneva: CERN, 2016. URL: http://cds.cern.ch/record/2206272 (cit. on pp. 15, 18).

[46] Y. Nagashima. *Beyond the standard model of elementary particle physics*. Weinheim, Germany: Wiley-VCH Verlag, 2014. ISBN: 9783527411771. URL: http://www-spires.fnal.gov/spires/find/books/www?cl=QC793.2.N34::2014 (cit. on pp. 21, 24, 27–29, 32).

[47] O. Klein. "Quantum Theory and Five-Dimensional Theory of Relativity. (In German and English)". In: *Z. Phys.* 37 (1926). [Surveys High Energ. Phys.5,241(1986)], pp. 895–906. DOI: 10.1007/BF01397481 (cit. on pp. 21, 23).

[48] S. Cullen and M. Perelstein. "SN1987A constraints on large compact dimensions". In: *Phys. Rev. Lett.* 83 (1999), pp. 268–271. DOI: 10.1103/PhysRevLett.83.268. arXiv: hep-ph/9903422 [hep-ph] (cit. on p. 25).

[49] S. Hannestad and G. G. Raffelt. "Supernova and neutron star limits on large extra dimensions reexamined". In: *Phys. Rev.* D67 (2003). [Erratum: Phys. Rev.D69,029901(2004)], p. 125008. DOI: 10.1103/PhysRevD.69.029901, 10.1103/PhysRevD.67.125008. arXiv: hep-ph/0304029 [hep-ph] (cit. on p. 25).

[50] L. J. Hall and D. Tucker-Smith. "Cosmological constraints on theories with large extra dimensions". In: *Phys. Rev.* D60 (1999), p. 085008. DOI: 10.1103/PhysRevD.60.085008. arXiv: hep-ph/9904267 [hep-ph] (cit. on p. 25).

[51] M. Fairbairn and L. M. Griffiths. "Large extra dimensions, the galaxy power spectrum and the end of inflation". In: *JHEP* 02 (2002), p. 024. DOI: 10.1088/1126-6708/2002/02/024. arXiv: hep-ph/0111435 [hep-ph] (cit. on p. 25).

[52] S. Heinemeyer, W. Hollik, and G. Weiglein. "Constraints on tan Beta in the MSSM from the upper bound on the mass of the lightest Higgs boson". In: *JHEP* 06 (2000), p. 009. DOI: 10.1088/1126-6708/2000/06/009. arXiv: hep-ph/9909540 [hep-ph] (cit. on pp. 32, 37).

[53] M. Carena et al. “Suggestions for benchmark scenarios for MSSM Higgs boson searches at hadron colliders”. In: *Eur. Phys. J.* C26 (2003), pp. 601–607. DOI: 10.1140/epjc/s2002-01084-3. arXiv: hep-ph/0202167 [hep-ph] (cit. on pp. 32, 37).

[54] S. Heinemeyer, W. Hollik, and G. Weiglein. “The masses of the neutral-even Higgs bosons in the MSSM: Accurate analysis at the two-loop level”. In: *The European Physical Journal C - Particles and Fields* 9.2 (1999), pp. 343–366. DOI: 10.1007/s100529900006. URL: http://dx.doi.org/10.1007/s100529900006 (cit. on pp. 32, 37).

[55] A. Djouadi. “The Anatomy of electro-weak symmetry breaking. II. The Higgs bosons in the minimal supersymmetric model”. In: *Phys. Rept.* 459 (2008), pp. 1–241. DOI: 10.1016/j.physrep.2007.10.005. arXiv: hep-ph/0503173 [hep-ph] (cit. on p. 33).

[56] N. Craig et al. “The Hunt for the Rest of the Higgs Bosons”. In: *JHEP* 06 (2015), p. 137. DOI: 10.1007/JHEP06(2015)137. arXiv: 1504.04630 [hep-ph] (cit. on p. 33).

[57] N. Craig, J. Galloway, and S. Thomas. “Searching for Signs of the Second Higgs Doublet”. In: (2013). arXiv: 1305.2424 [hep-ph] (cit. on p. 33).

[58] C. N. Yang. “Selection Rules for the Dematerialization of a Particle into Two Photons”. In: *Phys. Rev.* 77 (2 1950), pp. 242–245. DOI: 10.1103/PhysRev.77.242. URL: http://link.aps.org/doi/10.1103/PhysRev.77.242 (cit. on p. 34).

[59] L. D. Landau. “On the angular momentum of a system of two photons”. In: *Dokl. Akad. Nauk Ser. Fiz.* 60.2 (1948), pp. 207–209. DOI: 10.1016/B978-0-08-010586-4.50070-5 (cit. on p. 34).

[60] ATLAS Collaboration. “Search for extra dimensions in diphoton events using proton-proton collisions recorded at $\sqrt{s} = 7$ TeV with the ATLAS detector at the LHC”. In: *New J. Phys.* 15 (2013), p. 043007. DOI: 10.1088/1367-2630/15/4/043007. arXiv: 1210.8389 [hep-ex] (cit. on p. 34).

[61] CMS Collaboration. “Search for signatures of extra dimensions in the diphoton mass spectrum at the Large Hadron Collider”. In: *PRL* 108 (2012), p. 111801. DOI: 10.1103/PhysRevLett.108.111801. arXiv: 1112.0688 [hep-ex] (cit. on p. 34).

[62] V. M. Abazov et al. “Search for Randall-Sundrum gravitons in the dielectron and diphoton final states with 5.4 fb-1 of data from $p\bar{p}$ collisions at sqrt(s)=1.96 TeV”. In: *Phys. Rev. Lett.* 104 (2010), p. 241802. DOI: 10.1103/PhysRevLett.104.241802. arXiv: 1004.1826 [hep-ex] (cit. on p. 34).

[63] *Search for New Dimuon Resonances and Randall-Sundrum Gravitons (decaying to ee, $\mu\mu$, $\gamma\gamma$) at the Collider Detector at Fermilab*. Tech. rep. CDF Note 10479. Chicago: Fermilab, 2011. URL: https://www-cdf.fnal.gov/physics/exotic/r2a/20110603.fullgraviton/index.html (cit. on p. 34).

[64] *Combination of LEP Results on Direct Searches for Large Extra Dimensions*. Tech. rep. LEP Exotica WG 2004-03. Geneva: CERN, 2004. URL: http://lepexotica.web.cern.ch/LEPEXOTICA/notes/2004-03/ed_note_final.ps.gz (cit. on p. 34).

[65] *Search for neutral MSSM Higgs Boson at LEP*. Tech. rep. LHWG-Note 2005-01. Geneva: CERN, 2005. URL: http://lephiggs.web.cern.ch/LEPHIGGS/papers/July2005_MSSM/LHWG-Note-2005-01.pdf (cit. on pp. 36, 37).

[66] T. Aaltonen et al. "Search for Neutral Higgs Bosons in Events with Multiple Bottom Quarks at the Tevatron". In: *Phys. Rev.* D86 (2012), p. 091101. DOI: 10.1103/PhysRevD.86.091101. arXiv: 1207.2757 [hep-ex] (cit. on p. 36).

[67] A. Coll. "Search for extra dimensions in diphoton events from proton–proton collisions at $\sqrt{s} = 7$ TeV in the ATLAS detector at the LHC". In: *New Journal of Physics* 15.4 (2013), p. 043007. URL: http://stacks.iop.org/1367-2630/15/i=4/a=043007 (cit. on p. 38).

[68] G. Aad et al. "Search for charged Higgs bosons in the $H^{\pm} \to tb$ decay channel in pp collisions at $\sqrt{s} = 8$ TeV using the ATLAS detector". In: *JHEP* 03 (2016), p. 127. DOI: 10.1007/JHEP03(2016)127. arXiv: 1512.03704 [hep-ex] (cit. on p. 38).

[69] G. Aad et al. "Search for a Charged Higgs Boson Produced in the Vector Boson Fusion Mode with Decay $H^{\pm} \to W^{\pm}Z$ using pp Collisions at $\sqrt{s} = 8$ TeV with the ATLAS Experiment". In: *Phys. Rev. Lett.* 114.23 (2015), p. 231801. DOI: 10.1103/PhysRevLett.114.231801. arXiv: 1503.04233 [hep-ex] (cit. on p. 38).

[70] G. Aad et al. "Search for charged Higgs bosons decaying via $H^{\pm} \to \tau^{\pm}\nu$ in fully hadronic final states using pp collision data at $\sqrt{s} = 8$ TeV with the ATLAS detector". In: *JHEP* 03 (2015), p. 088. DOI: 10.1007/JHEP03(2015)088. arXiv: 1412.6663 [hep-ex] (cit. on p. 38).

[71] J. D. Jackson. "Classical Electrodynamics". In: first. Wiley, 1962. Chap. 14, p. 475 (cit. on p. 45).

[72] *Updated Luminosity Determination in pp Collisions at root(s)=7 TeV using the ATLAS Detector*. Tech. rep. ATLAS-CONF-2011-011. Geneva: CERN, 2011. URL: https://cds.cern.ch/record/1334563 (cit. on p. 46).

[73] ATLAS Collaboration. "ATLAS luminosity group public results". In: (2016). URL: https://twiki.cern.ch/twiki/bin/view/AtlasPublic/LuminosityPublicResults (cit. on pp. 47, 48).

[74] L. Evans and P. Bryant. "LHC Machine". In: *JINST* 3 (2008), S08001 (cit. on p. 49).

[75] *ATLAS public results*. URL: https://twiki.cern.ch/twiki/bin/view/AtlasPublic (cit. on p. 51).

[76] *CMS public results*. URL: http://cms.web.cern.ch/content/cms-collaboration (cit. on p. 51).

[77] *LHCb public results*. URL: http://lhcb-public.web.cern.ch/lhcb-public/ (cit. on p. 51).

[78] *ALICE public results*. URL: http://aliceinfo.cern.ch/Public/Welcome.html (cit. on p. 52).

[79] *Totem experiment at Cern*. URL: http://totem-experiment.web.cern.ch/totem-experiment/ (cit. on p. 52).

[80] *LHCf experiment at Cern*. URL: http://hep.fi.infn.it/LHCf/ (cit. on p. 52).

[81] T. Cornelissen et al. "The new ATLAS track reconstruction (NEWT)". In: *J. Phys. Conf. Ser.* 119 (2008), p. 032014. DOI: 10.1088/1742-6596/119/3/032014 (cit. on pp. 55, 78).

[82] T Cornelissen et al. *Concepts, Design and Implementation of the ATLAS New Tracking (NEWT)*. Tech. rep. ATL-SOFT-PUB-2007-007. ATL-COM-SOFT-2007-002. Geneva: CERN, 2007. URL: https://cds.cern.ch/record/1020106 (cit. on pp. 55, 78).

[83] *ATLAS: Detector and physics performance technical design report.* Vol. 1. CERN-LHCC-99-14, 1999 (cit. on pp. 59, 65).

[84] *ATLAS liquid-argon calorimeter: Technical Design Report*. Geneva: CERN, 1996. ISBN: 9789290830900 (cit. on pp. 59, 223).

[85] *ATLAS muon spectrometer: Technical Design Report*. Geneva: CERN, 1997 (cit. on p. 65).

[86] G. Aad et al. (ATLAS Collaboration). *Expected Performance of the ATLAS Experiment - Detector, Trigger and Physics*. 2009. arXiv: 0901.0512 [hep-ex] (cit. on p. 65).

[87] *The ATLAS Computing Technical Design Report*. CERN-LHCC/2005-022, 2005 (cit. on p. 67).

[88] M. Aaboud et al. "Performance of the ATLAS Trigger System in 2015". In: (2016). arXiv: 1611.09661 [hep-ex] (cit. on pp. 72, 73).

[89] ATLAS Collaboration. "ATLAS trigger operation public results". In: (2016). URL: https://twiki.cern.ch/twiki/bin/view/AtlasPublic/TriggerOperationPublicResults (cit. on p. 73).

[90] S. Agostinelli et al. "GEANT4: A Simulation toolkit". In: *Nucl. Instrum. Meth.* A506 (2003), pp. 250–303. DOI: 10.1016/S0168-9002(03)01368-8 (cit. on pp. 74, 78).

[91] G. Aad et al. "The ATLAS Simulation Infrastructure". In: *Eur. Phys. J.* C70 (2010), pp. 823–874. DOI: 10.1140/epjc/s10052-010-1429-9. arXiv: 1005.4568 [physics.ins-det] (cit. on p. 74).

[92] *Electron efficiency measurements with the ATLAS detector using the 2015 LHC proton-proton collision data*. Tech. rep. ATLAS-CONF-2016-024. Geneva: CERN, 2016. URL: http://cds.cern.ch/record/2157687 (cit. on pp. 75–77).

[93] W. Lampl et al. *Calorimeter Clustering Algorithms: Description and Performance*. ATL-LARG-PUB-2008-002. 2008 (cit. on p. 75).

[94] T. Cornelissen et al. "The global χ^2 track fitter in ATLAS". In: *J. Phys. Conf. Ser.* 119 (2008), p. 032013. DOI: 10.1088/1742-6596/119/3/032013 (cit. on p. 76).

[95] ATLAS Collaboration. *Improved electron reconstruction in ATLAS using the Gaussian Sum Filter-based model for bremsstrahlung*. ATLAS-CONF-2012-047. 2012. URL: http://cdsweb.cern.ch/record/1449796 (cit. on p. 76).

[96] ATLAS Collaboration. *Electron efficiency measurements with the ATLAS detector using the 2012 LHC proton–proton collision data*. ATLAS-CONF-2014-032. 2014. URL: http://cdsweb.cern.ch/record/1706245 (cit. on pp. 76, 93).

[97] G. Aad et al. "Electron and photon energy calibration with the ATLAS detector using LHC Run 1 data". In: *Eur. Phys. J.* C74.10 (2014), p. 3071. DOI: 10.1140/epjc/s10052-014-3071-4. arXiv: 1407.5063 [hep-ex] (cit. on pp. 76, 82, 87).

[98] *Measurement of the photon identification efficiencies with the ATLAS detector using LHC Run-1 data*. Tech. rep. CERN-EP-2016-110. arXiv:1606.01813. Comments: 40 pages plus author list (57 pages total), 17 figures, 2 tables, submitted to Eur. Phys. J. C, All figures including auxiliary figures are available at http://atlas.web.cern.ch/Atlas/GROUPS/PHYSICS/PAPERS/PER 2013-04/. Geneva: CERN, 2016. URL: https://cds.cern.ch/record/2158117 (cit. on p. 78).

[99] *ATLAS photon conversion fractions*. URL: https://atlas.web.cern.ch/Atlas/GROUPS/PHYSICS/PLOTS/EGAM-2015-004/index.html (cit. on p. 81).

[100] ATLAS Collaboration. "Expected photon performance in the ATLAS experiment". In: *ATL-PHYS-PUB-2011-007* (2011). URL: http://cdsweb.cern.ch/record/1345329 (cit. on pp. 81, 82).

[101] *Photon identification in 2015 ATLAS data*. Tech. rep. ATL-PHYS-PUB-2016-014. Geneva: CERN, 2016. URL: https://cds.cern.ch/record/2203125 (cit. on pp. 82–84).

[102] ATLAS Collaboration. "Electron and photon energy calibration with the ATLAS detector using LHC Run 1 data". In: *Eur. Phys. J. C* 74 (2014), p. 3071. DOI: 10.1140/epjc/s10052-014-3071-4. arXiv: 1407.5063 [hep-ex] (cit. on pp. 86, 88).

[103] *Electron and photon energy calibration with the ATLAS detector using data collected in 2015 at* $\sqrt{s} = 13$ TeV. Tech. rep. ATL-PHYS-PUB-2016-015. Geneva: CERN, 2016. URL: https://cds.cern.ch/record/2203514 (cit. on pp. 86, 89, 91).

[104] K. Rehermann and B. Tweedie. "Efficient Identification of Boosted Semileptonic Top Quarks at the LHC". In: *JHEP* 1103 (2011), p. 059. DOI: 10.1007/JHEP03(2011)059. arXiv: 1007.2221 [hep-ph] (cit. on p. 93).

[105] W Lampl et al. *Calorimeter Clustering Algorithms: Description and Performance*. Tech. rep. ATL-LARG-PUB-2008-002. ATL-COM-LARG-2008-003. Geneva: CERN, 2008 (cit. on p. 93).

[106] M. Cacciari, G. P. Salam and G. Soyez, "FastJet user manual". In: *Eur. Phys. J. C* 72 (2012), p. 1896 (cit. on p. 95).

[107] G. Aad et al. "Muon reconstruction performance of the ATLAS detector in proton–proton collision data at $\sqrt{s}$ =13 TeV". In: *Eur. Phys. J.* C76.5 (2016), p. 292. DOI: 10.1140/epjc/s10052-016-4120-y. arXiv: 1603.05598 [hep-ex] (cit. on pp. 103, 104).

[108] J. Illingworth and J. Kittler. "A survey of the Hough transform". In: *Computer Vision, Graphics, and Image Processing* 44.1 (1988), pp. 87 –116. ISSN: 0734-189X. DOI: http://dx.doi.org/10.1016/S0734-189X(88)80033-1. URL: http://www.sciencedirect.com/science/article/pii/S0734189X88800331 (cit. on p. 103).

[109] *Properties of Jets and Inputs to Jet Reconstruction and Calibration with the ATLAS Detector Using Proton-Proton Collisions at* $\sqrt{s} = 13$ *TeV*. Tech. rep. ATL-PHYS-PUB-2015-036. Geneva: CERN, 2015. URL: http://cds.cern.ch/record/2044564 (cit. on p. 105).

[110] *Selection of jets produced in 13TeV proton-proton collisions with the ATLAS detector*. Tech. rep. ATLAS-CONF-2015-029. Geneva: CERN, 2015. URL: http://cds.cern.ch/record/2037702 (cit. on p. 105).

[111] M. Cacciari, G. P. Salam, and G. Soyez. "The Anti-k(t) jet clustering algorithm". In: *JHEP* 04 (2008), p. 063. DOI: 10.1088/1126-6708/2008/04/063. arXiv: 0802.1189 [hep-ph] (cit. on p. 105).

[112] G. Aad et al. "Jet energy measurement with the ATLAS detector in proton-proton collisions at $\sqrt{s} = 7$ TeV". In: (2011). arXiv: 1112.6426 [hep-ex] (cit. on p. 105).

[113] *Estimate of the* m_H *shift due to interference between signal and background processes in the* $H \to \gamma\gamma$ *channel, for the* $\sqrt{s} = 8$ *TeV dataset recorded by ATLAS*. Tech. rep. ATL-PHYS-PUB-2016-009. Geneva: CERN, 2016. URL: http://cds.cern.ch/record/2146386 (cit. on p. 111).

[114] S. Alioli et al. "NLO Higgs boson production via gluon fusion matched with shower in POWHEG". In: *JHEP* 0904 (2009), p. 002. DOI: 10.1088/1126-6708/2009/04/002. arXiv: 0812.0578 [hep-ph] (cit. on p. 112).

[115] P. Nason and C. Oleari. "NLO Higgs boson production via vector-boson fusion matched with shower in POWHEG". In: *JHEP* 1002 (2010), p. 037. DOI: 10.1007/JHEP02(2010)037. arXiv: 0911.5299 [hep-ph] (cit. on p. 112).

[116] T. Gleisberg et al. "Event generation with SHERPA 1.1". In: *JHEP* 02 (2009), p. 007. DOI: 10.1088/1126-6708/2009/02/007. arXiv: 0811.4622 [hep-ph] (cit. on p. 113).

[117] *Study of the spin of the new boson with up to 25* fb^{-1} *of ATLAS data*. Tech. rep. ATLAS-CONF-2013-040. Geneva: CERN, 2013. URL: http://cds.cern.ch/record/1542341 (cit. on p. 115).

[118] B. Lenzi and D. Delgove. *Selection of the diphoton production vertex using multivariate techniques for* $H \to \gamma\gamma$ *and other analyses*. Tech. rep. ATL-COM-PHYS-2015-1321. Geneva: CERN, 2015. URL: https://cds.cern.ch/record/2062239 (cit. on p. 127).

[119] ATLAS Collaboration. "Measurement of isolated-photon pair production in pp collisions at $\sqrt{s} = 7$ TeV with the ATLAS detector". In: *JHEP* 1301 (2013), p. 086. DOI: 10.1007/JHEP01(2013)086. arXiv: 1211.1913 [hep-ex] (cit. on pp. 131, 154).

[120] ATLAS Collaboration. "Measurement of the isolated diphoton cross section in pp collisions at $\sqrt{s} = 7$ TeV with the ATLAS detector". In: *Phys. Rev. D* 85 (2012), p. 012003. DOI: 10.1103/PhysRevD.85.012003. arXiv: 1107.0581 [hep-ex] (cit. on p. 132).

[121] T. Binoth et al. "A full next-to-leading order study of direct photon pair production in hadronic collisions". In: *EPJ-C* 16 (2000), p. 311. DOI: 10.1007/s100520050024. arXiv: hep-ph/9911340 [hep-ph] (cit. on pp. 134, 152).

[122] E. Gross and O. Vitells. "Trial factors or the look elsewhere effect in high energy physics". In: *EPJ-C* 70 (2010), p. 525. DOI: 10.1140/epjc/s10052-010-1470-8. arXiv: 1005.1891 [physics.data-an] (cit. on p. 134).

[123] G. Cowan et al. "Asymptotic formulae for likelihood-based tests of new physics". In: *EPJ-C* 71 (2011). [Erratum: Eur. Phys. J.C73,2501(2013)], p. 1554. DOI: 10.1140/epjc/s10052-011-1554-0,10.1140/epjc/s10052-013-2501-z. arXiv: 1007.1727 [physics.data-an] (cit. on p. 134).

[124] O. Vitells and E. Gross. "Estimating the significance of a signal in a multi-dimensional search". In: *Astropart. Phys.* 35 (2011), pp. 230–234. DOI: 10.1016/j.astropartphys.2011.08.005. arXiv: 1105.4355 [astro-ph.IM] (cit. on pp. 134, 181).

[125] J. Bijnens et al. "QCD signatures of narrow graviton resonances in hadron colliders". In: *Phys. Lett.* B503 (2001), pp. 341–348. DOI: 10.1016/S0370-2693(01)00238-6. arXiv: hep-ph/0101316 [hep-ph] (cit. on p. 139).

[126] K. S. Cranmer. "Kernel estimation in high-energy physics". In: *Comput. Phys. Commun.* 136 (2001), pp. 198–207. DOI: 10.1016/S0010-4655(00)00243-5. arXiv: hep-ex/0011057 [hep-ex] (cit. on pp. 141, 235).

[127] M. Baak et al. "Interpolation between multi-dimensional histograms using a new non-linear moment morphing method". In: *Nucl. Instrum. Meth.* A771 (2015), pp. 39–48. DOI: 10.1016/j.nima.2014.10.033. arXiv: 1410.7388 [physics.data-an] (cit. on p. 141).

[128] ATLAS Collaboration. "Measurement of the isolated diphoton cross-section in pp collisions at $\sqrt{s} = 7$ TeV with the ATLAS detector". In: *Phys.Rev.* D85 (2012), p. 012003. DOI: 10.1103/PhysRevD.85.012003. arXiv: 1107.0581 [hep-ex] (cit. on p. 154).

[129] *Wikipedia, nested models*. URL: en.wikipedia.org/wiki/Statistical_model#Nested_models (cit. on p. 157).

[130] *Wikipedia, F-Test*. URL: en.wikipedia.org/wiki/F-test (cit. on p. 158).

[131] A. Collaboration. "Improved luminosity determination in pp collisions at $sqrt(s) = 7$ TeV using the ATLAS detector at the LHC". In: *Eur. Phys. J. C 73* (2013). URL: http://arxiv.org/pdf/1302.4393v2.pdf (cit. on pp. 170, 175).

[132] ATLAS HGamma Working Group. "Selection and performance for the $H \to \gamma\gamma$ and $H \to Z\gamma$ analyses". In: *ATL-COM-PHYS-2015-1326* (2015). URL: https://cds.cern.ch/record/2056957 (cit. on pp. 170, 175).

[133] I. Asimov. *Franchise, in Isaac Asimov: The Complete Stories Vol 1*. 1990 (cit. on pp. 179, 181, 218).

[134] E. Gross and O. Vitells. "Trial factors for the look elsewhere effect in high energy physics". In: *Eur. Phys. J* C70 (2010), p. 525 (cit. on p. 181).

[135] A. L. Read. "Presentation of search results: The CL_s technique". In: *J. Phys.* G28 (2002), p. 2963 (cit. on p. 181).

[136] S. S. Wilks. "The Large-Sample Distribution of the Likelihood Ratio for Testing Composite Hypotheses". English. In: *The Annals of Mathematical Statistics* 9.1 (1938), pp. 60–62. ISSN: 00034851. URL: http://www.jstor.org/stable/2957648 (cit. on p. 213).

[137] A. Wald. "Tests of Statistical Hypotheses Concerning Several Parameters When the Number of Observations is Large". English. In: *Transactions of the American Mathematical Society* 54.3 (1943), pp. 426–482. ISSN: 00029947. URL: http://www.jstor.org/stable/1990256 (cit. on p. 213).

[138] G. Cowan et al. "Asymptotic formulae for likelihood-based tests of new physics". In: *European Physical Journal C* 71 (Feb. 2011), p. 1554. DOI: 10.1140/epjc/s10052-011-1554-0. arXiv: 1007.1727 [physics.data-an] (cit. on p. 213).

[139] A. S. J. O. S. Arnold. *Kendall's Advanced Theory of Statistics, Vol. 2A: Classical Inference and the Linear Model 6th Ed*. Oxford Univ. Press, 1999 (cit. on p. 213).

So long and thanks...

... for all the fish.